Spin ensembles in superconducting nonlinear cavities

Mykhailo Savytskyi

A thesis in fulfilment of the requirements for the degree of
Doctor of Philosophy

UNSW
AUSTRALIA

School of Electrical Engineering and Telecommunications
Faculty of Engineering

July 15, 2021

Thesis Title and Abstract | Declarations | Inclusion of Publications Statement | Corrected Thesis and Responses

Thesis Title

Spin ensembles in superconducting nonlinear cavities

Thesis Abstract

Circuit quantum electrodynamics (cQED) provides a modern test bed for exploring the well-established physics of cavity quantum electrodynamics. cQED exploits circuit-based cavities that are fabricated on a chip and interfaced with real or artificial atoms to examine a range of light-matter interactions. It has gained considerable popularity and became one of the most powerful platforms to experimentally explore quantum mechanical effects in the solid state.

cQED offers a simple way to couple together distinct quantized degrees of freedom, and this has instigated a new sub-field often referred to as “hybrid quantum systems”. Through combining different quantum systems with superconducting circuits, one can deploy the cQED toolbox to deliver advantages in other fields. Recently, superconducting micro-resonators have been used in conjunction with microwave parametric amplifiers to push the detection sensitivity in Electron Spin Resonance (ESR) spectroscopy to the quantum noise limit. ESR spectroscopy is an important technique for studying the structure and function of materials, broadly utilized throughout chemistry, physics and biology and sensitive enhancement is often a highly prized goal.

The superconducting parametric amplifier circuits employed in previous quantum-limited ESR experiments have all been based on Josephson junction technology -- a lossless nonlinear element that enables many important cQED devices -- and are incompatible with the high magnetic fields often required by spins. Spin signals are collected using a linear resonator and must be routed to the amplifier (housed away from any magnetic fields) through various microwave components and cables, which introduce loss and complexity. In this thesis we develop a new type of superconducting parametric amplifier that utilizes a nonlinear kinetic inductance, called the KIPA. The amplifier contains no Josephson junctions and is compatible with the large magnetic fields relevant for ESR spectroscopy. We analyze the key properties of this new amplifier and demonstrate that it has excellent characteristics, including a quantum-limited noise performance and high dynamic range. In a break from previous work, we integrate the spins directly with this parametric amplifier and show that the spin signals can be collected and amplified all within the same device, greatly simplifying the quantum-limited spectrometer design.

By adopting analogues from optomechanics, we develop and lay the experimental groundwork for an idea that utilizes the nonlineaity of our KIPA circuit to parametrically cool a spin ensemble coupled to it. We show that we are able to induce a parametric interaction between the fundamental mode and first harmonic of the device, which can in-principle be used to cool the lower frequency mode. By coupling the electron spins to the fundamental mode, their polarization can be increased through Purcell relaxation (or radiative cooling), where the spins relax via photon emission into the device and thus thermalize to the photon temperature. This constitutes an active cooling process and can be used to lower the effective spin temperature below that of the cryostat to which the device is thermally anchored. Our proposed active cooling scheme would have application in low-temperature ESR spectroscopy, where the resulting population enhancement directly translates to a sensitivity gain.

This thesis presents a novel hybrid architecture that combines spins in a solid-state chip with a new type of high-performance superconducting parametric amplifier, allowing for high-sensitivity detection of the spins through parametric amplification and cooling, where both processes may be performed entirely on-chip. The results are of interest to a range of fields, particularly ESR spectroscopy and superconducting-based quantum information processing (QIP).

Thesis Title and Abstract | Declarations | Inclusion of Publications Statement | Corrected Thesis and Responses

ORIGINALITY STATEMENT

☑ I hereby declare that this submission is my own work and to the best of my knowledge it contains no materials previously published or written by another person, or substantial proportions of material which have been accepted for the award of any other degree or diploma at UNSW or any other educational institution, except where due acknowledgement is made in the thesis. Any contribution made to the research by others, with whom I have worked at UNSW or elsewhere, is explicitly acknowledged in the thesis. I also declare that the intellectual content of this thesis is the product of my own work, except to the extent that assistance from others in the project's design and conception or in style, presentation and linguistic expression is acknowledged.

COPYRIGHT STATEMENT

☑ I hereby grant the University of New South Wales or its agents a non-exclusive licence to archive and to make available (including to members of the public) my thesis or dissertation in whole or part in the University libraries in all forms of media, now or here after known. I acknowledge that I retain all intellectual property rights which subsist in my thesis or dissertation, such as copyright and patent rights, subject to applicable law. I also retain the right to use all or part of my thesis or dissertation in future works (such as articles or books).

For any substantial portions of copyright material used in this thesis, written permission for use has been obtained, or the copyright material is removed from the final public version of the thesis.

AUTHENTICITY STATEMENT

☑ I certify that the Library deposit digital copy is a direct equivalent of the final officially approved version of my thesis.

Thesis Title and Abstract | Declarations | **Inclusion of Publications Statement** | Corrected Thesis and Responses

UNSW is supportive of candidates publishing their research results during their candidature as detailed in the UNSW Thesis Examination Procedure.

Publications can be used in the candidate's thesis in lieu of a Chapter provided:

- The candidate contributed **greater than 50%** of the content in the publication and are the "primary author", i.e. they were responsible primarily for the planning, execution and preparation of the work for publication.
- The candidate has obtained approval to include the publication in their thesis in lieu of a Chapter from their Supervisor and Postgraduate Coordinator.
- The publication is not subject to any obligations or contractual agreements with a third party that would constrain its inclusion in the thesis.

☑ The candidate has declared that **their thesis contains no publications, either published or submitted for publication**.

Candidate's Declaration

I declare that I have complied with the Thesis Examination Procedure.

Abstract

Circuit quantum electrodynamics (cQED) provides a modern test bed for exploring the well-established physics of cavity quantum electrodynamics. cQED exploits circuit-based cavities that are fabricated on a chip and interfaced with real or artificial atoms to examine a range of light-matter interactions. It has gained considerable popularity and became one of the most powerful platforms to experimentally explore quantum mechanical effects in the solid state. cQED offers a simple way to couple together distinct quantized degrees of freedom, and this has instigated a new sub-field often referred to as "hybrid quantum systems". Through combining different quantum systems with superconducting circuits, one can deploy the cQED toolbox to deliver advantages in other fields. Recently, superconducting micro-resonators have been used in conjunction with microwave parametric amplifiers to push the detection sensitivity in electron spin resonance (ESR) spectroscopy to the quantum noise limit. ESR spectroscopy is an important technique for studying the structure and function of materials, broadly utilized throughout chemistry, physics and biology and sensitive enhancement is often a highly prized goal.

The superconducting parametric amplifier circuits employed in previous quantum-limited ESR experiments have all been based on Josephson junction technology – a lossless nonlinear element that enables many important cQED devices – and are incompatible with the high magnetic fields often required by spins. Spin signals are collected using a linear resonator and must be routed to the amplifier (housed away from any magnetic fields) through various microwave components and cables, which introduce loss and complexity. In this thesis we develop a new type of superconducting parametric amplifier that utilizes a nonlinear kinetic inductance, called the KIPA. The amplifier contains no Josephson junctions and is compatible with the large magnetic fields relevant for ESR spectroscopy. We analyze the key properties of this new amplifier and demonstrate that it has excellent characteristics, including a quantum-limited noise performance and high dynamic range. In a break from previous work, we integrate the spins directly with this parametric amplifier and show that the spin signals can be collected and amplified all within the same device, greatly simplifying the quantum-limited spectrometer design.

By adopting analogues from optomechanics, we develop and lay the experimental groundwork for an idea that utilizes the nonlinearity of our KIPA circuit to parametrically cool a spin ensemble coupled to it. We show that we can induce a parametric interaction between the fundamental mode and first harmonic of the device, which can in-principle be used to cool the lower frequency mode. By coupling the electron spins to the fundamental mode, their polarization can be increased through Purcell relaxation

(or radiative cooling), where the spins relax via photon emission into the device and thus thermalize to the photon temperature. This constitutes an active cooling process and can be used to lower the effective spin temperature below that of the cryostat to which the device is thermally anchored. Our proposed active cooling scheme would have application in low-temperature ESR spectroscopy, where the resulting population enhancement directly translates to a sensitivity gain.

This thesis presents a novel hybrid architecture that combines spins in a solid-state chip with a new type of high-performance superconducting parametric amplifier, allowing for high-sensitivity detection of the spins through parametric amplification and cooling, where both processes may be performed entirely on-chip. The results are of interest to a range of fields, particularly ESR spectroscopy and superconducting-based quantum information processing (QIP).

Acknowledgements

This PhD project is a result of efforts and support from many people whom I am deeply grateful.

First of all, I would like to thank Dr Jarryd Pla for giving me the opportunity to become your first PhD student and to work on this amazing project with you. I also thank you for your supervision of my work, for your patience, for many fruitful discussions and for the great support in my research. I am grateful for entrusting me to join you in building and setting up the new lab. And finally, you provided me with a fantastic opportunity to spend four unforgettable years in Australia. Thank you!

I am thankful to Prof. Andrea Morello for your support of my work, for being my co-supervisor, for our many interesting discussions and for accepting me as a part of your group.

I thank Daniel Parker, a brilliant engineer and fellow student, for your support with hardware and software that made the experiments presented in this thesis possible. I want to thank Wyatt Vine for helping me with measurements, productive discussions and boost of excitement during hard times.

I would like to express my gratitude to Prof. Tim Duty for providing the dilution refrigerator setup that was used for the experiments presented in one of the chapters.

I am also grateful to Prof. Torsten Lehmann, Dr Aaron Michael, Dr Fay Hudson, Dr Tuomo Taantu, Dr Arne Laucht for supporting and monitoring the progress of my PhD studies.

I thank Joanna Szymanska, Dr Andrew See, Josiah Firth, Prof. Andrew Dzurak and all ANFF-NSW staff members for training and advising me in regards of nanofabrication and for providing me with the opportunity to fabricate my devices for this PhD project. For the support and continuous supply of liquid helium and liquid nitrogen required to operate the cryogenic setup I thank Dr Rodrigo Ormeno.

I thank Dr Vivien Schmitt, Dr Vincent Mourik and Dr Tim Botzem for providing useful tips and discussions on handling microwave equipment, operation of cryostats and nanofabrication. Also, I am grateful to the group of Prof. Andrea Morello for creating a pleasant working atmosphere in the office and for all our parties together.

I am very thankful to my family and their limitless support in all my endeavours. Especially, to my brother, Rostyslav Savytskyy, whose wisdom, advice and appreciation were extremely important for me.

Finally, I would like to thank my wife, Tetiana, whose love and support over the years has been crucial in the completion of this PhD. Thank you for your courage to adventures that yielded so many happy memories. I look forward to having many more together in the years to come.

Contents

List of Figures

List of Tables

Acronyms

3WM	three wave mixing
4WM	four wave mixing
AWG	arbitrary waveform generator
BCS	Bardeen-Cooper-Schrieffer
CPMG	Carr-Purcell-Meiboom-Gill
CPW	coplanar waveguide
cQED	circuit quantum electrodynamics
CQED	cavity quantum electrodynamics
CST	Computer Simulation Technology
DPA	degenerate parametric amplifier
EBL	electron beam lithography
EM	electromagnetic
ESD	electrostatic discharge
ESR	electron spin resonance
FEM	finite element method
FID	free induction decay
FZ	float-zone
HEMT	High Electron Mobility Transistor
IDC	interdigitated capacitor
IVC	inner vacuum chamber
JPA	Josephson parametric amplifier
KIPA	kinetic inductance parametric amplifier
LGR	loop-gap resonator
LO	local oscillator
LPF	low-pass filter
MKID	microwave kinetic inductance detectors
MOS	metal-oxide-semiconductor

NI	National Instruments
PBG	photonic bandgap
PCB	printed circuit board
QHO	quantum harmonic oscillator
QIP	quantum information processing
RIE	reactive ion etching
RMS	root-mean-square
RWA	rotating wave approximation
SMU	source measurement unit
SNR	signal-to-noise ratio
SQUID	superconducting quantum interference device
TEM	transverse electromagnetic
TL	transmission line
TLS	two level system
US	ultrasonicate
VNA	vector network analyzer

Chapter 1

Introduction

1.1 The dawn of quantum experiments

At the end of nineteenth century physicists believed that their understanding of the nature was close to being complete [1]. This notion was backed by their classical theory based on Newtonian mechanics [2], where everything is deterministic and can be predicted a priori. However, there were some "minor discrepancies" that could not be explained with classical theory. For instance, according to the theory the distribution of electromagnetic radiation of a black body at higher frequencies (toward the ultraviolet end of the spectrum) should become infinite, known as the ultraviolet catastrophe. Contrary to this, experiments proved the opposite – it approaches zero. The controversy was resolved by a new theory, now called quantum mechanics, first introduced in 1900 by Max Planck [3]. This theory of atoms and subatomic particles introduced concepts such as quanta of energy, particle-wave duality, superposition and entanglement – foreign concepts to physicists at the time.

At the beginning of twentieth century the founders of quantum mechanics used a tool known as thought (or gedanken) experiments to test their theories, since it was technically impossible to perform experiments with single photons, atoms or electrons at the time. These experiments required apparatus with detection sensitivities close to the level of a single quanta. This all changed over the space of a century thanks to the development of modern technologies. The quantum thought experiments became real. The first single-atom experiments were performed with ions confined in electromagnetic traps [4]. The ions were localized using gradients of magnetic and electric fields, and light transmitted through them carried information on their quantum states, which could be detected and analyzed.

Another early experimental study of the interactions of photons and matter were performed on atoms in 3D electromagnetic cavities [5], [6]. These breakthrough experiments led to the 2012 Nobel Prize in Physics [7] and an entirely new field of study called cavity quantum electrodynamics (CQED), a sub-field of quantum optics. For cavity QED in the microwave domain, the photons are confined in a high quality factor microwave cavity that typically has walls made from a low-loss superconducting material. The atoms are prepared in excited Rydberg states that possess large electric dipole moments. This results in an enhanced interaction strength (coupling) between the photons and the atoms. After passing through the cavity, the atoms are measured by a state-selective field-ionization detector. Depending on the atom-photon interaction

time one can infer information on the cavity field evolution [8].

1.2 cQED

The groundbreaking cavity QED experiments of the late twentieth century involving single atoms and quantized electromagnetic fields revealed the rich nature of light-matter interactions and the potential to exploit them in new technologies. At the end of twentieth century, enabled by increasing access to advanced micro- and nanofabrication facilities at the research institution level, cavity QED experiments were translated to two dimensions, leading to the establishment of the new sub-field of circuit QED (cQED) [9], [10]. Here the 3D cavity with highly reflective walls is replaced with a planar circuit-based resonator (often called cavities as well) fabricated on a dielectric substrate (e.g. silicon or sapphire). In cQED the natural atoms can be replaced by mesoscopic quantized electrical circuits that mimic the energy spectra of real atoms, and are thus typically called artificial atoms [11]. The majority of artificial atoms are made from lumped-element LC resonant circuits with integrated Josephson junctions, which add anharmonicity to produce unequal energy level spacings.

cQED has facilitated fundamental investigations in light-matter interactions, for example, to measure and entangle macroscopic quantum objects [12]. Artificial atoms have been exploited to catch and reverse quantum jumps [13], supporting the modern quantum trajectory theory [14], [15]. Moreover, cQED has been instrumental in scaling up quantum computers made from superconducting circuits [16]. A wide variety of superconducting quantum bits (qubits) have been developed from artificial atoms, including the "Cooper pair box" (or charge qubit) [17], "flux qubit" [18], "phase qubit" [19], "transmon" [20] and the "fluxonium" [21]. The high quality factors provided by superconducting circuit resonators allowed for strong coupling with superconducting qubits, resulting in practical realizations of the coherent transfer of excitations between resonators and qubits. [22]. In conjunction with the development of fast control electronics cQED enables the successful interconnection of substantial numbers of superconducting qubits [23] facilitating complex quantum circuits for implementing quantum error correction [12].

Aside from their utility in quantum information processing, cQED devices provide a platform for connecting different quantum degrees of freedom together. Planar

resonators offer the means to deliver classical and non-classical states of light to an ancillary system of interest. cQED has facilitated the study of hybrid quantum systems, where new technologies are being developed that combine the strengths of different physical systems [24].

1.3 Hybrid systems

The pioneering early work in cQED positioned it as an excellent testbed for exploring the control of quantum states of artificial atoms and provided a new way to interact with other systems.

cQED techniques have successfully been integrated with a diverse range of quantum systems, such as phonons in surface acoustic resonators [25] and bulk acoustic resonators [26]. Magnetic coupling of single electron spins [27] and ensembles of spins [28] with microwave resonators has also been achieved in a cQED context. Moreover, moving to high-density spin systems like ferromagnets has even allowed the coupling of magnons (or spin waves) to superconducting circuits [29]. cQED can therefore be used to probe previously unexplored quantum regimes of a variety of physical systems.

The connection of different quantum systems via cQED allows for the creation of hybrid quantum devices [24], where the primary goal is to exploit the inherent advantages of different systems to perform a task that none of the systems could achieve in isolation. However, interfacing distinct quantum systems can present several challenges in practice. For example, the systems of interest may have substantially different natural excitation frequencies, resulting in the need for a transducer [30]. Another problem can arise from if the systems share a weak coupling, relative to their individual rates of loss. For instance, the coupling of a single electron spin to the mode of a microwave resonator (~ 50 Hz [31]) is typically many orders of magnitude smaller than the photon loss rates from cavities (> 10 kHz [32]) and spin dephasing rates (> 1 kHz [33]), making the coherent transfer of quantum information between the systems a formidable challenge. For this reason, electron spin ensembles are typically employed – they lead to collective effects that can enhance the coupling rate, allowing coherent transfer to take place [34].

This thesis is concerned with hybrid devices combining superconducting circuits and spin ensembles. Instead of focusing on coherent interactions we work with a weakly-

coupled spin-resonator system and use QED phenomena such as the Purcell effect as well as parametric interactions to deliver new techniques and devices for enhanced electron spin resonance (ESR) spectroscopy – a widely used method for characterization of paramagnetic materials in biology, chemistry, and physics [35].

Many efforts have been made to improve the sensitivity of detection in ESR through the use of superconducting circuits. Recent pioneering research has demonstrated spin sensitivity enhancement by integrating quantum-limited microwave parametric amplifiers into the signal detection chain [31]. Planar superconducting resonators are used to inductively couple to the spins; the small structures enhance the magnetic field fluctuations and lead to greater spin-resonator couplings (relative to typical 3D cavities) and thus improved sensitivities. Reducing the size of the inductive element in the resonator can further confine the magnetic mode volume and thereby enhance magnetic field fluctuations and the detection sensitivity [36], [37]. Another cQED approach to increase ESR sensitivity was demonstrated using engineered quantum states of light, where degenerate parametric amplifiers were employed to squeeze the background vacuum noise as the spins emit their signals, leading to a higher signal-to-noise ratio (SNR) [38]. Finally, the most recent efforts in the field have shown another route to boost spin signals through hyper-polarization, achieved via radiative cooling of a spin ensemble [39].

In this thesis we take a step further and combine an electron spin ensemble directly with a nonlinear superconducting resonator that can be used as a parametric amplifier. We show that this combination has great potential for improving SNR and thus sensitivity in ESR spectroscopy. The nonlinearity of the resonator enables a range of parametric processes, of which we explore amplification and cooling in this thesis.

1.4 Thesis outline

The thesis begins with a general introduction to the field of cQED and presents a theoretical treatment of the quantum mechanical states of light in a resonant microwave circuit. After having introduced the physics of linear microwave resonators, we discuss how nonlinearities can be added to enable frequency tunability and parametric processes. We then present classical and quantum mechanical treatments of the physics behind the other important component of our hybrid devices – electron spins. The spin system employed in this work is provided by bismuth (^{209}Bi) dopants in silicon.

We discuss the properties of this system in detail and present theory to describe the interaction of spins with the mode of a microwave resonator.

In Ch. 3 we outline details of the device design, fabrication and packaging. We also introduce the cryogenic systems utilized in our experiments along with a detailed account of the microwave measurement setup, including the cryogenic microwave components and the room temperature measurement electronics. At the end of this chapter we provide a description of some important ESR pulse sequences that are used later in our experiments.

In Ch. 4 we present an experimental study of the application of our nonlinear resonator as a parametric amplifier. The amplifier uses a three wave mixing (3WM) process to achieve both phase-insensitive and phase-sensitive parametric amplification. We explore the ability of the amplifier to perform squeezing by observing the amplification and deamplification of coherent signals. Finally we measure the amplifier noise temperature and show that it operates at the quantum noise limit.

In Ch. 5 we apply the parametric amplification capability of our device to ESR spectroscopy. We first utilize the device as a cavity to inductively detect spin echo signals from an ensemble of bismuth donors and characterize their ESR transitions. Next, we add a pulsed pump tone when the echo response is expected and show that both detection and parametric amplification of spin signals can be implemented entirely on-chip, resulting in a substantial measurement SNR.

In Ch. 6 we explain how our device can be used to parametrically cool the spins. We start with a theoretical framework on the parametric cooling of a mode in a multimode nonlinear resonator. Following this we experimentally demonstrate parametric coupling of two of the modes in our resonator and characterize important system parameters. We further show that we are able to achieve strong coupling between these two modes. Finally, we outline steps and device modifications that are necessary to fully implement the parametric spin cooling protocol.

In Ch. 7 we briefly summarize the main results achieved in this thesis and outline our future work.

Chapter 2

Background

This chapter provides the reader with a concise theoretical framework required to understand the experiments described in this thesis.

2.1 Superconducting microwave resonators

In this section we introduce the physical description of a confined mode of electromagnetic radiation and use it to explore the astonishing physics of light-matter interactions. We will study the superconducting resonator as an ideal device with which to implement a range of technologies that exploit rich physics.

The discussion will start with an introduction to the transmission line concept. Initially we consider the microwaves propagating along the transmission line classically. Following this we impose boundary conditions to confine modes in a transmission line resonator, leading to a quantum mechanical treatment of the quantization of a single electromagnetic mode and a description of the quantum states of light in a resonator.

Our discussion is followed by considering the impact of the external microwave circuitry on the resonator performance needed to measure the resonator dynamics. Then to describe the intra-cavity electromagnetic field we employ the quantum input-output theory.

Though superconductors are generally treated as lossless materials, the microwave resonators made of them are not lossless. This leads to the appearance of additional channels for photons to leak out of the resonator resulting in a loss of quantum information. Moreover, these channels can facilitate the injection of thermal photons from the bath surrounding the cavity leading to the loss of coherence and heating of the electromagnetic environment inside the cavity. Therefore, in the end of this section we discuss the origin of losses in microwave superconducting resonators and how they can be mitigated.

2.1.1 Infinitely long transmission line

In this thesis we operate close to the microwave X-band frequency range (more specifically around 7 GHz). The wavelength at this frequency is approximately 4 cm in vacuum (i.e. $\epsilon_r = 1$). The devices we use to perform experiments have silicon as a dielectric media which reduces the wavelength to approximately 30% of its value in vacuum (see Sec. 3.1). The dimensions of the cavity should be of the same order to resonate at these frequencies – exact dimensions depend on the type of resonator implemented (e.g. quarter or half wavelength). Since the size of the circuit is comparable to the electrical wavelength, there is a spatial variation of the electrical variables like cur-

rent and voltage in addition to their time dependence. For this reason we introduce the transmission line (TL) approach that includes the time and spacial dependence of the electric and magnetic energies [40]. Whilst this thesis will be concerned with microwave signals, the theory that follows is general and applies to signals of any frequency.

A TL is a structure that allows microwaves to propagate. An example of a transmission line is the coaxial cable, a popular line used to transport microwaves signals without significant dissipation (see Fig. 2.1). Let us first consider an infinitely long transmission line. Electric and magnetic energy are distributed along the length of the TL, giving rise to the term "distributed" element. The TL can be modeled as an infinite series of infinitesimally short segments of the TL. This allows us to assume that the electric and magnetic energy is stored locally in each segment, and we refer to the segments as "lumped" elements. The standard lumped element circuit of an infinitesimally short segment of the TL is shown in Fig. 2.1. It has a resistance and inductance connected in series, as well as a shunt capacitance and conductance per unit length labeled as L_x, R_x, C_x and G_x, respectively.

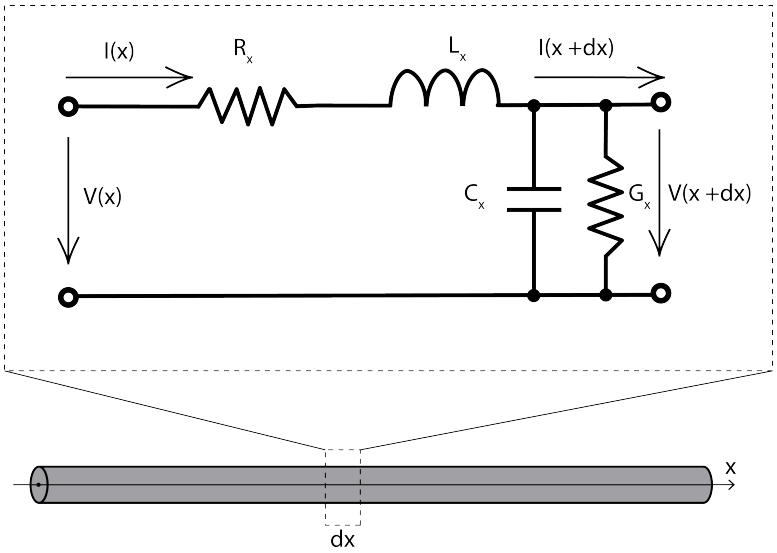

Figure 2.1: The lumped element circuit representation of an infinitesimally short segment of transmission line, schematically depicted as a coaxial cable.

By analyzing this electrical circuit with the help of Kirchhoff's voltage and current laws, one can easily derive the well-known telegrapher's equations, where $\mathcal{V}(x,t)$ and

$\mathcal{I}(x,t)$ are the voltage and current at position x and time t:

$$\begin{aligned}\frac{\partial \mathcal{V}(x,t)}{\partial x} &= -R_x \mathcal{I}(x,t) - L_x \frac{\partial \mathcal{I}(x,t)}{\partial t} \\ \frac{\partial \mathcal{I}(x,t)}{\partial x} &= -G_x \mathcal{V}(x,t) - C_x \frac{\partial \mathcal{V}(x,t)}{\partial t}\end{aligned} \tag{2.1}$$

Solving the telegrapher's equations for a sinusoidal steady-state condition, we obtain a set of traveling wave equations for the voltage and current:

$$\begin{aligned}\mathcal{V}(x) &= \mathcal{V}_0^+ e^{-\gamma x} + \mathcal{V}_0^- e^{\gamma x} \\ \mathcal{I}(x) &= \mathcal{I}_0^+ e^{-\gamma x} + \mathcal{I}_0^- e^{\gamma x}\end{aligned} \tag{2.2}$$

where a negative exponent represents a wave propagating in the $+x$ direction and a positive exponent wave in the $-x$ direction. γ is a complex propagation constant that accounts for microwave losses in the line (α) and the line's dispersion or phase constant (β):

$$\gamma = \alpha + j\beta = \sqrt{(R_x + j\omega L_x)(G_x + j\omega C_x)}$$

The line impedance is defined as:

$$Z_0 = \frac{\mathcal{V}_0^+}{\mathcal{I}_0^+} = -\frac{\mathcal{V}_0^-}{\mathcal{I}_0^-} = \sqrt{\frac{R_x + j\omega L_x}{G_x + j\omega C_x}} \tag{2.3}$$

In practice, the TL we utilize is made of a superconducting metal and all the measurements presented in this thesis are done at cryogenic temperatures, well below the critical temperature of the superconductor (T_c). This leads to the condition where the metal resistance R_x and the dielectric conductance G_x are approximately zero, yielding $\alpha = 0$. A more detailed discussion on the superconducting microwave TL losses can be found in Sec. 2.1.8. As a result, the characteristic line impedance reduces to $Z_0 = \sqrt{L_x/C_x}$.

2.1.2 Lagrangian and classical Hamiltonian of a transmission line

Previously we derived telegrapher's equations that describe the propagation of electromagnetic (EM) waves along a TL. Here we describe the EM waves in TL using a generalized approach by constructing a Lagrangian ($\mathcal{L}$). This method is widely used in physics and allows to characterize the state of the system at a certain time. In classical

mechanics, the Lagrangian is simply the difference between the kinetic and potential energy of the system. In the case of EM waves, we substitute them with electrical and magnetic energies. Moreover, based on Lagrangian we can readily derive the classical Hamiltonian which later is converted into quantum mechanical Hamiltonian.

For this reason we need to choose the generalized coordinates of our system. Conventionally, the magnetic flux ϕ and electric charge $q = C_x(\partial\phi/\partial t)$ that are stored in the inductor and capacitor of our line are chosen. Following the approach outlined in Refs. [41], [42], the local voltage on the TL can be represented by using the flux variable ϕ:

$$\mathcal{V}(x,t) = \frac{\partial\phi(x,t)}{\partial t} \tag{2.4}$$

and the local current has the following form:

$$\mathcal{I}(x,t) = -\frac{\partial\phi(x,t)}{L_x\partial x} \tag{2.5}$$

We can readily construct the Lagrangian for the TL by taking the difference of the kinetic (T) and potential energies (V):

$$\mathcal{L} = T - V = \int_0^\infty dx\mathcal{L}(x,t) = \int_0^\infty dx\Big[\frac{C_x}{2}\Big(\frac{\partial\phi}{\partial t}\Big)^2 - \frac{L_x}{2}\Big(\frac{\partial\phi}{L_x\partial x}\Big)^2\Big] \tag{2.6}$$

Using the Euler-Lagrange equation that is given by:

$$\frac{d}{dt}\left(\frac{\partial\mathcal{L}}{\partial\dot{\phi}}\right) - \frac{\partial\mathcal{L}}{\partial\phi} = 0 \tag{2.7}$$

we can derive the equation of motion for the flux. This equation has the form of a wave equation which leads to similar expressions for the voltage and current derived previously:

$$v_p^2\frac{\partial^2\phi}{\partial x^2} - \frac{\partial^2\phi}{\partial t^2} = 0 \tag{2.8}$$

where $v_p = 1/\sqrt{L_xC_x}$ is the phase velocity.

Since the charge density is canonically conjugate to the flux coordinate $q = \partial\mathcal{L}/\partial\dot{\phi}$, we can derive the classical Hamiltonian using $\mathcal{H}(x,t) = \dot{\phi}q - \mathcal{L}(x,t)$, which leads to:

$$\mathcal{H} = \int dx\Big[\frac{1}{2C_x}q^2 + \frac{1}{2L_x}(\partial_x\phi)^2\Big] \tag{2.9}$$

2.1.3 Transmission line resonator

So far we have only considered the problem of an infinitely long TL. We can restrict the TL to a finite length by including terminations at the input and output. The most common passive electrical terminations are an open-circuit, short-circuit and 50 Ω resistor. The latter is designed to suppress the reflections off the end of the TL by matching its characteristic impedance. Other terminations define boundary conditions that can produce reflections of the waves, leading to the appearance of standing waves at certain frequencies. As a result, the waves no longer propagate freely, but instead form standing waves confined in the length of TL. Such a section of TL that confines electromagnetic energy in this way is said to form a resonator. In what follows, we will discuss two types of microwave resonators with differing boundary conditions - these resonators are of practical importance and will be utilized in our experiments.

If a section of TL of length l has open ends, the current at the terminations must vanish:

$$\mathcal{I}(0,t) = \mathcal{I}(l,t) = 0$$

or equivalently,

$$\frac{\partial\phi(0,t)}{\partial x} = \frac{\partial\phi(l,t)}{\partial x} = 0$$

This condition restricts modes supported in the TL resonator to those for which l is a positive integer (k) multiple of a half wavelength $l = k \cdot \lambda/2$, therefore, we refer to this structure as a $\lambda/2$ resonator. Here k identifies the mode number and each mode has its own resonance frequency $\omega_k = \pi k/(l\sqrt{L_x C_x})$. The functions describing the spatial variation of the flux and its conjugate (charge) are as follows:

$$\begin{aligned} \phi(x,t) &= \sqrt{2/\pi k}\sum_k \phi_k(t)\cos(k\pi x/l) \\ q(x,t) &= \sqrt{2\pi k}/l\sum_k q_k(t)\cos(k\pi x/l) \end{aligned} \tag{2.10}$$

In the case of one open and one short-circuit terminated end, the boundary conditions are $\mathcal{I}(0,t) = 0$ and $\mathcal{V}(l,t) = 0$ and require:

$$\frac{\partial\phi(0,t)}{\partial x} = 0$$

$$\frac{\partial\phi(l,t)}{\partial t} = 0$$

This leads to the similar harmonic spatial distribution of flux and charge, however, the set of modes that can reside inside this structure is limited to those for which l is an odd integer multiple of a quarter wavelength, i.e. with $k = 1/2, 3/2, 5/2, \ldots$. This type of transmission line is designated a $\lambda/4$ resonator.

2.1.4 Quantum harmonic oscillator

After we derived the classical Hamiltonian of an EM wave propagating in a TL, we transform it into quantum mechanical representation. It is well established that EM radiation is quantized [6]. The rigorous quantization of an EM field can be found in Refs. [43], [44]. Here we consider only a single mode of an EM field that is well-known to behave as a quantum harmonic oscillator (QHO).

The classical canonically conjugate variables of flux ϕ and charge q (which also happen to be observable/measurable quantities) are promoted to quantum mechanical operators:

$$\phi \rightarrow \hat{\Phi}$$

$$q \rightarrow \hat{\mathcal{Q}}$$

Since the variables are canonically conjugate, their associated operators obey the well-known commutation relation $[\hat{\Phi}, \hat{\mathcal{Q}}] = i\hbar$. Based on the classical Hamiltonian Eq. 2.9, the quantum mechanical Hamiltonian for a single mode of radiation can be written as:

$$\hat{H} = \frac{1}{2C}\hat{\mathcal{Q}}^2 + \frac{1}{2L}\hat{\Phi}^2 \tag{2.11}$$

We introduce the annihilation $\hat{a}$ and creation $\hat{a}^\dagger$ operators of a QHO, which obey the commutation relation $[\hat{a}, \hat{a}^\dagger] = 1$. Writing the flux and charge operators in terms of $\hat{a}$ and $\hat{a}^\dagger$ [41]:

$$\begin{aligned} \hat{\Phi} &= \sqrt{\frac{\hbar Z_0}{2}}(\hat{a} + \hat{a}^\dagger) \\ \hat{\mathcal{Q}} &= -i\sqrt{\frac{\hbar}{2Z_0}}(\hat{a} - \hat{a}^\dagger) \end{aligned} \tag{2.12}$$

This simplifies the Hamiltonian to the well-known form for a QHO:

$$\hat{H} = \hbar\omega_0(\hat{a}^\dagger\hat{a} + 1/2) = \hbar\omega_0(\hat{n} + 1/2) \tag{2.13}$$

Here $\omega_0 = \sqrt{1/(LC)}$ is the angular frequency of the mode, and $Z_0 = \sqrt{L/C}$ its characteristic impedance. The number state operator $\hat{n} = \hat{a}^\dagger \hat{a}$ defines the number of photons in the QHO. We can also calculate the quantum operators for the current and voltage based on the flux and charge operators:

$$\begin{aligned} \hat{\mathcal{I}} &= \frac{\hat{\Phi}}{L} = \omega_0 \sqrt{\frac{\hbar}{2Z_0}} (\hat{a} + \hat{a}^\dagger) \\ \hat{\mathcal{V}} &= \frac{\hat{\mathcal{Q}}}{C} = -i\omega_0 \sqrt{\frac{\hbar Z_0}{2}} (\hat{a} - \hat{a}^\dagger) \end{aligned} \tag{2.14}$$

The uncertainty of an operator $\hat{A}$ is defined as $\delta\hat{A} = \sqrt{\langle \hat{A}^2 \rangle - \langle \hat{A} \rangle^2}$, where $\langle \hat{A} \rangle = \langle \psi | \hat{A} | \psi \rangle$ signifies the expectation of the operator $\hat{A}$ for the system in the state $|\psi\rangle$. For a QHO in the ground (or so-called vacuum) state $|0\rangle$, the voltage and current exhibit root-mean-square (RMS) fluctuations with a strength:

$$\begin{aligned} \delta\hat{\mathcal{I}} &= \omega_0 \sqrt{\frac{\hbar}{2Z_0}} \\ \delta\hat{\mathcal{V}} &= \omega_0 \sqrt{\frac{\hbar Z_0}{2}} \end{aligned} \tag{2.15}$$

It is worth noting that these non-zero fluctuations have very profound consequences in practice and manifest, for example, in the Casimir effect [45] and Lamb shift [46], [47]. Even though the current and voltage expectations values $\langle \mathcal{I} \rangle$ and $\langle \mathcal{V} \rangle$ are zero, their variances $\langle \mathcal{I}^2 \rangle$ and $\langle \mathcal{V}^2 \rangle$ are not. The vacuum state with zero photons generates current and voltage fluctuations that translate into vacuum fluctuations of the magnetic and electric fields. These fluctuations facilitate interactions between resonators and other quantum systems and are of utmost importance for cQED [22] and hybrid systems [48].

2.1.5 Quantum states of electromagnetic radiation

The quantized EM field exists in a number of exotic quantum mechanical states. In this paragraph we outline the most relevant quantum states of light and their properties.

So far we have used flux and charge variables to describe the quantum state of radiation. This was a convenient choice to map the EM waves onto our TL components. However, these variables are not unique and we are free to choose other canonically

conjugate pairs to describe the system.

A classical monochromatic signal of frequency ω can be represented as a complex number $S = Ae^{i(\omega t+\phi)}$, where A is the signal amplitude, ϕ is its phase and t represents time. We can write this signal in a static "phasor" notation that separates the time dependence $S = Ae^{i(\omega t+\phi)} = Ae^{i\phi}e^{i\omega t} = Me^{i\omega t}$. Here M is a phasor that can be expressed in terms of the quadratures I and Q following Euler's formula:

$$M = Ae^{i\phi} = A(\cos\phi + i\sin\phi) = I + iQ \tag{2.16}$$

where I and Q are the "in-phase" and "quadrature" components, respectively [49]. These quadratures are canonically conjugate, thus we can easily promote these variables to quantum mechanical operators, expressing them as functions of the annihilation and creation operators:

$$\begin{aligned} \hat{I} &= \frac{\hat{a} + \hat{a}^\dagger}{2} \\ \hat{Q} &= \frac{\hat{a} - \hat{a}^\dagger}{2i} \end{aligned} \tag{2.17}$$

The Hamiltonian Eq. 2.11 can also be generalized and rewritten in terms of quadratures:

$$\hat{H} = \frac{1}{2C}\hat{\mathcal{Q}}^2 + \frac{1}{2L}\hat{\Phi}^2 = \hbar\omega_0\left(\frac{\hat{\mathcal{Q}}^2}{\mathcal{Q}_0^2} + \frac{\hat{\Phi}^2}{\Phi_0^2}\right) = \hbar\omega_0\left(\hat{Q}^2 + \hat{I}^2\right) \tag{2.18}$$

where normalization factors are $\mathcal{Q}_0 = \sqrt{2\hbar/Z_0}$ and $\Phi_0 = \sqrt{2\hbar Z_0}$.

In what follows, we will use $\hat{I}$ and $\hat{Q}$ more often than $\hat{\Phi}$ and $\hat{\mathcal{Q}}$ to describe the states of light since they are more general and are more readily measured in experiments, as we will explain in Ch. 3, 4, 5.

Fock states

The so-called number states $|n\rangle$ are the eigenstates of a quantum harmonic oscillator (Eq. 2.13), where n corresponds to the number of photons in a single mode. They are often referred to as Fock states, named after the Soviet physicist Vladimir Fock. These states form a complete set of basis vectors for a Hilbert space [43], allowing Fock's representation to describe any electromagnetic radiation state, making it a fundamental tool in quantum mechanics.

One of the key properties of Fock states is that the expectation values of flux and

charge are always zero irrespective of the photon number:

$$\begin{aligned}\langle\hat{\Phi}\rangle &= \sqrt{\frac{\hbar Z_0}{2}}\langle n|\hat{a}+\hat{a}^\dagger|n\rangle = \sqrt{\frac{\hbar Z_0}{2}}\left(\langle n|\hat{a}|n\rangle + \langle n|\hat{a}^\dagger|n\rangle\right) = 0 \\ \langle\hat{\mathcal{Q}}\rangle &= -i\sqrt{\frac{\hbar}{2Z_0}}\langle n|\hat{a}-\hat{a}^\dagger|n\rangle = -i\sqrt{\frac{\hbar}{2Z_0}}\left(\langle n|\hat{a}|n\rangle - \langle n|\hat{a}^\dagger|n\rangle\right) = 0\end{aligned} \tag{2.19}$$

According to the Heisenberg uncertainty principle [50] they should have non-zero variances, which in fact, as we show, depend on the number state. For instance, let us look at the flux and charge density fluctuations of the microwave resonator treated as quantum harmonic oscillator. The expectation of the square of the flux and charge for the system in the Fock state $|n\rangle$ are:

$$\begin{aligned}\langle\hat{\Phi}^2\rangle &= \frac{\hbar Z_0}{2}\langle n|(\hat{a}+\hat{a}^\dagger)^2|n\rangle = \hbar Z_0(n+\frac{1}{2}) \\ \langle\hat{\mathcal{Q}}^2\rangle &= -\frac{\hbar}{2Z_0}\langle n|(\hat{a}-\hat{a}^\dagger)^2|n\rangle = \frac{\hbar}{Z_0}(n+\frac{1}{2})\end{aligned} \tag{2.20}$$

The uncertainties of these conjugate variables exhibit a dependence on the number of photons:

$$\begin{aligned}\delta\hat{\Phi} &= \sqrt{\langle\hat{\Phi}^2\rangle - \langle\hat{\Phi}\rangle^2} = \sqrt{\hbar Z_0(n+\frac{1}{2})} \\ \delta\hat{\mathcal{Q}} &= \sqrt{\langle\hat{\mathcal{Q}}^2\rangle - \langle\hat{\mathcal{Q}}\rangle^2} = \sqrt{\frac{\hbar}{Z_0}(n+\frac{1}{2})}\end{aligned} \tag{2.21}$$

It then follows that the uncertainty relation for the flux and charge is:

$$\delta\hat{\Phi}\delta\hat{\mathcal{Q}} \geq \frac{\hbar}{2}(2n+1) \tag{2.22}$$

For the generalized and dimensionless quadrature operators introduced earlier, it can be shown that the following uncertainty relation holds:

$$\delta\hat{I}\delta\hat{Q} \geq \frac{1}{4}(2n+1) \tag{2.23}$$

This means that we cannot precisely determine the quantities $\langle\hat{\Phi}\rangle$ ($\langle\hat{I}\rangle$) and $\langle\hat{\mathcal{Q}}\rangle$ ($\langle\hat{Q}\rangle$) simultaneously. The uncertainty for a measurement is minimum when $n = 0$, in which case:

$$\delta\hat{I}\delta\hat{Q} \geq \frac{1}{4} \tag{2.24}$$

This brings us to the special case of Fock states when $n = 0$. This corresponds to the system in the ground state $|0\rangle$, which is often referred to as the "vacuum state" since it contains zero photons. The uncertainty is spread equally between the two quadratures, such that standard deviation of each is given as:

$$\delta\hat{I} = \delta\hat{Q} = \frac{1}{2} \tag{2.25}$$

Coherent states

A coherent state $|\alpha\rangle$ is the state of a QHO that most closely replicates the oscillatory motion of a classical wave. When discussing coherent states it is helpful to define the displacement operator [43]:

$$\hat{D}(\alpha) = e^{\alpha\hat{a}^\dagger - \alpha^*\hat{a}} \tag{2.26}$$

where $\alpha = |\alpha|e^{i\phi}$ is a complex number. A coherent state is generated by applying the displacement operator to the vacuum state:

$$|\alpha\rangle = \hat{D}(\alpha)|0\rangle \tag{2.27}$$

Moreover, the coherent state is an eigenstate of the annihilation operator $\hat{a}|\alpha\rangle = \alpha|\alpha\rangle$ and a linear superposition of photon number states:

$$|\alpha\rangle = e^{-|\alpha|^2/2} \sum \frac{\alpha^n}{(n!)^{1/2}}|n\rangle \tag{2.28}$$

It is worth noting that photons in a coherent state exhibit a Poisson probability distribution:

$$P(n) = |\langle n|\alpha\rangle|^2 = \frac{|\alpha|^{2n}e^{-|\alpha|^2}}{n!} \tag{2.29}$$

with a mean number of photons $\langle\hat{n}\rangle = \langle\alpha|\hat{a}^\dagger\hat{a}|\alpha\rangle = |\alpha|^2$. The coherent state is a minimum uncertainty state with $\delta\hat{I}\delta\hat{Q} \geq 1/4$, regardless of the coherent state amplitude.

The quantum states of a QHO can be conveniently represented in quadrature phase space as shown in Fig. 2.2. They are depicted as colored regions with centers corresponding to their mean field amplitudes and areas to their uncertainties.

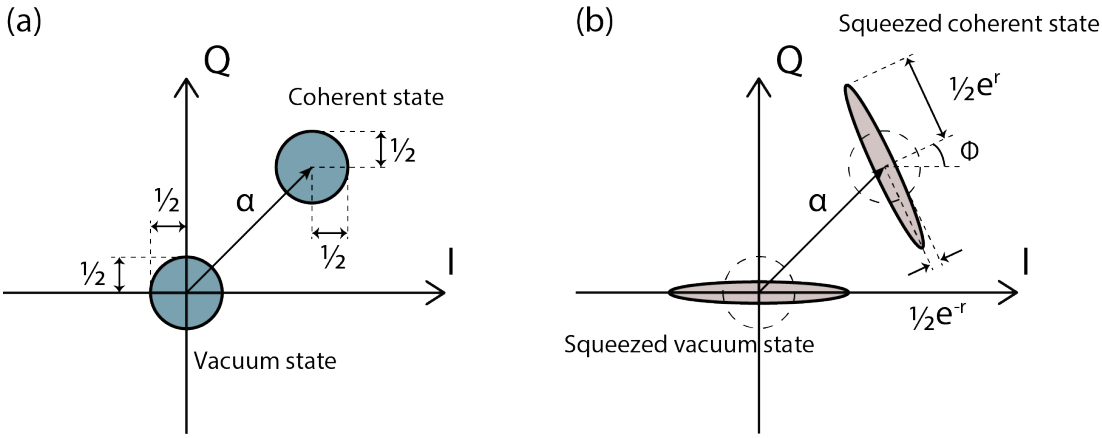

Figure 2.2: States of electromagnetic radiation in phase space. **a)** Vacuum and coherent states. **b)** Squeezed vacuum and squeezed coherent states.

Squeezed states

Squeezed states are states with a reduced quantum uncertainty. The uncertainty in one of the field quadratures may be reduced at the expense of an increased uncertainty in the other, so long as the uncertainty principle is satisfied. This can be used to lower the noise in a measurement where the signal is aligned with the squeezed quadrature. The nonlinear resonators explored in this thesis are highly effective at squeezing, as will be presented in Ch. 4.

The squeezed states are obtained by acting on any state with the squeezing operator $\hat{S}(\epsilon)$. When it operates on the state $|0\rangle$ it produces a squeezed vacuum. When it operates on $\hat{D}(\alpha)|0\rangle$ (where $\hat{D}(\alpha)$ is the displacement operator) it produces a squeezed coherent state. The squeezing operator is defined as:

$$\hat{S}(\epsilon) = exp\left[\frac{\epsilon^*}{2}\hat{a}^2 - \frac{\epsilon}{2}\hat{a}^{\dagger 2}\right] \tag{2.30}$$

and the squeezing parameter $\epsilon = re^{i2\phi}$ is a complex number. For squeezed vacuum and coherent states, the noise on each quadrature is then:

$$\begin{aligned} \delta\hat{I} &= \frac{1}{2}e^{-r} \\ \delta\hat{Q} &= \frac{1}{2}e^{+r} \end{aligned} \tag{2.31}$$

Thermal states

Since the cavity has a non-zero temperature, it is said that its electromagnetic mode is in thermal equilibrium with a bath at temperature T, and the cavity is in a thermal state. Such a thermal state is an incoherent mixture of Fock states and thus the number of photons in this state is not well defined, being best described by black-body radiation [51], [52] that follows Bose-Einstein statistics. The mean number of photons with energy $\hbar\omega$ in a single mode at thermal equilibrium is:

$$\langle n_{th} \rangle = \frac{1}{e^{\frac{\hbar\omega}{k_B T}} - 1} \tag{2.32}$$

When the temperature T decreases, the number of thermal photons asymptotically decreases to zero. For high temperatures, $\langle n_{th} \rangle$ displays a linear dependence on T. For the thermal state, the uncertainty on each quadrature is equal:

$$\delta\hat{I} = \delta\hat{Q} = \sqrt{\frac{2n_{th} + 1}{4}} \tag{2.33}$$

2.1.6 Probing the resonator

To excite a resonant mode and probe its field we must couple the resonator to external circuitry. One method for driving and characterizing the resonator is to connect it via capacitance C_{in} to a transmission line with a characteristic impedance Z_0 (usually $Z_0 = 50\ \Omega$) that leads to a microwave test equipment (e.g. a microwave signal generator, vector network analyzer, signal analyzer, etc.). For simplicity, the resonator can be modeled using an effective inductance, capacitance, and resistance connected in parallel as a LCR circuit (shown in Fig. 2.3a). The LC section of the resonant circuit is a good approximation for a lossless TL. The resistance R models dissipative losses of microwave photons residing in the resonator and is the result of unavoidable imperfections, the origins of which are discussed in Sec. 2.1.8.

The internal quality factor Q_{int} is a figure of merit used to quantify resonator losses. It is defined as the ratio of the maximum energy stored in the resonator to the energy dissipated per cycle of oscillation. The internal quality factor can be expressed in terms

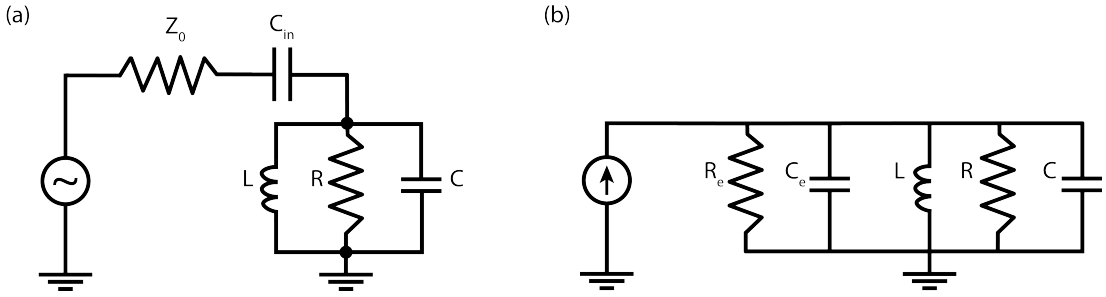

Figure 2.3: **a)** Lumped element circuit of the LCR resonator coupled to a transmission line and a signal source. **b)** Norton equivalent circuit of the LCR resonator coupled to a transmission line and a signal source.

of the various circuit elements as:

$$Q_{int} = \omega_0 RC = \frac{\omega_0}{\kappa_{int}} = \frac{R}{Z_r} \tag{2.34}$$

where κ_{int} is the internal loss rate, $\omega_0 = \sqrt{1/(LC)}$ is the resonant frequency and $Z_r = \sqrt{L/C}$ is the impedance of the resonator.

To estimate how the external circuit modifies the properties of the resonator it is helpful to write down the Norton equivalent circuit (see Fig. 2.3b). In this case the frequency dependent effective resistance of the resonator including the external line is:

$$\frac{1}{R_{tot}(\omega)} = \frac{1}{R} + \frac{1}{R_e(\omega)} \tag{2.35}$$

with $R_e(\omega) = Z_0 + 1/(\omega^2 C_{in}^2 Z_0)$ and the effective capacitance is:

$$C_{tot}(\omega) = C + \frac{C_{in}}{1 + (\omega C_{in} Z_0)^2} \tag{2.36}$$

The frequency of the resonator is modified as well since the capacitance of the effective resonant circuit now includes the coupling capacitance $\omega_0^{tot} = \sqrt{1/(LC_{tot})}$.

The presence of external circuit adds an effective resistance R_e to the resonator, resulting in an additional channel of microwave field loss. This loss is not inherent to the resonator but accounts for coupling of the microwaves to the measurement circuitry. We can quantify the coupling losses in a similar way to the internal losses, introducing the external (or coupling) quality factor:

$$Q_{ext} = \frac{R_e}{Z_r} = \frac{\omega_0}{\kappa_{ext}} \tag{2.37}$$

where κ_{ext} is the external (coupling) loss rate. As a result, the total quality factor of the resonator that accounts for all internal and external losses and defines the resonator bandwidth is written as:

$$\frac{1}{Q_{tot}} = \frac{1}{Q_{int}} + \frac{1}{Q_{ext}} \tag{2.38}$$

2.1.7 Input-output formalism

Since we will be interested in the quantum dynamics of the field inside our resonators we need to treat the resonator as a quantum mechanical system. Gardiner and Collett [53] developed a formalism, referred to as input-output theory, to describe the equations of motion of an open quantum system, such as a bosonic resonator mode coupled to external feed lines and intrinsic channels for loss. This approach allows us to relate the classical scattering matrix formalism used to characterize microwave networks with the quantum mechanical parameters of our system. To apply this theory to our system, a couple of approximations are made, as discussed below.

The input and output fields are treated as an external bath with a continuum of modes - quite often represented by a heat bath in thermal equilibrium with its environment (i.e. the bath modes are in thermal states). In our experiments the resonators are driven by classical fields that can be represented as coherent states (recall Sec. 2.1.5) and the internal losses are modeled by an additional port at thermal equilibrium. The interaction between the system (resonator) and the bath is assumed to be linear and independent of frequency. Additionally, the dynamics of the system of interest should have a narrow frequency bandwidth. All of these assumptions become valid if the resonator has a high-quality factor.

The total Hamiltonian treated under the input-output formalism including the resonator and the bath is:

$$\hat{H} = \hat{H}_{sys} + \hat{H}_{bath} + \hat{H}_{int} \tag{2.39}$$

where $\hat{H}_{sys}$ is the Hamiltonian of the system we are probing, $\hat{H}_{bath}$ is the Hamiltonian of the bath, and $\hat{H}_{int}$ is the interaction Hamiltonian between the system and the bath. The Hamiltonian of the microwave resonator, as described in Sec. 2.1.4, can be written in the form of a quantum harmonic oscillator $\hat{H}_{sys} = \hbar\omega_0(\hat{a}^\dagger\hat{a} + \frac{1}{2})$.

To describe the time evolution of this system we can write the quantum Langevin

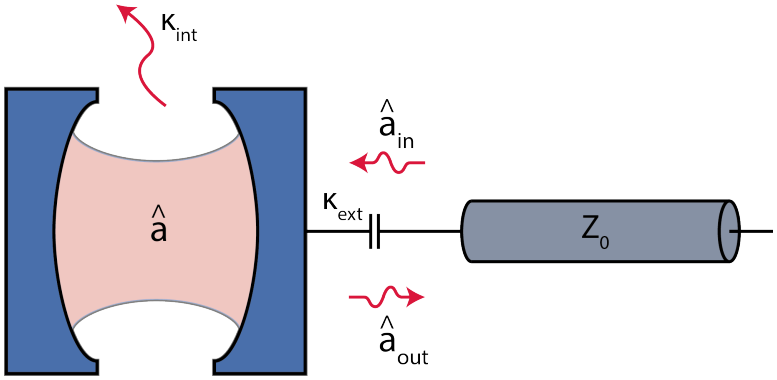

Figure 2.4: Illustration of the input-output model for the cavity probed in reflection. The input field $\hat{a}_{in}$ is delivered to the cavity via a transmission line with characteristic impedance Z_0. The reflected field $\hat{a}_{out}$ follows the same path but in the reverse direction.

equation in the Heisenberg picture:

$$\dot{\hat{a}}(t) = -\frac{i}{\hbar}[\hat{a}(t), \hat{H}_{sys}] - \frac{\kappa_{int} + \kappa_{ext}}{2}\hat{a}(t) + \sqrt{\kappa_{ext}}\hat{a}_{in}(t) + \sqrt{\kappa_{int}}\hat{f}_{in}(t) \tag{2.40}$$

Using the time-reversed Langevin equation derived by Gardiner and Collett [53], the following relation between the input $\hat{a}_{in}$, output $\hat{a}_{out}$ and intra-resonator $\hat{a}$ fields can be found:

$$\hat{a}_{out}(t) = -\hat{a}_{in}(t) + \sqrt{\kappa_{ext}}\hat{a}(t) \tag{2.41}$$

The rigorous derivations of the last two equations are performed in [43], [53], [54]. The first term in Eq. 2.40 is the Heisenberg equation of motion for the mode operator $\hat{a}$, the second term describes damping of the mode due to the internal κ_{int} and external κ_{ext} couplings in the system, and the third is the coupling to the external line (bath), which describes the coherent drive field. The last term represents the noise fluctuations $\hat{f}_{in}$ introduced to the mode via an additional channel at a rate κ_{int}. All the coupling rate parameters introduced in Eqs. 2.40 and 2.41 are consistent with the parameters mentioned in previous sections. The schematic representation of the input-output model under consideration is shown in Fig. 2.4.

Inserting $\hat{H}_{sys}$ into Eq. 2.40 leaves us with the input-output equation for a single port resonator:

$$\dot{\hat{a}}(t) = -i\omega_0\hat{a}(t) - \frac{\kappa_{int} + \kappa_{ext}}{2}\hat{a}(t) + \sqrt{\kappa_{ext}}\hat{a}_{in}(t) + \sqrt{\kappa_{int}}\hat{f}_{in}(t) \tag{2.42}$$

The input-output fields can be mapped to the input $P_{in} = \hbar\omega|\hat{\alpha}_{in}|^2$ and output

$P_{out} = \hbar\omega|\hat{\alpha}_{out}|^2$ microwave powers, where $\hat{\alpha}_{in,out}$ are complex numbers representing the coherent state amplitude. The mean intra-resonator field under an external classical drive is written as $\langle\hat{a}\rangle = \alpha(t)$. The mean of quantum noise fluctuations $\langle\hat{f}_{in}\rangle$ is zero. The Langevin is then written as:

$$\dot{\alpha}(t) = -i\omega_0\alpha(t) - \frac{\kappa_{int} + \kappa_{ext}}{2}\alpha(t) + \sqrt{\kappa_{ext}}\alpha_{in}(t) \tag{2.43}$$

Eq. 2.43 can be solved for the intra-resonator field in the frequency domain by defining the Fourier transform:

$$\alpha(t) = \frac{1}{\sqrt{2\pi}}\int_{-\infty}^{+\infty} e^{-i\omega(t-t_0)}\alpha(\omega)d\omega \tag{2.44}$$

We can derive the intra-resonator field as:

$$\alpha(\omega) = \frac{\sqrt{\kappa_{ext}}}{\frac{\kappa_{ext}+\kappa_{int}}{2} - i(\omega - \omega_0)}\alpha_{in}(\omega) \tag{2.45}$$

The input-output relation for the fields may then be expressed in the frequency domain:

$$\alpha_{out}(\omega) = \frac{\frac{\kappa_{ext}-\kappa_{int}}{2} + i(\omega - \omega_0)}{\frac{\kappa_{ext}+\kappa_{int}}{2} - i(\omega - \omega_0)}\alpha_{in}(\omega) \tag{2.46}$$

Using Eq. 2.45, we can estimate the mean intra-resonator photon number of the cavity mode (at frequency $\omega = \omega_0$) with $\langle n\rangle = |\alpha|^2$:

$$\langle n\rangle = \frac{4\kappa_{ext}P_{in}}{\hbar\omega_0(\kappa_{ext} + \kappa_{int})^2} \tag{2.47}$$

As noted at the beginning of this section, the input-output resonator fields allows us to derive the conventional scattering matrices. Since we consider only a single-port device, the complex reflection coefficient S_{11} is:

$$S_{11} = \frac{\alpha_{out}(\omega)}{\alpha_{in}(\omega)} = \frac{\frac{\kappa_{ext}-\kappa_{int}}{2} + i(\omega - \omega_0)}{\frac{\kappa_{ext}+\kappa_{int}}{2} - i(\omega - \omega_0)} \tag{2.48}$$

2.1.8 Losses in superconducting resonators

Microwave resonators made from superconducting materials exhibit extremely small intrinsic losses when operated below their superconducting critical temperature. Below

we outline the sources of loss that limit the quality factors in typical superconducting resonator devices.

In superconducting materials electrons form Cooper pairs that enable current transport without dissipation. The binding energy of the Cooper pairs defines the superconducting critical temperature T_c of the material. If the temperature is higher than T_c the material is in the "normal state", where there are no Cooper pairs and current is carried by normal electrons. At non-zero temperatures below T_c, there exist residual single electrons called quasiparticles. The quasiparticles are a source of dissipative loss that becomes prominent at temperatures close to T_c, or when the device is subjected to radiation that can break the Cooper pairs [55], [56].

Radiation loss is a common source of loss for microwave resonators. It origins from the extension of the electromagnetic field into the dielectric surrounding the resonator. This type of loss is typical for microstrip resonators (see Fig. 2.5a) [57]. For coplanar waveguide (CPW) resonators the radiation loss is greatly reduced due to the ground planes located in the close vicinity to the central conductor which helps localizing the field (see Fig. 2.5b). Reduction of the width of the central conductor can further suppress radiation losses [58]. Another approach to protect the field from radiation loss is to reduce the available density of states of the environment [59]. The resonator field decays into the bath with a continuum of modes. By modifying the density of states of the environment we can reduce the rate of emission. This can be achieved, for example, by embedding the resonator in a 3D cavity.

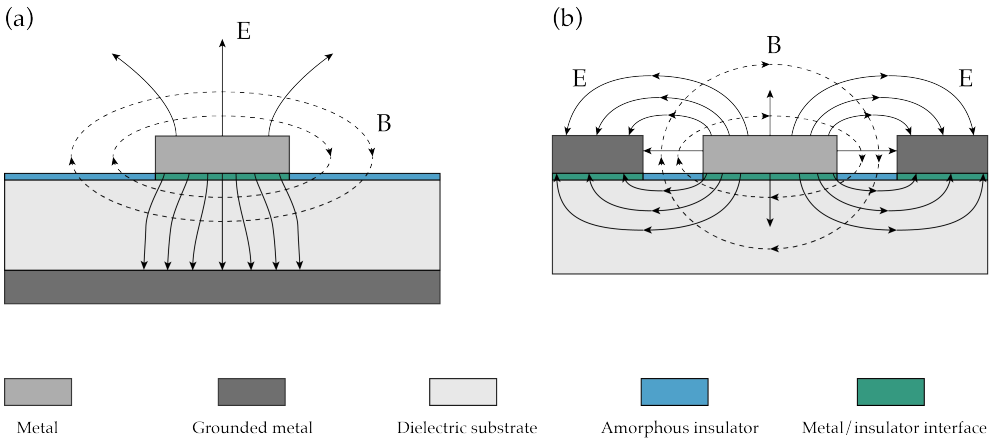

Figure 2.5: Illustration of the quasi-TEM mode (see Ch. 3, Sec. 3.1.1) residing in **a)** microstrip and **b)** CPW resonators. Solid and dashed lines represent the distribution of the electric and magnetic fields, respectively.

Another important source of loss arises from two level system (TLS). A TLS is

any defect with an electric dipole that can resonantly absorb microwave energy at the resonator frequency. TLSs can be found at the amorphous insulator surface of the dielectric substrate on which the resonator is fabricated (see Fig. 2.5), at the metal/insulator interfaces and in the bulk of the dielectric material [60]. An identifiable feature of TLS-based losses is the microwave power dependence of the resonator's quality factor. At low powers and cryogenic temperatures, the majority of TLSs are in the ground state. The microwave power delivered to the resonator can be absorbed by the TLSs to bring them to the excited state. This is accompanied by a characteristic drop in the resonator's internal quality factor, as compared to the internal quality factor measured at high powers. As the microwave power is increased the TLSs eventually saturate and are no longer able to absorb the resonator field, leading to an enhanced quality factor that is limited by some other source of loss. However, as is the case for some of the experiments performed in this thesis, it is often necessary to operate a resonator at powers corresponding to single (or fewer) microwave photon occupation. To minimize losses associated with TLSs, regions with high electric field amplitude (voltage anti-nodes) should be placed on carefully treated dielectric surfaces [61], [62] and the resonator's design can be optimized to lower the electric field amplitudes that interact with the TLS electric dipoles.

An externally applied magnetic field can also lead to an increase in the internal loss rate of the superconducting resonator. Depending on the orientation of the magnetic field relative to the plane of thin superconducting film, different mechanisms that deteriorate the internal quality factor Q_{int} will be important. If the field is parallel to the film, it will increase the number of quasiparticles by reducing the superconducting gap energy, as will be explained in Sec. 2.2.2. In our experiments we work exclusively with NbTiN superconducting films, which is a type-II superconductor. Magnetic fields perpendicular to a thin film of NbTiN produces localized regions of normal metal where the field is able to penetrate the film [63]. As a result, supercurrents circle around these normal metal centers and generate Abrikosov vortices (fluxons) [64], which can act as a dissipative channel for microwave signals and cause additional losses inside the resonator.

2.2 Nonlinear elements in superconducting cavities

The treatment of standard circuit components as linear elements is an approximation that holds when their input stimuli are kept below certain conditions. Driven hard enough, all circuits eventually become nonlinear [65].

Depending on the application, this nonlinear circuit behavior can either limit device performance or be used to unlock new functionalities. For instance, nonlinear frequency conversion is widely used in modern electronics. This includes frequency doubling (or second harmonic generation) in signal generators [66], frequency mixers for sum and difference frequency generation [67], parametric amplification [68], etc.

Generally, to induce strong nonlinear effects in a medium it should be pumped with a high intensity field. In optics, lasers can be used to produce high intensity fields. The invention of the laser [69] has enabled extensive studies to be performed on nonlinear interactions in optical materials exploiting electro-optic or magneto-optic Kerr effects [70].

Nowadays, the progress in micro- and nano-fabrication techniques has made it possible to study nonlinear effects at the quantum mechanical level. In the context of quantum computing, sensitive measurements of qubits (superconducting, spin and optical based) has been achieved by exploiting nonlinearities to enable quantum-noise-limited parametric amplification of signals [71], [72]. Moreover, the same nonlinear parametric amplifiers can be used to generate nonclassical states of light by means of squeezing one of the quadratures [73], thus going beyond the standard quantum limit.

As will be presented in this thesis, the use of superconducting nonlinear resonators allows one to explore many interesting parametric effects in the microwave domain such as frequency conversion, amplification, and squeezing, with application in spin resonance spectroscopy and QIP. In the following sections we explain what type of nonlinearity our devices employ.

2.2.1 SQUIDs

The most common way to generate parametric processes in cQED is through introducing a nonlinear element into a superconducting resonant circuit. This is usually achieved by embedding a variable inductance in the form of a superconducting quantum interference device (SQUID) [74], [75].

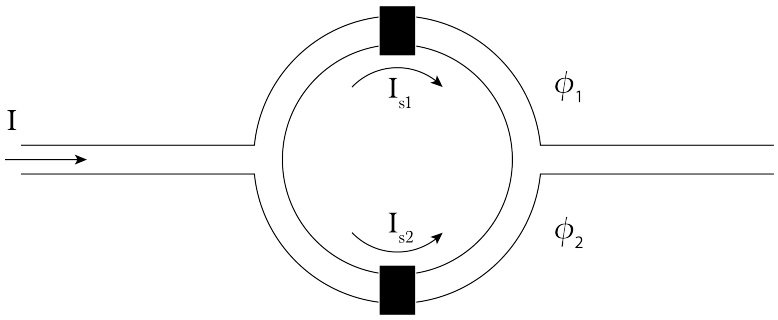

Figure 2.6: Illustration of a SQUID consisting of two Josephson junctions connected in parallel. Each Josephson junction consists of two superconducting leads separated by thin insulating layer shown as a black rectangle.

A SQUID [76] consists of two Josephson junctions [77]–[79] connected in parallel to form a loop (see Fig. 2.6). A single Josephson junction consists of two superconducting leads separated by thin insulating layer that allows the tunneling of Cooper pairs from one lead to the other. DC and AC Josephson effects describe the current and voltage across a junction with respect to the phase difference ϕ between the wavefunctions of the superconductors:

$$\begin{aligned} I &= I_c \sin\phi \\ V &= \frac{\Phi_0}{2\pi}\frac{d\phi}{dt} \end{aligned} \tag{2.49}$$

where I_c is the critical current of the Josephson junction and $\Phi_0 = h/(2e)$ is the magnetic flux quantum. Allowing for a time-dependent current across the junction we find:

$$\begin{aligned} \frac{dI}{dt} = I_c\cos(\phi)\frac{d\phi}{dt} &= I_c\cos(\phi)V\frac{2\pi}{\Phi_0} \\ V = \frac{\Phi_0}{2\pi}\frac{1}{I_c\cos(\phi)}\frac{dI}{dt} &= L_j\frac{dI}{dt} \end{aligned} \tag{2.50}$$

where it becomes apparent that the Josephson junction acts as an inductor with inductance L_j, which is dependent on the phase ϕ. In a SQUID configuration, the phase difference between the currents is dependent on the magnetic flux. For symmetric Josephson junctions the effective inductance of a SQUID is given by the following equation [80]:

$$L_{SQUID}(\Phi_{ext}) = \frac{\hbar}{4eI_c|\cos(\frac{\pi\Phi_{ext}}{\Phi_0})|} \tag{2.51}$$

where I_c is the critical current of the SQUID and Φ_{ext} is the external magnetic flux that penetrates the loop formed by two Josephson junctions.

Despite the popularity of SQUIDs, these nonlinear circuits are generally quite fragile. Firstly, they are sensitive to electrostatic discharge (ESD) and special care must be exercised when handling devices that incorporate SQUIDs. Secondly, parametric amplifiers built using SQUIDs usually have a small 1 dB compression point (the maximum input signal that can be effectively amplified) which is explained by their inherently small critical currents I_c [74], [81]. Moreover, typical Josephson junctions are made of aluminum/aluminum oxide/aluminum and they have a low critical magnetic field (around 10 mT for bulk aluminum [82]) which makes them difficult to integrate with spin systems in solid state devices.

2.2.2 Kinetic inductance

The devices explored in this thesis rely on a nonlinearity originating from a phenomenon known as kinetic inductance. Kinetic inductance is a well know property of high conductivity materials (such as superconductors) [83], and has been widely utilized in microwave kinetic inductance detectors (MKID) community [84]–[87]. In this section we briefly review the underlying physics of kinetic inductance following the treatment by Zmuidzinas [88], a pioneer in the field of MKIDs.

Based on the Bardeen-Cooper-Schrieffer (BCS) theory of superconductivity [89], [90], the Mattis-Bardeen equations [91] for the complex conductivity $\sigma(\omega) = \sigma_1(\omega) - i\sigma_2(\omega)$ of a superconductor at microwave frequencies ω can be written:

$$\sigma_1(\omega) = \frac{2\sigma_n}{\hbar\omega}\int_{\Delta}^{\infty} dE \frac{E^2 + \Delta^2 + \hbar\omega E}{\sqrt{(E^2-\Delta^2)((E+\hbar\omega)^2-\Delta^2)}}[f(E) - f(E+\hbar\omega)] \tag{2.52}$$

$$\sigma_2(\omega) = \frac{\sigma_n}{\hbar\omega}\int_{\Delta}^{\Delta+\hbar\omega} dE \frac{E^2 + \Delta^2 - \hbar\omega E}{\sqrt{(E^2-\Delta^2)(\Delta^2-(E-\hbar\omega)^2)}}[1 - 2f(E)] \tag{2.53}$$

where σ_n is a normal state conductivity, 2Δ is the superconducting energy gap and $f(E)$ describes the distribution of quasiparticles (broken Cooper pairs) which is given by Fermi-Dirac statistics. The real part (Eq. 2.52) corresponds to dissipation losses in the superconductor originating from quasiparticles. The inertia of the superconduct-

ing electrons (Cooper pairs) is responsible for the imaginary part of the conductivity (Eq. 2.53). At temperatures well below T_c the real part of the conductivity tends exponentially towards zeros, however, the same is not true for the imaginary part, which effectively leads to the appearance of an inductance in superconductors at microwave frequencies. For $T << T_c$ both components of the complex conductivity are proportional to the quasiparticle density:

$$n_{qp} = 4N_0 \int_{\Delta}^{\infty} dE \frac{E}{\sqrt{E^2 - \Delta^2}} f(E) \tag{2.54}$$

where N_0 is the single-spin density of electron states at the Fermi energy.

In the thin film limit (where the superconductor thickness is smaller than the penetration depth) the surface inductance can be written [92]:

$$L_k = \left(\frac{l}{w}\right) \frac{\hbar R_s}{\pi \Delta} \frac{1}{\tanh(\frac{\Delta}{2k_B T})} \tag{2.55}$$

with l and w representing the length and the width of the superconducting structure and R_s the normal-state sheet resistance.

Introducing a DC current to the film suppresses the superconducting energy gap (relative to its zero-temperature value Δ_0) by increasing the density of quasiparticles [93]:

$$\frac{\Delta_0 - \Delta}{\Delta_0} = 2 \int_{\Delta}^{\infty} dE \frac{1}{\sqrt{E^2 - \Delta^2}} f(E) \tag{2.56}$$

As a result, the kinetic inductance has both a temperature and current dependence. In terms of an applied current, L_k can be written as [88]:

$$L_k(I) = L_k(0) \left(1 + \frac{I^2}{I_2^2} + \frac{I^4}{I_4^4} + \dots\right) \tag{2.57}$$

where I_2 and I_4 set the scales for the quadratic and quartic current nonlinearities of the kinetic inductance and $L_k(0)$ is its zero-bias value. Since the inductance depends on the applied current, it is said to be a nonlinear inductance. As we will discuss in Ch.3, this current dependence of the kinetic inductance can be used to produce frequency-tunable nonlinear resonators.

It is worth noting that our experiments combine superconducting resonators with spins in solids, exposing the devices to external magnetic fields that generate circulating currents in the superconducting films, which can further enhance the kinetic inductance.

2.3 Quantum limits to amplification

In cQED quite often one works with very low power signals that can reach the single photon level. Microwave cQED experiments are generally performed at cryogenic temperatures to enter the quantum regime ($\hbar\omega \gg k_B T$), where noise consists primarily of vacuum fluctuations $\hbar\omega/2$ of the field. To process such small signals we must first amplify them above the thermal noise level at room temperature, where they are sent to be digitized and analyzed. However, all amplifiers add an amount of noise to the signal during the amplification process. In classical electronics this results from the motion of charge carriers and is known as Johnson-Nyquist noise [94], [95], which can be conveniently characterized by a noise temperature that quite often is correlated with the physical temperature. As such, amplifiers designed to operate at cryogenic temperatures add less noise than room temperature ones [96]. To detect signals at the single photon level one needs to ensure that the amplifier added noise does not mask the signal, i.e. it must be practically noiseless. However, there is a fundamental limit posed by quantum mechanics on the minimum noise added by an amplifier.

In quantum mechanics fields can be described by their annihilation $\hat{a}$ and creation $\hat{a}^\dagger$ operators, or alternatively, by the quadratures $\hat{I}$ and $\hat{Q}$. These operators satisfy the standard bosonic commutation relation $[\hat{a}, \hat{a}^\dagger] = 1$. Since they do not commute, we cannot measure them simultaneously with an arbitrary precision, according to the Heisenberg uncertainty principle [50]. Qualitatively, this can be used to explain why amplifiers add quantum noise. They cannot output a (phase preserved) enlarged copy of the signal because it requires precise knowledge of the field expectations of both $\hat{a}$ and $\hat{a}^\dagger$. This is reconciled by adding noise to the output signal. In what follows, which is based on the treatment outlined in Refs. [97], [98], we present a derivation of this minimum added quantum noise.

Let's assume we amplify an input signal $\hat{a}$ with a linear power gain G and that the gain is applied equally to both signal quadratures (known as phase-preserving or phase-insensitive amplification). We expect an output field $\hat{b}$ satisfying the following relations:

$$\begin{aligned} \hat{b} &= \sqrt{G}\hat{a} \\ \hat{b}^\dagger &= \sqrt{G}\hat{a}^\dagger \end{aligned} \tag{2.58}$$

Since the output signal is a state of an electromagnetic field, it must also satisfy the commutation relation $[\hat{b}, \hat{b}^\dagger] = 1$. However, this is clearly not possible using the

operators defined in Eq. 2.58. To resolve this we must add another mode to the output signal as follows:

$$\begin{aligned}\hat{b} &= \sqrt{G}\hat{a} + \hat{\mathcal{N}} \\ \hat{b}^\dagger &= \sqrt{G}\hat{a}^\dagger + \hat{\mathcal{N}}^\dagger\end{aligned} \tag{2.59}$$

The operator $\hat{\mathcal{N}}$ represents noise added by the amplifier, which is random and uncorrelated with the input signal. To ensure that the output field $\hat{b}$ satisfies the standard bosonic commutation relation, we must have:

$$[\hat{\mathcal{N}}, \hat{\mathcal{N}}^\dagger] = 1 - G \tag{2.60}$$

We can express the noise operator in terms of an added mode of an electromagnetic field $\hat{c}$ when $G > 1$:

$$\begin{aligned}\hat{\mathcal{N}} &= \sqrt{G-1}\hat{c}^\dagger \\ \hat{\mathcal{N}}^\dagger &= \sqrt{G-1}\hat{c}\end{aligned} \tag{2.61}$$

In this model $\hat{c}$ represents a single additional input mode, which is amplified by a gain $G - 1$. This mode is the so-called idler mode in parametric amplifiers.

The amplifier output noise can be calculated from the variance of the output field $(\delta\hat{b})^2$. Using Eq. 2.59 and the bosonic commutation relations for the input and output fields [98]:

$$(\delta\hat{b})^2 \geq G(\delta\hat{a})^2 + \frac{|G-1|}{2} \tag{2.62}$$

In the high gain limit we have $G \approx G - 1$ and the input referred noise is written as:

$$(\delta\hat{b})^2/G \geq (\delta\hat{a})^2 + \frac{1}{2} \tag{2.63}$$

This inequality specifies that at least half a photon of noise should be added to the input signal during phase preserving amplification. If $G = 1$, i.e. the signal is not amplified, the amplifier is not required to add any noise.

The derivation above was for the situation when we amplify both amplitudes of the field equally. In certain scenarios it is sufficient to amplify only a single quadrature.

We could define the output field operators in the following way:

$$\begin{aligned} \hat{b} &= \sqrt{G}\hat{a} \\ \hat{b}^\dagger &= \frac{\hat{a}^\dagger}{\sqrt{G}} \end{aligned} \tag{2.64}$$

It is clear that such a definition of operators satisfies the commutation relations for the input and output fields. Physically, this definition implies that we are amplifying one field quadrature and deamplifying the other. This leads to the input referred noise:

$$(\delta\hat{b})^2/G \geq (\delta\hat{a})^2 \tag{2.65}$$

This type of amplification is known as phase sensitive, since the gain depends on which quadrature the input field occupies. Remarkably, phase sensitive amplification can be performed without adding any noise.

2.4 Hybrid systems

The following section starts with a description of the interaction between an electron spin system and a classical microwave magnetic field, followed by an introduction to spin relaxation and decoherence processes. We then introduce the Jaynes-Cummings Hamiltonian to describe the coupling of a single electron spin with a quantized electromagnetic field. We end by discussing an important phenomenon in QED and this thesis, the Purcell effect.

2.4.1 Spins in a classical magnetic field

Electrons posses a magnetic dipole moment $\hat{\mu} = -\gamma_e \hat{S}$ that results from an intrinsic angular momentum called spin, where $\gamma_e = 28$ GHz/T is the gyromagnetic ratio for a free electron and $\hat{S}$ is a vector of the spin operators introduced below. For a single electron subject to an external magnetic field $\overrightarrow{B}(t)$, its energy can be described by the following Hamiltonian:

$$\hat{H} = -\hat{\mu} \cdot \overrightarrow{B}(t) \tag{2.66}$$

The energy of the spin is minimized if it is aligned anti-parallel to the applied field (assuming γ_e to be positive). At zero temperature an ensemble of electron spins will thermalize to this lowest energy state (the ground state) yielding a maximum net magnetization $M_{max} = N\mu$, where N is total number of spins. However, at non-zero temperatures the existence of thermal excitations will reduce the polarization of the ensemble by a fraction $\rho = \tanh(\hbar\omega/2k_BT)$, calculated from the Boltzmann distribution of spin populations of the ground and excited states. The macroscopic magnetization is expressed as the net magnetic moment per unit volume V:

$$M = \frac{\rho}{V}\sum_{i=1}^{N}\mu_i \tag{2.67}$$

The equation of motion for the magnetization vector in static external magnetic field is given by:

$$\frac{d\overrightarrow{M}}{dt} = \gamma_e\overrightarrow{M} \times \overrightarrow{B_0} \tag{2.68}$$

This describes a torque acting on the net magnetic moment, which causes it to precess about the $\overrightarrow{B_0}$ field. The net magnetization is a bulk property that can be described classically, however, this is not a valid treatment of a single spin, which must be treated with a quantum mechanical framework. The frequency of precession, which is also called the Larmor frequency, is given as:

$$\omega_s = -\gamma_e B_0 \tag{2.69}$$

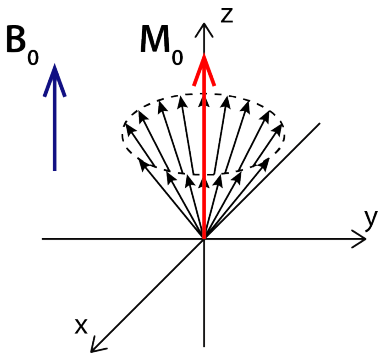

Figure 2.7: Precession of the magnetization of a spin ensemble in a static magnetic field.

The precession of the magnetization vector due to a static $\overrightarrow{B_0}$ field along the z axis is depicted in Fig. 2.7. ESR experiments are usually performed by applying a linearly polarized magnetic field oscillating at microwave frequencies, applied perpendicular to the strong static $\overrightarrow{B_0}$ field [99]. Linearly polarized fields are easier to implement in practice, and the superconducting resonators we exploit produce these fields. A linearly polarized field $\overrightarrow{B_1}(t) = 2B_1[\cos(\omega_{mw}t), 0, 0]$ can be decomposed as a linear combination of clockwise

(CW) and counter-clockwise (CCW) circularly polarized/rotating signals (see Fig. 2.8):

$$\overrightarrow{B_1} = \overrightarrow{B_{1ccw}} + \overrightarrow{B_{1cw}} = B_1[\cos(\omega_{mw}t), \sin(\omega_{mw}t), 0] + B_1[\cos(\omega_{mw}t), -\sin(\omega_{mw}t), 0] \tag{2.70}$$

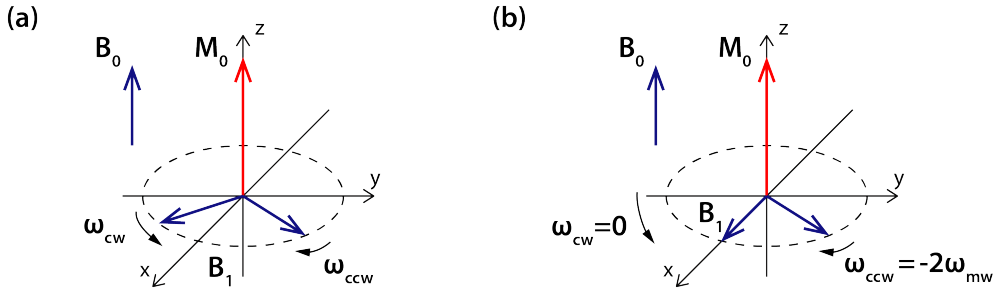

Figure 2.8: **a)** Linearly polarized oscillating magnetic field, depicted as two circulating B_1 magnetic fields in the laboratory frame. **b)** B_1 field in the rotating frame.

This treatment allows for a simpler understanding and calculation of the magnetization vector dynamics when operating in a reference frame that rotates at an angular frequency ω_{mw}. In this rotating frame, the CCW polarized component (which rotates at the frequency ω_{mw} in the laboratory frame) becomes stationary (i.e. $\omega_{ccw} = 0$ in the rotating frame). The CW component (which rotates at the frequency $-\omega_{mw}$ in the laboratory frame) precesses at an effective frequency of $\omega_{cw} = -2\omega_{mw}$ in the rotating frame. The CW term is neglected when $2\omega_{mw} >> -\gamma_e B_1$ by invoking the "rotating wave approximation" (RWA), as this represents a drive that is far off-resonance from the spins. When the perpendicular field is on-resonance with the spins ($\omega_{mw} = -\gamma_e B_0$), then even a weak AC drive $B_1 << B_0$ results in a significant precession about the B_1 axis. On the other hand, if the field is off-resonance, it does not have a strong effect on the magnetization.

The equations of motion in the rotating frame, known as Bloch equations, can be written:

$$\frac{dM_x}{dt} = -(\omega_s - \omega_{mw})M_y = -\Delta_s M_y \tag{2.71}$$

$$\frac{dM_y}{dt} = (\omega_s - \omega_{mw})M_x + \gamma_e B_1 M_z = \Delta_s M_x - \omega_1 M_z \tag{2.72}$$

$$\frac{dM_z}{dt} = -\gamma_e B_1 M_y = \omega_1 M_y \tag{2.73}$$

where we assume a $\overrightarrow{B_1}$ field along x in the rotating frame, a $\overrightarrow{B_0}$ along z, with $\Delta_s = \omega_s - \omega_{mw}$ the detuning and $\omega_1 = -\gamma_e B_1$ being the frequency of precession of

the magnetization about the $\overrightarrow{B_1}$ microwave field direction. The magnetization vector precesses about the vector sum of the magnetic fields in the rotating frame, which is tilted by an angle $\alpha = \arctan(\omega_1/\Delta_s)$ from z axis and generates an effective precession frequency:

$$\omega_{eff} = \sqrt{\Delta_s^2 + \omega_1^2} \tag{2.74}$$

For a phase-shifted linearly polarized magnetic field $\overrightarrow{B_1}(t) = 2B_1[\cos(\omega_{mw}t+\phi), 0, 0]$, can be decomposed in the rotating frame as $\overrightarrow{B_1} = B_1[\cos(\phi), \sin(\phi), 0]$. Thus, by controlling the phase ϕ of the drive field we can choose the orientation of the effective B_1 field and the axis of precession.

Inductive detection

In the case where the B_1 field is applied for well-defined time t_p (along x axis) and on-resonance with the spins ($\omega_{mw} = \omega_s$), the magnetization vector is rotated by an angle $\alpha = \omega_1 t_p$. We can thus produce an arbitrary magnetization rotation by controlling the strength of the B_1 drive field and/or the duration of the pulse. Fig. 2.9 depicts the case where the magnetization is rotated by magnetization by $\alpha = \pi/2$.

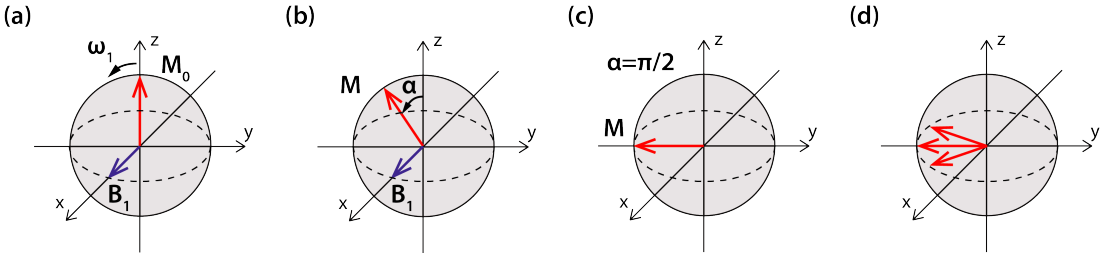

Figure 2.9: Polarized spins in a static magnetic field B_0 oriented along z-axis (not shown). **a)-b)** B_1 field applied along the x-axis generating spin precession around $\overrightarrow{x}$ in the rotating frame. **c)** The B_1 field produces $\pi/2$ rotation and is then turned off. **d)** The spins start to dephase in $x-y$ plane.

After tipping the magnetization by $\pi/2$ it will precess in the laboratory frame about $\overrightarrow{z}$. If we place detection coils in the $x-y$ plane close to our sample, the rotating magnetization vector will induce an electromotive force (EMF) proportional to $M_y - iM_x$ in the coils due to Faraday's law, which can be measured. This inductive detection scheme is the basis for modern ESR spectroscopy. In our experiments, planar superconducting resonators play the part of the inductive coils, and can be used to measure the precession of small spin ensembles.

Relaxation

The induced EMF in a spin resonance experiment will not persist indefinitely. Incoherent processes affecting the spins result in a loss of the net magnetization. Below we distinguish and discuss two types of relaxation: longitudinal and transverse.

Longitudinal relaxation

The spins, through interactions with their environment, will reach a state of thermal equilibrium where only a proportion of them are in their ground state, anti-aligned with the B_0 field. This fraction is given as

$$p = \tanh\left(\frac{\hbar\omega_s}{2kT_s}\right) \tag{2.75}$$

for spin $S = 1/2$ particles [100] at a temperature T_s.

The environmental interactions that cause the spins to thermalize to their environment leads to longitudinal (or energy) relaxation, which brings the magnetization M_z (for $B_0 \parallel \overrightarrow{z}$) back to the equilibrium magnetization value M_0 after being disturbed (e.g. by a B_1 pulse). The mechanism for longitudinal relaxation of spins in solids is typically mediated by phonons in the crystal lattice [101]. This spin-lattice relaxation follows an exponential decay described by a characteristic relaxation time T_1:

$$\frac{dM_z}{dt} = -\frac{(M_z - M_0)}{T_1} \tag{2.76}$$

Transverse relaxation

Transverse relaxation, also known as decoherence in the field of quantum information processing, describes the relaxation of the magnetization vector in the $x - y$ plane (i.e. normal to the direction of B_0 field). The characteristic time of transverse relaxation T_2 is different from but limited by the longitudinal relaxation time $T_2 \leq 2T_1$:

$$\frac{dM_{x,y}}{dt} = -\frac{M_{x,y}}{T_2} \tag{2.77}$$

Accounting for longitudinal and transverse relaxation processes, the Bloch equations

can be extended:

$$\frac{dM_x}{dt} = -\Delta_s M_y - \frac{M_x}{T_2} \tag{2.78}$$

$$\frac{dM_y}{dt} = \Delta_s M_x - \omega_1 M_z - \frac{M_y}{T_2} \tag{2.79}$$

$$\frac{dM_z}{dt} = \omega_1 M_y - \frac{M_z - M_0}{T_1} \tag{2.80}$$

Transverse relaxation can be caused by spin-spin interactions [99]. This yields a homogeneous broadening of the ESR spectra with a linewidth proportional to $1/T_2$. The ESR community distinguishes several primary spin-spin interaction mechanisms, including spectral diffusion, instantaneous diffusion and spin diffusion.

Spectral diffusion occurs when spins that are excited by a B_1 pulse experience magnetic field fluctuations originating from spins outside of the pulse bandwidth (i.e. non-resonant spins). Stochastic flip-flops of the non-resonant spins leads to a random walk of the excited spin precession frequencies, contributing to transverse relaxation [102]. Instantaneous diffusion plays a dominant role for large spin concentrations. The spins "see" the magnetic dipole field produced by their neighbours, which changes sign when the spins are flipped by a B_1 field. Instantaneous diffusion is notoriously difficult to remove in practice due to its dynamic behaviour with applied pulses [103]. The final mechanism, spin diffusion [99], is caused by direct dipolar flip-flops between spins excited by a pulse (resonant spins) and spins that have not. Spin diffusion exhibits a strong dependence on the distance between the resonant and non-resonant spins (and thus the concentration), where smaller spin-spin separations lead to higher rates of diffusion.

Another contributing factor to transverse relaxation is inhomogeneous broadening. Inhomogeneous broadening is produced by local magnetic field inhomogeneities that create a distribution of spin Larmor precession frequencies. The inhomogeneities may exist in the external B_0 field, result from unresolved hyperfine interactions with surrounding nuclei etc. In response, the spins fan out (or 'dephase') in the $x - y$ plane, reducing the net magnetization. The linewidth of an inhomogeneously broadened spectra is proportional to $1/T_2^*$, which can be (and often is) much larger than the $1/T_2$. However, in contrast to homogeneous broadening, all inhomogeneous broadening mechanisms are static, and can be reversed by the application of appropriate pulse sequences [104].

2.4.2 Single spin in quantized field of a cavity

In this section we consider the system of a single electron spin interacting with a single-mode cavity field. Typically in electron and nuclear spin spectroscopy the electromagnetic field driving spin rotations is described classically, whereas the spin is treated as a quantum mechanical object. This is called the semi-classical approach. On the other hand, the Jaynes-Cummings model [105] is a fully quantum-mechanical theory that treats both the field and spins as quantum objects and is the basis of cQED. We employ the Jaynes-Cummings model in this thesis and provide here a concise overview of its basic formulation.

Jaynes-Cummings Hamiltonian

The total Hamiltonian of the system under investigation can be written as:

$$\hat{H}_{JC} = \hat{H}_s + \hat{H}_c + \hat{H}_i \tag{2.81}$$

where the first term describes the spin Hamiltonian, the second term stands for the cavity Hamiltonian and the last term characterizes the interaction between the two systems.

As introduced in Sec. 2.4.1, a spin interacts with a magnetic field through its magnetic dipole moment (see Eq. 2.66). A single electron spin 1/2 particle has two eigenstates and embodies the prototypical two-level system. For simplicity, we call these states the ground state $|g\rangle$ with eigenenergy E_g and excited state $|e\rangle$ with eigenenergy E_e. The energy difference between these two states defines the transition frequency $\omega_s = (E_e - E_g)/\hbar$, which corresponds to the Larmor frequency of Eq. 2.69.

The Hamiltonian for a spin in an external magnetic field B_0 oriented along the z-axis is:

$$\hat{H}_s = -\gamma_e B_0 \hat{S}_z = \omega_s \hat{S}_z \tag{2.82}$$

To describe the quantum spin operators $\hat{S}$ we first introduce the Pauli matrices:

$$\hat{\sigma}_x = \begin{pmatrix} 0 & 1 \\ 1 & 0 \end{pmatrix}, \ \hat{\sigma}_y = \begin{pmatrix} 0 & -i \\ i & 0 \end{pmatrix}, \ \hat{\sigma}_z = \begin{pmatrix} 1 & 0 \\ 0 & -1 \end{pmatrix} \tag{2.83}$$

Together with the identity matrix, they form a basis for the vector space of 2×2 Hermitian matrices. The electron spin operators are simply the Pauli matrices scaled

by an angular momentum $\hbar/2$:

$$\hat{S}_{x,y,z} = \frac{\hbar}{2}\hat{\sigma}_{x,y,z} \tag{2.84}$$

The Hamiltonian 2.82 can be thus be rewritten in the following form:

$$\hat{H}_s = \frac{\hbar\omega_s}{2}\hat{\sigma}_z \tag{2.85}$$

The magnetic dipole moment of the spin can be also represented in the basis $V = \{|g\rangle, |e\rangle\}$ (i.e. the eigenstates of the $\hat{\sigma}_z$ operator), according to the spectral decomposition theorem [12]:

$$\hat{\mu} = \gamma_e \hat{S} = \gamma_e \sum_{i,j} |i\rangle\langle i|\hat{S}|j\rangle\langle j| = \sum_{i,j} M_{i,j}\hat{\sigma}_{ij} \tag{2.86}$$

where $|i\rangle$ and $|j\rangle$ are elements of the basis V, $\hat{\sigma}_{ij} = |i\rangle\langle j|$ is the transition operator and $M_{i,j} = \langle i|\hat{S}|j\rangle$ the matrix element that governs the transition probability. When $i \neq j$, the transition operator causes the two-level system to gain or lose an excitation. In terms of the Pauli matrices, such "raising" and "lowering" operators are expressed as:

$$\hat{\sigma}_\pm = \hat{\sigma}_x \pm i\hat{\sigma}_y \tag{2.87}$$

Explicitly, the raising operator $\hat{\sigma}_+$ creates a spin excitation $\hat{\sigma}_+|g\rangle = |e\rangle$ and the lowering operator $\hat{\sigma}_-$ destroys an excitation $\hat{\sigma}_-|e\rangle = |g\rangle$.

The Hamiltonian of the cavity (with a resonance frequency ω_r) is written in the form of a quantum harmonic oscillator (see Sec. 2.1.4):

$$\hat{H}_c = \hbar\omega_r(\hat{a}^\dagger\hat{a} + \frac{1}{2}) \tag{2.88}$$

It is worth mentioning that the constant term $\hbar\omega_r/2$, corresponding to the energy of the vacuum, is usually neglected in the Jaynes-Cummings Hamiltonian as it simply represents an energy offset to all states.

Since the size of an electron is much smaller than the wavelength of the field, it is reasonable to assume that the spin interacts with the oscillating magnetic field B_1 produced by the cavity via a magnetic dipole interaction and the spatial variation of the field can be safely ignored:

$$\hat{H}_{int} = \hat{\mu} \cdot \hat{B}_1 \tag{2.89}$$

The field $\hat{B}_1$ can be expressed via bosonic creation and annihilation operators in a

similar way to the current fluctuations of a resonator as described in Eq. 2.14:

$$\hat{B}_1 = \delta B(\hat{a} + \hat{a}^\dagger) \tag{2.90}$$

with δB representing the root-mean-square vacuum fluctuations of the magnetic field. Combining Eqs. 2.86-2.90, we arrive at the interaction Hamiltonian:

$$\hat{H}_{int} = \sum_{i,j} M_{ij}\hat{\sigma}_{ij}\delta B(\hat{a} + \hat{a}^\dagger) = \sum_{i,j} \hbar\hat{\sigma}_{ij}(g_{ij}\hat{a} + g_{ij}^*\hat{a}^\dagger) \tag{2.91}$$

where $g_{ij} = M_{ij}\delta B/\hbar$ is the coupling strength of a single spin with the resonator field. A further simplification of the Hamiltonian comes by equating the forward and reverse transition probabilities between the ground and excited states $M_{ij} = M_{ji}$, which yields $g_{ij} = g_{ji} = g$. Using the spin raising and lowering operators, the interaction term becomes:

$$\hat{H}_{int} = \hbar g(\hat{\sigma}_- + \hat{\sigma}_+)(\hat{a} + \hat{a}^\dagger) \approx \hbar g(\hat{\sigma}_+\hat{a} + \hat{\sigma}_-\hat{a}^\dagger) \tag{2.92}$$

Here we have used the RWA to neglect fast rotating (non energy conserving) terms $\hat{\sigma}_-\hat{a}$ and $\hat{\sigma}_+\hat{a}^\dagger$, which correspond to two-photon processes. However, this approximation becomes invalid when the systems enter the ultra-strong coupling regime, where $g \approx \omega_r$ [106], [107]. This thesis predominantly considers systems in the weak and strong coupling regimes with $g \ll \omega_r$. As a result, the appropriate form of Jaynes-Cummings Hamiltonian is:

$$\hat{H}_{JC} = \frac{\hbar\omega_s}{2}\hat{\sigma}_z + \hbar\omega_r\hat{a}^\dagger\hat{a} + \hbar g(\hat{\sigma}_+\hat{a} + \hat{\sigma}_-\hat{a}^\dagger) \tag{2.93}$$

Depending on the size of the rate of the interaction between the systems g in comparison to their individual loss rates, we define two regimes:

- Weak coupling: if $g \ll \kappa, \gamma$, where κ is the resonator linewidth and γ is the spin dephasing rate (or the spin linewidth). In this case the excitation is lost to the bath before it can be coherently transferred between the systems.

- Strong coupling: if $g \gg \kappa, \gamma$. In this case the excitation is coherently transferred between the systems resulting in Rabi oscillations as well as a hybridisation of the spin and cavity eigenstates.

A useful figure of merit to quantify the coupling regime is the cooperativity $C = g^2/(\kappa\gamma)$, which is the ratio of the "good system coupling" to "bad system couplings". For $C \ll 1$ the system is in the weak coupling regime, whilst for $C \gg 1$ the spin is strongly

coupled to the resonator. The intermediate coupling regime, when $C \approx 1$, is also of interest for quantum information processing. This scenario describes an "impedance matched" system, where the coupling rate of the microwave field to the external port of the resonator matches the microwave absorption rate of the spin. It has been shown that this can be used to achieve unit-efficiency transfer of single microwave photons to the spin system, with application in quantum memories [108], [109].

Purcell relaxation

The spontaneous emission rates of electron or nuclear spin systems in the solid state are usually incredibly small, and relaxation is dominated by other processes including spin-lattice (i.e. phonon-mediated) or spin-spin (i.e. spin diffusion) [99]. However, in 1946 Edward Purcell showed that the spontaneous emission rate can be enhanced if a spin system is placed inside a resonant cavity [110], [111]. According to Purcell, the probability of spontaneous emission can be calculated from:

$$A_\nu = \frac{8\pi\nu^2}{c^3} h\nu \frac{8\pi^3\mu^2}{3h^2} \; [sec^{-1}] \tag{2.94}$$

where ν is the transition frequency, c is the speed of light and μ is the dipole moment. In this expression, the factor $(8\pi\nu^2)/c^3$ describes the number of radiation oscillators per unit volume per unit frequency at frequency ν, or in other words the photon density of states. For a spin placed inside a resonant circuit this term must be modified, since there is only one oscillator in the frequency range ν/Q available. As a result, the spontaneous emission rate can be increased by many orders of magnitude, with the enhancement depending on the cavity quality factor Q and the resonant mode volume. The mode volume determines the concentration of the cavity vacuum energy, a smaller volume produces larger vacuum fluctuation field strengths and consequently greater spontaneous emission rates. Expressing the Purcell-enhanced relaxation rate of spins inside a cavity in terms of our circuit-QED parameters (the single spin-resonator coupling strength g and cavity linewidth κ) [48]:

$$\Gamma_P = \frac{\kappa g^2}{\kappa^2/4 + \delta^2} \tag{2.95}$$

where $\delta = \omega_r - \omega_s$ is the spin-cavity frequency detuning.

This effect provides a convenient method for initialising a quantum system and has been used in superconducting qubits as a fast reset [59], [112]. It is particularly im-

portant for spin systems, which can display very long intrinsic T_1 times at milli-Kelvin temperatures, ranging from seconds to hours [113]. Despite the Purcell effect initially being proposed as a method to reduce relaxation times in nuclear spin resonance experiments, it was only very recently demonstrated for the first time with electron spins [48]. It has since been used as a valuable tool in low temperature ESR spectroscopy experiments as a way to enhance experimental repetition times [31], [36]. For an in-depth theoretical explanation of the Purcell effect, the reader is directed to Ref. [6].

2.5 ^{209}Bi donors in silicon

Natural silicon is comprised of three stable isotopes ^{28}Si, ^{29}Si, ^{30}Si with abundances of 92.2%, 4.7% and 3.1%, respectively. The ^{29}Si isotope is the only one with a non-zero nuclear spin $I = 1/2$ [114]. This positions silicon as an excellent host for spin-based quantum technologies, offering a magnetically silent environment. By enriching silicon chips in the ^{28}Si isotope, one can further reduce the ^{29}Si nuclear spin noise [115], producing what's often referred to as a "semiconductor vacuum". Much experimental work has been undertaken to demonstrate record breaking coherence times for spins in silicon – primarily in donor-based systems – making this system one of the most coherent in the solid state. Tyryshkin measured T_2 times exceeding seconds for donor-bound electrons [103], whilst Saeedi showed that the nuclear spins of ionized ^{31}P donors can preserve their coherence for hours [116].

The semiconductor industry has utilized dopant atoms in silicon to tailor the electrical properties of classical microelectronic devices for more than half a century. Over the years, the metal-oxide-semiconductor (MOS) fabrication process was developed which now allows the large-scale production of pristine silicon devices with features measuring several nanometers in size. The controllability and scalability of silicon electronics, together with the high spin coherence times possible in this system instigated a seminal proposal for a spin-based silicon quantum computer in 1998 [117].

Group V elements, such as phosphorus (^{31}P), arsenic (^{33}As), antimony (^{121}Sb), and bismuth (^{209}Bi) all serve as donors in silicon (see Table 2.1). They can be introduced into the substrate during the silicon crystal growth, known as bulk-doping, or by ion-implantation.

Phosphorus is a common group V donor used in quantum technological application

Donor	I	A (MHz)	a_0 (nm)	E_b (meV)
^{31}P	1/2	117.53	16.8	45.6
^{75}As	3/2	198.35	15.5	53.8
^{121}Sb	5/2	186.80	17.3	42.8
^{123}Sb	7/2	101.52	17.3	42.8
^{209}Bi	9/2	1475.4	11.5	71

Table 2.1: Group V donor properties.

because of its nuclear spin of one-half ($I = 1/2$), which yields a relatively simple four-dimensional Hilbert space when coupled to its donor-bound electron spin ($S = 1/2$). However, recently considerable attention has been directed to the high nuclear spin donors ^{123}Sb and ^{209}Bi. These donors exhibit many interesting properties, including quadrupole moments that allow pure electrical driving of the nuclear spin states [118]. Bismuth has the greatest nuclear spin $I = 9/2$ and therefore offers largest Hilbert space. In addition, bismuth has the strongest hyperfine coupling constant $A/2\pi = 1475.4$ MHz [101], which originates from a magnetic interaction between the electron and nuclear spins and is proportional to the overlap of the electron wavefunction with the nucleus. The large I and hyperfine constant of ^{209}Bi leads to a sizable zero-field splitting of 7.375 GHz – a value in the operational frequency range of typical superconducting qubit circuits. This raises the intriguing prospect of combining these two systems in a hybrid device, where the bismuth is utilized as a long-term storage element for single microwave photons states of the superconducting qubits.

The Si:^{209}Bi system has demonstrated excellent electron and nuclear spin coherence properties, partially owing to its small Bohr radius 11 nm [119] that results from its strong electron binding energy $E_b = 71$ meV [120]. The 20-dimensional electron-nuclear Hilbert space produces rich physics, including operational sweet spots, or "clock transitions", where to the first order the spin transition frequencies are insensitive to magnetic field fluctuations ($df/dB \to 0$) or strain/electric field sweet-spots where sensitivity to changes in A is reduced ($df/dA \to 0$) [121]. This leads to improved coherence properties of bismuth donors tuned to clock transitions, where T_2 times up to 100 ms have been observed even in natural silicon samples [122].

In this thesis we explore the use of nonlinear superconducting cavities in quantum technologies related to ESR spectroscopy. The spins in this work are provided by bismuth donors in isotopically enriched ^{28}Si substrates which were selected for their long coherence times and compatibility with our superconducting resonator fabrication

process (presented in Sec. 3.2). In the following section we discuss additional details relating specifically to the bismuth spin system.

2.5.1 ESR transitions

Bismuth is a group V element that acts as an electron donor in silicon. When cooled to cryogenic temperatures, the extra valence electron of the bismuth donor becomes weakly bound to the Coulomb potential of its nucleus. In the neutral D^0 charge state, ^{209}Bi presents a two-spin electron ($S = 1/2$) nuclear ($I = 9/2$) system, strongly coupled via a hyperfine interaction A. The Hamiltonian describing the donor in an external static magnetic field B_0 aligned along z-axis (assuming an isotropic hyperfine interaction) can be written in the following form [122]:

$$\hat{H}/\hbar = B_0 \cdot (\gamma_e \hat{S}_z \otimes 1 - \gamma_n 1 \otimes \hat{I}_z) + A\hat{S} \cdot \hat{I} \tag{2.96}$$

where $\gamma_e/2\pi = 27.997$ GHz/T and $\gamma_n/2\pi = 6.9$ MHz/T are the gyromagnetic ratios of the bismuth electron and nucleus [122], respectively. The first term corresponds to the electron Zeeman interaction, the second term represents the nuclear Zeeman energy and the last term describes the hyperfine interaction. $\hat{S}$ and $\hat{I}$ are vectors containing the electron and nuclear spin operators, respectively.

This Hamiltonian results in 20 B_0-dependent energy levels as depicted in Fig. 2.10 – a plot known as the Breit-Rabi diagram. For $A \ll \gamma_e B_0$, which is generally the case for most of the group V donors at spin transition frequencies typically of interest ($\omega_s/2\pi \gtrsim 5$ GHz), the Hamiltonian is diagonal in the Zeeman eigenstate basis, namely $\{|m_S, m_I\rangle\}$, where $m_S = \pm\frac{1}{2}$ and $m_I = -I, -I+1, \ldots, I-1, I$ are the electron and nuclear spin projections on the axis of quantization (here the z-axis). However, due to the strong hyperfine interaction present in bismuth donors, the electronic and nuclear spin states hybridize. The relevant quantum numbers in this case are the total spin $F = I \pm S$ and its z-projection $m_F = m_S + m_I$.

In the low field limit where the hyperfine coupling strength is larger than the Zeeman interaction ($B_0 < A/\gamma_e \approx 50$ mT), the energy states can be grouped into $F = 4$ ground and $F = 5$ excited multiplets, separated by a large splitting of $5A/2\pi = 7.375$ GHz at zero magnetic field. In this regime the eigenstates are described in the "coupled" basis $\{|F, m_F\rangle\}$. In the high field limit ($B_0 \gg A/\gamma_e \approx 50$ mT), the electron and nuclear

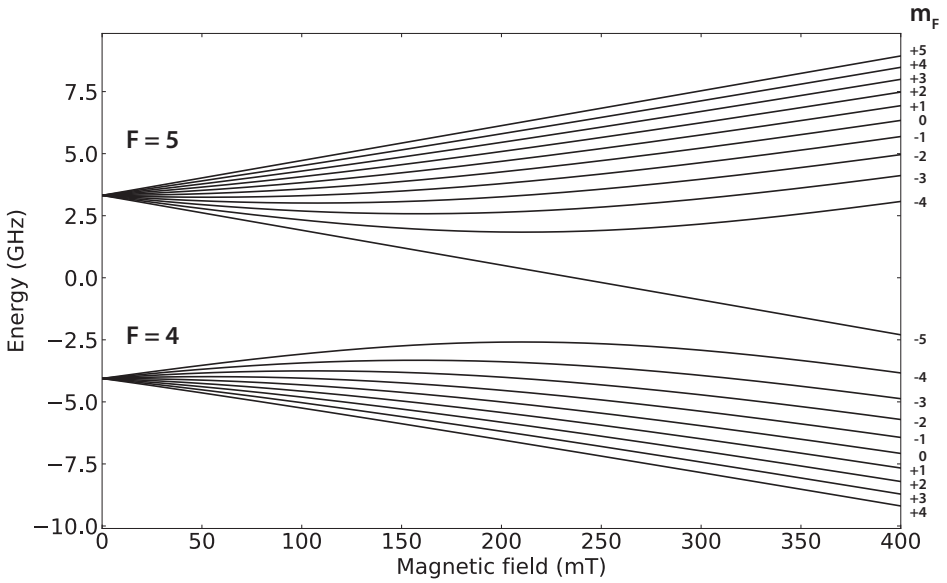

Figure 2.10: Neutral bismuth donor energy levels in the presence of external magnetic field.

spins become "decoupled" and may be expressed in the $\{|m_S, m_I\rangle\}$ basis. A detailed theoretical analysis of the bismuth electron-nuclear spin states can found in Refs. [121], [123].

Transitions between different states are possible only if the transition matrix element is non-zero. For example, the two-level system with ground state $|g\rangle$ and excited state $|e\rangle$ can be driven by $\hat{S}_x$ (i.e. a drive field B_1 normal to the direction of B_0) only if $\langle e|\hat{S}_x|g\rangle \neq 0$. For bismuth, the allowed ESR transitions strongly depend on field of operation.

In the high field limit, the selection rules for transitions driven by the $\hat{S}_x$ and $\hat{S}_y$ operators are standard: $\Delta m_S = \pm 1$ and $\Delta m_I = 0$. Transitions through the $\hat{S}_z$ operator are forbidden at high field. In the low field limit, two pairs of transitions with non-zero matrix elements for the $\hat{S}_x$ and $\hat{S}_y$ operators can be identified. The first has the selection rule $\Delta F = \pm 1$ and $\Delta m_F = \pm 1$ and the second $\Delta F = \pm 1$ and $\Delta m_F = \mp 1$. Succinctly, this can be written as $\Delta F \Delta m_F = \pm 1$. Interestingly, the strong electron-nuclear spin coupling at low magnetic fields allows certain transitions driven by the $\hat{S}_z$ operator, corresponding to the selection rule $\Delta F = \pm 1$ and $\Delta m_F = 0$. Practically, such S_z-type transitions are excited by parallel alignment of the B_1 and B_0 fields.

ESR clock transitions

Donor systems with nuclear spins $I \geq 1$ exhibit ESR clock transitions. Clock transitions are classified as being of magnetic-type when $df/dB \to 0$ or electric-type when $df/dA \to 0$. At these "sweet spots" the system is protected, to the first order, from noise that couples in to the system either magnetically, or via the hyperfine interaction. Since bismuth has the largest nuclear spin amongst the group V donors, it also has the most clock transitions.

In Table 2.2 we provide details of the ESR magnetic field clock transitions for all group V donors in silicon. Bismuth is the only element in this table that has the clock transition at sufficiently large frequencies to be interfaced with superconducting qubits, making it an exceptional candidate spin system for quantum memory applications. The hyperfine clock transitions for the group V donors are outlined in Table 2.3.

Donor	I	Magnetic field (mT)	Frequency (GHz)	Transition $\Delta F = +1, m_F$
^{75}As	$\frac{3}{2}$	3.8	0.384	$-1 \leftrightarrow 0$
^{121}Sb	$\frac{5}{2}$	3.4	0.552	$-1 \leftrightarrow 0$
		10.4	0.482	$-2 \leftrightarrow -1$
^{123}Sb	$\frac{7}{2}$	1.8	0.403	$-1 \leftrightarrow 0$
		5.5	0.376	$-2 \leftrightarrow -1$
		9.3	0.314	$-3 \leftrightarrow -2$
^{209}Bi	$\frac{9}{2}$	26.6	7.338	$-1 \leftrightarrow 0$
		79.8	7.032	$-2 \leftrightarrow -1$
		133.3	6.372	$-3 \leftrightarrow -2$
		187.8	5.214	$-4 \leftrightarrow -3$

Table 2.2: Magnetic field clock transitions. Data extracted from Ref. [122].

Donor	I	Magnetic field (mT)	Frequency (GHz)	Transition $\Delta m_S = +1, m_I$
^{75}As	$\frac{3}{2}$	53	1.43	$-1/2$
^{121}Sb	$\frac{5}{2}$	117	3.21	$-1/2$
		39	0.92	$-3/2$
^{123}Sb	$\frac{7}{2}$	114	3.17	$-1/2$
		38	0.98	$-3/2$
		23	0.49	$-5/2$
^{209}Bi	$\frac{9}{2}$	2607	72.64	$-1/2$
		868	23.18	$-3/2$
		519	12.57	$-5/2$
		369	7.30	$-7/2$

Table 2.3: Hyperfine interaction clock transitions. Data extracted from Ref. [122].

Chapter 3

Experimental methods

The experiments described in this thesis were performed on two devices using two different experimental setups.

The first device consists of a microwave superconducting resonator fabricated on top of an isotopically enriched silicon wafer containing ion-implanted bismuth donors. This silicon chip is wire bonded to a printed circuit board (PCB) and housed inside a copper enclosure. The enclosure is mounted to the cold finger of a ^{3}He cryogenic refrigerator that cools the device down to a temperature of 400 mK. The experiments carried out utilizing this experimental setup are presented in Ch. 5 and Ch. 6.

The second device is a microwave superconducting resonator of comparable design to the one used in the spin-based experiments, but with a few critical design alterations that provide it with important properties for low-noise amplification and squeezing. It is fabricated on top of natural silicon wafer without any implanted donors. This chip is wire bonded to exactly the same PCB as the first device, and placed inside an enclosure. The enclosure is thermally anchored to the cold finger of a dilution ^{3}He-^{4}He cryogenic refrigerator, allowing for measurements to be performed below 20 mK. These experiments are presented in Ch. 4.

In this chapter we present the device design, measurement setups and techniques utilized in our experiments. We start by describing the unique design of the microwave superconducting resonator used throughout this thesis. To implement our design on a silicon chip we utilize micro- and nanofabrication techniques with the specific steps outlined here. Following this we describe how the resonator is packaged for measurement and present the experimental setups used for device characterisation. We conclude this chapter by introducing the ESR control sequences, generated by our room-temperature setup, that are used to probe the electron spin ensemble for the experiments presented in Ch. 5.

3.1 Device design

The devices used in the experiments throughout the thesis exhibit a nonlinearity originating from kinetic inductance (see Sec. 2.2.2). This inductance can be readily controlled in-situ through the application of DC currents. However, introducing DC currents to a microwave resonator without introducing losses poses a significant challenge. To overcome this hurdle we exploit a microwave photonic bandgap (PBG) structure [124]. This design consists of interchanging low- and high-impedance sections of a transmission line to produce a band-stop filter in the microwave frequency range. The bandstop filter (which can alternatively be described as a microwave Bragg reflector) allows us to effectively decouple a resonant segment of TL from the external circuitry, without having to create a gap in the line – the standard way to produce a distributed resonator. Since the PBG structure is continuous, it allows the passage of DC currents through the resonator.

The resonator and PBG are implemented using coplanar waveguide (CPW) technology, which is introduced in this section. CPWs are a great choice for maintaining high resonator quality factors and are easy to produce with standard clean-room fabrication processes. Next, we describe how to construct the PBG structure from CPWs and how to integrate it with the resonator.

3.1.1 Coplanar waveguide

A coplanar waveguide consists of a conductor separated from a pair of ground planes, fabricated on top of a dielectric substrate (of height H). The central conductor line width is parameterized by w and its distance to each ground plane (or, the gap) is given by g (see Fig. 3.1). Other parameters of the CPW, such as its characteristic impedance (Z_0), phase velocity (v_p) and line propagation constant (γ) depend on its exact geometry and material properties. It is not always trivial to calculate these parameters analytically. They are often approximated using conformal mapping techniques [125]. Another common approach to CPW design is to utilize an electromagnetic simulator.

To design our devices we make use of two commercially-available electromagnetic software packages, Sonnet® and Computer Simulation Technology (CST) Microwave Studio. Sonnet is exclusively used here to simulate planar geometries and employs a rigorous Method of Moments EM analysis based on Maxwell's equations. Sonnet is

a "2.5D" solver, capable of simulating planar circuits with multiple dielectric and/or conductor layers, providing S-, Y-, Z-parameters or SPICE models as an output. On the other-hand, CST is a finite element method (FEM) simulator with powerful 3D full-wave solvers, capable of providing detailed EM field profiles for complex circuits and true 3D geometries (like cavities).

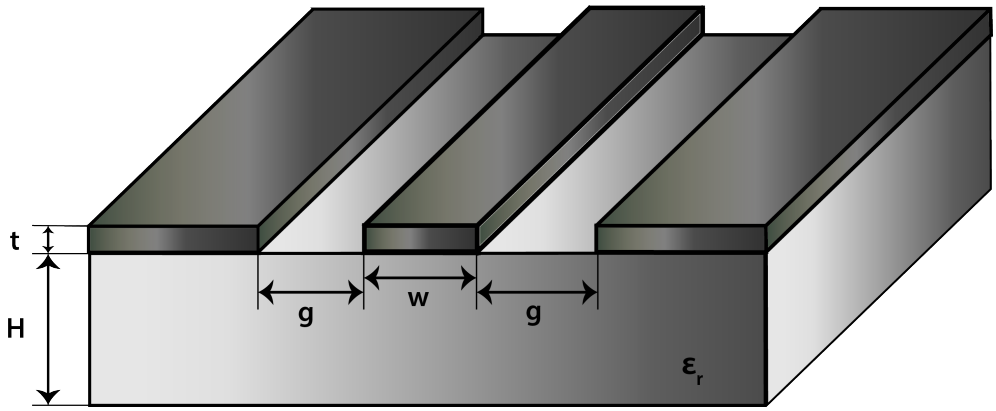

Figure 3.1: The conventional coplanar waveguide implementation consists of a dielectric substrate (light gray) with a conductive (dark gray) layer on top.

A CPW supports a transverse electromagnetic (TEM) like wave, which has electric and magnetic fields polarizations perpendicular to each other and to the direction of the propagation [40], [125]. When a TEM wave propagates in a uniform dielectric medium it maintains a constant phase velocity. However, the EM wave that is supported by a CPW propagates partially in the dielectric substrate underneath the conductor, and partially in the dielectric above it. Since these two dielectric media usually have different dielectric constants, the wave has longitudinal components of the fields and does not represent a true TEM mode, but rather a hybrid mode. It is common to describe this wave as quasi-TEM, since these longitudinal components are small and quite often neglected in the analysis (see Fig. 2.5b).

To estimate the effective dielectric constant ϵ_{eff} of the CPW we calculate the mean of the dielectric constants of two insulators surrounding the conductor. In the case of air or vacuum ($\epsilon_{air} = 1$) above the conductor and a substrate with dielectric constant ϵ_r underneath, we have:

$$\epsilon_{eff} = \frac{\epsilon_r + 1}{2} \tag{3.1}$$

This effective dielectric constant allows us to estimate the phase velocity of the

quasi-TEM wave propagating along the CPW:

$$v_p = \frac{c}{\sqrt{\epsilon_{eff}}} \tag{3.2}$$

where c is the speed of light in vacuum. Since the conductor film is typically much thinner than the substrate ($t \gg H$), we can consider the dielectric substrate as an infinitely thick layer and calculate the characteristic impedance as:

$$Z_0 = \frac{30\pi}{\sqrt{(\epsilon_r + 1)/2}} \frac{K(k_0^*)}{K(k_0)} \tag{3.3}$$

where $K(x)$ is the complete elliptic integral of the first kind with arguments provided by the CPW geometry:

$$\begin{aligned} k_0 &= \frac{w}{w + 2g} \\ k_0^* &= \sqrt{1 - k_0^2} \end{aligned} \tag{3.4}$$

3.1.2 Coplanar waveguide resonator

$\lambda/2$ resonator

A half-wavelength ($\lambda/2$) CPW resonator is defined by imposing open boundary conditions at two points along the central conductor, separated by a half-wavelength (see Sec. 2.1.3). The open boundary is generally implemented by introducing a discontinuity/gap into the central line [126]. The resonator is then capacitively coupled to the transmission line at either end and the strength of the coupling is determined by the size of discontinuity.

Fig. 3.2a depicts the voltage and current distributions for the fundamental mode of a half-wavelength resonator. At the open ends of the resonator the current goes to zero, whereas the voltage displays antinodes. The harmonics of this structure appear at frequencies:

$$f_n = \frac{n v_p}{2l} \tag{3.5}$$

where l is the resonator length, v_p represents its phase velocity and n is a positive integer.

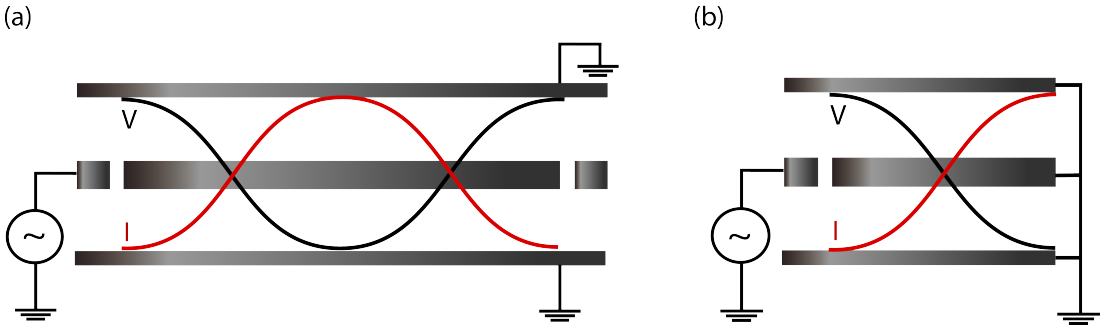

Figure 3.2: Schematics of the **a)** $\lambda/2$ CPW resonator and **b)** $\lambda/4$ CPW resonator, connected to a microwave source. The fundamental mode current and voltage spatial distributions are shown in red and black, respectively. Figure adopted from Ref. [127].

$\lambda/4$ resonator

The other type of distributed resonator we consider here is the quarter-wavelength ($\lambda/4$) CPW resonator. It is implemented by leaving one end of the central line open and shorting the other to ground. Hence, a current node forms at the open end and a voltage node at the shorted end (see Fig. 3.2b). The harmonic frequencies are determined by its length and phase velocity as:

$$f_n = \frac{(2n-1)v_p}{4l} \tag{3.6}$$

with n a positive integer.

The interdigitated capacitor

The fraction of kinetic inductance present in the resonant section of the CPW is determined by several parameters (recall Sec. 2.2.2). To increase the nonlinearity of our devices, we can reduce the thickness of the superconducting film, which results in a higher room-temperature sheet resistance R_s and a larger per-square value of the kinetic inductance as shown in Fig. 3.3. In addition, we may reduce the width of the central conductor w (see Eq. 2.55) to raise the effective number of squares in the resonator wire and hence the total kinetic inductance. Whilst the strong nonlinearity is desirable in our work, the higher inductance of the TL leads to a large characteristic impedance, which has several detrimental effects. For example, a high resonator impedance reduces its zero-point current (and hence magnetic field) fluctuations, lowering the spin-resonator coupling strength. In Ch. 6 a resonator high impedance is a major hurdle to achieving Purcell-limited relaxation and radiative spin cooling. In addition, in the amplification

experiments of Ch. 4 a smaller resonator impedance reduces the power requirements (it provides a larger pump current for a given power), which is important for minimizing heating and reaching the quantum-noise-limit of amplification.

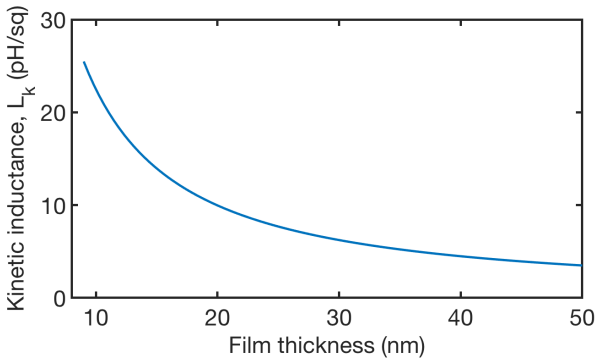

Figure 3.3: Calculated dependence of the kinetic inductance per-square on the NbTiN film thickness. The estimated values of sheet resistance R_s, required in Eq. 2.55, were derived from the empirical data provided by Dr Robin Cantor from the company "Star Cryo".

To compensate for the high kinetic inductance and reduce the impedance, we introduce an interdigitated capacitor (IDC) to the resonant CPW section. The IDC is a microwave planar capacitor that consists of a dense set of interlocking fingers between the central conductor and ground plane, as shown in Fig. 3.4. This structure boosts the capacitance per unit length and therefore lowers the characteristic impedance $Z_0 = \sqrt{L/C}$, where L and C are the inductance and capacitance per unit length, respectively. The enhanced L and C in the resonator can reduce considerably its phase velocity $v_p = 1/\sqrt{LC}$, which shortens the resonator length.

To engineer the IDC resonator with the desired capacitance we perform an EM simulation. Fig. 3.5 depicts the dependence of the IDC CPW characteristic impedance Z_0 on the capacitor finger length h, extracted from Sonnet simulations for a $w = 2$ μm wide central line with a kinetic inductance of $L_k = 8.55$ pH/sq, corresponding to an 18 nm thick NbTiN film.

3.1.3 Microwave photonic bandgap

The PBG is a periodic structure of interchanging low- and high-impedance TLs that effectively form an LC ladder filter [40] (see Fig. 3.6). It creates a bandstop re-

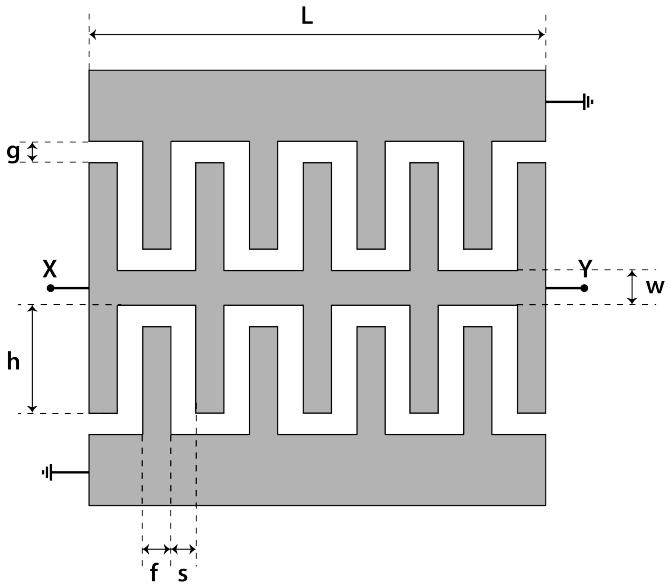

Figure 3.4: A CPW transmission line with interdigitated capacitor fingers to ground.

gion of frequencies in which electromagnetic waves cannot propagate, hence the name "photonic bandgap". The LC ladder or stepped-impedance filter can readily be designed using the $ABCD$ matrix approach [40]. For a section of TL with length l and characteristic impedance Z_0, the $ABCD$ matrix is written in the following form:

$$ABCD = \begin{pmatrix} \cos(\beta l) & iZ_0 \sin(\beta l) \\ (i/Z_0)\sin(\beta l) & \cos(\beta l) \end{pmatrix} \tag{3.7}$$

where $\beta = \omega/v_p$ is the phase constant. We find the total $ABCD$ matrix for the complete PBG structure by taking the product of the matrices for each individual CPW section. The order of multiplication should be the same as the order of the CPW sections in the PBG, since matrix multiplication is not necessarily commutative. The final $ABCD$ matrix can be conveniently converted to the conventional scattering matrix S:

$$\begin{pmatrix} S_{11} & S_{12} \\ S_{21} & S_{22} \end{pmatrix} = \begin{pmatrix} \frac{A+B/Z_0-CZ_0-D}{A+B/Z_0+CZ_0+D} & \frac{2(AD-BC)}{A+B/Z_0+CZ_0+D} \\ \frac{2}{A+B/Z_0+CZ_0+D} & \frac{-A+B/Z_0-CZ_0+D}{A+B/Z_0+CZ_0+D} \end{pmatrix} \tag{3.8}$$

Based on the $ABCD$ matrix approach described above we use the numerical software package Matlab to calculate the bandstop parameters of the PBG structure (see Appendix A for a copy of the script). The parameters for each CPW segment used in the calculation (i.e. the impedance Z_0 and effective dielectric constant ϵ_{eff}) are

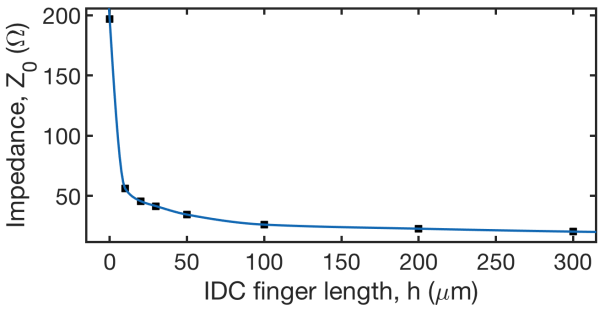

Figure 3.5: Characteristic impedance of the CPW with IDC as a function of the finger length. Data obtained from Sonnet simulations. The width of the central line $w = 2$ μm, the finger width $f = 4$ μm, the separation between fingers $s = 4$ μm and the distance to the ground plane $g = 2$ μm are all kept constant in the simulation. The solid line serves as a guide to the eye and does not represent a fit.

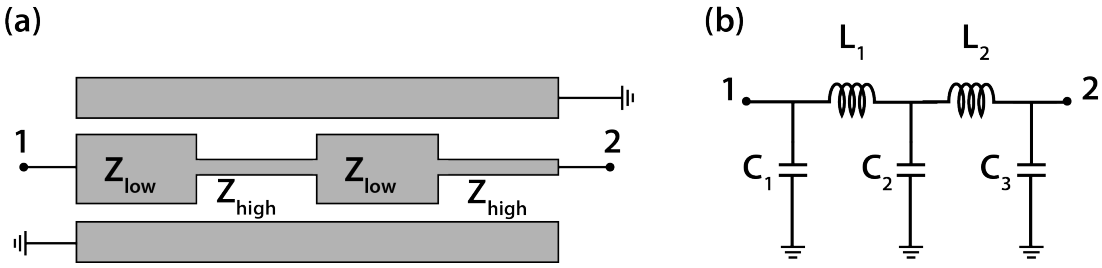

Figure 3.6: **a)** Schematics and **b)** equivalent circuit of the PBG structure implemented with coplanar waveguide technology. Here 1 and 2 identify the input and output ports, respectively.

obtained from Sonnet simulations. We calculate the transmission spectrum S_{21} of the specific design implemented in the device used for our experiments in Ch. 5, 6 and plot the result in Fig. 3.7. The low- and high-impedance CPW sections have lengths $l_{low} = 3.4$ mm and $l_{high} = 3.455$ mm, with corresponding impedances $Z_{low} = 30.9$ Ω and $Z_{high} = 120.3$ Ω. The design entails four cells, where a single cell is defined as a concatenated block of a low- and high-impedance CPW segment.

3.1.4 Photonic bandgap resonator

$\lambda/2$ resonator

The conventional way of defining a CPW resonator is by introducing a gap (discontinuity) to the central line, as depicted in Fig. 3.2. Reflections occur at the discontinuities

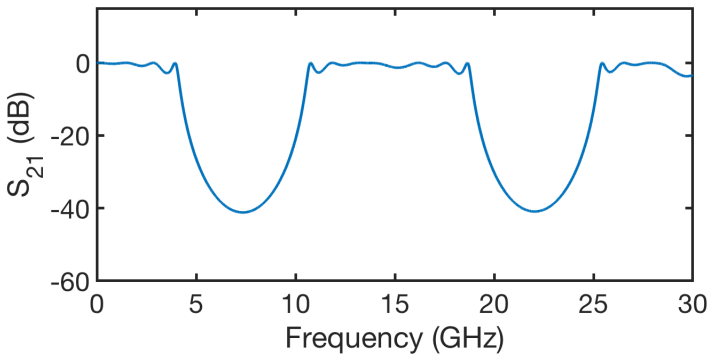

Figure 3.7: Transmission spectrum S_{21} for the PBG structure calculated using the $ABCD$ matrix approach.

and lead to the formation of standing waves, or resonances. Unfortunately, this type of coupling, known as capacitive, does not support the DC currents needed in our experiments to control the nonlinear kinetic inductance of the resonators. For this reason we use the PBG design to define the resonator [124].

As noted, the PBG implements a bandstop filter that decouples its output from the port/feed-line and thus can be used to confine a field inside a section of CPW and define a resonator. Since there are no breaks in the central conductor DC currents can be passed through the device. By placing a CPW section of length $\lambda/2$ between two PBGs, we obtain a half-wavelength resonator. The schematic for such a resonator is presented in Fig. 3.8a. The PBG structure can be thought as a microwave analog to the well-known Bragg mirror or Bragg reflector in optics. Since the number of cells and impedance step within the Bragg reflector are both finite, the mode extends beyond the resonator region and into the PBG structure [128]. The finesse of the confined mode and consequently the external quality factor of the resonator can be adjusted by engineering the photonic bandstop filter.

Increasing the number of cells within the PBG provides a deeper bandstop region and, therefore, a larger external quality factor of the resonator (i.e. a smaller coupling rate of the resonator to the feedlines). The same holds true for the Z_0 ratio of the PBG high- and low-impedance sections. The length of these sections determine the center frequency of the bandstop region and its span.

The transmission spectra for the PBG half-wavelength resonator formed with two Bragg reflectors is obtained from a Sonnet simulation and shown in Fig. 3.9. The Sonnet model contains four cells (repetitions of low- and high-impedance CPW sections) connecting each end of the resonator (cavity) to a microwave port. The low-impedance

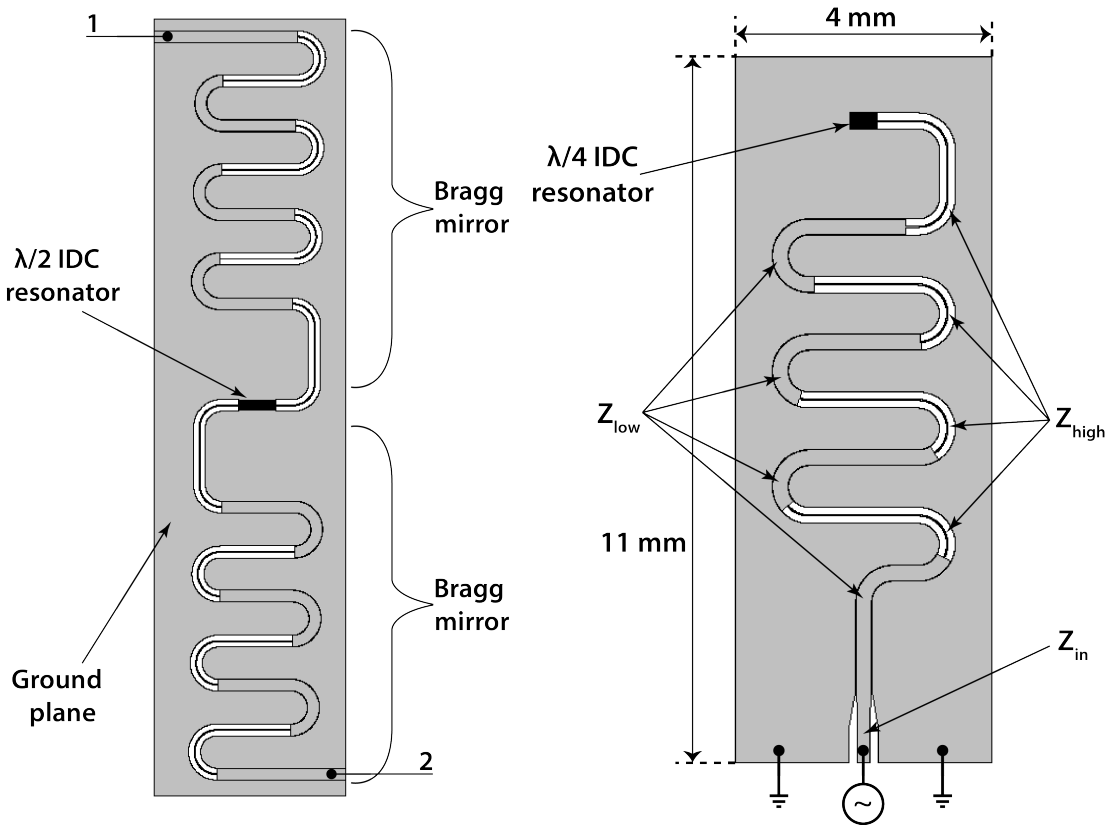

(a) $\lambda/2$ PBG resonator.

(b) $\lambda/4$ PBG resonator.

Figure 3.8: Schematics of the Bragg mirror/PBG-type resonators implemented using coplanar waveguide technology.

section has a central conductor width of $w = 242$ μm and a ground plane gap of $g = 4$ μm, providing $Z_{low} = 26$ Ω. The high-impedance section, with $w = 40$ μm and $g = 105$ μm, has an impedance $Z_{high} = 87$ Ω. Each section is $l = 3$ mm long. The resonator section in this model is defined by an IDC coplanar waveguide with length $L = 788$ μm and width $w = 2$ μm. The IDC finger length is $h = 100$ μm, with a width $f = 4$ μm wide and pitch $s = 4$ μm. The kinetic inductance is calculated from Eq. 2.55 based on T_c and R_s for a 20 nm thick NbTiN film and is found to be $L_k = 7.45$ pH/sq. The geometric inductance is estimated to be $L_g \approx 4.2$ nH, which constitutes about 60 % of the total inductance within the resonator section. The application of a DC current is simulated by simply modifying the value of L_k in accordance with Eq. 2.57. We estimate that the application of a DC bias current close to the critical current of the superconductor $I_c \approx 5$ mA increases the kinetic inductance to $L_k = 7.78$ pH/sq, and consequently the resonant frequency is lowered by $\Delta F \approx 100$ MHz (see Fig. 3.9).

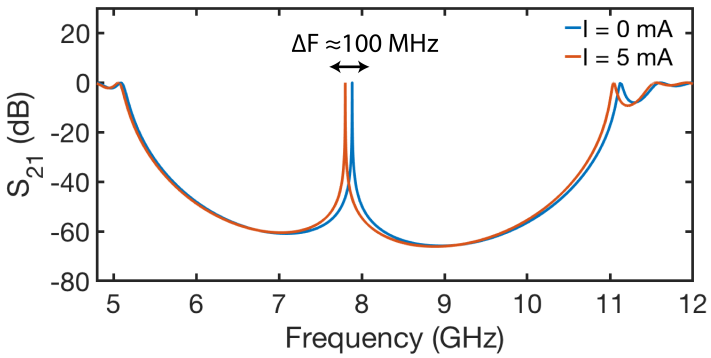

Figure 3.9: Transmission spectra S_{21} of the $\lambda/2$ PBG resonator obtained from Sonnet simulations. The blue spectrum is obtained for an L_k at zero bias current. The red spectrum is taken with the value of L_k for an applied DC bias current of approximately 5 mA.

We can also simulate the transmission spectra for the PBG resonator using the Matlab $ABCD$ matrix approach described earlier. Here we simply add an additional $ABCD$ matrix for the resonant section of the transmission line to the PBG cells. The matrices are multiplied in the order that they appear from the device input. This method provides a much simpler and faster way to estimate the transmission spectra for the PBG resonators as shown in Fig. 3.10, but is less accurate than the full method of moments calculation performed in a Sonnet simulation. The resonance peak position from the Matlab calculations is in close agreement with the peak obtained from Sonnet simulations.

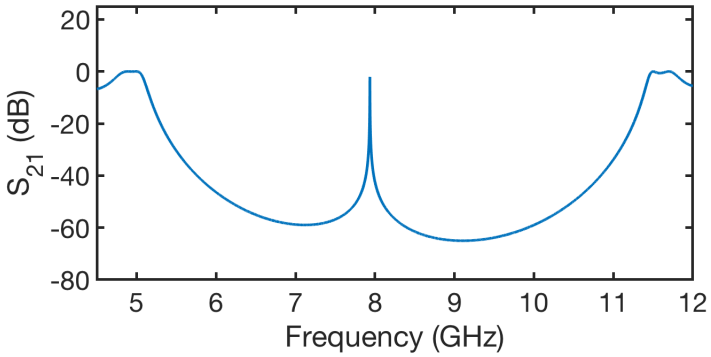

Figure 3.10: Transmission spectra S_{21} of the $\lambda/2$ PBG resonator obtained from Matlab $ABCD$ matrix calculations. The spectrum is simulated for an L_k at zero bias current.

$\lambda/4$ resonator

We can also use the PBG structure to implement a quarter-wavelength resonator, as shown in Fig. 3.8b. One end of the resonator is shorted to the ground plane and the other is coupled to the external circuitry via the stepped-impedance bandstop filter.

The reflection spectra of the quarter-wavelength PBG resonator can be simulated in the same way as for the half-wavelength designs. In the simulations we assume a lossless resonator and according to Eq. 2.48, when $Q_i \to \infty$ (i.e. $Q_i \gg Q_c$) the magnitude of the reflection spectra around the resonant frequency is unity – the resonator perfectly reflects the incoming signal. To extract information on the resonator frequency and its external quality factor Q_c we instead analyze the phase response, which undergoes a 180° phase shift around the resonance frequency. Indeed, the S_{11} magnitude response for the quarter-wavelength PBG resonator presented in Fig. 3.11a, calculated using the Matlab $ABCD$ matrix approach, is flat in the bandstop region, whilst its phase response exhibits a clear shift around 8 GHz, the expected resonance frequency. The device simulated here has the same four cell PBG structure design as the one simulated in the previous section.

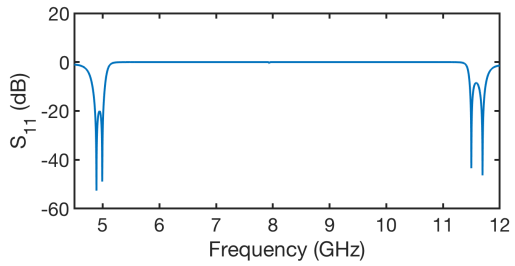

(a) Magnitude response.

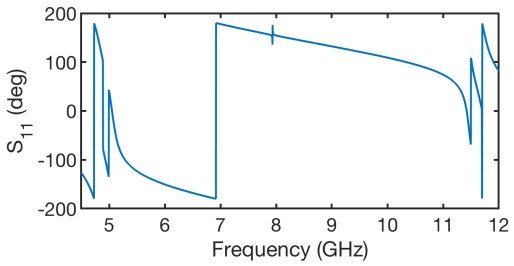

(b) Phase response. At the expected resonance frequency at approximately 8 GHz a clear phase shift is visible.

Figure 3.11: Reflection spectra (S_{11}) of the $\lambda/4$ PBG resonator calculated in Matlab. The bandstop region is the same as in Fig. 3.10.

3.2 Device fabrication

3.2.1 Ion implantation

Prior to fabricating the superconducting circuit resonators, we first perform ion-implantation to introduce bismuth dopants into the silicon chip, which will be used in the experiments of Chs. 5, 6. The silicon sample we use is a high-resistivity non-compensation-doped 300 μm thick float-zone (FZ) grown natural silicon (100) substrate. Silicon produced with the float-zone growth method is preferred since it is generally of a much higher purity (i.e. less impurities) than what is obtained with other techniques such as the Czochralski method. Details of crystal growth based on zone melting process can be found in Refs. [129]–[131]. To maximize the coherence time of the electron spin ensemble, a 20 μm thick epitaxial layer of silicon enriched 99.95% in the isotope ^{28}Si is grown on top the natural FZ silicon handle wafer. The bismuth ions are implanted within this 20 μm ^{28}Si layer.

With the help of the freely-available software SRIM [132], which is based on a Monte Carlo simulation method, we calculated the required energies and fluences of the bismuth implants to achieve a desired implantation profile and donor concentration. We target a uniform implantation profile over a depth of ~ 2 μm with a concentration of $\sim 1 \times 10^{17}/\text{cm}^3$ (see Fig. 3.12). This relatively high concentration was selected to enhance the spin ensemble echoes in our experiments, whilst still being well-below the metallic doping limit, which is around $2 \cdot 10^{19}$ cm^{-3} [133] for bismuth. Since bismuth is a particularly heavy donor, it requires large accelerations (up to 7 MeV) for these implantation depths. As such, our implantations were performed at the Australian Facility for Advanced Ion Implantation Research (AFAiiR), part of the Heavy Ion Accelerator Facility (HIAF) at the Australian National University. All implants are made at a 7° angle of incidence to the silicon (100) surface to prevent ion-channeling of the bismuth [134].

Silicon is a group IV element arranged in a diamond cubic lattice. The four valence electrons of each silicon atom are locked into covalent bonds with their neighbors. At room temperature silicon is a semiconductor with a 1.12 eV band gap and a six-fold degenerate conduction band (i.e. with a minimum along each of the $\pm X$, $\pm Y$ and $\pm Z$ directions). Bismuth donors are substitutional impurities in silicon. They replace a silicon atom forming covalent bonds with the adjacent silicon atoms and donate one electron to the conduction band. At cryogenic temperatures the bismuth ions retain their extra valence electron, which provides the electron spin in our experiments.

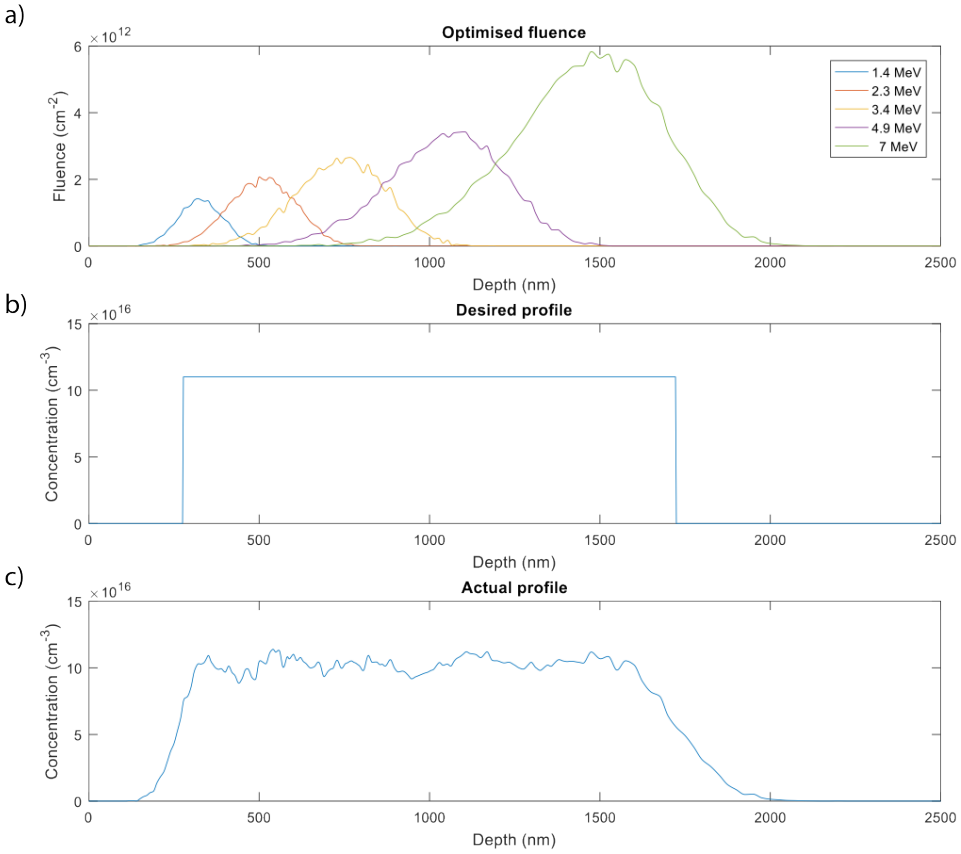

Figure 3.12: **a)** SRIM implantation fluences for a range of bismuth ion acceleration energies. The angle of incidence to the silicon surface is 7°. **b)** The desired bismuth implantation profile. **c)** The predicted implantation profile obtained from the multi-energy SRIM simulations shown in **a)**.

The high atomic mass of ^{209}Bi results in extensive damage to silicon crystal lattice upon implantation, leading to a large number of defects. We anneal the wafer under a nitrogen atmosphere at 800°C for 20 min. This serves to both repair implantation damage and incorporate the bismuth ions into the lattice, a process known as electrical activation [135], [136]. Our annealing recipe is expected to activate 60% of the implanted ions, based on Hall effect measurements of a sample annealed under similar conditions [135].

3.2.2 Resonator

Following ion implantation and donor activation, we pattern superconducting resonators on the surface of the silicon. The resonators (of the PBG design) are made in a NbTiN superconducting film. We chose NbTiN because it has a high R_s and thus a large high kinetic inductance, providing a sizable nonlinearity that will be used in our experiments. NbTiN also has a high critical temperature $T_c \approx 13$ K, which eases requirements on the base temperature of cryostat and leads to lower losses originating from quasiparticle residual resistance (Sec. 2.1.8). Finally, NbTiN has a relatively high critical magnetic field B_c, which is important for experiments where we integrate resonators with the bismuth donor spins.

The film thickness of the resonators used in different experiments varies. When coupling to spins, we desire a small amount of nonlinearity to allow for resonator frequency tunability and to facilitate parametric processes. However, excess kinetic inductance will reduce the signal collected from the spins, as it is a form of inductance that has no coupling with the spins. The device used for the spin experiments (described in Ch. 5 and 6) is made from a 50 nm NbTiN thick film which is deposited by magnetron sputtering on top of the bismuth-implanted ^{28}Si epitaxially-grown layer of silicon.

The second device, utilized for the amplification experiments performed in Ch. 4, does not involve spins and has a requirement for a high nonlinearity to achieve large amplifier gain-bandwidth-products. This device is made from a

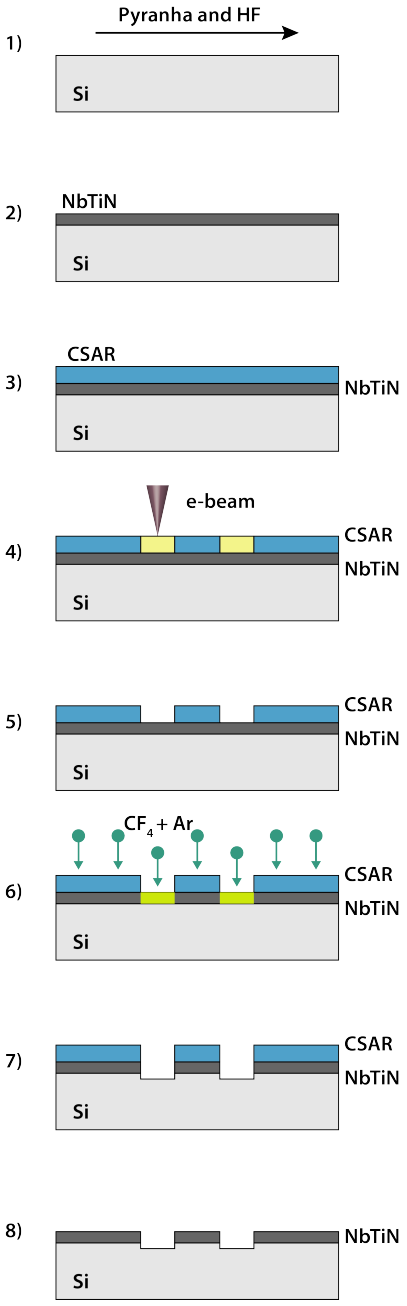

Figure 3.13: Steps for fabricating the PBG superconducting microresonators used in our experiments.

thinner NbTiN film measuring 9.5 nm in thickness and is deposited on top of a high resistivity (> 5 kΩcm) natural silicon FZ sample, without any implanted donors.

Given the smallest feature of our superconducting resonators is approximately 1 μm, a resolution just out of reach for standard optical lithography tools, we use electron beam lithography (EBL) to write the resonator pattern in a resist mask on the silicon chip. Aside from the high resolution, another advantage of using EBL is that the mask is defined in software and is thus trivial to modify, which allows fast turn-around of devices in the prototyping stage. This is very important when considering new resonator geometries since numerous trials are required to optimise the resonator design. Maskless optical lithography tools would be ideal for this purpose, since they have writing speeds several orders of magnitude larger than an EBL and can achieve minimum feature sizes down to 400 nm [137].

We now describe the steps for fabricating the superconducting PBG resonator, the process is presented pictorially in Fig. 3.13.

- Step 1, clean: The silicon sample is first cleaned in a piranha solution (a 3:1 mixture of sulfuric acid H_2SO_4 and 30% hydrogen peroxide H_2O_2) for 10 minutes on a hotplate set to 115°C in order to remove any organic contaminates. Following this the sample is rinsed in deionized (DI) water for 10 minutes. Next a 15 second dip in a hydrofluoric (HF) acid bath (10:1 mixture, with 10 parts water to 1 part 49% HF) is performed to strip the native oxide, followed by 5 minute a DI rinse.

- Step 2, metal deposition: A high quality NbTiN film is deposited on the silicon by magnetron sputtering a NbTi target in a N_2 gas atmosphere. The sputtering is a commercial service performed by Dr Robin Cantor at the company "Star Cryo".

- Step 3, resist: We spin the positive electron-beam resist AR-P 6200, referred to as CSAR 62 (purchased from the company "Allresist") on top of NbTiN film at a speed 4000 rpm for 60 seconds to achieve a 200 nm thick resist layer. We bake the sample at 150°C for 3 minutes to remove solvents and harden the resist.

- Step 4, exposure: Next we use a Raith-150 TWO EBL system to expose the resonator pattern on the chip at a beam acceleration of 20 kV and an aperture of 60 μm.

- Step 5, develop: We develop the exposed chip in n-amyl acetate for 60 seconds, followed by a 30 second rinse in isopropanol (IPA). A short (1 minute) and low-

power (50 W) oxygen plasma ash is then performed to remove any residual CSAR in the exposed and developed regions.

- Steps 6-7, etch: We remove the NbTiN regions exposed by the above steps with reactive ion etching (RIE), using an in-house built hollow cathode tool. The etch is performed with a CF_4/Ar ion plasma and removes the NbTiN at a rate of 4.5 nm/min.

- Step 8, final clean: After the RIE we strip off any residual CSAR using the "Allresist" remover AR 600-71.The sample is placed in the remover and left in an ultrasonic bath for 10 minutes to help remove any stubborn patches of hardened resist.

It is worth mentioning that CSAR was used here instead of the more conventional e-beam resist polymethyl methacrylate (PMMA) because of CSARs superior etching selectivity. Nevertheless, PMMA may also be used as a mask in this process, so long as the resist layer is made sufficiently thick to withstand the RIE process.

All fabrication processes were carried out in the ANFF-NSW clean-room facilities, which are graded ISO 5/Class 100 (EBL) and ISO 7/Class 10000 (RIE). Additional fabrication details and parameters can be found in Appendix B.

3.3 Packaging of the device

In the experiments described in the following chapters we utilize the quarter-wavelength photonic bandgap resonator design. This design is chosen over the half-wavelength version since it occupies only half of the area (conserving our very rare ^{28}Si enriched wafer) and the single port means all of the signal in an experiment is effectively collected. The latter (efficient signal collection) can be achieved in the half-wavelength resonator when measured in transmission only if there is a very large asymmetry between the coupling rates to the input and output ports.

After fabrication of the photonic bandgap resonator, the silicon chip is secured with a small amount of wax to a printed circuit board (PCB) that was specifically designed for this chip. The PCB is made on a Rogers RO3006 0.635 mm thick laminate covered with 1 oz of copper on both sides with an immersion silver finish. This board contains

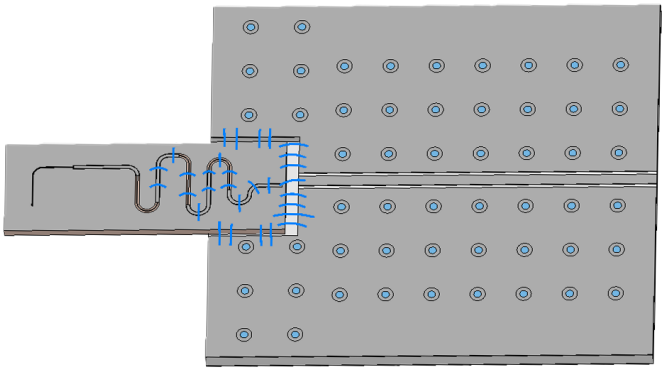

Figure 3.14: A schematic (taken from a CST model) of the $\lambda/4$ PBG resonator wire bonded to the PCB. Bond wires are depicted in blue. The circular objects on the PCB represent vias.

of a single 50 Ω CPW trace connected to the external measurement line at one end via a surface-mount mini-SMP (SMPM) microwave connector (see Fig. 3.15a). The other end of the PCB is wire bonded to the input port of the superconducting resonator. The bond wires are 50 μm in diameter and made from aluminum. The transmission line on the PCB is surrounded by an array of vias connecting top and bottom ground planes in order to suppress unwanted parasitic modes. The circuit board also has a milled region without any metalization to accommodate the silicon chip. A schematic of the PCB and device is illustrated in Fig. 3.14. We bond across the first few cells in the resonator PBG structure in order to connect the ground planes. This is critical for suppressing parasitic CPW modes and unintended ground plane resonances in the device [138], particularly provided our PCB design does not completely enclose the chip (for reasons detailed below) to allow for bonding to all regions of the ground plane.

The PCB provides a means to decouple the resonator from the port. Much like an optical Bragg reflector, the PCB supports a fraction of the mode field inside of it. As the ground plane separation is relatively large in this part of the device, radiation losses are a serious concern (Sec. 2.1.8). To suppress radiation losses, we place the chip inside of a 3D copper cavity (see Fig. 3.15a) with a fundamental frequency slightly higher than the superconducting resonator. The PCB allows most of the chip to protrude into the microwave cavity via a rectangular waveguide with a cutoff frequency far-exceeding that of the cavity. This helps us to maintain a high internal quality factor of the 3D cavity ($Q_i \approx 2000$), which would otherwise be destroyed by the presence of the PCB and bond wires. The copper enclosure is thermally anchored to the cold finger in a ^{3}He adsorption refrigerator or a ^{3}He/^{4}He dilution refrigerator, depending on the experiment.

(a) Silicon chip with PCB mounted in a 3D copper cavity.

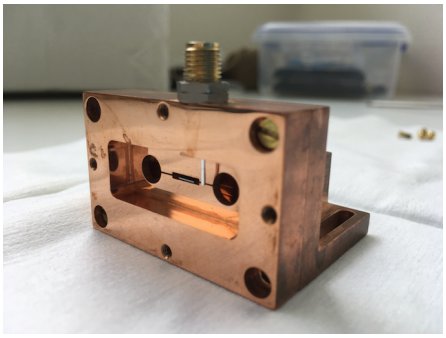

(b) 3D copper cavity represented by a loop-gap resonator.

Figure 3.15: Packaging of the device.

Figure 3.16: Device attached to the cold finger of a ^{3}He adsorption cryogenic refrigerator.

We have used a 3D loop-gap resonator (LGR) embedded in a rectangular cavity [139], [140]. A notable feature of the LGR is the spatial separation between the electric and magnetic field components of its resonant modes. The magnetic field profile of the LGR mode is primarily concentrated in the middle rectangular box region where the silicon chip rests, whilst the electric field is strongest in the small gaps that connect the box to the outer loops. Since the chip does not disturb the electric field of the mode, it has minimal influence on its resonance frequency. In addition, the AC magnetic field of the LGR can, in principle, be used to perform spin resonance. For the experiments described in this thesis the LGR acts as a Purcell filter to suppress the radiation losses of the superconducting resonators.

To probe the 3D cavity a microwave antenna (composed of a straight piece of silver-plated copper wire) is connected

to the measurement setup via a SMA adapter, as shown in Fig. 3.15b. For the experiments described in the following chapters we only use this microwave port to monitor the frequency of the 3D cavity. For this reason, after initial characterization of the LGR the SMA connector was removed and the port sealed with several layers of conductive tape. A picture of the cavity and device attached to the cold finger of a ^{3}He refrigerator is shown in Fig. 3.16.

The PBG resonator pattern was designed with Matlab numerical $ABCD$ matrix calculations and Sonnet simulations (Sec. 3.1). However, we have also constructed a full 3D model of the device including the PCB, bond wires and 3D cavity, which we simulate in CST Microwave Studio (part of the model is shown in Fig. 3.14). The superconducting film was modeled as an infinitely thin perfect electric conductor with a surface impedance defined by the kinetic inductance of the superconducting material. The current density distribution in Fig. 3.17 confirms that the mode is not perfectly confined inside the resonator and extends into the PCB structure, as expected. In this simulation we extract the fraction of magnetic energy stored in the resonator section is about 20%. This fraction can vary depending on the resonator impedance and the PBG design and therefore has room for optimization.

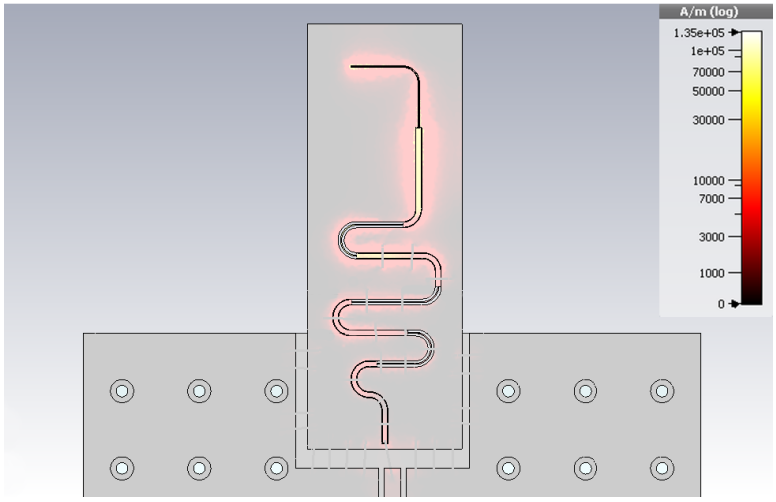

Figure 3.17: CST simulation results of the $\lambda/4$ PBG resonator showing the current density distribution throughout the device.

3.3.1 Practical considerations

There are a few practical considerations that should be taken into account when finalizing the resonator design. The CPW is meandered in order to minimize its footprint. To ensure that there is no cross-talk between the adjacent meandered PBG sections, the separation between them should be at least three times the total width of the low-impedance CPW section [141]. In addition, the bond wires connecting separate ground planes should be spaced with maximum separation of $\lambda/4$. We do not bond across the last two PBG cells of the resonator, as we have observed a degradation of its internal quality factor at temperatures above 1 K or magnetic fields $\gtrsim 50$ mT when we do, which we believe is due to ohmic losses in the aluminum bond wires which become normal under these conditions.

Another important parameter for our device is the critical current, above which the superconducting material becomes normal. The parametric effects that we will be interested in scale with the DC bias current, as too does the resonator frequency tunability, so achieving a high critical current is important. The critical current is an inherent property of the material that can be related to the nonlinear current parameter I_2 (Eq. 2.57) [88]. However, it has been shown in Refs. [142], [143] that the resonator design also impacts its value. For example, to avoid current crowding (regions in the device where the current becomes concentrated and causes the critical current to be exceeded locally) we minimize the presence of any sharp corners and steep transitions where it is possible to do so without compromising the device performance.

To conclude, the PBG microwave resonator design offers a simple and elegant solution to tune the kinetic inductance of a cavity via a DC bias current in a way that does not deteriorate its quality factor. Moreover, the fabrication of the device is simple and requires only a single-layer lithography step, as has been described above. As there are no Josephson junctions, the resonators are extremely robust to electrostatic discharge and have much larger power-handling capabilities.

3.4 Cryogenic measurement setup

In this section we describe two different cryogenic measurement setups used to perform the experiments presented in the following chapters. We start with a brief review

of the working principles of the cryogenic systems, followed by a detailed description of the microwave components installed for the experiments.

3.4.1 ^{3}He refrigerator

Cryostat

The experiments described in Ch. 5 and 6 were performed in a ^{3}He adsorption-type cryogenic refrigerator. The refrigerator is a single-shot system, where a charge of helium gas purified in the ^{3}He isotope is condensed into a liquid by passing it through a heat exchanger that's held at a temperature of $\sim$ 1.5 K. The 1.5 K temperature is maintained by pumping on a small pot of liquid ^{4}He (filled from a larger bath of helium that needs to be replenished periodically) to reduce its vapor pressure and therefore lower its temperature from 4.2 K to 1.5 K. The ^{3}He gas circulates in a closed-loop of tubes and liquefies at a temperature of 3.2 K. After liquefaction, the ^{3}He is brought to an even lower temperature through a technique known as adsorption pumping. A piece of charcoal that's held at 1.5 K (located in the closed tube system) traps gas molecules that evaporate from the ^{3}He liquid, reducing its vapor pressure and lowering the liquid temperature to $\sim$ 0.3 K. The system is classified as single-shot, since eventually all of the ^{3}He liquid will boil off and become trapped in the charcoal. At this point the charcoal sorb must be heated (approximately to a temperature of 40 K) to expel the gas, so it can once again be condensed into a liquid. This is a process known as regeneration, and the duration between regeneration events is referred to as the system hold-time.

The ^{3}He cryostat we used is a custom made system from the company ICE Oxford. It comprises a liquid helium dewar surrounded by both vacuum and liquid nitrogen shields to protect the liquid ^{4}He bath from external heat sources and thus minimize boil-off. The "insert" is the part of the fridge that contains all of the refrigerator and cold experimental components (^{3}He circulation system, experimental wiring, sample space etc.). The device is clamped to a gold-plated copper flange located inside the insert and attached to the coldest point (the pot where the ^{3}He liquefies), which is colloquially known as the cold finger. Together with the cryogenic components, the device is sealed inside a copper radiation shield and held under vacuum, forming the inner vacuum chamber (IVC). To cool down the refrigerator the insert is slowly placed into the liquid ^{4}He bath.

The ^{3}He cryogenic system has a cooling power, at the ^{3}He pot, of about 50 μW

at 300 mK and 2 mW at 500 mK base temperatures, according to the manufacturer. This allows us to cool a considerable amount of microwave components down is a short amount of time. The process of cooling the insert from room temperature to 400 mK takes about 5 hours.

The fridge is equipped with a two-dimensional superconducting vector magnet. The primary magnet is a solenoid that can be used to generate a vertically-oriented magnetic field with a strength of up to 2 T. The second magnet is of a split pair geometry and can produce a field up to 1 T in the horizontal plane. The magnets are located at the bottom of the liquid helium dewar and have a hollow bore 10 cm in diameter to allow the IVC (and therefore device) to pass through.

Cryogenic experimental setup

All of the devices we measure are single-port resonators and the experimental setups are therefore designed to perform measurements in reflection. For some experiments we are interested in signals at a single photon level and it is important to reduce any black body radiation or thermal microwave photons coming from the room temperature setup – a common problem in cQED. This is achieved by installing cryogenic microwave attenuators (made by the company XMA Corporation) at each temperature stage of the fridge, attenuating the thermal photons and helping to thermalize the cables and the field to these temperatures. The attenuators are dissipative elements and they therefore add an additional heat load to the stage at which they are installed, this must be taken into consideration when selecting their values to ensure the fridge can function properly.

The number of thermal photons coming from the room temperature setup is given by the Bose-Einstein distribution

$$n_{th} = \frac{1}{\exp(\hbar\omega/k_B T) - 1} \tag{3.9}$$

where k_B is the Boltzmann constant and $\omega/2\pi$ is the frequency of the signal. This expression simplifies to $n_{th} = k_B T/\hbar\omega$ in the high temperature limit ($k_B T \gg \hbar\omega$). Placing an attenuator with linear attenuation constant X in the signal path, the number of thermal photons is reduced to $n_{att} = n_{th}/X$. The attenuator can be modeled as a beam-splitter in quantum optics [43], with a transmission coefficient $1/X$. One port of the beam-splitter is the signal, whilst the other is noise $n_{add} = n_{th} + 1/2$, where the $1/2$ term represents the zero-point fluctuation of the microwave field. The final goal is

to ensure that the noise in the microwave lines at the lowest temperature stage of the system is dominated by the value of n_{add} at that temperature (i.e. $T \approx 400$ mK in the case of a ^{3}He refrigerator), not by thermal photons from other stages.

A detailed schematic of the microwave wiring inside the ^{3}He insert is depicted in Fig. 3.18. We use four microwave lines inside the fridge to run the experiments described in the next chapters. All of the lines, except those that extract the reflected from the device (the "Signal OUT" line), are semi-rigid cupronickel coaxial (CN/CN) cables with an outer diameter of 2.19 mm. The "Signal OUT" line (see Fig. 3.18) is superconducting (NbTi/NbTi) between the 400 mK and 4 K stages and from 4 K to room temperature are made from a cupronickel cable with a silver-plated inner conductor (SCN/CN). Prior to the first amplification stage, any attenuation of the signal reflected from the device will directly impact the signal-to-noise ratio. The NbTi/NbTi and SCN/CN output cable is critical for minimizing this loss.

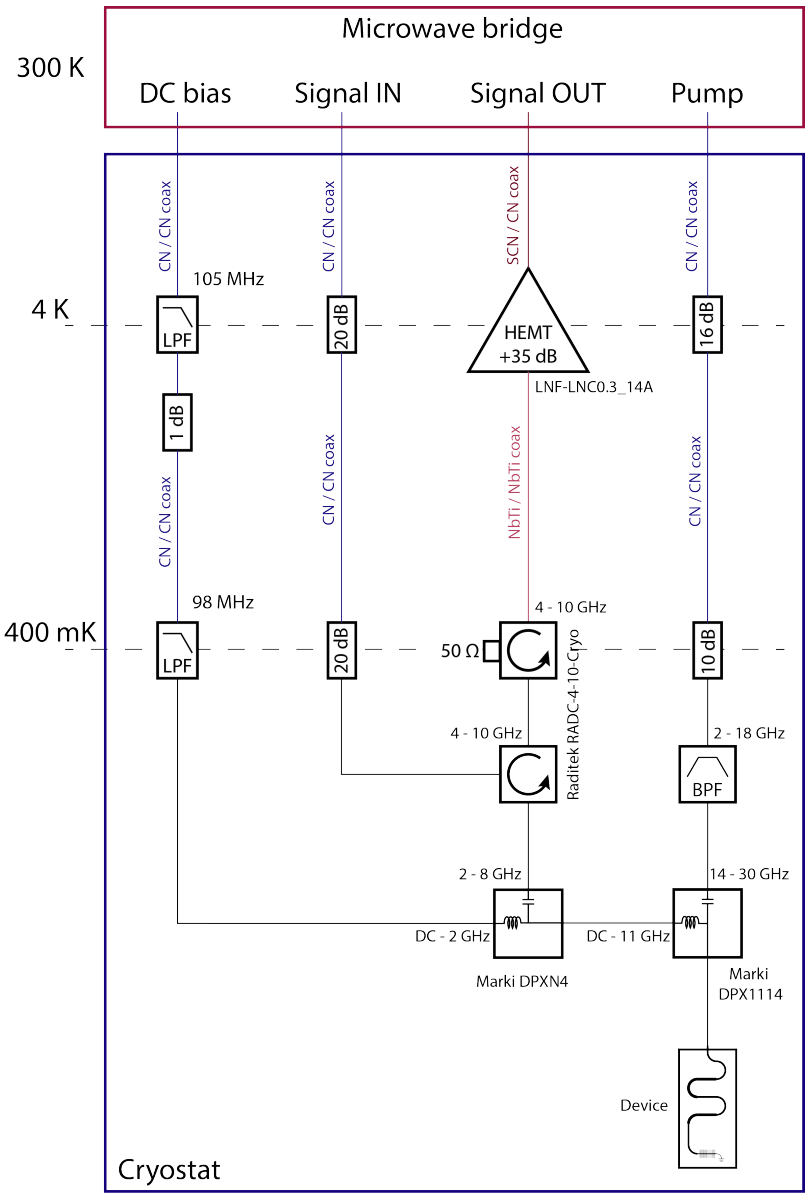

Figure 3.18: Schematics of the microwave wiring inside the ^{3}He refrigerator.

The microwave signal that drives the superconducting resonator is delivered via the "Signal IN" line. We typically operate at signal frequencies around $\omega/2\pi = 7.3$ GHz. The signal is attenuated by 20 dB at 4 K, reducing the number of thermal photons from about $n_{th} = 900$ at room temperature to 20 photons. It is attenuated by another 20 dB at 400 mK, resulting in a total of ~ 1 thermal photon at the base temperature of the system.

Once at the 400 mK plate the input signal is routed via a cryogenic microwave circulator (Raditek RADC-4-10-Cryo-0.02-4K-S23-1WR-DMS-b) to the first diplexer (Marki DPXN4). The diplexer combines the input signal (at 7.3 GHz) and the DC bias current, supplied via the "DC bias" line. The DC line has two low-pass filters (with cut-offs at 100 MHz), one at 4 K and the other at 400 mK, to remove high-frequency noise from the room temperature electronics. The combined microwave input signal and the DC bias is sent to a second diplexer (Marki DPX1114), which is used to introduce a high frequency pump tone at approximately 14.6 GHz. The common port of the second diplexer attaches to the SMPM connector of the device PCB. The pump tone allows us to drive parametric processes in the resonator and is described in the following chapters. The "Pump" line is also heavily filtered and attenuated to reduce the number of thermal photons as much as possible, whilst still allowing the relative high pump powers we need to drive the parametric processes to reach the device.

The signal reflects from the device and returns via the two diplexers to the circulator, which then routes it through an isolator to a high electron mobility transistor (HEMT) cryogenic amplifier (Low Noise Factory LNF-LNC0.3_14A). The HEMT amplifier serves to boost the signal above the noise level at room temperature before sending it out of the refrigerator.

Amplifiers necessarily add noise to a signal, as was demonstrated by Caves [98] in his quantum theory for noise limits in amplification. A matched 50 Ω load at a temperature T_R produces a thermal noise power within the bandwidth B equal to $P_R = k_B T_R B$. If this load is connected to the input of an amplifier with a linear power gain G, we obtain an output noise power of $P_{out} = G k_B (T_R + T_{amp}) B$, where T_{amp} is the equivalent noise temperature added by the amplifier. Quite often the amplifiers are cascaded, i.e. multiple amplifiers are connected in series to increase the overall system gain. In this case, the total equivalent noise temperature of the system (referred to the input of the first amplifier) is given by Friis formula:

$$T_{eq} = T_1 + \frac{T_2}{G_1} + \frac{T_3}{G_1 G_2} + \dots \tag{3.10}$$

where T_1, T_2, T_3, ... and G_1, G_2, G_3, ... are the noise temperatures and linear power gains of the first, second and the third amplifiers, respectively. It is clear that the noise temperature of the first amplifier is the most influential, since the noise of the latter stage amplifiers are attenuated by increasing amounts of gain. For this reason we use the cryogenic low-noise HEMT amplifier as the first amplifier on our output line. Its has a low noise temperature of $T_n \approx 4$ K.

The microwave isolator located just before the cryogenic amplifier at 400 mK serves to attenuate 4 K thermal and any HEMT noise that may reflect back down towards the device.

Finally, we use room temperature electronics and a custom-built microwave modulation/demodulation configuration to generate the input signal and detect the device output, labeled as the microwave bridge in Fig. 3.18. Details of the microwave bridge is described in Sec. 3.5.

3.4.2 ^{3}He-^{4}He dilution refrigerator

Cryostat

For the measurements presented in Ch. 4 we used a Bluefors ^{3}He-^{4}He dry dilution refrigerator (fridge). A dilution fridge reaches base temperatures more than an order of magnitude colder than a ^{3}He system. The system we use achieves the lowest temperature of 20 mK. In Ch. 4 we study the noise properties of a new type of quantum amplifier. In order to demonstrate that the amplifier reaches the quantum limit of noise performance, it is critical to operate at temperatures where $k_B T \ll \hbar\omega$, which demands the use of a dilution refrigerator.

The working principle of a dry dilution fridge is more complex than the ^{3}He system previously described and a detailed explanation can be found in Ref. [144]. The coldest part of the dilution refrigerator is called the mixing chamber – this is where the cold finger and device are attached. The cooling power of the fridge derives from a phase separation that occurs in liquid helium mixture containing both isotopes ^{3}He and ^{4}He. The ^{3}He-^{4}He mixture sits in the "mixing chamber" and is comprised of two phases: the dilute phase (composed of 6.6% ^{3}He and 93.4% ^{4}He) and the concentrated phase (with a 100% ^{3}He concentration). A heater on the mixing chamber at the dilute phase causes ^{3}He to be distilled from the mixture. The ^{3}He gas is then pumped away, condensed into a liquid and added to the concentrated phase. The distillation of ^{3}He from the dilute

phase creates a diffusion of ^{3}He across the concentrated/dilute phase boundary. The process of moving ^{3}He across the boundary is endothermic and, as result, consumes heat from the environment thus cooling the mixing chamber in the process.

Cryogenic experimental setup

The microwave wiring inside the dilution fridge was designed with the same considerations as in the ^{3}He system. The primary difference being that the dilution fridge has a lower base temperature and additional thermal stages, requiring extra attenuation.

We use four coaxial lines in the dilution fridge to deliver the DC bias current, high frequency pump tone and input and output microwave signals to/from the device. A detailed schematic of the measurement setup is shown in Fig. 3.19. The output signal, after being amplified with a HEMT cryogenic amplifier at 4 K, goes through a second HEMT at room temperature before being sent to a microwave switch. The switch directs the signal either to a vector network analyzer (VNA) or a homodyne detection setup. The input signal is provided by an ultra-low-phase-noise microwave generator (Keysight E8267D) or the VNA, with the selection made by another microwave switch. The experiments performed using this setup do not require short microwave pulses, which allows for a simplified room temperature configuration as compared to the ^{3}He system.

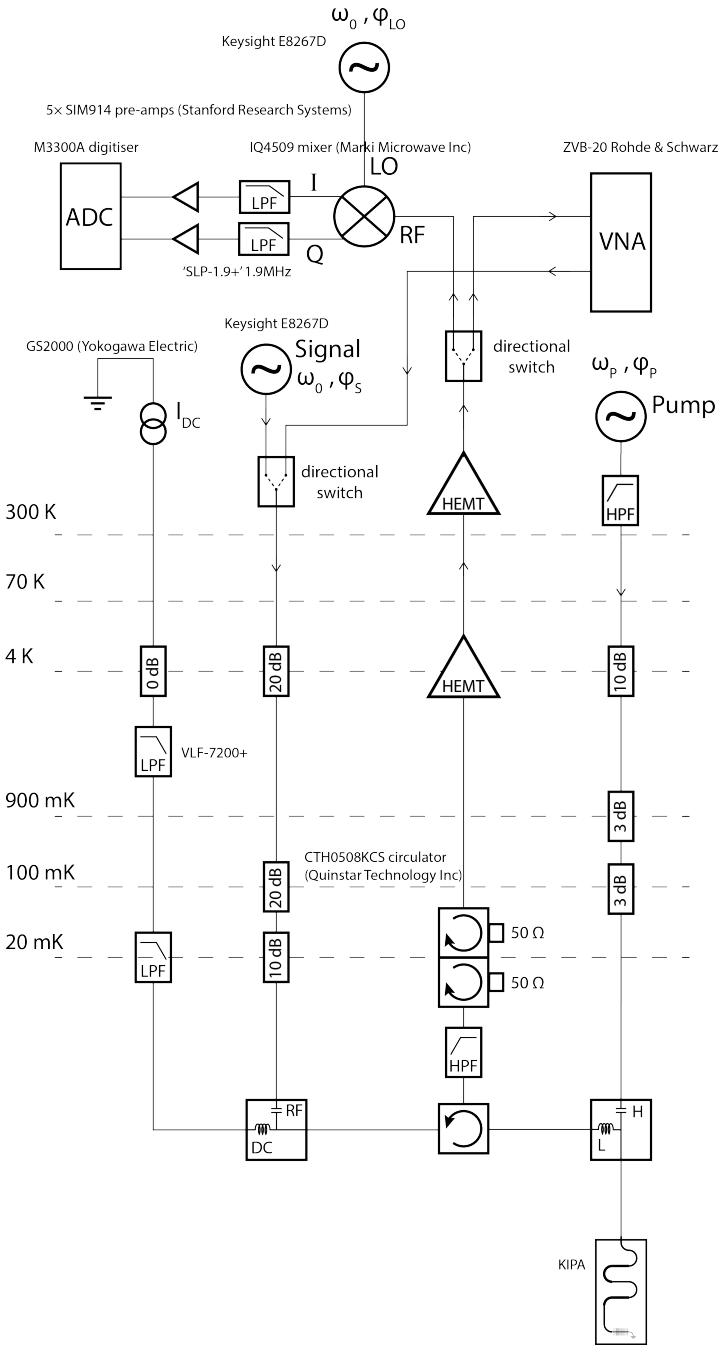

Figure 3.19: Schematics of the measurement setup for experiments performed in the ^{3}He-^{4}He dilution refrigerator.

3.5 Room temperature measurement setup

Quick characterization of our devices is performed with a VNA – an instrument used to measure the scattering (S) matrix of a microwave circuit. The VNA generates a continuous microwave signal that is fed to the "Signal IN" line of the setup (see Fig. 3.18). The signal propagates through the system to the device and then returns to the VNA via the "Signal OUT" line. This allows us to characterize the resonator and extract important parameters such as its quality factor by fitting the scattering matrix response with an appropriate function (see Eq. 2.48).

To perform the pulsed ESR experiments (see Sec. 3.6) we must deliver short microwave excitations to the device. For this reason we have designed and made a custom "microwave bridge". Microwave bridge is a term coined in conventional ESR spectroscopy that describes the collection of equipment (typically housed in a single box) used for pulse conditioning and signal detection. Here it represents the room temperature measurement setup used for experiments performed on the ^{3}He refrigerator, the detailed schematic of which is depicted in Fig. 3.20. The bridge is based on homodyne modulation and demodulation techniques [49].

The signal reflected from the device (at frequency ω_0) is routed to the "Signal OUT". After the cold amplification stage it is amplified by a further two stages at room temperature and bandpass filtered. In between the room temperature amplification stages we include a fast microwave switch. This switch has an important role in "blanking" the high-power pulses that are sent to the spins, which reflect off the resonator and could damage components along the detection stage. The switch is "unblanked" to capture the spin signals, which is passed to an "I-Q mixer". The mixer multiplies the signal with an additional supplied local oscillator (LO) tone $S_{LO}(t) = A_{LO}\cos(\omega_0 t)$, generated with the same microwave source that produces the signal. The output of the mixer contains signal components at the sum and difference frequencies. In homodyne detection the LO frequency is set equal to the signal frequency (i.e. they are both ω_0), so that the mixer produces signals at DC and $2\omega_0$. The high frequency component in the mixer output can be readily removed with a low-pass filter (LPF), leaving only the DC component. These DC components at each output of the mixer are proportional to the quadratures I and Q of the reflected signal (see Sec. 2.1.5). They are further boosted with RF amplifiers, passed through anti-aliasing filters and then digitized using a fast analog-to-digital converter (Keysight M3102A).

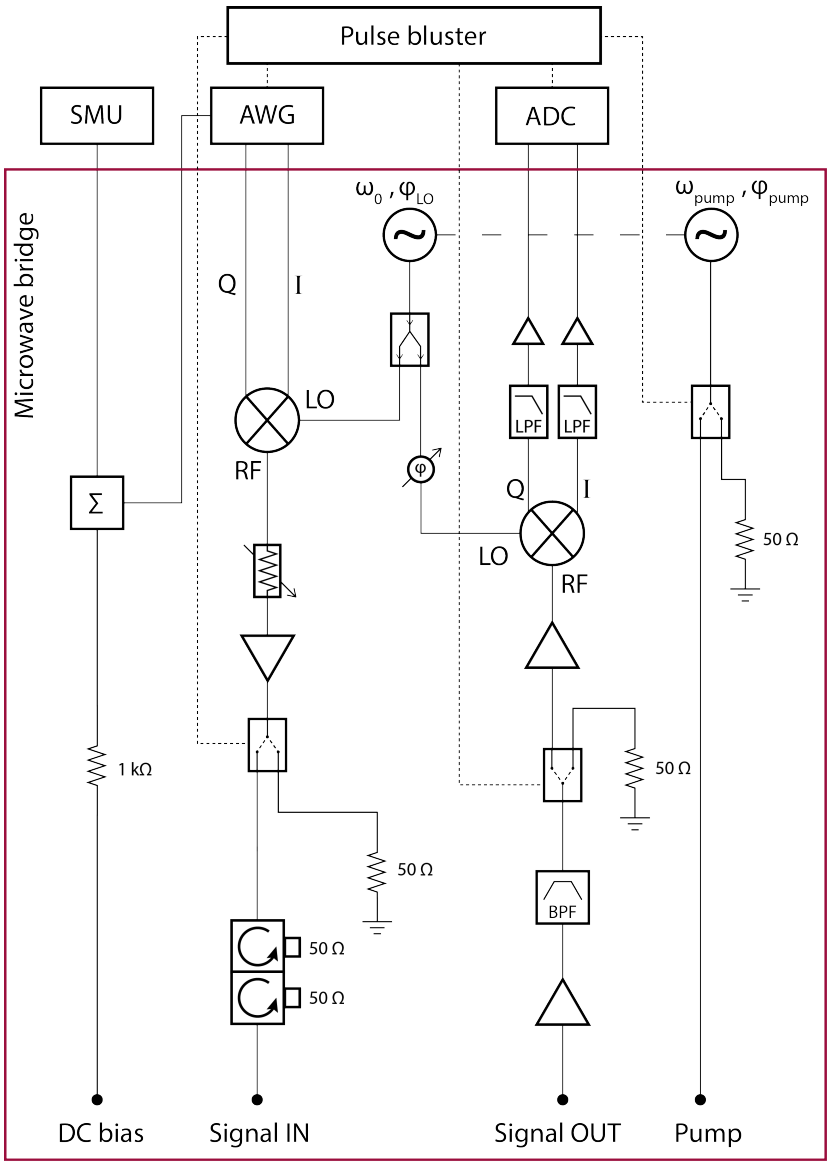

Figure 3.20: Detailed schematics of the room temperature microwave measurement setup used with the ^{3}He cryogenic setup. Microwave sources for the local oscillator (LO) and pump are phase-locked (dashed line). The dotted lines represent the equipment synchronization orchestrated by the "PulseBluster" fast pulse generator.

Knowledge of the "in-phase" I and "quadrature" Q components of the field allows us to calculate its amplitude and phase, fully characterizing the resonator response. The microwave signal that we receive back from resonator can be expressed in terms of the quadratures as:

$$S(t) = A_r e^{i(\omega_r t + \phi_r)} = M e^{i\omega_r t} = (I + iQ)e^{i\omega_r t} \tag{3.11}$$

Consequently, the amplitude and phase of this signal are:

$$\begin{aligned} A_r &\propto \sqrt{I^2 + Q^2} \\ \phi_r &= \arctan(Q/I) \end{aligned} \tag{3.12}$$

To generate our pulsed microwave signals, we use the same approach as for detection but in the reverse direction. The low frequency I and Q "baseband" signals (here with frequency components from DC to a few hundred megahertz) are generated with the help of an arbitrary waveform generator (AWG) (Keysight M3202A). The baseband quadrature signals are mixed with a local oscillator tone using an I-Q mixer, resulting in a modulated microwave signal with carrier frequency ω_0. By adjusting the relative weighting of the I and Q components, we can control the phase of the resulting signal. The local oscillator used in the signal generation scheme is split from the same microwave source as used for demodulation (see Fig. 3.20), ensuring phase coherence between the signals is maintained. Afterwards, the modulated tone is routed through a variable attenuator to provide amplitude control followed by a high-power amplifier to boost the signal up to a maximum power of 20 dBm. The signal then passes through a fast microwave switch to help suppress any local oscillator leakage when the signal is supposed to be off. Finally, the pulses are sent to the fridge (as shown in Fig. 3.18) via two microwave isolators to deal with any reflections of the high-power pulses that may occur along the input line.

The high frequency pump tone is generated by another microwave source that has its internal clock synchronised with the signal/LO source. This tone is routed via a microwave switch to the "Pump" line of the fridge. The DC bias signal is provided by a source measurement unit (SMU) (National Instruments (NI) PXIe-4139), which allows us to continuously monitor whether the superconducting resonator switches to the normal state during a measurement. To allow for fast control of the resonator frequency we combine the output of the SMU with a small RF signal generated by the AWG. This combined signal is sent to the "DC bias" fridge line.

Pulse generation and instrument synchronization is provided by a "PulseBlaster ESR Pro" (Spin Core), with a clock frequency of 250 MHz.

3.6 Pulsed ESR

In Ch. 5 we use the nonlinearity of our resonator to improve the signal-to-noise ratio of pulsed electron spin resonance (ESR) spectroscopy experiments. We presented the basic concept of ESR in Sec. 2.4.1. In the following section, we describe common ESR pulse sequences used to probe the dynamics of spins that we will utilize in our experiments.

3.6.1 Hahn echo pulse sequence

Arguably the most important pulse sequence used in spin resonance is the conventional Hahn echo [104]. This sequence is the basis for many others that belong to the wider class of control sequences known as dynamical decoupling [145].

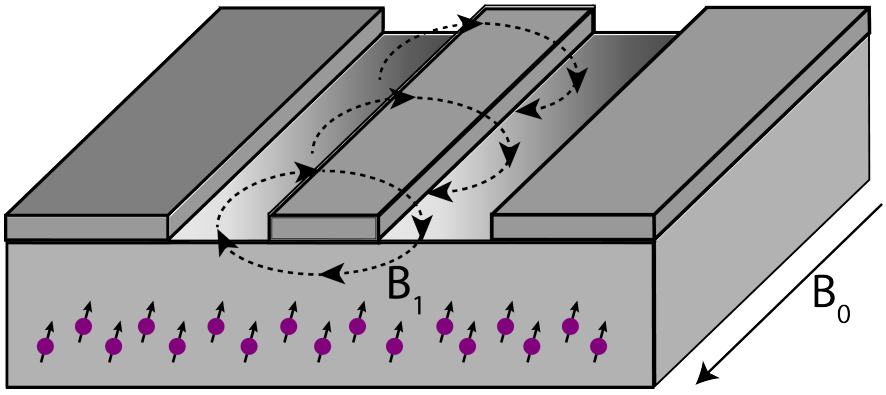

Figure 3.21: Schematics of a CPW-based resonator in a static magnetic field B_0, showing the B_1 field used to drive spin rotations. The spins are implanted in the silicon substrate underneath the resonator, represented as purple dots.

The superconducting device with implanted bismuth donors is placed in a strong static field B_0, aligned parallel to the plane of the superconducting film (along z axis). The magnetic field causes spin precession about the z axis with a Larmor frequency ω_s

(see Sec. 2.4.1). For electron spins this frequency is typically in the microwave domain. The linearly polarized B_1 field used to generate spin rotations is delivered through the superconducting PBG resonator fabricated on top of the silicon chip that hosts the electron spin ensemble (see Fig. 3.21). The B_1 field in our experiment is oriented along the x axis. We select a magnetic field B_0 to ensure that the spins are on-resonance with the drive field $\omega_s = \omega_{mw}$.

In the rotating frame (Sec. 2.4.1), the applied B_1 field is stationary and causes the spins to precess about the x axis. The strength of the B_1 field determines the Larmor frequency ω_1, more commonly defined as the Rabi frequency. By controlling the strength of the B_1 field and/or the time it is applied for, we can rotate the net spin magnetization M_0 by an arbitrary angle about the x axis.

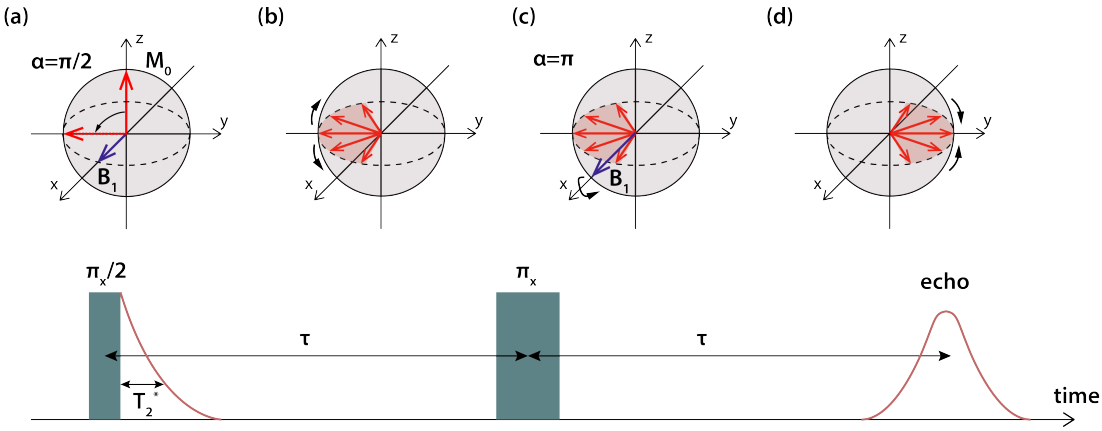

Figure 3.22: Hahn echo pulse sequence. **a)** We apply a $\pi_x/2$ pulse to tip the magnetization vector along the $-y$ direction. **b)** The magnetization starts to dephase in the $x-y$ plane, resulting in a FID signal. **c)** At a time τ after the first pulse, we apply the refocusing pulse π_y. **d)** After waiting another period τ a spin echo is observed.

The first pulse of the Hahn sequence is timed to deliver a $\pi/2$ rotation on the Bloch sphere, causing the spins to point along the $-y$ axis (see Fig. 3.22). We let the spins freely precess for a time τ where they dephase due to homogeneous and inhomogeneous line broadenings mechanisms (Sec. 2.4.1). The dephasing caused by homogeneous broadening is irreversible. On the contrary, dephasing caused by inhomogeneous broadening (i.e. static offsets in the spin frequencies) can be reversed. We apply a second pulse to produce a π rotation of the spins about the x axis, which serves to rephase any inhomogeneous broadening and refocus the spin magnetization along the $+y$ axis after another time τ. The π rotation is therefore often called the refocusing pulse. Shortly after the spins recover their magnetization along the $+y$ axis they rapidly dephase once

more. The resulting signal inductively detected via the resonator is called a "spin echo" and is formed from two back-to-back free induction decays (FID).

The spin echo signal is widely used in ESR to extract important information from a spin system, such as longitudinal and transverse relaxation rates.

Pulse calibration

In order to minimize rotation errors in the Hahn echo sequence, we must first calibrate our pulses. This is done here by measuring Rabi oscillations of the integrated echo signals [99] as the duration or amplitude of the pulses in the sequence are varied. Since our resonator has a high quality factor ($Q_{tot} \approx 30,000$), we typically fix the pulse length at the minimum value allowed by the resonator bandwidth $t = 1/\kappa = Q_{tot}/\omega$ (approximately a few microseconds). We set both the $\pi/2$ and π pulse to have the same duration (so that they have the same spectral width) and control the individual pulse amplitudes to achieve our desired rotation angles. By keeping the first pulse of the Hahn echo sequence fixed and varying the amplitude of the second pulse (π-pulse) the echo signal displays an oscillatory response. If the second pulse amplitude delivers a rotation that is an odd integer multiple of π, then the echo amplitude is maximum. However, if the rotation is an even integer multiple of π then the spins are not refocused and the echo amplitude is zero. From the Rabi oscillations we can determine the approximate pulse amplitude required to deliver our $\pi/2$ and π rotations.

To improve the signal-to-noise ratio (SNR) of the detected spin echo we repeat the experiment multiple times at each pulse power and average the results. To ensure the spins are in the same initial state before the pulse sequence we must allow them to relax to their ground state. As such, we insert a waiting time between repetitions that exceeds the longitudinal relaxation time. By waiting for $5T_1$ we can ensure that more than 99% of the spins will relax to their ground state [146]. The T_1 time for electron spins in the solid state can be extremely long, even exceeding hours [101]. However, in a resonator device one can exploit Purcell-enhanced relaxation to reduce this time below a second [48]. Alternatively, high spin concentrations can lead to spin diffusion, which may reduce T_1 to more manageable values [147]. In any case, averaging single shots of a Hahn echo is a time-consuming task, thus we must consider other ways to boost the SNR.

3.6.2 Carr-Purcell-Meiboom-Gill pulse sequence

In 1954 Carr and Purcell proposed a simple extension to the Hahn echo sequence which was to apply multiple refocusing pulses instead of just one, effectively reducing the free precession time τ before rephasing occurs and hence enhancing the transverse relaxation time of a spin system [148]. The Carr-Purcell (CP) pulse sequence starts with the usual tipping $\pi/2$-pulse, followed after time τ by a train of refocusing π-pulses. The duration between the π-pulses is 2τ. A spin echo forms a time τ after each π pulse, which can be detected inductively. The amplitude of the echo after consecutive π pulses decays as a result of inhomogeneous broadening [99].

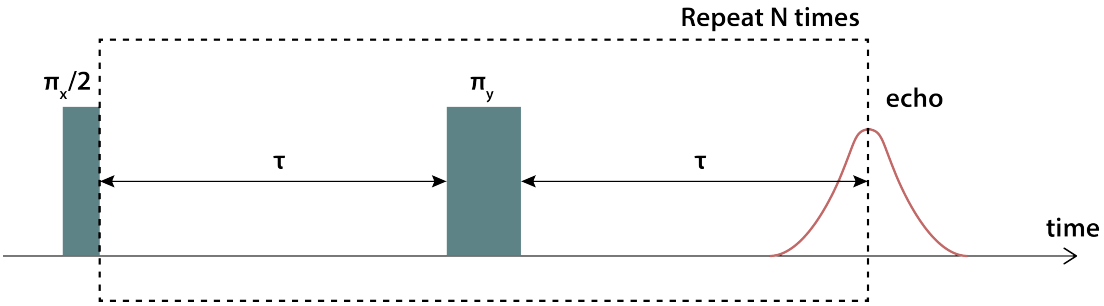

Figure 3.23: Schematic representation of the CPMG pulse sequence. Pulses have the same power but different duration.

The CP pulse sequence described above assumes that ideal pulses are applied to the spin system. However, in practice they are not ideal, and even the minor imperfections in the π-pulse amplitude, phase or timing will accumulate after being repeated several times and leads to an enhanced echo decay (unrelated to the intrinsic decoherence mechanisms). In 1958 Meiboom and Gill proposed a slight modification of CP sequence to compensate for possible pulse imperfections [149]. Their CPMG (Carr-Purcell-Meiboom-Gill) sequence is identical to the CP protocol apart from the phase of the pulses. The initial $\pi/2$-pulse is applied along the x axis whilst the following π-pulses are generated along the y axis (see Fig. 3.23). In this way small pulse errors are corrected after every second π pulse [149].

One major advantage of the CPMG sequence in ESR spectroscopy is the enhancement it can provide to the SNR [150] of a measurement. In a single pulse sequence we retrieve N spin echoes, where N is a number of π-pulses. Averaging over these echoes boosts the SNR by a factor of $\sqrt{N}$ (in practice the enhancement is lower due to echo decay) without the need for waiting long times between sequences for the spins to relax.

3.6.3 T_2 measurements

The coherence time T_2 for a spin system can be measured by monitoring the echo amplitude of a Hahn sequence as we increase τ. The Hahn protocol only refocuses noise that changes over a timescale slower than the experiment 2τ. As τ is increased, the spins experience dynamic noise that's not corrected after the π pulse. We fit the decay of the echo amplitude against the total free precession time 2τ to extract T_2.

As noted, we may use the CPMG sequence to extend the measured coherence time of our spins. To perform an echo decay measurement with the CPMG sequence we can either add pulses to the sequence with a fixed inter-pulse separation τ, plotting the echo magnitude as a function of the pulse number, or we can use a fixed number of pulses and vary τ. These two approaches are fundamentally different when one considers their spectral properties and they are sensitive to different components of the spectral density of the underlying noise processes [145]. Depending on the exact frequency dependence of the decohering noise, it is usually the case that the coherence time (T_{2CPMG}) measured with CPMG is greater than the T_2 extracted from a Hahn sequence. CPMG is called a dynamical decoupling sequence, since our applied dynamics (periodic π rotations) decouples the spins from their noisy environment.

3.6.4 T_1 measurements

In order to characterize the longitudinal relaxation time we consider two different approaches. In both techniques the Boltzmann population of the spins is first driven away from thermal equilibrium with a pulse. A delay immediately after the pulse provides time for the spins to undergo longitudinal (T_1) relaxation before we probe the spin population difference with a Hahn echo measurement. The approaches differ in the method used to initially drive the spins away from equilibrium.

Inversion recovery

To measure the longitudinal relaxation rate we need to disturb the spins and observe their recovery dynamics. The first method for achieving this is called an "inversion recovery" [99]. Initially in thermal equilibrium, the spins are inverted by a π-pulse (see Fig. 3.24). At different times T_{wait} during the relaxation process (probed with separate measurements) the population is inferred with the help of a spin echo sequence (Hahn

echo or CPMG). The echo will evolve from a reduced, ideally negative, amplitude for the inverted ensemble to a positive amplitude at sufficiently long T_{wait}, once all of the spins have relaxed. The characteristic time for the echo amplitude to fully recover is T_1.

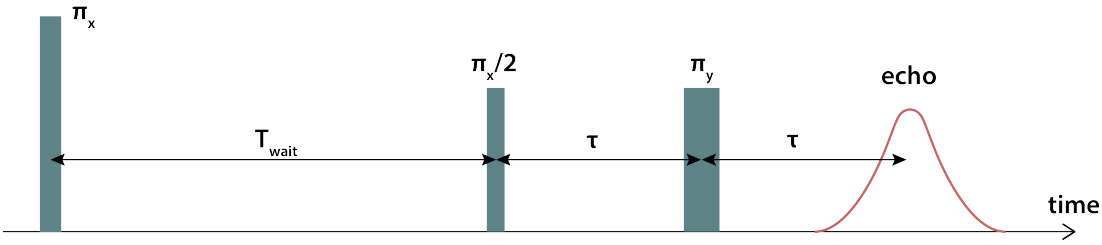

Figure 3.24: Inversion recovery pulse sequence. Typically the π_x inversion pulse is short and high power (i.e. broadband) so as to invert the maximum number of spins. A smaller subset of spins is probed with the Hahn echo sequence by using slightly longer and lower power pulses.

Saturation recovery

In the second approach, called "saturation recovery", instead of applying an initial π inversion pulse, we send a long high power pulse to saturate the spins [99]. The magnetization for this state can be calculated from the Bloch equations (Eqs. 2.78-2.80) by assuming steady-state conditions (where the time derivatives of the magnetization components are zero). This gives:

$$M_x = M_0 \frac{\omega_1 \Delta_s T_2^2}{1 + S_{cw} + \Delta_s^2 T_2^2} \tag{3.13}$$

$$M_y = M_0 \frac{\omega_1 T_2}{1 + S_{cw} + \Delta_s^2 T_2^2} \tag{3.14}$$

$$M_z = M_0 \frac{1 + \Delta_s^2 T_2^2}{1 + S_{cw} + \Delta_s^2 T_2^2} \tag{3.15}$$

where $S_{cw} = \omega_1^2 T_1 T_2$ is the saturation parameter for a continuously driven sample. If $S_{cw} >> 1$ all components of the magnetization approach zero. This implies that the spin magnetization is equally distributed across all directions in space, representing a spin population distribution out of thermal equilibrium. The next steps are identical to the inversion recovery – we wait a time T_{wait} and then probe the spin population with an echo measurement. However, in this case the spin echo signal will recover from an initial value of zero (when $T_{wait} \ll T_1$). One advantage of the saturation recovery

measurement is that it is able to suppress spin-diffusion mechanisms to some extent [99], revealing true intrinsic spin energy relaxation mechanisms.

Chapter 4

The Kinetic Inductance Parametric Amplifier

I acknowledge the efforts of my colleague and fellow student, Daniel Parker, who worked tirelessly on many of the measurements detailed in this chapter.

4.1 Introduction

An increasing number of contemporary experiments in condensed matter physics work with extremely weak microwave signals, down to the level of a single photon. To detect such weak signals one must be able to amplify them without adding excessive amounts of noise. In this regard cryogenic microwave amplifiers represent an enabling technology. Parametric amplifiers are a special class of microwave amplifier that can operate at the quantum-noise-limit.

For typical cQED experiments, in order to resolve a single photon signal, a chain of multiple amplifiers is utilized, where the first one should add the minimum amount of noise, i.e. be quantum noise limited. Moreover, this quantum noise limited parametric amplifier should have gain above a specific threshold to suppress the influence of the noise injected by the second amplifier (cryogenic HEMT amplifier) in the detection chain. A HEMT amplifier usually provides a gain of 30−40 dB and its noise temperature is about 3−4 K, which is the lowest noise temperature amongst the semiconductor-based amplifiers. The effective noise temperature of vacuum fluctuations (half of quanta) can be written as $\hbar\omega/2k_b$, which corresponds to 170 mK at 7 GHz. According to Friis formula (Eq. 3.10), if the first amplifier adds not more than half a photon of noise, in order for it to be the dominant source of noise, its gain should be larger than 15 dB. In our setup, there is approximately 4.5 dB of insertion loss in the components between the kinetic inductance parametric amplifier (KIPA) and the HEMT, thus 20 dB of gain is required for quantum noise limited operation. In this case the weak signal will not be masked by the noise added by the following amplifiers and lossy components in the amplification chain. The use of parametric quantum noise limited amplifiers have enabled the high-fidelity readout of superconducting qubits [151], increased the sensitivity of the electron spin resonance spectroscopy [31], and are even aiding the search for dark matter [152].

Parametric amplifiers can be operated in two modes: phase insensitive or phase sensitive (refer to Sec. 2.3). The amplitude of an electromagnetic field input to an amplifier can be described by dimensionless quadrature field operators $\hat{I}_{in}$ and $\hat{Q}_{in}$ (see Sec. 2.1.5). A phase insensitive amplifier applies a linear gain G equally to both quadratures $\langle\hat{I}_{out}\rangle = \sqrt{G}\langle\hat{I}_{in}\rangle$ and $\langle\hat{Q}_{out}\rangle = \sqrt{G}\langle\hat{Q}_{in}\rangle$, where $\hat{I}_{out}$ and $\hat{Q}_{out}$ represent the field amplitudes at the output of the amplifier. This type of amplification results in the addition of at least 1/4 photon of noise to each quadrature in the process [98]. Conversely, for a phase-sensitive amplifier, one field quadrature is amplified $\langle\hat{I}_{out}\rangle = \sqrt{G}\langle\hat{I}_{in}\rangle$, whilst

the other is de-amplified $\langle \hat{Q}_{out} \rangle = \langle \hat{Q}_{in} \rangle / \sqrt{G}$. This definition of quadrature gain allows for noiseless amplification of one quadrature. The noiseless nature of a phase-sensitive amplifier makes it distinctly useful for detecting small microwave signals, particularly those at the single photon level.

In the microwave domain, the Josephson parametric amplifier (JPA) defines the state-of-the-art in phase-sensitive amplification technology. A JPA consists of one or more Josephson junctions embedded in a low quality factor superconducting resonator. Vacuum squeezing has been achieved with JPAs employing single cavity modes (so-called degenerate parametric amplifiers) at the level of 10 dB [153] and through the entanglement of two distinct cavity modes ($>$ 12 dB) [154]. However, recent experimental [38], [155] and theoretical [156] investigations of JPAs has uncovered differences between the JPA and ideal degenerate parametric amplifier (DPA) Hamiltonians, which become significant in the high gain limit ($>$ 10 dB) and constrain the amount of achievable squeezing. Higher-order nonlinearities originating from the physics of Josephson junctions limit the useful linear regime of operation, with typical 1 dB-compression points measuring less than -110 dBm for 20 dB of gain [74].

In this chapter we present results that show our current-biased PBG resonator (Sec. 3.1.4) can be used to implement a near-ideal degenerate parametric amplifier, with excellent performance as a noiseless phase-sensitive amplifier and a potential source of highly-squeezed microwave states of light. This technology has a number of attractive advantages relative to other types of quantum-limited microwave amplifiers – the device contains no Josephson junctions making it robust to electrostatic discharge, it has an extremely high power-handling capability due to the large critical current of the NbTiN film and it is produced with a simple single-step lithography process as described Sec. 3.2.2.

4.2 Theory of parametric amplification

All devices explored in this thesis exhibit a nonlinear kinetic inductance (see Sec. 2.2.2). This form of nonlinear inductance is analogous to an optical Kerr media. When two tones of microwave current simultaneously pass through the kinetic inductance device a process known as four wave mixing (4WM) can occur. If one of the tones (the "pump") is much larger in power than the other (the "signal") then the 4WM process can facili-

tate a transfer of energy from pump to signal, producing amplification. Here two pump photons generate one signal photon and a photon in a new tone called the "idler" [157], [158], as depicted schematically in Fig. 4.1. The idler is required so that the amplifier output field operators satisfy the standard bosonic commutation relations (see Sec. 2.3). If the pump and signal frequencies are the same, then the resulting amplification is said to be degenerate. If the frequencies are different by an amount $\Delta\omega$ then the resulting amplification is non-degenerate.

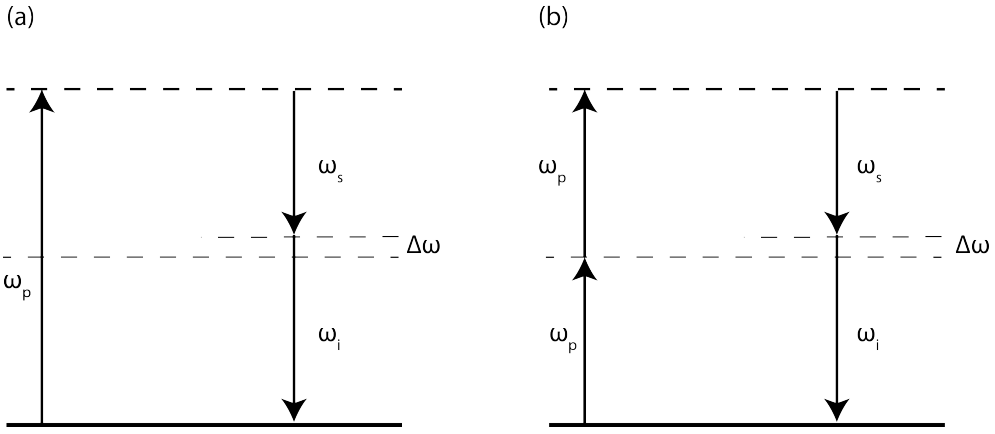

Figure 4.1: Feynman diagrams for **a)** 3WM and **b)** 4WM processes. ω_p, ω_s, ω_i represents the angular frequencies of pump, signal and idler photons, respectively. $\Delta\omega$ represents an arbitrary frequency detuning from the degenerate mode of amplification.

If a DC current bias is applied on top of the microwave tones, i.e. $I = I_{DC} + I_{\mu w}$, then the kinetic inductance obtains both odd and even power dependencies on the microwave current:

$$L_k(I) = L_{k0}\left[1 + \left(\frac{I_{DC}}{I_2}\right)^2 + \frac{2I_{DC}I_{\mu w}}{I_2^2} + \left(\frac{I_{\mu w}}{I_2}\right)^2\right] \tag{4.1}$$

In addition to the Kerr component ($I_{\mu w}^2$), a new term linear in $I_{\mu w}$ appears which can facilitate a three wave mixing (3WM) process, where one pump photon at roughly twice the signal frequency splits to produce a signal and an idler photon. Amplification by three wave mixing (3WM) has been demonstrated recently in several traveling wave devices [159], [160]. However, it is known that at high pump powers, when $I_{\mu w} \geq 2I_{DC}$, the competition between 4WM and 3WM processes degrades the parametric gain [161] in these wide-band devices and limits the amplifier performance.

A simple model that describes the performance of a 3WM parametric amplifier can be adopted from quantum optics, the model is often referred to as the DPA [162],

[43]. Here a nonlinear medium is placed inside a single mode cavity and pumped at twice the resonant frequency of the cavity. In optics, for example, this induces periodic modulation of the refractive index of the nonlinear environment inside the cavity which leads to changes of its optical path length and, therefore, its resonant frequency. These conditions facilitate the energy transfer from the strong pump tone to the resonant mode of the cavity. The Hamiltonian can be written as follows [156]:

$$\hat{H} = \omega_0 \hat{a}^\dagger \hat{a} + \chi(\hat{a}^{\dagger 2} \hat{a}_p + \hat{a}^2 \hat{a}_p^\dagger) \tag{4.2}$$

where ω_0 is the frequency of the cavity, χ is the strength of the nonlinearity, and $\hat{a}, \hat{a}^\dagger, \hat{a}_p, \hat{a}_p^\dagger$ are the annihilation and creation operators for excitations in the cavity mode and pump field, respectively. The first term in Eq. 4.2 is the Hamiltonian for a linear quantum harmonic oscillator and the second term captures the interactions between the pump and the cavity, where one pump photon is exchanged with two cavity photons and vice versa. In the strong classical pump regime we can use the approximation $\hat{a}_p \approx \alpha_p e^{-i\omega_p t}$, where pump frequency is $\omega_p \approx 2\omega_0$. We assume, without loss of generality, that α_p (the pump amplitude) is a real number. The DPA Hamiltonian is then obtained by rewriting the Hamiltonian 4.2 in a frame rotating at half the pump frequency [156], [43]:

$$\hat{H}_{DPA} = \delta \hat{a}^\dagger \hat{a} + \frac{\lambda}{2} \hat{a}^{\dagger 2} + \frac{\lambda^*}{2} \hat{a}^2 \tag{4.3}$$

with the detuning $\delta = \omega_0 - \omega_p/2$ and the amplitude of the pump $\lambda = 2\chi\alpha_p$.

Inserting the $\hat{H}_{DPA}$ into Eq. 2.40, introduced in Sec. 2.1.7, provides us with the equation of motion for the intra-cavity field:

$$\dot{\hat{a}}(t) = -\frac{i}{\hbar}[\hat{a}(t), \hat{H}_{DPA}] - \frac{\kappa_{int} + \kappa_{ext}}{2} \hat{a}(t) + \sqrt{\kappa_{ext}} \hat{a}_{in}(t) + \sqrt{\kappa_{int}} \hat{f}_{in}(t) \tag{4.4}$$

The field $\hat{a}_{in}$ represents the input signal to be amplified, whilst $\hat{f}_{in}$ represents the input mode that mixes in noise with the signal. κ_{int} and κ_{ext} are the internal and external loss rates of the cavity, respectively. The solution is found in Fourier domain using the boundary condition listed in Eq. 2.41 [156]:

$$\hat{a}_{out}(\omega) = g_s \hat{a}_{in}(\omega) + g_i \hat{a}_{in}^\dagger(-\omega) + \sqrt{\frac{\kappa_{int}}{\kappa_{int} + \kappa_{ext}}} \Big((g_s + 1) \hat{f}_{in}(\omega) + g_i \hat{f}_{in}^\dagger(-\omega) \Big) \tag{4.5}$$

where $\hat{a}_{out}$ represents the amplified signal. The amplitude gains of the signal g_s and

idler g_i are defined as:

$$g_s = \frac{\kappa_{ext}(\frac{\kappa_{int}+\kappa_{ext}}{2}) - i\kappa_{ext}(\delta+\omega)}{\delta^2 + (\frac{\kappa_{int}+\kappa_{ext}}{2} - i\omega)^2 - |\lambda|^2} \tag{4.6}$$

$$g_i = -\frac{i\kappa_{ext}\lambda}{\delta^2 + (\frac{\kappa_{int}+\kappa_{ext}}{2} - i\omega)^2 - |\lambda|^2} \tag{4.7}$$

A full microscopic derivation of the Hamiltonian for the KIPA was performed by Daniel Parker and is presented elsewhere [163].

4.3 Device and setup

The KIPA device we analyze in this chapter is fabricated from a 9.5 nm thick film of NbTiN on a FZ silicon substrate with dimensions 11 mm by 4 mm. Its geometry was described in detail in Sec. 3.1. In summary, it is a CPW quarter-wavelength resonator with an in-built IDC that is attached to the end of a PBG structure and shorted to ground (see Fig. 3.8b). It is designed to produce a resonance at the center of the PBG band-stop region $\omega_0/2\pi \approx 7.2$ GHz. The IDC increases the effective capacitance per-unit-length of the resonant segment and thus lowers the impedance of the resonator to $Z_0 = \sqrt{L/C} \approx 45\ \Omega$. By lowering the impedance we produce larger pump currents for a given pump power, helping to minimize device heating. The internal quality factor ($Q_{int} \approx 16000$) of the resonator is much greater than the coupling quality factor ($Q_{ext} \approx 160$) putting it in the highly over-coupled regime ($Q_{ext} \ll Q_{int}$). The silicon chip is wire-bonded to a PCB and then packaged into a 3D copper cavity, according to the procedure described in Sec. 3.3.

The PBG structure that confines the resonance allows us to pass a DC current through the device. In addition, the PBG has a passband that covers the frequency $2\omega_0$. The PBG resonator is therefore an ideal device with which to perform amplification through 3WM. Critically, the resonant nature of our KIPA strongly suppresses 4WM and higher-order processes, and as we will see permits extremely high levels of pure 3WM gain.

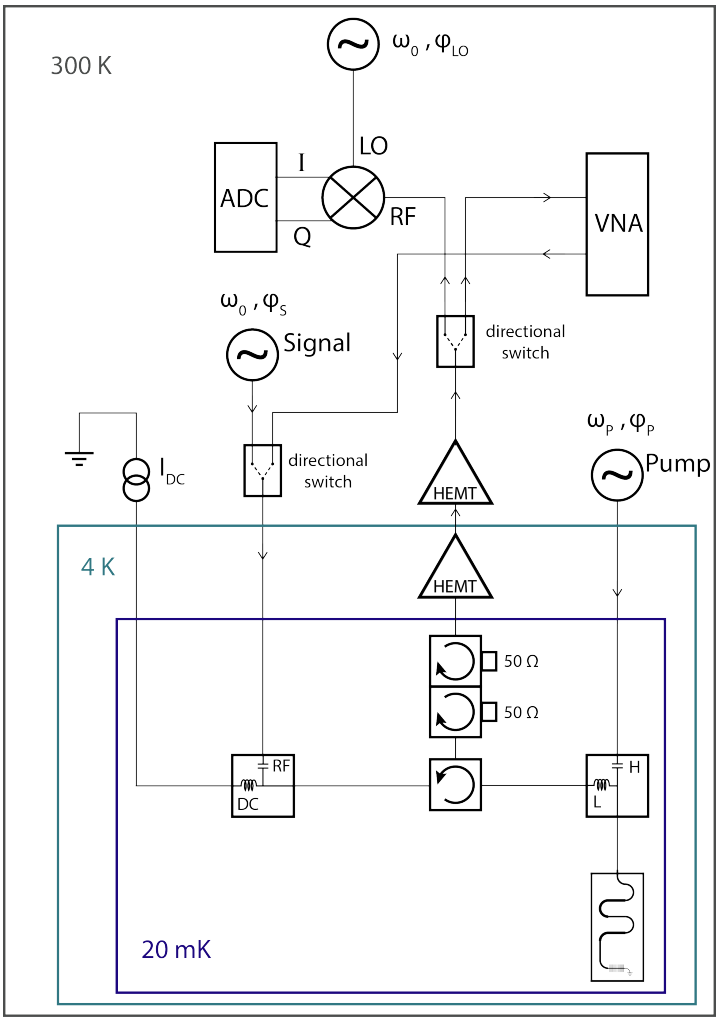

Figure 4.2: Simplified schematic of the measurement setup used for KIPA characterization.

The KIPA device is thermally anchored to the 20 mK stage of a dilution refrigerator. A simplified schematic of the measurement setup is presented in Fig. 4.2. The full schematic can be found in Sec. 3.4.2 (Fig. 3.19). To use the KIPA, we feed the combined bias current, signal and pump into the port of the device. The tones undergo mixing in the resonator and the reflected amplified signal is routed to a HEMT amplifier at 4 K. This is followed by a third low-noise amplification stage at room temperature before being measured with a VNA or undergoing homodyne detection.

The frequency response of the KIPA, measured using the VNA, as a function of applied DC current (without the pump tone) is presented in Fig. 4.3. This frequency dependence illustrates the nonlinear response of the kinetic inductance to the applied current, which is fitted to Eq. 2.57 with extracted fit parameters $I_2 = 11.418$ mA and $I_4 = 5.251$ mA.

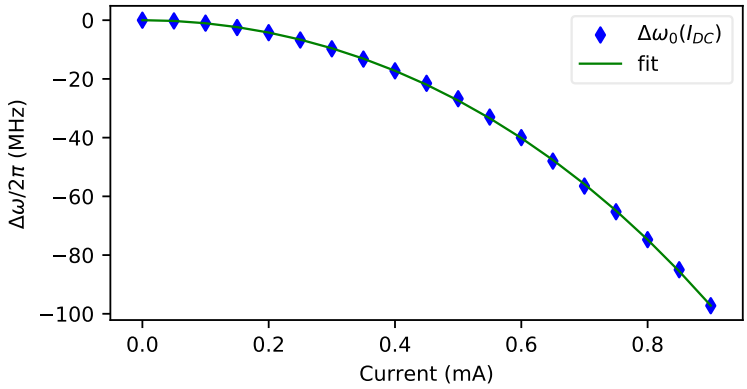

Figure 4.3: The dependence of the fundamental mode frequency on the applied bias current. The frequency drops as the current (and therefore kinetic inductance) increases, as expected.

We observe a resonance frequency shift of 100 MHz for a 0.9 mA bias current. For the remainder of this chapter, the bias current is set to 0.834 mA, which is close to the critical current of the film but with a sufficient margin for additional microwave currents applied through the pump and signal without causing the film to turn normal.

4.4 Parametric amplification

4.4.1 Phase insensitive parametric amplification

By adding a pump tone at the frequency $\omega_p/2\pi = 14.381$GHz and bias current $I_{DC} = 0.834$ mA, the KIPA produces an amplification feature centered around $\omega_p/4\pi = 7.1905$ GHz (see Fig. 4.4). The output of the pump, produced by a low-phase-noise microwave source (Keysight Technologies, E8267D), is routed via a highpass filter (Mini-circuits, TB-HFCN-9700+) to suppress the pump subharmonics. The voltage source (Yokogawa, GS2000) is connected in series with a 10 kΩ resistor at room temperature to provide the required DC current. We use the VNA (Rohde & Schwarz, ZVB-20) to probe the S_{11} magnitude response of the KIPA at approximately half the pump frequency.

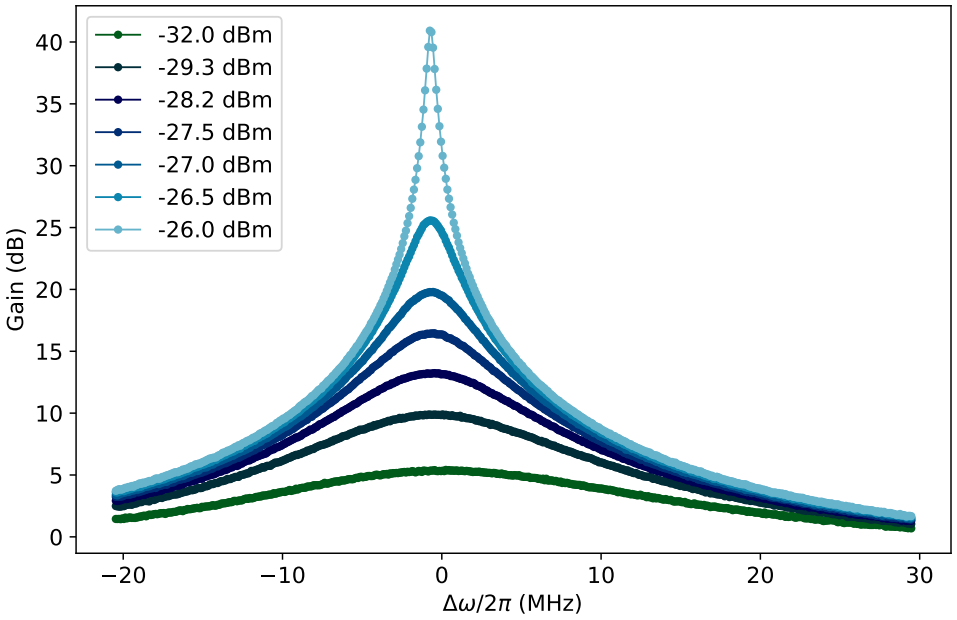

Figure 4.4: Phase insensitive gain of the KIPA at different pump powers (see inset) as a function of the signal frequency detuning from $\omega_p/2$, i.e. $\Delta\omega/2\pi = (\omega - \omega_p/2)/2\pi$.

By supplying a DC current to the KIPA we induce 3WM, resulting in an amplified signal tone ω_s at the device output and an idler at the frequency ω_i such that energy is conserved in this process $\omega_p = \omega_s + \omega_i$. Phase insensitive (or non-degenerate) gain occurs when $\omega_s = \omega_p/2 + \Delta\omega$ with $|\Delta\omega|$ exceeding the measurement bandwidth resolution (the idler frequency is outside the measured frequency band) [156].

To estimate the baseline of the magnitude response, we disable the pump but leave

the bias current active, which yields an approximately flat magnitude response. We subtract this baseline measurement from the magnitude response of the gain curves to obtain the data presented in Fig. 4.4. The phase insensitive gain increases with the pump power and is found to be in excess of 40 dB before the KIPA crosses the threshold where spontaneous parametric oscillations occur [164]. In addition, we measure a 3 dB bandwidth of 6 MHz at a gain of 20 dB, comparable to resonant JPAs [74].

4.4.2 Phase sensitive parametric amplification

When applying a signal tone at exactly half the pump frequency $\omega_s = \omega_p/2$, the KIPA enters the degenerate mode of operation, producing phase sensitive gain as the signal and idler tones interfere. To characterize the device in this mode of operation, the signal line is connected to another microwave source (Keysight Technologies, E8267D), which is configured for linear phase modulation at ω_s. A signal power of ~ -95 dBm is applied at the input of the sample. The pump and signal sources are phase locked using a high stability 1 GHz reference clock. Depending on the precise phase difference between the signal and the pump we either de-amplify or amplify the signal, as shown in Fig. 4.5. The phase sensitive gain is measured with the help of the VNA operated as a spectrum analyzer, using it to only measure the incident power. Configuring the network analyzer for a zero-span (i.e. time-dependent) measurement that is triggered off the edge of the linear (sawtooth) phase ramp, we obtain the data presented in Fig. 4.5.

Since it is the relative phase between the pump and signal tones that determines the amplifier gain, we arbitrarily set the maximum de-amplification to occur at $\phi_{pump} = 0$ with the maximum amplification therefore appearing at $\phi_{pump} = \pi/2$. A de-amplification gain up to 26 dB was observed with a maximum amplification gain of 50 dB recorded for the same pump power. Compared to phase insensitive (non-degenerate) amplification, an additional 6 dB gain is observed in degenerate mode due to the constructive interference that occurs between the signal and idler [98].

Next we probe the power-handling capability of the KIPA by repeating the above gain measurements for a range of input signal powers. The maximum of the phase-sensitive gain curve is plotted as a function of the signal power in Fig. 4.6. An important figure of merit for any amplifier is the "1 dB-compression point" P_{1dB}, which is power at the output of the amplifier where the maximum gain reduces by 1 dB, typically due

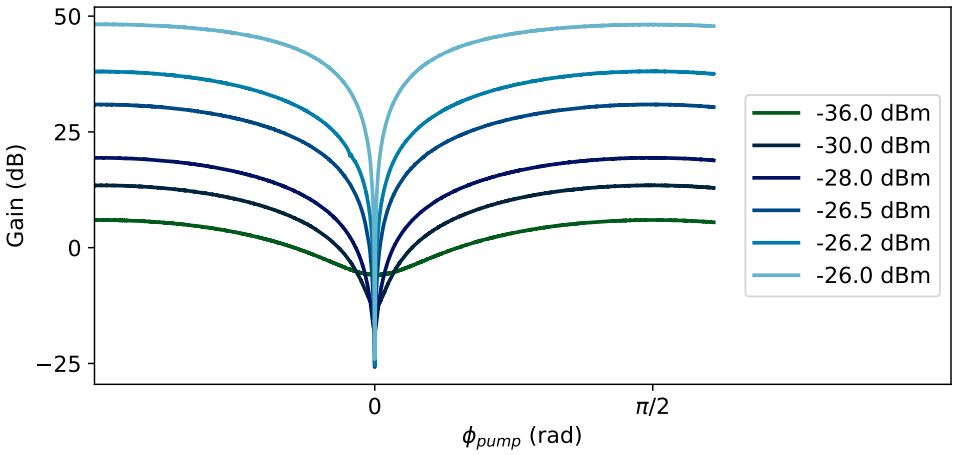

Figure 4.5: Phase sensitive gain of the KIPA at different pump powers as a function of the pump phase ϕ_{pump}. The maximum of the gain is aligned with $\phi_{pump} = \pi/2$.

to high-order nonlinearities that create unwanted mixing processes which take power away from the signal and pump.

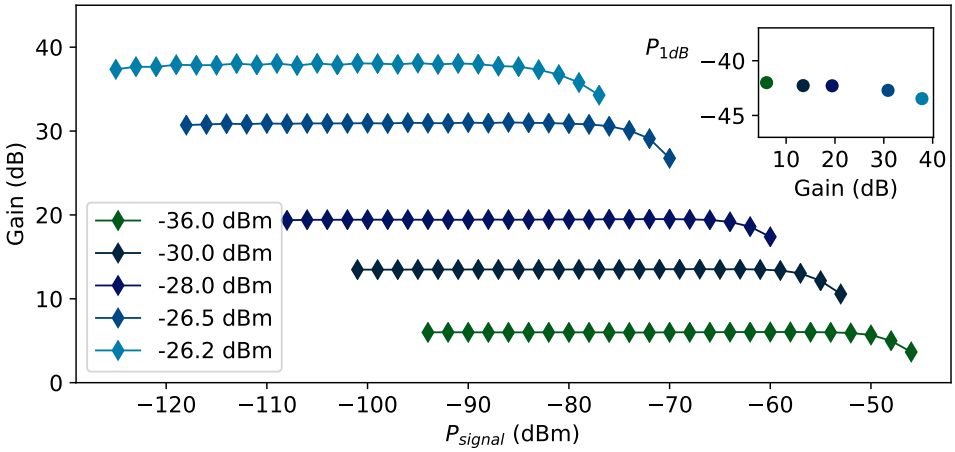

Figure 4.6: Phase sensitive gain as a function of the input signal power for different pump powers (listed in the legend). The 1-dB compression point output power as a function of the gain is shown in the inset.

The inset of Fig. 4.6 depicts the degenerate 1 dB-compression point of the KIPA as a function of gain (or pump power). For $\sim$ 20 dB of phase sensitive gain, we find a minimum compression power of -61.7 dBm at the KIPA input, comparable to the compression performance of kinetic inductance traveling wave amplifiers [159], [165] and many orders of magnitude higher that Josephson junction based parametric amplifiers

[74]. The output power of the KIPA for this measurement was close to the input power 1 dB-compression point of the cryogenic HEMT amplifier (−40 dBm). It is thus possible that the true KIPA 1 dB-compression point is higher than we report here.

4.5 Squeezing of a coherent state

The phase dependent interference of the signal and idler fields in a DPA results in an affine transformation applied to the IQ-plane of the input field, also commonly called the squeezing transformation [98]. The fields, which initially occupy a circular region on the IQ-plane, are stretched to form an ellipse, with the area being conserved in the process (see Sec. 2.1.5). To test this feature of the phase sensitive amplifiers, we connect the output of the detection chain to a homodyne detection setup consisting of an IQ mixer (Marki Microwave Inc, IQ4509), with local oscillator supplied by a third independent microwave source (Keysight Technologies, E8267D), which is phase locked with a 1 GHz reference clock to the pump and signal sources. The local oscillator is set to the signal frequency of $\omega_s = 7.1905$ GHz. The I and Q outputs of the mixer first pass through 1.9 MHz low pass anti-aliasing filters (Mini-Circuits Technologies, SLP-1.9+), followed by two 5 × pre-amplifiers (Stanford Research Systems, SIM914) connected in series for a total linear amplitude gain of 25 on each channel. I and Q are then digitized using a fast digitizing card (Keysight Technologies, M3300A) with a sample rate of 6.25 MS/s.

When the KIPA is off, the input coherent state phase sweep traces out a circle on the IQ-plane. Activating the KIPA maps the circle to an ellipse at the detector as it is shown in Fig. 4.7. Ellipse measurements were performed with the pump and local oscillator phases fixed, while the signal phase is stepped. Each (I, Q) pair is measured by averaging 10^6 samples collected at each phase. The entire phase sweep is performed in less than 60 s to minimize errors due to slow phase drift between the signal and pump.

Importantly, the ellipses do not show any “S-type” distortions (or “banana curves”), even for a degenerate gain of 30 dB. Usually, Hamiltonian non-idealities manifest as an S-shaped distortion of the phase space at high gains, as has been experimentally observed in Refs. [38], [155] and modeled in Ref. [156] in JPAs for gains typically exceeding 10 dB. Further increases in gain (up to 50 dB) did not produce any obvious

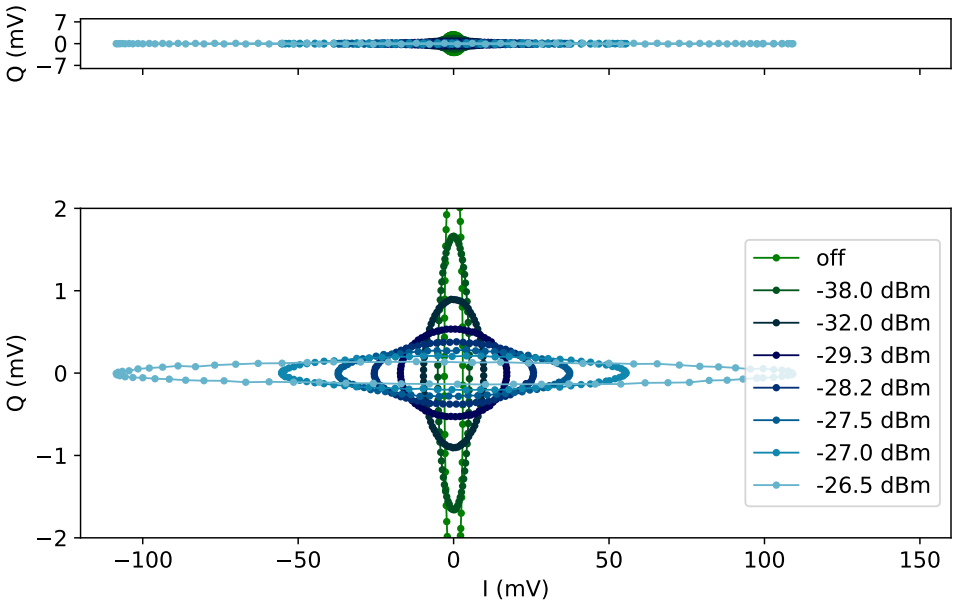

Figure 4.7: KIPA response to coherent inputs of constant amplitude and varying phase plotted on two different scales. Top: outputs are plotted with an equal aspect ratio, where the reflected input sweep with the KIPA off is observed as a circle (green). Turning the KIPA on stretches the circle to an ellipse, which resembles a blue line in this plot. Bottom: the same outputs plotted with an exaggerated scale along Q so that the elliptical transformation may be observed. Solid lines are a guide for the eye.

distortions, though at these higher gains the signal power had to be reduced to avoid saturating the cryogenic HEMT and room temperature amplifiers, resulting in significant degradation in the SNR. The lack of S-type features at high gain support the idea that the KIPA is well-approximated by an ideal DPA.

The deamplification level G_S is defined as the greatest reduction in amplitude of an input coherent state by the squeezing transformation. We additionally define the amplification level G_A as being the corresponding increase in gain that occurs orthogonal to the axis of deamplification. G_S and G_A are measured after aligning the amplification and deamplification axes along I and Q respectively, and averaging multiple measurements. We measure G_S (G_A) by taking the ratio of the peak to peak amplitudes of the pump off response and pump on response on Q (I) after averaging. Fig. 4.8 presents our results, where up to 26 dB of deamplification is observed for 30 dB of amplification.

The high level of deamplification achieved with the KIPA can be used to squeeze the vacuum noise level, which can be used to enhance the signal-to-noise ratio (SNR) in experiments and has been successfully deployed in gravitational wave detection [166], the search for axions [152] and in electron spin resonance (ESR) spectroscopy [38]. These measurements show that the Hamiltonian non-idealities that limit typical JPA squeezers do not seem to effect the KIPA even up to large gains as high as 30 dB. Future work will focus on verifying the squeezing capabilities of the device by analyzing the statistical properties of squeezed vacuum and thermal states input to the amplifier.

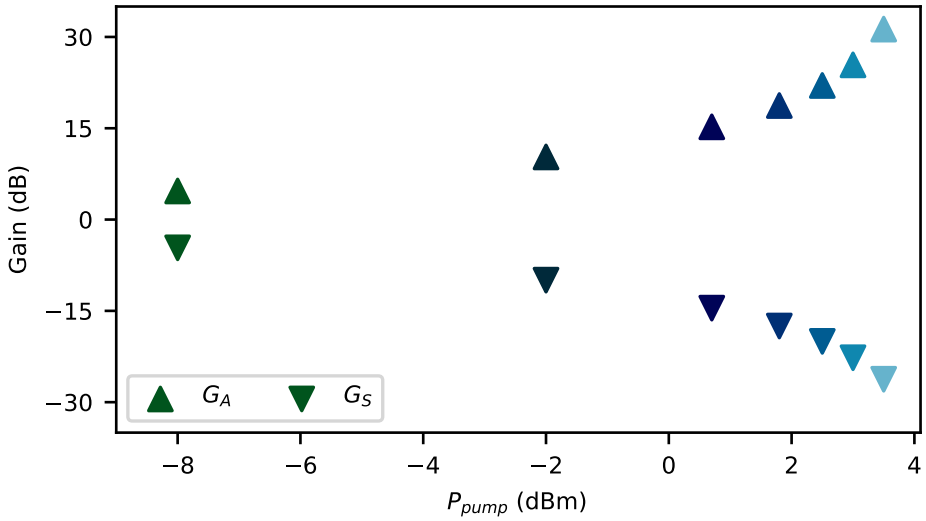

Figure 4.8: The deamplification G_S and amplification G_A as a function of pump power. Points are extracted from the ellipses presented in Fig. 4.7.

4.6 Calibrating the photon-to-power conversion factor

The amount of noise added to a signal during amplification, quantified by the amplifier noise temperature, is a primary factor in determining the SNR of a measurement. For a detection chain containing a series of amplifiers, it is the noise temperature of the first amplifier that typically dictates the overall system SNR (see Fig. 4.9). As a fundamental limit [98], a phase insensitive amplifier must add at least 1/2 a photon of noise to a signal – an equivalent noise temperature of $T_n = \hbar\omega/2k_B \approx 170\,\mathrm{mK}$ at a

frequency of $\omega/2\pi = 7.2\,\text{GHz}$. Conversely, no noise is added by an ideal phase sensitive DPA ($T_n = 0\,\text{mK}$).

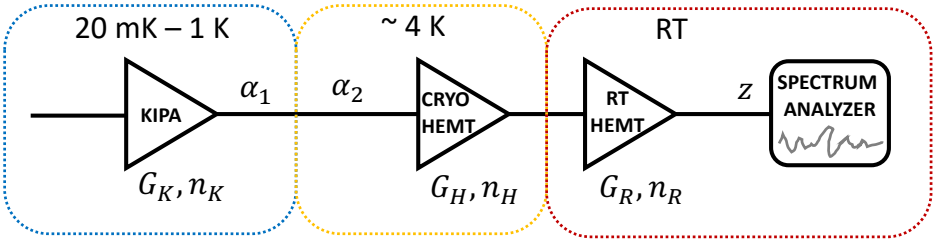

Figure 4.9: Detection chain containing a series of amplifiers and possible loss at different temperature stages.

In order to study the noise performance of the KIPA, we first need to convert the measured noise power (using spectrum analyzer) at the output of the measurement detection chain to an equivalent number of photons at the input of the device. We use the simple schematic in Fig. 4.9 to model the noise in our experiment. The model includes the KIPA with a linear power gain G_K and an effective noise contribution n_k (in dimensionless units of photons), as well as the cold HEMT amplifier and the room-temperature amplifier with gains and noise contributions G_H/ G_R and n_H/n_R, respectively. We also take into account loss in the cables and microwave components, which acts like a beam splitter in quantum optics, transmitting a fraction α of the incident power and mixing in to the output a component $(1-\alpha)$ of a thermal field at the temperature of the loss. We split the loss into two components, one at the mixing chamber α_1 with noise n_1 and any attenuation at higher temperature stages (before the HEMT) with transmission α_2 and effective noise n_2. The parameter z converts the dimensionless photon numbers to a power, as measured on the spectrum analyzer.

When the KIPA is on (i.e. amplifying), we calculate the output noise power as:

$$\begin{aligned} P_{ON} &= \{[n_1 G_K + n_k(G_K - 1)]\,\alpha_1\alpha_2 + n_1(1-\alpha_1)\alpha_2 + n_2(1-\alpha_2) + n_H\}\,G_H G_R z \\ &= [(n_1 + n_k)(G_K - 1)\alpha_1\alpha_2 + n_{sys}]\,G_H G_R z \end{aligned} \tag{4.8}$$

The first term on the right hand side of line 1 represents the amplified fluctuations/noise of the input field $n_1 = 1/2 + n_{th}$, where n_{th} is the Bose factor from Eq. 2.32 that describes the thermal population of the field. The second term is the amplified noise

added by the KIPA, which vanishes at unity gain (i.e. when the amplifier is turned off). The third and fourth terms are the noise fields mixed in by the cold and hot losses and the last term is the noise added by the HEMT. Note, we ignore the noise added by the room temperature amplifier since we assume that the HEMT gain is sufficiently large that the amplified cold noise terms dominate the output signal. In the second line we introduce the "system noise" $n_{sys} = n_1\alpha_2 + n_2(1-\alpha_2) + n_H$, which is the non-KIPA related noise referred to the input of the HEMT.

Measuring the output noise with the KIPA off ($G_K = 1$) yields a power:

$$P_{OFF} = n_{sys} G_H G_R z \tag{4.9}$$

The difference of these two measurements gives:

$$\begin{aligned} P_{ON} - P_{OFF} &= (n_1 + n_k)(G_K - 1)\alpha_1\alpha_2 G_H G_R z \\ &= (n_1 + n_k)(G_K - 1)G_T \end{aligned} \tag{4.10}$$

Where we have defined the photon-to-power conversion factor $G_T = \alpha_1\alpha_2 G_H G_R z$. The KIPA noise component n_k can contain several contributions, it includes noise added by the idler mode $n_i = 1/2 + n_{th}$ and additional terms if there is any loss present, which we represent with n_{k0}. Both the signal and idler fields have the same temperature and therefore the same Bose factor n_{th}, which can be controlled with the base temperature of the dilution refrigerator. We can rewrite the output power difference signal as:

$$P_{ON} - P_{OFF} = (2n_{th} + 1 + n_{k0})(G_K - 1)G_T \tag{4.11}$$

Eq. 4.11 provides a method to experimentally extract the conversion factor G_T; we can simply monitor the difference in the output noise power (for the KIPA on and off) as we sweep the fridge temperature (and therefore n_{th}), extracting the gradient of $P_{ON} - P_{OFF}$ vs. n_{th}, i.e. $m = 2(G_K - 1)G_T$. At each temperature we measure the output noise power difference for 9 different values of the linear power gain G_K on a spectrum analyzer. We plot $P_{ON} - P_{OFF}$ versus n_{th} for each G_K in Fig. 4.10a and the extracted gradient from each gain trace is shown in Fig. 4.10b as a function of $G_K - 1$. The slope of Fig. 4.10b then directly provides $2G_T$, yielding the conversion factor $G_T = 7.15(13) \times 10^{-4}$ pW/photon for our setup.

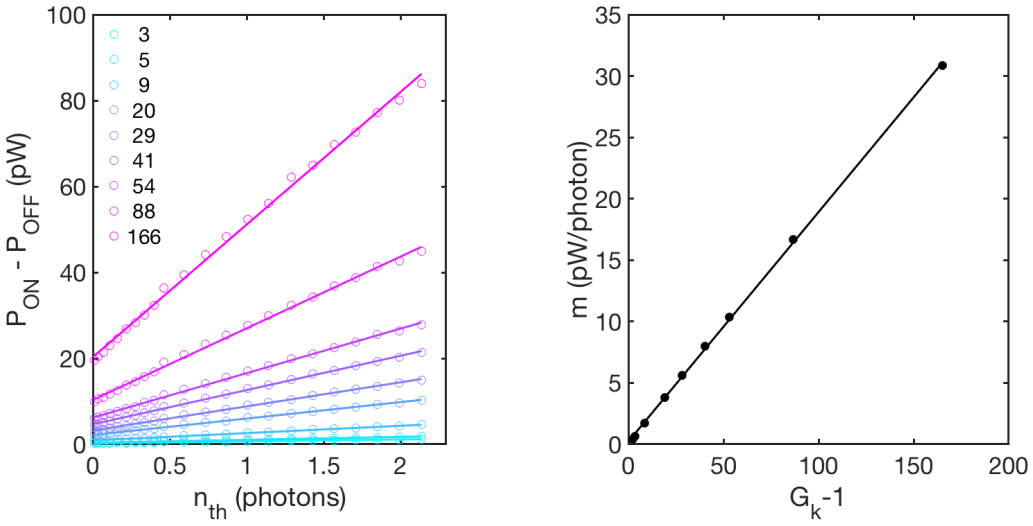

(a) (b)

Figure 4.10: **a)** The output noise power difference versus n_{th} (controlled by varying the base temperature of the dilution refrigerator) for different values of the linear power gain G_K. **b)** The extracted gradient from each gain trace in **a)** as a function of $G_K - 1$.

4.7 Noise properties

In this section we explore the KIPA noise properties. This is done by again monitoring the output power of the measurement setup on the spectrum analyzer without an input signal. The device is tested in both degenerate and non-degenerate amplification modes and also when it is off, which gives a measure of the background system noise. The measured output power is converted to an equivalent number of photons referred to the output of the KIPA using the factor G_T that was found from the analysis in Sec. 4.6.

The measured noise consists of three main components. The first one originates from the equilibrium fluctuations of the electromagnetic field (n_{eq}), which itself is comprised of both thermal photons (n_{th}) and the fluctuations of the vacuum $n_{eq} = n_{th} + 1/2$. In addition, we include any additional noise introduced by the KIPA (n_k) due to fundamental quantum limitations and/or loss. The last noise component stems from the system noise (n_{sys}) defined previously, which is generated by the following amplifiers and higher temperature stages.

In degenerate mode, only a single field quadrature is amplified yielding an effective *input-referred* noise of $n = (n_{th} + 1/2)/2 + n_k + n_{sys}/G_K$, which for a quantum-limited

degenerate amplifier ($n_k = 0$) at zero temperature ($n_{th} = 0$) and with infinite gain is $n = 1/4$ photons. In non-degenerate mode, noise from both field quadratures is amplified and contributes to the output signal, resulting in an input-referred noise of $n = n_{th} + 1/2 + n_k + n_{sys}/G_K$. For a non-degenerate quantum-limited amplifier ($n_k = 1/2$) the minimum amount of added noise is thus $n = 1$ photon.

In Fig. 4.11a, we plot the input-referred number of photons by further dividing the output signal by the KIPA gain G_K. For the non-degenerate measurement we detune the center frequency of the spectrum analyzer by 500 kHz from $\omega_p/2$ and both of the KIPA on measurements are recorded at a degenerate gain of 31 dB and a non-degenerate gain of 25 dB.

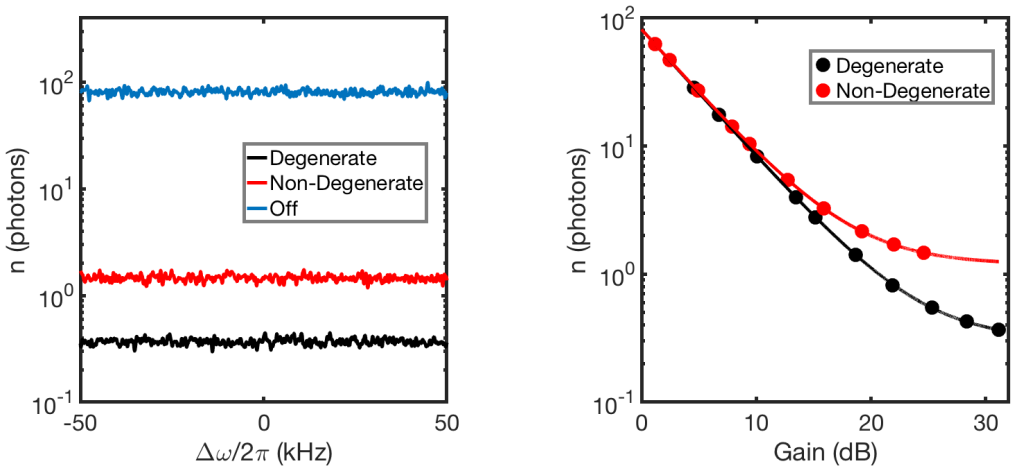

Figure 4.11: **a)** Input-referred noise of the KIPA measured with a spectrum analyzer for the different modes of amplification. **b)** KIPA input-referred noise as a function of gain when operated in both degenerate and non-degenerate modes. At low gains the noise is determined by the system contribution, whilst at large gains the measured noise reflects that added by the KIPA.

To determine if the KIPA is quantum limited, we plot the input-referred noise n against gain G_K, as shown in Fig. 4.11b. Fitting each data set with the expression $n = n_0 + n_{sys}/G_K$, we obtain $n_0 = (n_{th} + 1/2)/2 + n_k = 0.30(3)$ in the degenerate case and $n_0 = n_{th} + 1/2 + n_k = 1.12(12)$ in non-degenerate. These numbers are exceptionally close to their ideal values of 0.25 and 1, with the differences being only a small fraction of the quantum noise level (i.e. $n_0 - n_{0Q} \ll n_{0Q}$, with $n_{0Q} = 0.25$ or 1 depending on the mode of operation) and we therefore conclude that the KIPA is quantum noise limited. Both fits produce $n_{sys} = 78$, which is the strength of the system noise. The

estimated loss between the KIPA output and input of the cryogenic HEMT amplifier is ~ 4.5 dB, indicating that the system noise at the input of the HEMT is ~ 28 photons – a value in agreement with that measured in other setups [38]. This loss originates from the insertion loss of the microwave components (a diplexer, a bias-tee, two circulators and high pass filter) and cables used to route the amplified signal. The amount of loss was estimated at room temperature with the help of VNA and represents a worst-case value.

4.8 Conclusions

We have presented a simple and versatile parametric amplifier called a KIPA, fabricated from a thin film of NbTiN. For the bias conditions tested, we report up to 40 dB of phase insensitive gain and up to 50 dB of phase sensitive gain. Our device features an exceptionally high input 1 dB-compression point of approximately -60 dBm at its input for 20 dB of gain, making it suitable for a wide range of cryogenic microwave measurements. Furthermore we find our amplifier is quantum limited in its noise performance.

The simple design and fabrication of the KIPA opens up new experimental possibilities where quantum limited microwave amplifiers may be integrated 'on-chip' with other quantum systems. We envisage using this amplifier in applications such as electron spin resonance spectroscopy, where the KIPA can serve as both the microwave cavity and first-stage amplifier to push the boundary of spin detection sensitivity (see Ch. 5).

Chapter 5

Parametric amplification of spin echoes

I acknowledge my colleague and fellow student, Wyatt Vine, who worked on many of the measurements detailed in this chapter.

5.1 Motivation

ESR spectroscopy is a well-established technique used to analyze the paramagnetic species within samples in a diverse range of fields including physics, chemistry and biology [99]. The conventional spectrometer used in ESR consists of a 3D microwave cavity that inductively detects weak signals from electron spins precessing in an external magnetic field. The signal induced in the cavity by a single electron spin is extremely small, thus samples typically must contain large ensembles of spins ($\sim 10^{13}$) to produce signals with sufficient SNR [99] for detection. As a direct result of the rapid progress in the field of cQED, where manipulation and detection of weak signals (at the level of single microwave photons) has now become commonplace [167], the sensitivity of the inductive ESR spectroscopy was recently pushed to the quantum limit [31], [168]. The use of high quality factor superconducting micro-resonators for inductive spin detection in conjunction with quantum-limited parametric amplifiers (see Ch. 4) permitted the demonstration of a record breaking detection sensitivity down to ~ 10 spins in a single shot measurement [36], [37].

Typically, a quantum-limited ESR spectrometer involves a complex and fragile measurement setup. The most fragile of the components is the Josephson parametric amplifier (JPA), which is commonly employed for the first amplification stage in the detection chain due to its quantum-limited noise performance. As was already noted in the previous chapter, they consists of one or many Josephson junctions, which are susceptible to electrostatic discharge. Moreover, the 1 dB-compression point of these amplifiers is restricted to about -110 dBm [74], which greatly limits the signals that can be applied to the spins in a typical pulsed experiment. As was pointed in Ref. [38] the nonlinearity in operation of JPAs might cause power dependent phase shifts and power saturation of squeezed states that have higher power than vacuum. To avoid the distortion of the signal, they had to limit the power of the spin echo signal well below the 1 dB-compression point. In addition, the weak signal emitted by spins into superconducting cavity must be passed to the JPA via coaxial cables, microwave circulators and other components, which introduce loss typically in the range of $1 - 3$ dB [38].

We propose to use the kinetic inductance parametric amplifier (KIPA) introduced in Ch. 4 as both a superconducting cavity for inductive detection of the electron spins, whilst simultaneously serving as an on-chip quantum-limited parametric amplifier. The KIPA's near ideal DPA performance and simplicity in design makes it a perfect candidate for integration with ESR spectroscopy experiments. Moreover, in this architecture

there is no need to tune the frequency of the parametric amplifier to match the signal frequency, since the KIPA and the microwave cavity are one and the same.

5.2 Device and setup

The device used in the experiments described in this chapter consists of a PBG-confined quarter-wavelength cavity, similar in design to the KIPA described in Ch. 4. The resonator is made of a 50 nm thick NbTiN film lithographically defined on top of a silicon chip that has been implanted with bismuth donors in a surface layer of isotopically enriched ^{28}Si. The implantation details can be found in Sec. 3.2.1. The silicon chip is wire bonded to a PCB and placed inside a 3D copper cavity, as described in Sec. 3.3.

The resonator section is implemented as a CPW line without an IDC structure (as was utilized in Ch. 4) with a central line of width $w = 1$ μm and ground plane gaps of $g = 10$ μm. The length of the resonant section is $L = 1.75$ mm. According to Sonnet simulations (taking into account kinetic inductance $L_k = 3.5$ pH/sq) this geometry is expected to exhibit a characteristic impedance of approximately $Z_r = 200$ Ω and a resonant frequency of 7.3 GHz. The PBG structure that confines the resonant mode of the device consists of four cells that result in the transmission spectrum presented in Fig. 3.7. The design and fabrication details of the PBG resonator are outlined in Sec. 3.1 and Sec. 3.2.

The measurements were conducted in the ^{3}He refrigerator at a 400 mK base temperature (see Sec. 3.4.1). Detailed schematics of the cryogenic and room temperature measurement setups were presented in Fig. 3.18 and Fig. 3.20, respectively. A simplified experimental setup used in this chapter, portraying the most important components, is presented in Fig. 5.1.

5.2.1 Device characterization

The resonator is measured in reflection using a VNA. The output port of the VNA sends a signal down an attenuated coaxial line which is routed to the device via a circulator. The signal reflected from the resonator is returned to the VNA via another

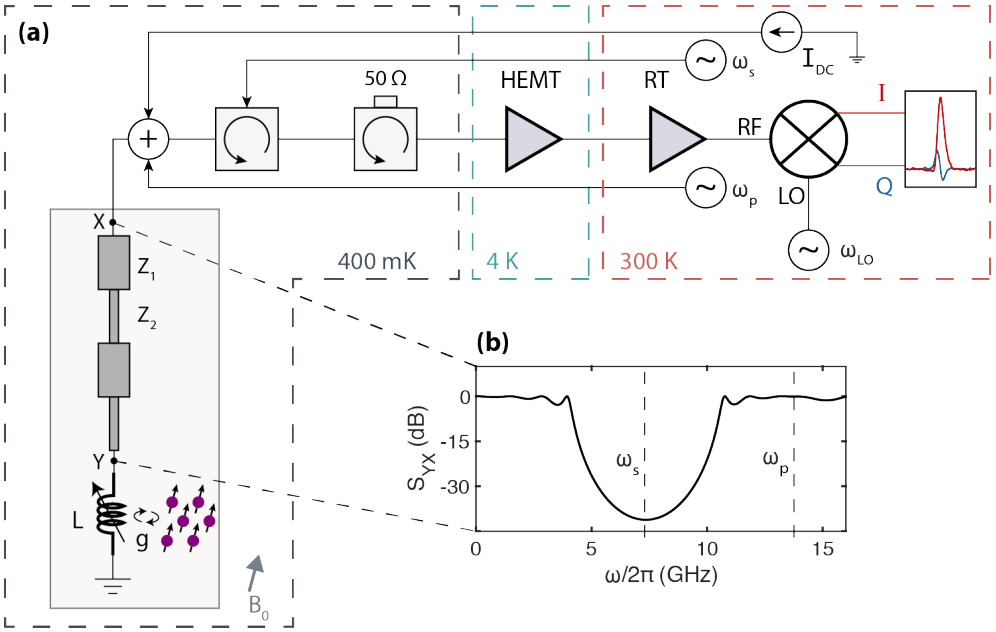

Figure 5.1: **a)** Simplified schematic of the experimental setup, illustrating the PBG resonator/KIPA inductively coupled to a spin ensemble (purple), amplification stages at 4 K (HEMT) and room temperature, followed by homodyne detection. The pump tone ω_p, input signal ω_s and DC current I_{DC} are generated at room temperature and combined at 400 mK. **b)** Simulated transmission spectrum of the PBG structure demonstrating locations of the signal and pump tone frequencies.

coaxial cable that passes through an additional microwave isolator to protect the spins and the KIPA from thermal noise emitted by the higher temperature stages. This allows us to measure the amplitude and phase of the S_{11} response for the device and experimental setup.

Using Eq. 2.48 we fit the measured response and extract the resonator properties such as its resonance frequency (ω_0), internal (Q_{int}) and external (Q_{ext}) quality factors. An example of the fitting routine is shown in Fig. 5.2. The circle fit technique for complex resonator scattering data is described in Ref. [169], and throughout this thesis we utilize the algorithm detailed there to fit our resonances. Even though the algorithm corrects for the electrical delay imposed by the measurement lines, in order to get the most accurate fits we first subtract the line response obtained in a separate measurement with the resonator detuned in frequency. This allows us to remove any frequency response of the line not related to the device that might complicate the fitting routine.

It is clear that the resonator line-shape (the dip in the S_{11} magnitude plot, Fig. 5.2b) is not an ideal Lorentzian, as predicted by Eq. 2.48, but rather displays some asymme-

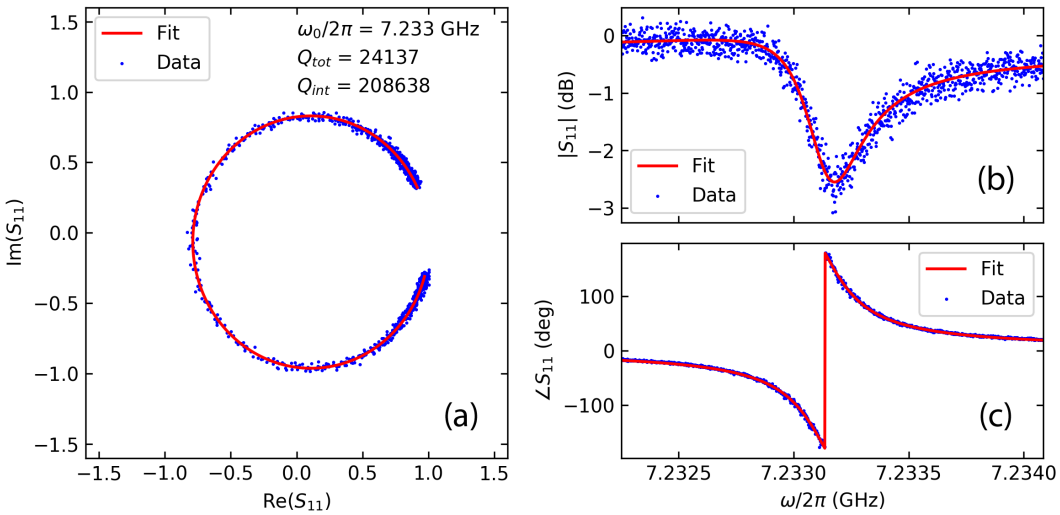

Figure 5.2: Fit of the fundamental mode S_{11} response. **a)** The S_{11} measurement forms a circle when plot on a complex plane. **b)** The magnitude of the reflected signal as a function of frequency. The dip indicates the absorption of some microwave power by the resonator. **c)** The phase response of the complex S_{11} reflection measurement, indicating that the resonator is in the over-coupled regime ($Q_{int} > Q_{ext}$).

try. The precise origin of this asymmetric response is still under debate [169], though it is suggested to stem from impedance mismatches in the vicinity of the resonator [170]. To take this asymmetry into account we substitute the real external coupling rate κ_{ext} with the complex term $\kappa_{ext,asym} = \kappa_{ext}e^{i\phi}$, where the phase ϕ represents the degree of an asymmetry. Based on the fits shown in Fig. 5.2, we find the fundamental mode of the resonator has a frequency of $\omega_0/2\pi = 7.233$ GHz and a linewidth $\kappa \approx 280$ kHz determined by its internal $Q_{int} \approx 2 \cdot 10^5$ and external $Q_{ext} \approx 0.3 \cdot 10^5$ quality factors.

Next we apply a DC bias current to the device, which is utilized later to enable amplification through 3WM (see Sec. 4.2). We connect a NI source measurement unit (SMU) (operated as a voltage source) through a room temperature 1 $k\Omega$ resistor to the device. The DC current was ramped up from 0 mA until we reached the critical current, which is around 4.5 mA for this device. For each current we measured the complex reflection S-parameter. The resonant frequency and quality factors have been extracted from the fits and plotted in Fig. 5.3 as a function of the DC bias current.

For the DC current sweep the microwave power generated by the VNA is kept constant. We estimate the power to be -117 dBm $\pm$ 2 dBm at the resonator input, determined by performing line loss calibration measurements in a separate cool-down. At zero bias current this power corresponds to $\langle n \rangle \approx 10^3$ photons on average residing

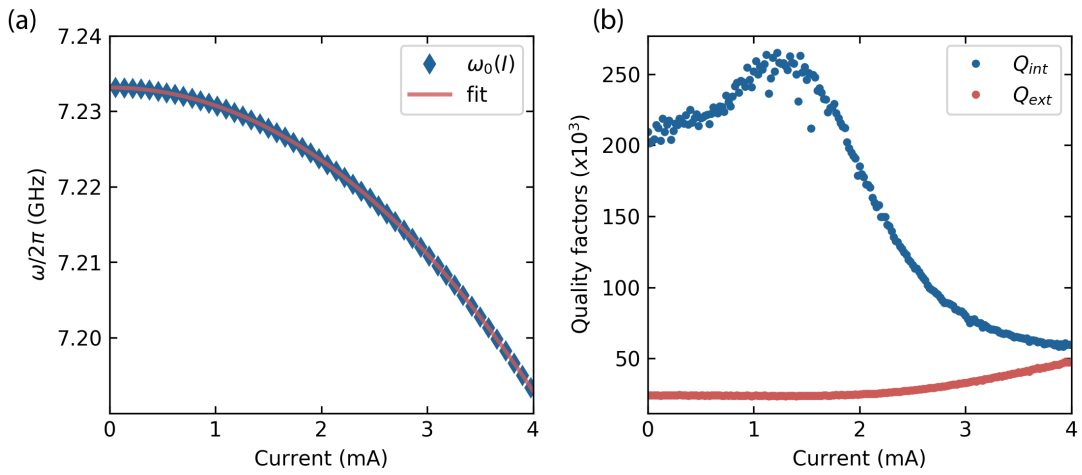

Figure 5.3: **a)** Dependence of the resonance frequency of the fundamental mode on the applied bias current. The frequency drops as the current increases due to the expected increase of its kinetic inductance. **b)** The internal and external quality factors of the fundamental mode as a function of the bias current.

in the resonator (see Eq. 2.47). This number varies slightly for different bias currents since the coupling rates are not constant.

The frequency of the current-biased resonator decreases as the current is increased, which is perfectly described by the expected current dependence of the kinetic inductance according to Eq. 2.57. Based on this equation we fit the frequency response to the biquadratic polynomial $\omega_0/2\pi = a + bI^2 + cI^4$ resulting in coefficients $a = 7.233$ (GHz), $b = -2.3712 \cdot 10^{-3}$ (GHz/mA^2) and $c = -8.84348 \cdot 10^{-6}$ (GHz/mA^4). The experimental data and fit are shown in Fig. 5.3. The increase of the bias current inevitably leads to an increase in the number of quasiparticles inside the superconducting material. They act as dissipative loss centers and deteriorate the internal quality factor when the current increases significantly. Curiously, there is a small unexplained increase in the internal quality factor starting at $I_{DC} = 1$ mA before it begins to drop at high currents. The slight increase in the external quality factor likely results from a combination of effects related to the PBG structure; the current will shift resonator frequency relative to the center of the bandstop region and the impedance of the PBG sections are also expected to change slightly.

The dependence of the fundamental mode on the signal power, down to the single photon level, is measured at a constant bias current of 3.3 mA. This bias current value is kept the same for all measurements described in this chapter (unless stated otherwise) and corresponds to the frequency $\omega_0/2\pi = 7.206$ GHz. The fit results from the power-

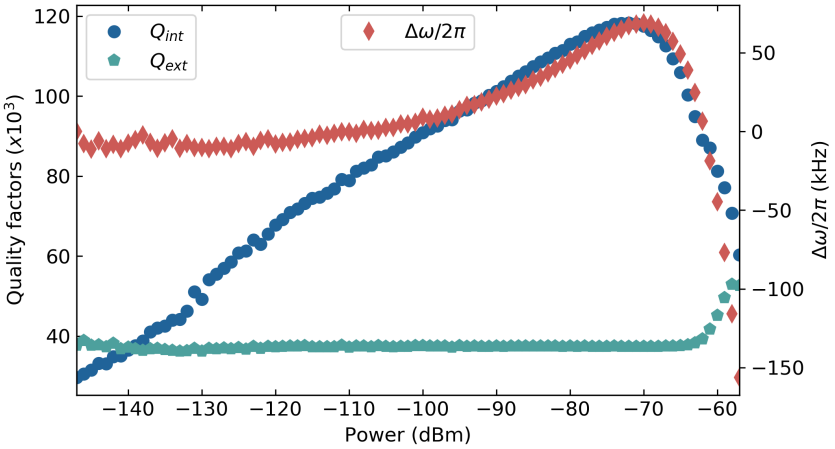

Figure 5.4: The fundamental mode fit parameters as a function of the power at the resonator input. The left axis represents the quality factors of the mode and the right axis depicts the resonance frequency shift relative to the single photon level.

dependence measurement are presented in Fig. 5.4. At the minimum input power of approximately −147 dBm the average number of intra-cavity photons approaches unity. When the power is increased the internal quality factor increases. This power dependence indicates that the device suffers from losses due to the TLSs. Depending on the TLSs-resonant mode interaction mechanism, at low power the internal quality factor of the resonator can exhibit a different behaviour to the typically observed saturation [171]. When the power is large (i.e. greater than −70 dBm) the frequency of resonator shifts down and the resonator enters the bifurcation (unstable) regime [172], [173]. The external quality factor is constant over a wide range of input powers and increases at about −60 dBm, which could simply be related to fitting errors as the resonator becomes unstable.

5.2.2 Resonator - spin ensemble coupling

The calculation of the coupling strength between the PBG resonator and spin ensemble is reasonably well-understood and studied problem [174]–[176]. In our device coupling distribution is expected to be highly inhomogeneous due to the broad implantation profile (recall Sec. 3.2.1) and inhomogeneous B_1 field generated by the narrow central line of the resonator. To estimate this coupling profile, we model this central line as 1 μm wide and 50 nm thick superconducting inductive wire. The wire is placed

parallel to the external static magnetic field $\vec{B}_0$. As a result, current in this wire generates a $\vec{B}_1$ field perpendicular to $\vec{B}_0$. This $\vec{B}_1$ field then drives the $\hat{S}_x$ transitions of the spins located underneath the wire. Using the simulation software Comsol Multiphysics, which is based on finite element analysis, and setting the current distribution in the superconducting wire to that presented in Ref. [177], we compute the magnetic field B_1 distribution. The magnetic field is scaled to the level of the RMS vacuum fluctuations δB_1 using Eq. 2.15. The projections of this field (located in the plane perpendicular to the resonator wire axis) along x and y axes are presented in Fig. 5.5.

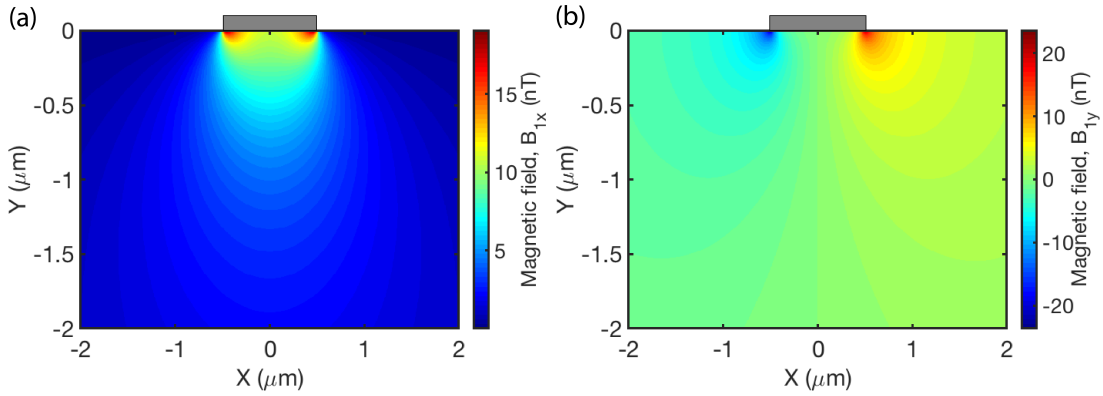

Figure 5.5: The projection on **a)** x and **b)** y axis of the magnetic field vacuum fluctuations generated by the 1 μm wide inductive wire located at $Y = 0$ (silicon chip surface).

To calculate the distribution of coupling rates to the spin ensemble $\rho(g)$, we first calculate the spin-resonator coupling strength g for each spin in the region implanted under the wire. We calculate g as:

$$g = \gamma_e * \delta B_1(x, y) * M_{ij} \tag{5.1}$$

where M_{ij} is the transition matrix element that, for example, we can consider for $|F, m_F\rangle = |4, -4\rangle \rightarrow |5, -3\rangle$ transition at $B_0 \approx 360$ mT and set it to 0.43 (see Sec. 2.5.1). We calculate the coupling strength g for spins in the implantation profile detailed in Sec. 3.2.1 and produce a coupling distribution $\rho(g)$. We plot the normalized coupling distribution $\frac{g^2}{g_{ens}^2}\rho(g)$ shown in Fig. 5.6. The ensemble coupling rate g_{ens} is defined as:

$$g_{ens} = \left(\int g^2 \rho(g)\, dg \right)^{1/2} \tag{5.2}$$

As can be seen in Fig. 5.6, the spin coupling distribution is quite inhomogeneous,

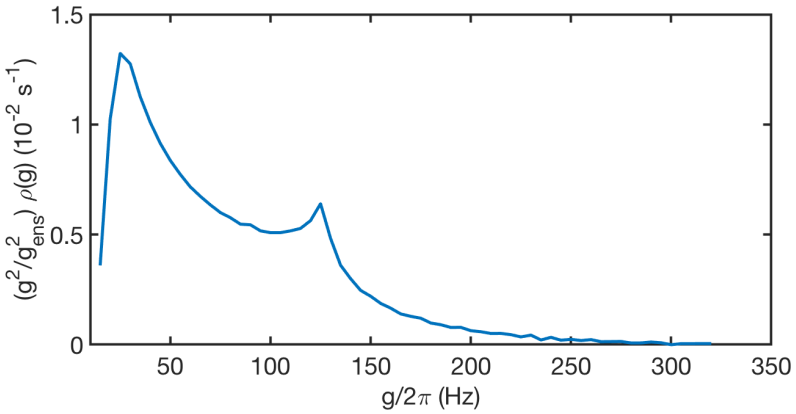

Figure 5.6: Calculated resonator-spin ensemble coupling strength distribution normalized by $(g/g_{ens})^2$.

with a predominant peak in g at approximately 20 Hz. An inhomogeneous resonator-spin coupling distribution is common when working with superconducting micro-resonators [178] and has previously been used in tandem with strain generated by the resonators to perform spatially-dependent spectroscopy of donors in devices [174], [176], [179].

5.3 Spin echoes

In order to bring the bismuth donor spins into resonance with the cavity, we apply an external magnetic field $\overrightarrow{B_0}$ parallel to the plane of the thin superconducting NbTiN film and aligned along the quarter-wavelength resonant CPW section to ensure $\overrightarrow{B_0} \perp \overrightarrow{B_1}$. This results in 20 electro-nuclear energy states of the neutral ^{209}Bi donor system (see Sec. 2.5) that can be studied using pulsed ESR spectroscopy techniques (see Sec. 3.6).

The oscillating magnetic field $\overrightarrow{B_1}$ generated by the resonator can drive resonant $\hat{S}_x$ transitions with non-zero matrix elements (see Sec. 2.5.1). By scanning the magnitude of $\overrightarrow{B_0}$ and applying a 200 pulse Carr-Purcell-Meiboom-Gill (CPMG) sequence (see Fig. 5.7a) at each field, we excite all ESR transitions up to 360 mT, as illustrated in Fig. 5.7. Fig. 5.7b shows the transition frequencies of ^{209}Bi in the low-field limit, calculated based on the Hamiltonian presented in Eq. 2.96. The horizontal dashed line depicts the frequency of the superconducting cavity. At points of crossing with the spin transition frequencies we observe peaks in the integrated spin echo signal, shown

in Fig. 5.7c.

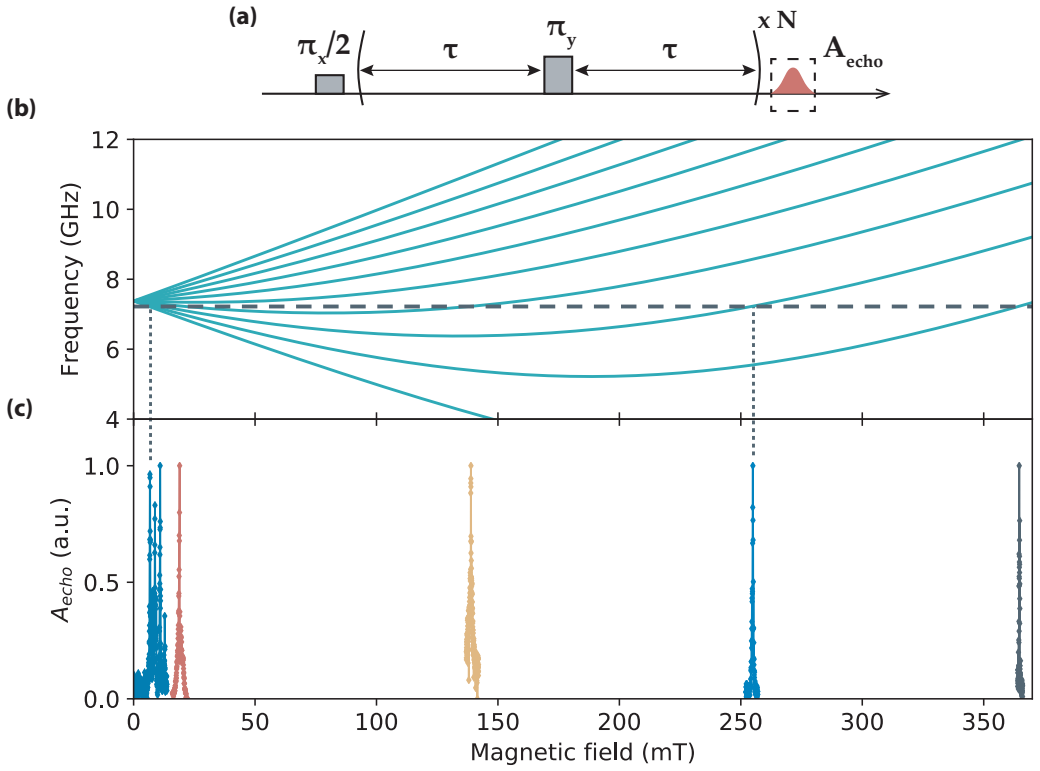

Figure 5.7: **a)** CPMG pulse sequence used to detect spin echoes. Here $N = 200$ and $\tau = 120$ μs. **b)** ESR transition frequencies of the neutral ^{209}Bi donor spin system in the low magnetic field limit. Horizontal dashed line represents the frequency of the superconducting cavity employed to control spins and inductively detect their response. **c)** Detected integrated normalized spin echoes as the magnetic field $|\overrightarrow{B_0}|$ is swept. Vertical dashed lines highlight the transitions investigated in this chapter.

The use of a CPMG pulse sequence to trigger the emission of multiple echoes ($N = 200$) in a single measurement allowing us to enhance the SNR, ideally by a factor $\sqrt{200}$ but typically smaller due to the existence of pulse errors and decoherence [31], as compared to a conventional Hahn echo pulse sequence. To further increase the SNR, we repeat the CPMG sequence 5 times at each value of the magnetic field (with a repetition time of $T_{rep} = 5$ s) and average the result. The relative shape and phase of the pulses are controlled by IQ-modulation of a local oscillator at the resonator/spin frequency ($\omega_{LO} = \omega_0$) with a baseband signal supplied by an arbitrary waveform generator (AWG) (M3202A, Keysight Technologies). We ensure suppression of any local oscillator leakage between pulses by additionally gating the output with a fast microwave switch. The

resulting spin echo signals are routed via a double circulator to a low-noise HEMT amplifier at 4 K, a further room temperature amplification stage (with a total gain of 75 dB), before undergoing homodyne demodulation by mixing the signal with the local oscillator carrier at ω_{LO}. The resulting baseband spin signal is filtered, amplified and digitized. All signals are further digitally filtered at 200 kHz and have a linear baseline subtracted. The echoes are digitally rotated in the IQ-plane to minimize $\int_{-T_e/2}^{+T_e/2} Q(t)\,dt$ (with T_e the duration of an echo) in the time domain in which the echo is recorded. This maximizes the echo's alignment along the I quadrature.

The duration of the pulses are the same for both the $\pi/2$ and π rotations $t_p = 3$ μs and the waiting time between pulses is $\tau = 120$ μs. It is worth noting that here the pulse duration is shorter than the characteristic decay time of the cavity, often called ring-down time, defined as $t_{cav} = 2/\kappa \approx 7$ μs. In this case the pulse amplitude inside the cavity rises linearly until the end of the pulse duration and then exponentially decay (with a time constant t_{cav}) during the ring-down time [180]. The power of the $\pi/2$ pulse is set lower than the π pulse by an amount 6 dB, corresponding to half the $\overrightarrow{B_1}$ amplitude (and therefore rotation angle) for the $\pi/2$ pulse. This approach ensures the same bandwidth for each pulse in the sequence, so that the spins excited by the initial pulse are effectively refocused by the following pulses [82].

In Fig. 5.7c we plot the integrated echo signal obtained from the demodulated quadratures $I(t)$ and $Q(t)$. The echo magnitude is calculated as $A(t) = \sqrt{I(t)^2 + Q(t)^2}$, and its area is defined as $A_{echo} = \int_{-T_e/2}^{+T_e/2} A(t)\,dt$. An example of a single trace of an echo from which we extract the integrated magnitude is presented in Fig. 5.8. For the most of spin echo experiments presented in this chapter we focus on the low-field transition at ~ 6.78 mT, which corresponds to the $|F, m_F\rangle = |4, -4\rangle \rightarrow |5, -5\rangle$ transition (see Sec. 2.5.1).

To calibrate the optimal length and power of pulses a Rabi oscillation experiment is performed [99]. The refocusing π pulse power in the CPMG sequence is swept and the integrated echo magnitude recorded, resulting in the damped oscillations presented in Fig. 5.9. The maximum of this plot occurs when the refocusing pulse nominally performs a π rotation of the spin ensemble magnetization, indicating the correct powers to use in our experiments.

Next we perform an inversion recovery experiment to measure the longitudinal spin relaxation time T_1. This relaxation time dictates how long we must wait between sequences when repeating measurements, the so-called repetition time T_{rep}. We first apply a π pulse, called inversion pulse, to invert the magnetization of spin ensemble as

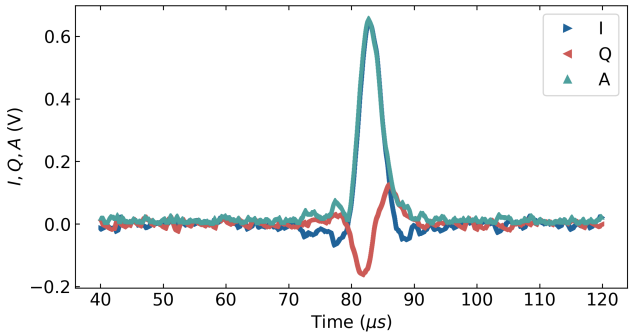

Figure 5.8: Spin echo signal in time domain. Averaged quadratures $I(t)$ and $Q(t)$ are shown in blue and red, respectively. Echoes were digitally rotated in the IQ-plane to maximize the echo's alignment along I. The echo magnitude $A(t)$ is presented in green. The duration of the echo is approximately $T_e = 8$ μs.

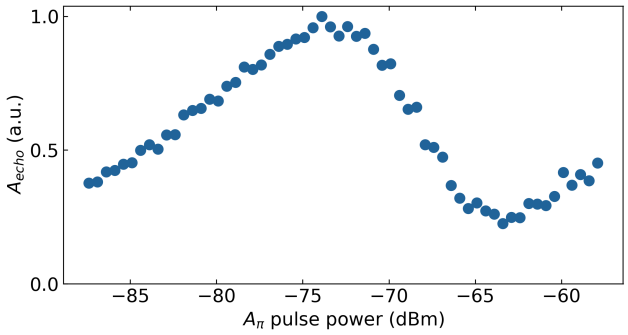

Figure 5.9: Rabi oscillations measured by sweeping the amplitude of the refocusing π pulse in the CPMG sequence.

explained in Sec. 3.6.4. Next we pause for a period T_{wait} before performing a CPMG pulse sequence to probe the spins magnetization. The duration of the pulses are the same for both the $\pi/2$ and π rotations $t_p = 10$ μs and the waiting time between pulses is $\tau = 75$ μs. This CPMG sequence consists of $N = 200$ π pulses and is averaged 3 times with repetition time $T_{rep} = 30$ s to allow for full relaxation of spins. We show the result of this experiment for different T_{wait} times in Fig. 5.10. The characteristic time of the exponential decay is T_1, which we find here to be $T_1 = 600$ ms. Thus, to allow full relaxation of the spins between measurements, the wait time between pulse sequences should be sufficiently larger than T_1. Often in hybrid systems employing high quality factor superconducting cavities, this T_1 time can be limited by Purcell relaxation [48]. We investigate the spins longitudinal relaxation mechanisms further in Sec. 6.4.3 of the next chapter.

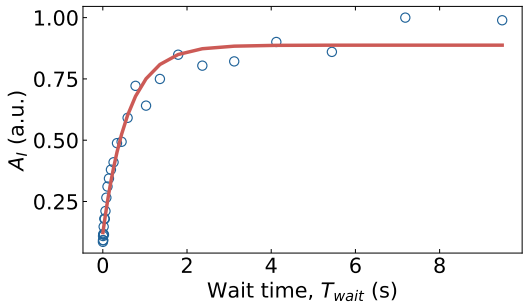

Figure 5.10: Measurement of the longitudinal relaxation time of the electron spins with an inversion recovery experiment. An exponential fit to the normalised integrated quadrature I signal A_I allows us to extract a $T_1 = 600$ ms.

We measure the transverse relaxation time T_2 using the CPMG dynamical decoupling sequence (see Sec. 3.6.3). Here we perform an echo decay measurement by adding pulses to the CPMG sequence with a fixed inter-pulse delay $2\tau = 240$ μs, plotting the integrated echo amplitude as a function of the pulse number N (see Fig. 5.11a). We managed to detect up to 500 echoes in this experiment and each echo was averaged 200 times. The repetition time of the sequence was $T_{rep} = 5$ s. We fit the resulting decay to the function $A_{echo}(t) = \exp\left(-(2\tau N/T_2)^{\beta}\right)$ and find $T_2 = 14$ ms (see Fig. 5.11b). This exceptionally long T_2 is permitted by the ^{28}Si isotope enrichment of the silicon chip and shows the great promise of donors in silicon for quantum information processing applications.

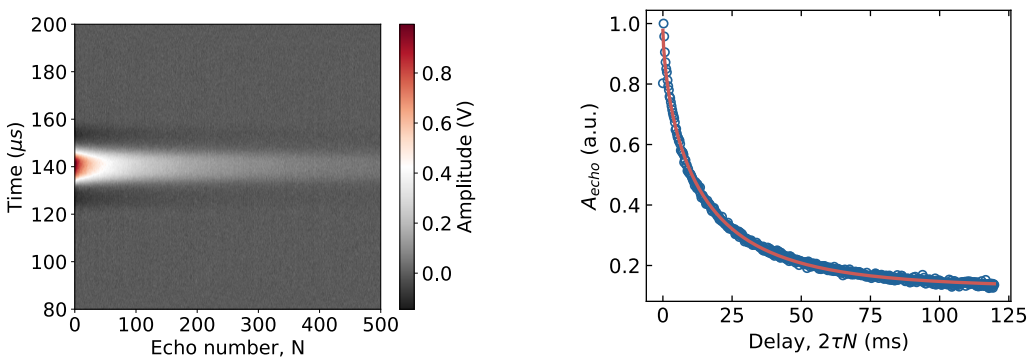

(a) (b)

Figure 5.11: Measurement of transverse relaxation time T_2 of the electron spins using a CPMG pulse sequence. **a)** Single quadrature echo amplitude $I(t)$ decay with increasing pulse number N. **b)** The decay of the integrated echo amplitude as a function of the total free precession time after the initial $\pi/2$ pulse. This decay is fit to the function $A_{echo}(t) = \exp\left(-(2\tau N/T_2)^{\beta}\right)$ allowing us extract $T_2 = 14$ ms.

5.4 Parametric amplification of spin echoes

So far we have simply employed the KIPA as a superconducting cavity to deliver control pulses to the spin ensemble and inductively detect their emitted spin echoes. We now introduce a DC-bias current to the superconducting cavity $I_{DC} = 3.3$ mA, which allows us to amplify the echo signals with a pump tone through the process of 3WM.

We first characterise the parametric gain of the KIPA with a VNA measurement. The pump is routed to the device via a fast microwave switch (allowing us to operate the pump in pulsed mode, if required), attenuators, a bandpass filter and finally a diplexer (DPX1114, Marki Microwave Inc.) that combines the pump with the other tones. In the device the DC current (I_{DC}), strong microwave pump (ω_p) and signal (ω_0) are all mixed to produce parametric amplification (see Ch. 4). The pump tone is generated by an independent low phase noise microwave source (E8267D, Keysight Technologies) – see setup schematics in Figs. 3.18 and 3.20.

Despite the device reported in this chapter having a slightly different design to the one measured in Ch. 4, they both operate as phase sensitive parametric amplifiers that work on the principle of 3WM. In Fig. 5.12a we present the reflection measurements of the KIPA when the pump tone is off and the signal power at the device input is $P_0 = -137.9$ dBm. The fitting routine indicates that the device operates close to the critical coupling regime, with an internal quality factor $Q_i = 31.5 \cdot 10^3$ and external quality factor $Q_c = 39.1 \cdot 10^3$. Application of the pump tone with frequency $\omega_p \approx 2\omega_0$, where $\Delta\omega = \omega_0 - \omega_p/2 < \kappa$ i.e. half of the pump frequency lies within the resonator bandwidth ($\Delta\omega$ exceeds the VNA bandwidth) results in non-degenerate (phase-insensitive) parametric amplification. A measurement of the KIPA gain curve when operating in the non-degenerate mode is shown in Fig. 5.12a (red data points). When $\omega_p = 2\omega_0$ the KIPA works as a phase-sensitive amplifier, producing degenerate gain. The degenerate amplification is studied as a function of the pump power and reveals a maximum gain (found by sweeping the pump phase) as large as 30 dB, as shown in Fig. 5.12b.

Next we combine amplification with the pulsed spin experiments by introducing the pump for a duration that overlaps with the time window where we expect a spin echo to form. The LO and the pump source are phase-locked since we operate the KIPA in phase sensitive/degenerate mode. Whilst performing non-degenerate amplification of the spin echo signal is possible, the existence of the idler mode complicates the

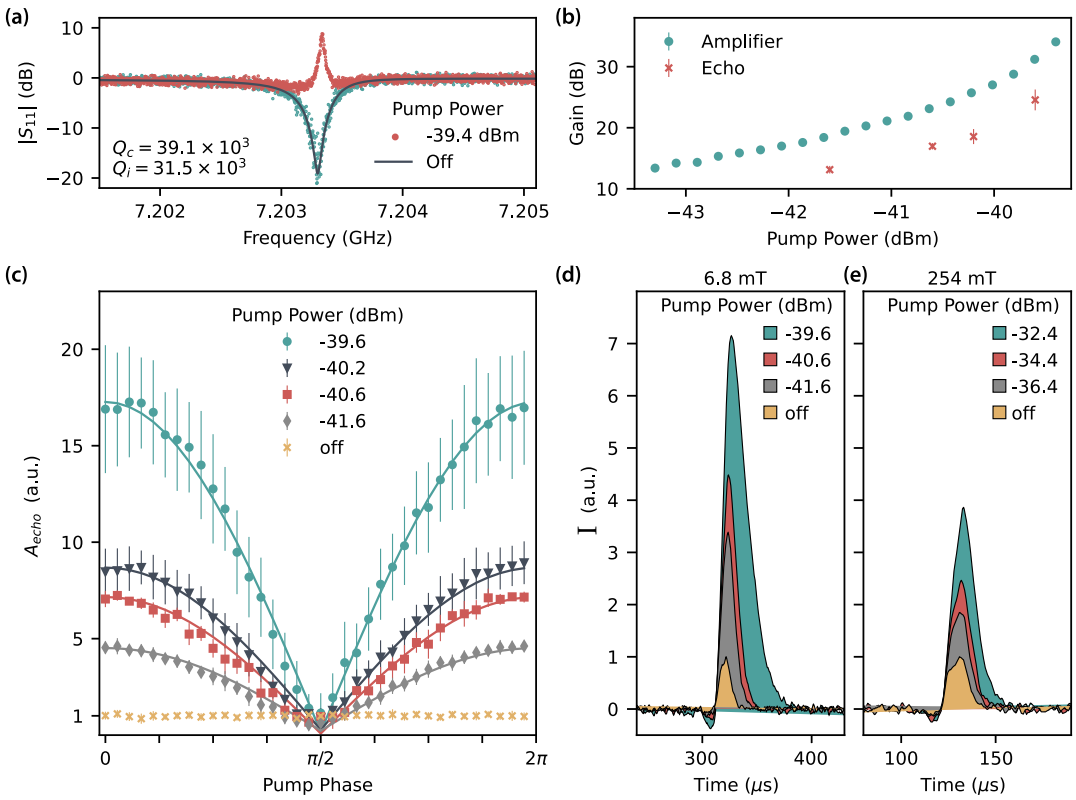

Figure 5.12: **a)** Reflection measurement of the resonator (KIPA) without the pump tone (green) and with the pump tone (red). The data was recorded with a VNA. **b)** Gain produced by the KIPA in the degenerate mode of amplification (green) as well as the power gain (SNR improvement) of the spin echo signals with amplification as a function of the pump power. **c)** Pump phase dependence of the amplified spin echo signals. The traces are adjusted to align the maximum integrated echoes at $\phi_p = 0$ rad. At each phase the amplified integrated echo magnitude is measured 210 times and the mean is recorded. The error bars correspond to the standard deviation of the repetitions. The data has been normalized so that the spin echo signal measured without parametric amplification (yellow) is equal to unity. The solid lines serve as guides to the eye and do not represent fits. **d)** Averaged spin echo amplitudes in the time domain as a function of pump power at $\phi_p = 0$ rad (maximum gain). The measurement was performed at 6.78 mT. **e)** Averaged spin echo amplitude in time domain as a function of pump power at $\phi_p = 0$ rad. The measurement was performed at 254 mT.

resulting demodulated signal. The idler should be filtered out, however, to do that we require the signal bandwidth to be significantly smaller than the cavity bandwidth (since both the signal and idler need to be supported within the cavity resonance), which is not the case here where both bandwidths are approximately equal. Exploiting

phase-sensitive amplification means we do not need to worry about filtering the idler tone, which combines with the signal constructively to provide an extra 6 dB of power gain relative to phase insensitive operation.

In the following experiments we utilize a Hahn echo pulse sequence to investigate the spin echo amplification. The duration of both pulses is fixed at $t_p = 10$ μs, which provides an excitation bandwidth ($\propto 1/t_p$) slightly smaller than the cavity linewidth ($\kappa = \omega_0/Q$). This ensures that the resulting spectral content of the signal is contained within the degenerate amplification bandwidth. The pulse amplitudes are set to -83.9 dBm and -80.9 dBm at the device input for the $\pi/2$ and π pulses, respectively, whilst the free evolution period between the pulses is $\tau = 300\mu$s. We repeat the pulse sequence at a rate of 1 Hz, which is close to the reported relaxation rate $1/T_1$ in order to speed up the collection of samples. This results in a residual magnetization of the spins after each pulse sequence (i.e. saturation). The echo sequence and repetition rate is kept constant throughout our experiments so that all measurements are saturated equally.

The pump tone (which is gated with a microwave switch) is sent to the KIPA 50 μs after the refocusing pulse and left on for 500 μs to overlap with and amplify the echo signal. We plot the integrated parametrically amplified echo signal as a function of the pump tone phase in Fig. 5.12c. The integrated echo magnitudes in this plot have the background noise subtracted, a process achieved in two steps. First, we perform the Hahn echo pulse sequence with the pump on around the time of echo emission. We then repeat the exact same pulse sequence with the refocusing pulse amplitude set to zero (blank pulse sequence), which does not produce any echo and only the noise is amplified. The reported amplified echo signals are obtained by taking the difference of the integrated data from both measurements. We present some examples of the time domain spin echoes measured at 6.78 mT as a function of the pump power in Fig. 5.12d.

In Fig. 5.12b we plot the maximum integrated echo gain from the measurements in Fig. 5.12c, along with the measured degenerate KIPA gain found by sending down a continuous wave signal with the spins detuned from the resonator frequency. We observe qualitative agreement between the two measurements. The echo gain is smaller than the degenerate gain measured with a continuous signal by ~ 6 dB, which is likely due to the wider spectral bandwidth of the echoes which sample a broader range of the gain curve (Fig. 5.12a), whilst the continuous tone experiences the maximum possible gain. The single shot power SNR enhancement of the spin echo signal as a function of

degenerate power gain is presented in Fig. 5.13a and calculated as:

$$\text{SNR improvement} = 20\log_{10}\left(\frac{\text{SNR}_{on}}{\text{SNR}_{off}}\right) \tag{5.3}$$

where

$$\text{SNR}_{on,off} = \frac{A_{echo} - A_{blank}}{A_{blank}} \tag{5.4}$$

is the SNR of the echo signal when the pump tone is delivered to the cavity (SNR_{on}) and when the pump tone is off (SNR_{off}). A_{blank} represents the integrated noise produced by blank pulse sequence. In this plot the KIPA gain is interpolated from the data in Fig. 5.12b. We achieve up to 25 dB improvement in the power SNR of the detected echo and the linear dependence of the data again confirms the qualitative agreement. We note that the 25 dB enhancement in the power SNR, which corresponds to a linear amplitude SNR improvement of 17.8, is several factors greater than what has been achieved in other quantum-limited ESR spectrometers [31], [168], despite this work being performed at a higher temperature (400 mK compared to 20 mK) and with the parametric amplifier placed in a magnetic field.

To test our parametric amplifier at even higher magnetic fields that are more typical for conventional ESR experiments (i.e. at X-band frequencies corresponding to $B_0 \approx 0.34$ T for a $g = 2$ spin) we operate on the $|F, m_F\rangle = |4, -3\rangle \rightarrow |5, -2\rangle$ bismuth spin transition, which is at $B_0 = 254$ mT for our resonator. At this magnetic field the internal quality factor of the resonator reduces to $Q_{int} \approx 20 \cdot 10^3$, however, amplification is still possible. Fig. 5.12e depicts the parametrically-amplified spin echoes for different pump powers obtained at $B_0 = 254$ mT. We report an amplitude magnification by up to four times, with an equivalent increase in the SNR. Achieving echo amplification in such a large magnetic field is an outstanding outcome and demonstrates the robustness of the KIPA and the realistic application of this technology to ESR spectroscopy.

Finally, to test the bandwidth of the KIPA we sweep the length of both pulses simultaneously (and therefore their spectral properties) at different values of the pump power (see Fig. 5.13b). We find that the linear echo gain saturates at smaller pulse lengths for the lower pump power measurement, since the reduced gain provides a larger amplifier bandwidth due to the fixed gain-bandwidth-product of the KIPA [74]. The data presented in Fig. 5.13b has been digitally low-pass filtered with a 500 kHz cutoff frequency, greater than the bandwidth of the shortest pulses used in the measurement.

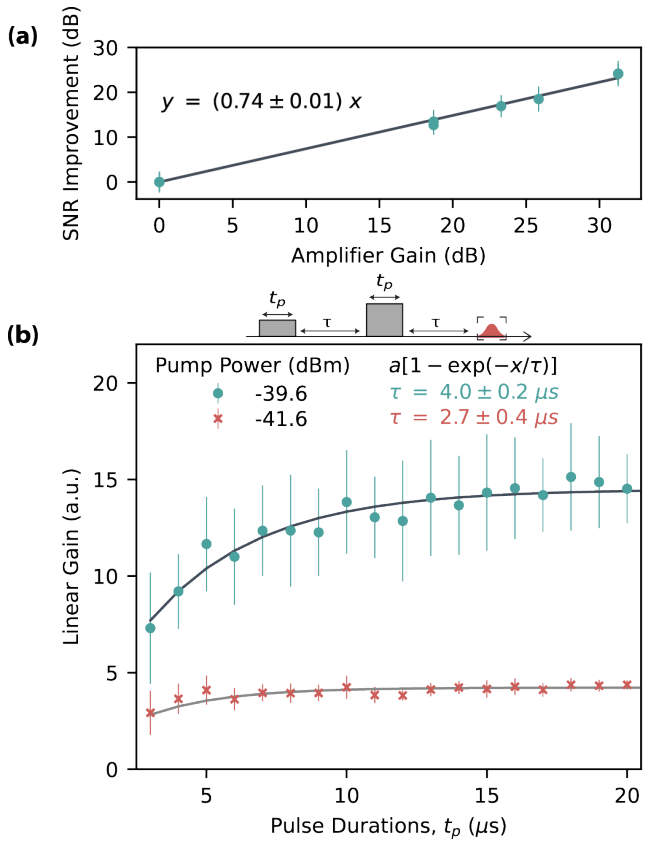

Figure 5.13: **a)** Power SNR enhancement of the spin echo signal as a function of the degenerate KIPA gain. **b)** Linear spin echo gain as a function of the π and $\pi/2$ pulse duration. Measurements are performed at $B_0 = 6.78$ mT for two different pump powers and hence KIPA gains.

5.5 Conclusions

We have demonstrated that a simple and versatile amplifier, the KIPA, can be used as a microwave cavity to inductively detect spin echoes and simultaneously act as a first-stage low-noise parametric amplifier. We report a 17.8 times improvement in the SNR of spin echo amplitude – a considerable enhancement that reduces measurement times by more than a factor of 300. Moreover, the KIPA is suitable to operate in large magnetic fields compatible with conventional ESR, tested here up to ~ 250 mT.

Improvement of the internal quality factor in future designs of the KIPA and better alignment of the chip inside the magnetic field could extend its use to even higher magnetic fields.

Chapter 6

Parametric spin cooling

In this chapter we present a scheme that enables parametric spin cooling in a cQED device. Our spin cooling proposal is supported with some preliminary experimental results.

6.1 Motivation

In this chapter we focus on a particular technique for improving sensitivity in ESR spectroscopy that is based on the enhancement of spin polarization.

The amplitude of a spin echo signal is proportional to the spin polarization, which for an ensemble of electron spins with $S = 1/2$ is simply defined as the difference between the number of spins in the ground $N_\uparrow$ and excited $N_\downarrow$ states [99]:

$$\Delta N = N_\uparrow - N_\downarrow \tag{6.1}$$

The thermal spin population is governed by the Boltzmann distribution (Eq. 2.75), allowing us to write the polarization in terms of the total number of spins $N = N_\uparrow + N_\downarrow$ in the following form [100]:

$$\Delta N = Np = N \tanh\left(\frac{\hbar\omega_s}{2k_B T_s}\right) \tag{6.2}$$

where ω_s is the spin Larmor frequency, T_s represents the spin temperature and k_B is the Boltzmann constant. Thus, to enhance the spin polarization, one must either increase ω_s or decrease T_s. Increasing ω_s by raising the magnetic field B_0 is not a viable strategy when performing ESR with superconducting resonators, due to the losses experienced by the resonators at high field. We therefore focus on methods to reduce the effective spin temperature T_s.

A novel technique for cooling spins using a high-Q superconducting resonator was recently demonstrated in Ref. [39]. In this experiment they utilize a lithographically defined superconducting niobium micro-resonator resonator fabricated on a silicon chip with implanted bismuth donors, which provides the ensemble of electrons spins to be cooled. There the spins are coupled to two relevant reservoirs, phonons in the host silicon lattice with temperature T_{phon}, and photons in the electromagnetic mode of the resonator with a temperature T_{phot}. The equilibrium temperature of the spins is determined by the rate at which the spin system spontaneously emits quanta of energy $\hbar\omega_s$ to each bath [39] and the individual bath temperatures.

In standard magnetic resonance experiments the rate of the phonon-mediated spin relaxation Γ_{phon} is many orders of magnitude larger than the photon-based (or radiative) relaxation process occurring at a rate Γ_{phot} [48]. As a result, the spin temperature is set by the temperature of the phonons in the host lattice T_{phon} [99].

The Purcell effect (Sec. 2.4.2) provides a way to significantly enhance the rate of

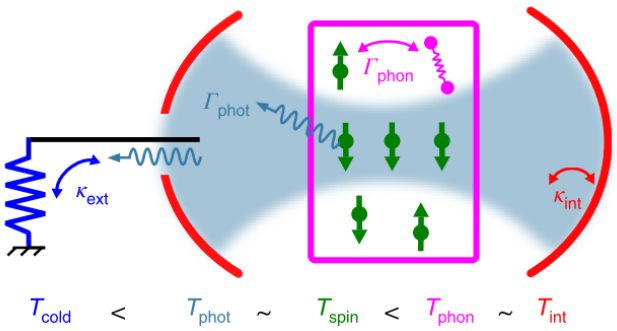

Figure 6.1: Radiative spin cooling scheme. Image taken from Ref. [39].

radiative electron spin relaxation through the use of microwave resonators [48], [111]. The Purcell-enhanced relaxation rate of a spin (frequency ω_s) coupled to a resonator (frequency $\omega_r = \omega_s$) with an interaction strength g_{0s} is $\Gamma_{phot} = 4g_{0s}^2/\kappa$ (see Eq. 2.95), where $\kappa = \kappa_{int} + \kappa_{ext}$ is the total decay rate of the resonator, including internal losses (κ_{int}) and any coupling to external transmission lines (κ_{ext}). For $\Gamma_{phot} \gg \Gamma_{phon}$, we enter the so-called Purcell regime, where the spins thermalize via photon (rather than phonon) emission, with the relevant temperature being that of the electromagnetic field T_{phot}.

The Purcell regime was reached in the experiment reported in Ref. [39]. By cooling the microwave field, the effective bismuth spin ensemble temperature could be lowered below that of the chip (i.e. the phonon temperature). Fig. 6.1 presents a simplified schematic of the scheme followed in the experiment. The spins (green) are pictured inside the silicon crystal (magenta) and coupled to the high-Q superconducting cavity (red). The resonator is operated in the over-coupled regime ($\kappa_{ext} \gg \kappa_{int}$, where microwave photons in the mode are lost to the external transmission line. In this regime the resonator mode is thermalized to the electromagnetic field in the transmission line, as opposed to the various loss mechanisms inside the device (such as two-level systems) which have a temperature T_{phon}. A low loss superconducting NbTi coaxial cable connects the resonator external port to a 50 Ω load at a lower temperature ($T_{cold} = 20$ mK) than the chip ($T_{hot} = 850$ mK). In the absence of any loss between the resonator and the load, the temperature of the mode would become T_{cold}, despite the resonator being operated at the much warmer T_{hot}. Since the spins are in the Purcell regime, they thermalize to T_{cold}. Unavoidable loss of the microwave components used to connect the load and resonator (a circulator, directional coupler and a switch) meant that the temperature of the mode only reached a value of $T_{cold} = 500$ mK. Nevertheless, the authors

were able to observe an approximate doubling of the spin polarization (detected as an increase in the echo amplitude) when the resonator was connected to the cold load.

For this scheme to work we require $\kappa_{ext} \gg \kappa_{int}$, which is challenging provided the superconducting resonator must be placed in a magnetic field. Furthermore, this idea is only able to cool the spins to the lowest temperature available in the measurement system. Inspired by this impressive experiment, here we propose a new scheme to hyper-polarize an ensemble of electron spins and cool them to arbitrarily low temperatures. This scheme utilizes parametric processes facilitated by our nonlinear multimode circuit resonator and should even work in the under-coupled regime where $\kappa_{ext} < \kappa_{int}$. Through the application of a parametric drive, we show that we can couple the fundamental mode of our PBG resonator (to which the spins are coupled) to a higher frequency harmonic. This parametric coupling can be used to cool the fundamental mode and therefore the spins. Below we present a theoretical framework to understand and model this multimode parametric cooling idea.

6.2 Proposal

6.2.1 System Hamiltonian

The nonlinear NbTiN photonic bandgap (PBG) resonators (described in Ch. 3) support multiple modes that satisfy the open/short boundary conditions at either end of the resonant section (Sec. 2.1.3). We consider here the lowest two modes only; i.e. the fundamental mode and the first harmonic, though in-principle this scheme could extend to any modes supported. The kinetic inductance of the resonator (Eq. 2.57) depends on the total current flowing through it, including contributions from the various modes. The vacuum current fluctuations in the fundamental mode will modify the kinetic inductance seen by the first harmonic (and vice-versa) and therefore its resonance frequency, providing a means to couple the two modes together.

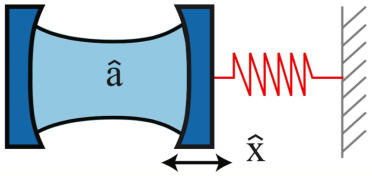

Figure 6.2: Optomechanical coupling scheme. An optical Fabry-Perot cavity has one movable mirror that forms part of a mechanical system. Image taken from Ref. [181].

This coupling mechanism resembles the one commonly employed in optomechanical systems, where an optical cavity is coupled to a mechanical resonator with vastly different natural oscillation frequencies [182]. The optical cavity is formed by two reflective mirrors, one mirror is fixed whilst the other is attached to a spring, thus forming a mechanical resonator. Such an optomechanical system is schematically depicted in Fig. 6.2. Displacements of the mechanical system (with annihilation operator $\hat{x}$) change the length of the optical cavity ($\hat{a}$) and modify its frequency, inducing a "parametric" coupling between the optical and mechanical modes. The Hamiltonian that describes this interaction between two quantum harmonic oscillators with frequencies ω_a and ω_b is written as [183]:

$$\hat{H} = \hbar\omega_a \hat{a}^\dagger \hat{a} + \hbar\omega_b \hat{b}^\dagger \hat{b} - \hbar g_0 \hat{a}^\dagger \hat{a}(\hat{b} + \hat{b}^\dagger) \tag{6.3}$$

where g_0 is the single photon coupling strength between two modes. The first term in Eq. 6.3 represents the energy of the harmonic "a", the second term describes the energy of the fundamental mode "b" and the last term is their nonlinear coupling induced by the field of "b". This standard optomechanical Hamiltonian is derived assuming $\omega_a >> \omega_b$ to ensure that the field in cavity "a" adiabatically adjusts to the parametrically modulated resonance frequency caused by the dynamics of cavity "b" [184]. This approximation is valid for optomechanical systems where the frequency of mechanical oscillator is many orders of magnitude smaller than the frequency of optical cavity. In the case of our multimode $\lambda/4$ microwave resonator with fundamental mode frequency $\omega_b/2\pi \approx 7.2$ GHz and first harmonic $\omega_a \approx 3\omega_b$ this approximation is not strictly valid. Nevertheless, we find our experimental results to be in good agreement with the theoretical predictions of this Hamiltonian. Future work is focused on deriving a first-principles microscopic Hamiltonian of our current-biased kinetic inductance resonator for a more rigorous description of the parametric inter-mode coupling.

Expanding on the analogy with an optomechanical system, the change in energy imparted on the first harmonic through the kinetic inductance shared with the fundamental mode is:

$$\Delta E_k = \frac{\Delta L_k(\mathcal{I}_b)}{2} \mathcal{I}_a^2 \tag{6.4}$$

with $\Delta L_k(\mathcal{I}_b)$ the change in kinetic inductance seen by mode "a" due to the zero-point fluctuations in mode "b". We note that although the spatial distributions of the two modes are orthogonal by definition, the mode currents enter in Eq. 6.4 as squares, and thus lead to a non-zero spatial overlap and an energy shift. The kinetic inductance shift has a quadratic dependence (Eq. 2.57) on the current in the fundamental mode

$\Delta L_k(\mathcal{I}_b) \propto \mathcal{I}_b^2$, which itself can be written in a form identical to the displacement operator for a mechanical resonator $\mathcal{I}_b \propto (\hat{b}+\hat{b}^\dagger)$ (see Eq. 2.14). Rewriting $\mathcal{I}_a^2 \propto (\hat{a}+\hat{a}^\dagger)^2$ and keeping only the energy-conserving terms, we find $\Delta E_k \propto \hat{a}^\dagger\hat{a}(\hat{b}+\hat{b}^\dagger)^2$. This is not the standard form of the optomechanical coupling [182], being quadratic instead of linear in the "displacement" operator $(\hat{b}+\hat{b}^\dagger)$. By introducing a DC current bias (in a similar vein to Eq. 4.1), so that $\Delta L_k(\mathcal{I}_b + I_{DC}) \propto \mathcal{I}_b^2 + 2I_{DC}\mathcal{I}_b + I_{DC}^2$, we recover the standard optomechanical coupling through the linear term $2I_{DC}\mathcal{I}_b$. Phenomenologically, the single photon coupling strength between the resonator modes can be expressed as:

$$g_0 = -\delta I_b \left| \frac{\partial \omega_a}{\partial I} \right|_{I_{DC}} \tag{6.5}$$

where δI_b is the zero-point current fluctuations of mode "b" (see Eq. 2.15) and $\partial\omega_a/\partial I$ is the shift in frequency of mode "a" due to current at the frequency of mode "b" with a DC bias I_{DC} applied. A future first-principles Hamiltonian of the DC-biased kinetic inductance resonator should, for example, be able to relate $\partial\omega_a/\partial I$ to macroscopic system parameters such as $Z_{a(b)}$ (the mode impedances), $I_{2a(2b)}$ (characteristic current nonlinearity strengths for the modes) and $\omega_{a(b)}$.

Our previous measurements indicate mode frequency resonance shifts of order 100 MHz for applied DC currents of several milliamps (Fig. 5.3). Together with our estimation for the zero-point current fluctuations $\delta I_b = \omega_b\sqrt{\hbar/2Z_b} \approx 20$ nA, we expect very small single photon coupling strengths, well within the weak coupling regime where $g_0 \ll \kappa_a, \kappa_b$. In optomechanics, one method to boost the mode coupling is to apply a strong pump tone (often called a drive) to mode "a" at the difference frequency of the two modes. Following Ref. [184], we introduce to the Hamiltonian a drive field with frequency ω_p and amplitude ϵ_a:

$$\hat{H} = \hbar\omega_a\hat{a}^\dagger\hat{a} + \hbar\omega_b\hat{b}^\dagger\hat{b} - \hbar g_0\hat{a}^\dagger\hat{a}(\hat{b}+\hat{b}^\dagger) + \hbar(\epsilon_a\hat{a}e^{-i\omega_p t} + \epsilon_a^*\hat{a}^\dagger e^{i\omega_p t}) \tag{6.6}$$

By entering a frame rotating at the drive frequency, accomplished with the unitary transformation $\hat{U} = e^{i\omega_p\hat{a}^\dagger\hat{a}t}$ ($\hat{H} \to \hat{U}\hat{H}\hat{U}^\dagger - i\hbar\hat{U}\partial\hat{U}^\dagger/\partial t$), we remove the time dependence from the driving terms:

$$\hat{H} = \hbar\Delta_a\hat{a}^\dagger\hat{a} + \hbar\omega_b\hat{b}^\dagger\hat{b} - \hbar g_0\hat{a}^\dagger\hat{a}(\hat{b}+\hat{b}^\dagger) + \hbar(\epsilon_a\hat{a} + \epsilon_a^*\hat{a}^\dagger) \tag{6.7}$$

where $\Delta_a = \omega_a - \omega_p$. It is common in optomechanics at this point to introduce the so-called linearized approximation [182] where we split the cavity field $\hat{a}$ into two

components, the average coherent amplitude $\langle \hat{a} \rangle = \alpha$ and a fluctuating term $\delta\hat{a}$:

$$\hat{a} = \alpha + \delta\hat{a} \tag{6.8}$$

This is equivalent to performing a unitary displacement transformation $D(\alpha) = e^{\alpha\hat{a}^\dagger - \alpha^*\hat{a}}$ with $\alpha = \epsilon_a/\Delta_a$ [184]. Applying the approximation 6.8 to the interaction part of the Hamiltonian (Eq. 6.7), we find:

$$\hat{H}_{int} = -\hbar g_0 \hat{a}^\dagger \hat{a}(\hat{b} + \hat{b}^\dagger) = -\hbar g_0 (\alpha + \delta\hat{a})^\dagger (\alpha + \delta\hat{a})(\hat{b} + \hat{b}^\dagger) \tag{6.9}$$

After expanding the interaction Hamiltonian in powers of α we omit the term $\hbar g_0 \delta\hat{a}^\dagger \delta\hat{a}$, which is much smaller than the terms proportional to the large drive α. The interaction Hamiltonian then becomes:

$$\hat{H}_{int} = -\hbar g_0 (\alpha^* \delta\hat{a} + \alpha \delta\hat{a}^\dagger)(\hat{b} + \hat{b}^\dagger) - \hbar g_0 |\alpha|^2 (\hat{b} + \hat{b}^\dagger) \tag{6.10}$$

The term proportional to $|\alpha|^2$ can additionally be dropped after implementing another displacement transformation [182], as it simply represents an average radiation-pressure force, or in our case a shift of the current origin. Without loss of generality we assume a real-valued drive amplitude $\alpha^* = \alpha$ so that the linearized interaction Hamiltonian is written:

$$\hat{H}_{int} = -\hbar g_0 (\alpha^* \delta\hat{a} + \alpha \delta\hat{a}^\dagger)(\hat{b} + \hat{b}^\dagger) = -\hbar g_0 \alpha (\delta\hat{a}^\dagger + \delta\hat{a})(\hat{b} + \hat{b}^\dagger) \tag{6.11}$$

Here the effective coupling between modes is now proportional to the drive amplitude $g = g_0\alpha$, providing us with an experimental knob to enhance the coupling strength.

In the case of a "red-detuned" drive, where $\Delta_a = \omega_b$ (or $\omega_p = \omega_a - \omega_b$), in the rotating frame we have two harmonic oscillators of equal frequency that can resonantly interchange quanta. Applying the RWA (see Sec. 2.4) to Eq. 6.11 with a red-detuned drive, we arrive at the "beam-splitter" interaction Hamiltonian in quantum optics:

$$\hat{H}_{int} = -\hbar g (\delta\hat{a}^\dagger \hat{b} + \delta\hat{a}\hat{b}^\dagger) \tag{6.12}$$

This resonant interaction can be intuitively understood based on energy conservation. A photon from the low frequency mode ω_b is up-converted to the high frequency mode ω_a by absorbing one photon from the drive field $\omega_p = \omega_a - \omega_b$. At the same

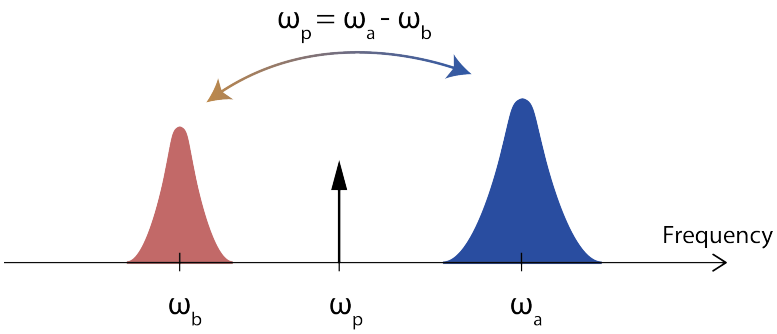

Figure 6.3: Illustration of the coherent photon exchange between two coupled cavity modes ω_a and ω_b, mediated by a pump tone ω_p.

time, a high frequency photon can be down-converted by emitting a photon at ω_p. The diagram of this interaction is illustrated in Fig. 6.3.

6.2.2 Input-output formalism

To describe the time evolution of the coupled mode fields, we apply the input-output formalism introduced in Sec. 2.1.7. We start by assuming the interaction Hamiltonian under the linearized approximation $\hat{H}_{int} = -\hbar g(\hat{a}^\dagger \hat{b} + \hat{a}\hat{b}^\dagger)$, with pump-enhanced coupling strength $g = g_0\alpha$. The quantum Langevin equations (Eq. 2.40) describing the dynamical evolution of the modes $\hat{a}$ and $\hat{b}$ in the rotating frame are then written as:

$$\dot{\hat{a}}(t) = -\frac{\kappa_a}{2}\hat{a}(t) - i\Delta_a\hat{a}(t) + ig\hat{b}(t) + \sqrt{\kappa_{a,ext}}\hat{a}_{in}(t) + \sqrt{\kappa_{a,int}}\hat{f}_{in}(t) \tag{6.13}$$

$$\dot{\hat{b}}(t) = -\frac{\kappa_b}{2}\hat{b}(t) - i\omega_b\hat{b}(t) + ig\hat{a}(t) \tag{6.14}$$

Here $\kappa_a = \kappa_{a,int} + \kappa_{a,ext}$ and κ_b are the total coupling rates to mode "a" and "b", respectively. A schematic illustration of the model described by these equation is shown in Fig. 6.4.

Mode "a" is driven by the field $\hat{a}_{in}$ in the external transmission line, coupled at a rate $\kappa_{a_{ext}}$. In the following experiments we measure mean values of the fields and therefore omit the noise fluctuations $\hat{f}_{in}$ in our Langevin equation, since $\langle\hat{f}_{in}\rangle = 0$. It is convenient to solve these equations in frequency domain by applying the Fourier

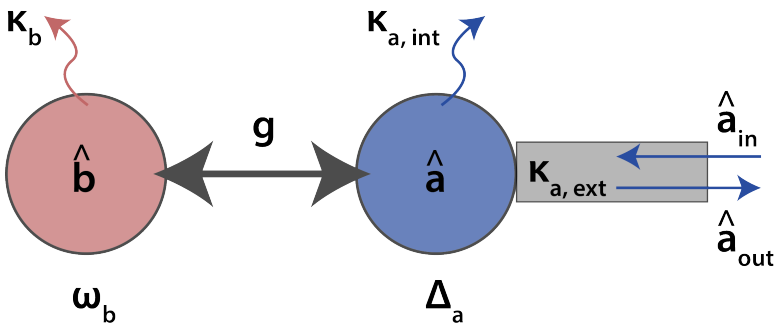

Figure 6.4: Input-output model for the coupled cavity modes in the rotating reference frame. The mode $\hat{a}$ is driven by $\hat{a}_{in}$ via the transmission line shown in gray.

transform (Eq. 2.44) to obtain:

$$-i\omega\hat{a}(\omega) = -\frac{\kappa_a}{2}\hat{a}(\omega) - i\Delta_a\hat{a}(\omega) + ig\hat{b}(\omega) + \sqrt{\kappa_{a,ext}}\hat{a}_{in}(\omega) \tag{6.15}$$

$$-i\omega\hat{b}(\omega) = -\frac{\kappa_b}{2}\hat{b}(\omega) - i\omega_b\hat{b}(\omega) + ig\hat{a}(\omega) \tag{6.16}$$

From Eq. 6.16 we can denote the field amplitude $\hat{b}(\omega)$ of the mode "b" as:

$$\hat{b}(\omega) = -\frac{g\hat{a}(\omega)}{\frac{i\kappa_b}{2} + \omega - \omega_b} \tag{6.17}$$

For a single port resonator the modes are fully characterized by the complex S_{11} scattering matrix parameter. Using the input/output identity $\hat{a}_{in} + \hat{a}_{out} = \sqrt{\kappa_{a,ext}}\hat{a}$ (see Eq. 2.41) S_{11} can be expressed as:

$$S_{11} = \frac{\langle\hat{a}_{out}\rangle}{\langle\hat{a}_{in}\rangle} = \frac{\sqrt{\kappa_{a,ext}}\langle\hat{a}\rangle - \langle\hat{a}_{in}\rangle}{\langle\hat{a}_{in}\rangle} \tag{6.18}$$

Substituting Eq. 6.17 into Eq. 6.15 and putting the resulting expression for $\hat{a}(\omega)$ into Eq. 6.18, we obtain:

$$S_{11} = \frac{-i\kappa_{a_{ext}}(\frac{i\kappa_b}{2} + \omega - \omega_b)}{g^2 - (\frac{i\kappa_b}{2} + \omega - \omega_b)(\frac{i\kappa_a}{2} + \omega - \Delta_a)} - 1 \tag{6.19}$$

To take us back to laboratory frame we make the substitution $\omega = \omega_{in} - \omega_p$, where ω_{in} is the frequency used to probe the resonator:

$$S_{11}(\omega_{in}) = \frac{-i\kappa_{a_{ext}}(\frac{i\kappa_b}{2} + \omega_{in} - \omega_p - \omega_b)}{g^2 - (\frac{i\kappa_b}{2} + \omega_{in} - \omega_p - \omega_b)(\frac{i\kappa_a}{2} + \omega_{in} - \omega_a)} - 1 \tag{6.20}$$

6.2.3 Parametric spin cooling requirements

Driving the nonlinear PBG resonator with a pump tone at frequency $\omega_p = \omega_a - \omega_b$ can induce a coherent exchange of photons between the coupled modes at ω_a and ω_b. Such a technique (referred to as sideband cooling in optomechanical systems [182]) allows for the reduction of thermal photons in the mode at ω_b. For an in-depth theoretical treatment of this cooling scheme we refer the reader to Refs. [185]–[187]. Ref. [188] reports the cooling of a mechanical system to its quantum mechanical ground state using this technique – a pioneering experimental demonstration of the power of parametric processed in QED systems.

When a photon from mode "b" is mixed with a pump photon at ω_p it can be up-converted to a single photon at $\omega_p + \omega_b$ (removing a photon from "b" in the process) or it can be down-converted into two photons with frequencies $\omega_p - \omega_b$ and ω_b (adding a photon to "b" in the process). By choosing $\omega_p = \omega_a - \omega_b$, we ensure that up-conversion is favored since the photon density of states at $\omega_p + \omega_b = \omega_a$ is enhanced by the resonant mode "a". The removal of photons from mode "b" leads to cooling. The rate of photon up-conversion Γ_- and down-conversion Γ_+ is given as [185], [188]:

$$\Gamma_\pm = \frac{4g^2\kappa_a}{\kappa_a^2 + 4(\Delta_a \pm \omega_b)^2} \tag{6.21}$$

The mode also undergoes transitions due to interactions with its thermal environment, coupled at the rate κ_b. Including both thermal bath and pump contributions we find the average number of photons $\langle n_b \rangle$ in mode "b" from the rate equation [182]:

$$\dot{\langle n_b \rangle} = (\langle n_b \rangle + 1)(\Gamma_+ + \Gamma_{+,th}) - \langle n_b \rangle(\Gamma_- + \Gamma_{-,th}) \tag{6.22}$$

where $\Gamma_{+,th} = \kappa_b \langle n_{b,th} \rangle$ is the rate at which thermal photons are removed from the mode, $\Gamma_{-,th} = \kappa_b(\langle n_{b,th} \rangle + 1)$ is the rate at which thermal photons are added to it and $\langle n_{b,th} \rangle$ is the average thermal occupation. The steady-state solution of Eq. 6.22 that further takes into account the non-zero photon occupancy of mode "a" $\langle n_a \rangle$ is [189]:

$$\langle n_b \rangle = \langle n_{b,th} \rangle \left(\frac{\kappa_b}{\kappa_a} \frac{4g^2 + \kappa_a^2}{4g^2 + \kappa_a \kappa_b} \right) + \langle n_a \rangle \left(\frac{4g^2}{4g^2 + \kappa_a \kappa_b} \right) \tag{6.23}$$

If mode "b" is not actively cooled (i.e. the pump tone is off), it has an average number of photons that tends to thermal equilibrium $\langle n_{b,th} \rangle$, as determined by the temperature of the resonator according to Eq. 2.32. On the other hand, when we drive at $\omega_p = \omega_a - \omega_b$ and activate photon up-conversion/cooling, the mode population can be lowered. From Eq. 6.23 it can be seen that the most efficient cooling occurs when $\kappa_a > g > \kappa_b$. In this regime photons from mode "b" are up-converted to mode "a", where they dissipate in the thermal bath at the higher frequency ω_a. This happens faster than the rate at which thermal photons at ω_b can repopulate "b", leading to cooling. In this regime the cooling rate is linear in g, which is controlled with the pump power. When we reach the strong-coupling regime $g > \kappa_a > \kappa_b$, the cooling becomes limited as the thermal photons Rabi oscillate between the modes. Eq. 6.23 places bounds on the achievable cooling: the first term cannot be smaller than $\langle n_{b,th} \rangle \kappa_b / \kappa_a$, whilst the second term (which arises from the photon population of mode "a") adds a contribution of approximately $\langle n_a \rangle$. As a result, the photon occupancy of mode "b" is always larger than the occupancy of photons in mode "a".

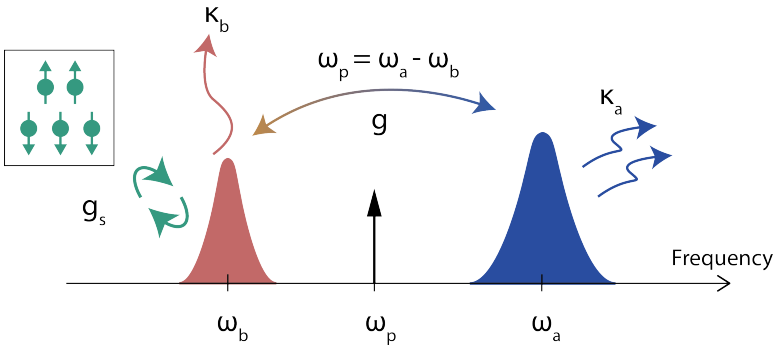

Figure 6.5: Illustration of the parametric spin cooling scheme implemented with coupled modes in a nonlinear resonator. Each electron spin in the ensemble is coupled to the mode at ω_b with a coupling strength g_s.

As shown in Ref. [39] and explained here in Sec. 6.1, the spins can thermalize to their electromagnetic environment if $\Gamma_{phot} \gg \Gamma_{phon}$, i.e. by entering the Purcell regime. If the spins are coupled to mode "b" in the Purcell regime, and the same mode is actively cooled as described above, then the effective spin temperature can be lowered. This parametric spin cooling scheme is depicted in Fig. 6.5. Since the harmonic to which mode "b" is coupled can, in-principle, be arbitrarily large in frequency, we can achieve very low spin temperatures, below that of the measurement system.

In the Purcell regime the thermal photon population $\langle n_{b,th} \rangle = 1/[\exp(\hbar\omega_b/k_B T) - 1]$

(Eq. 2.32) is related to the spin polarization $p = \tanh(\hbar\omega_b/2k_BT)$ (Eq. 6.2) via $p = 1/(2\langle n_{b,th}\rangle + 1)$ [39]. Applying the parametric drive will lower the average photon occupancy of mode "b" and reduce the effective spin temperature T, leading to an enhancement in the spin ensemble polarization of:

$$\eta = \frac{p_{on}}{p_{off}} = \frac{2\langle n_{b,th}\rangle + 1}{2\langle n_b\rangle + 1} \tag{6.24}$$

Here the spin polarization when the drive is on is denoted as p_{on} (with a photon population of $\langle n_b\rangle$) and p_{off} (with population $\langle n_{b,th}\rangle$) when it is off. This dynamic electron spin polarization technique is of broad use in ESR spectroscopy measurements as it provides a way to enhance SNR. Moreover, the only requirement for the spins is that they possess a magnetic moment that can be inductively coupled to the resonator, no specific level structure or ability to incorporate into a semiconductor lattice are assumed. This scheme will work for any $g_e \approx 2$ spin, as opposed to other methods for polarizing spin ensembles which use optical pumping techniques and rely on unique electronic level structures [190].

6.3 Implementation

The device used in the following proof-of-principle parametric cooling experiments is the same PBG quarter-wavelength design utilized in Ch. 5. Measurements were conducted in the ^{3}He cryogenic system at 400 mK using a slightly modified experimental setup to that shown in Sec. 3.4.1.

To characterize the first harmonic of the resonator at $3\omega_0 \approx 22$ GHz, the cryogenic circulator and low-noise HEMT amplifier must be removed from the detection chain, since they restrict the system bandwidth to frequencies between 3-10 GHz. The modified measurement setup is presented in Fig. 6.6.

The probe tone is generated by a VNA and routed to the resonator via a directional coupler "Pulsar CS10-56-436/20 1610" ($0.5 - 27$ GHz). The signal reflected from the device passes through the directional coupler and a diplexer before being sent out of the cryostat where it is then amplified and subsequently measured with the VNA. The high-pass frequency range of the diplexer has an upper cut-off of 8 GHz, however, we find that in practice signals at 22 GHz are transmitted with a small amount of

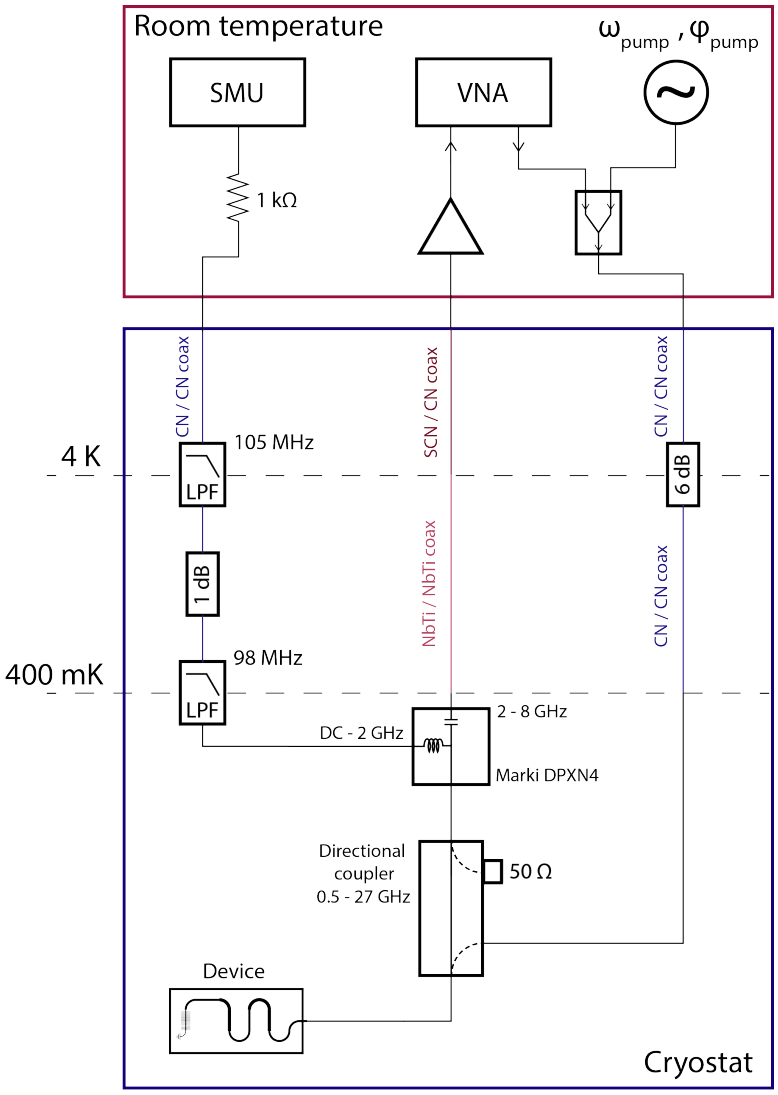

Figure 6.6: Experimental setup adapted for probing the first harmonic measurements of the resonator.

attenuation. We remove most of the fixed attenuators to compensate for the increase in line loss at $3\omega_0$ and because of the reduced measurement SNR without the cryogenic amplifier. The DC bias current is provided by a SMU configured as a voltage source and connected to the low frequency port of the diplexer through a 1 $k\Omega$ resistor. Finally, at room temperature we use a power combiner to add the strong pump tone (utilized for parametric mode coupling) with the probe signal from the VNA.

We note that this setup is only useful for characterizing both the fundamental and first harmonic modes of our PBG resonator in a single measurement. To study spin

cooling we do not require direct access to the first harmonic at $3\omega_0$ and the setup in Sec. 3.4.1 is preferred, since sufficient attenuation is critical to ensure that the photon population of the modes is not dominated by thermal noise of the higher temperature stages.

6.4 Experimental results

In this section we provide some initial experimental results towards the demonstration of parametric spin cooling, starting with a recap of the resonator fundamental mode characterization presented in Sec. 5.2.1. We then present measurements of the first harmonic mode and demonstrate a tunable inter-mode coupling through the application of a strong pump tone. At high drive powers we observe normal-mode splitting indicating that we reach the regime of strong coupling. Finally, we study the T_1 dynamics of a spin ensemble coupled to the resonator and discuss some technical hurdles that must be overcome to reach the Purcell regime.

6.4.1 Device characterization

Fundamental mode

The fundamental mode was observed at $\omega_0/2\pi = 7.233$ GHz with a zero DC current bias. The internal Q_{int} and external Q_{ext} quality factors were $2 \cdot 10^5$ and $3 \cdot 10^4$, respectively, yielding a linewidth of $\kappa \approx 280$ kHz (see Fig. 5.2). The frequency response of the fundamental mode to the current fluctuations can be derived from the fit shown in Fig. 5.3a. The fit is a simple polynomial with even powers of the current $\omega_0/2\pi = a + bI^2 + cI^4$. For the fundamental mode these coefficients are $a = 7.233$ (GHz), $b = -2.3712 \cdot 10^{-3}$ (GHz/mA^2) and $c = -8.84348 \cdot 10^{-6}$ (GHz/mA^4). The external quality factor Q_{ext} increased by a factor of two at the DC bias current of 4 mA, whilst the internal quality factor Q_{int} reduced by a factor of two in comparison to its value at zero DC current bias (see Fig. 5.3b).

First harmonic

The first harmonic was observed at $\omega_1/2\pi = 21.72$ GHz with a zero DC current bias. The fitting routine that allowed us to extract its resonance frequency is shown in Fig. 6.7.

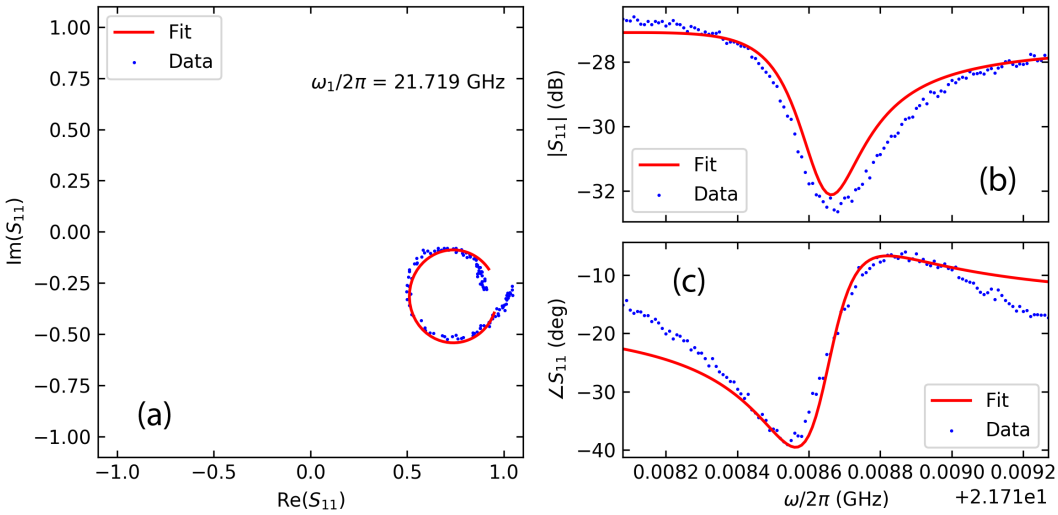

Figure 6.7: Fitting routine of the first harmonic. **a)** The resonant S_{11} forms a circle in a complex plane. **b)** The magnitude of the reflected signal as a function of frequency. The dip indicates absorption of the microwave power at the resonance frequency. **c)** The phase response of the complex S_{11} reflection.

Monitoring the resonator S_{11} response as a function of the applied DC current, we plot the frequency tunability of this mode in Fig. 6.8. As with the fundamental mode, its frequency tunability derives from the current dependence of the kinetic inductance, with the data fitting well to a biquadratic function $\omega_1 = a + bI^2 + cI^4$ where $a = 21.7187$ (GHz), $b = -8.8842 \cdot 10^{-3}$ (GHz/mA^2) and $c = -2.49 \cdot 10^{-5}$ (GHz/mA^4). Unfortunately, the large asymmetry in the S_{11} response of the first harmonic (see Fig. 6.7), possibly due to impedance mismatches in out-of-band components (like the diplexer) at this

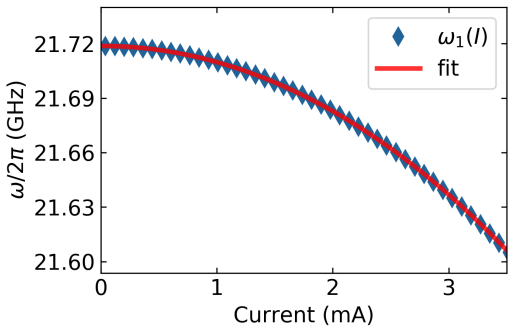

Figure 6.8: The current-dependence of the first harmonic resonance frequency. The frequency reduces as the current and consequently kinetic inductance increases.

frequency, meant that an accurate extraction of the quality factors wasn't possible.

6.4.2 Coupled modes

To enhance the coupling between the first harmonic and the fundamental mode of our quarter-wavelength PBG resonator we apply a strong parametric drive tone at their difference frequency, as proposed in Sec. 6.2. We first introduce a DC bias current of $I_{DC} = 3$ mA to enable an optomechanical coupling between the modes. The current shifts the fundamental mode to $\omega_0/2\pi = 7.20675$ GHz and the first harmonic to $\omega_1/2\pi = 21.6375$ GHz. We then perform S-parameter reflection measurements of the device centered about the two mode frequencies in the presence of strong pump tone. Fig. 6.9 shows the S_{11} measurements about each mode as the pump frequency ω_p is varied. When the pump frequency equals the difference frequency of the first harmonic and the fundamental mode, $\omega_p/2\pi = (\omega_1 - \omega_0)/2\pi \approx 14.43$ GHz, a hybridization of the modes occurs, indicating the onset of strong coupling. Another distinctive feature is observed at $\omega_p/2\pi \approx 14.4135$ GHz, exactly twice the fundamental mode frequency $\omega_0/\pi = 14.4135$ GHz, and corresponds to parametric amplification of the probe signal at ω_0. We studied this process in detail in Chs. 4 and 5.

In Fig. 6.9 the pump power was kept constant at $P_p = -45$ dBm at the device input. The probe signal power at the fundamental frequency was set to $P_s = -78$ dBm and $P_s = -60$ dBm at the first harmonic. A larger signal power is required to probe the first harmonic in order to compensate for the higher loss in the lines and microwave components at ω_1 compared to ω_0.

Next we study the coupling strength g between the modes as a function of the pump power with the pump frequency set precisely to the value $\omega_p = \omega_1 - \omega_0$. Fig. 6.10 shows reflection S-parameter measurements centered on the two modes, where the pump power is varied along the horizontal axis. The separation between the peaks defines the normal mode splitting $2g$. As the pump power is increased the normal-mode splitting (and therefore g) is observed to get larger (see Sec. 6.2).

To extract the important coupled-mode system parameters we fit the hybridized mode responses in the S_{11} measurements of Fig. 6.10 for the different pump powers using Eq. 6.20. In our model we considered a probe field applied to the first harmonic, however, here we measure the fundamental mode. We therefore exchange the role of the modes in our theoretical expression for S_{11} (Eq. 6.20). Sample reflection spectra of

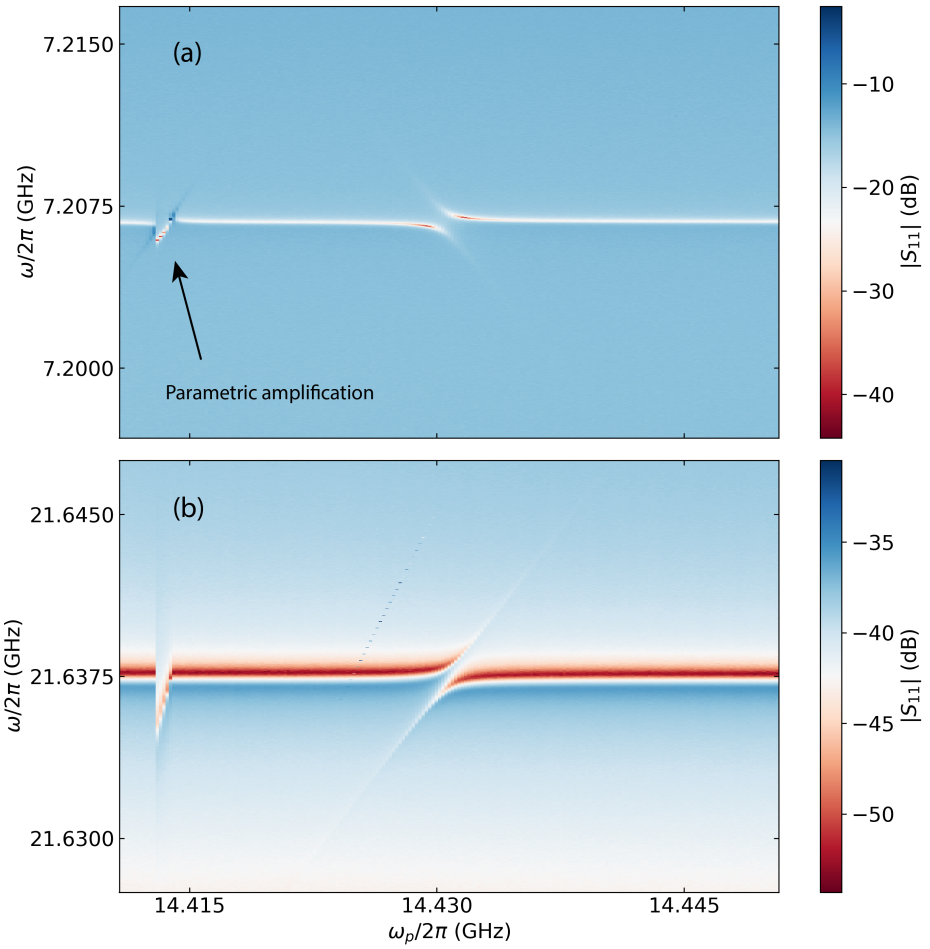

Figure 6.9: Mode response to a parametric pump tone with fixed power and varying frequency ω_p. Reflection measurements of the device centered on **a)** the fundamental mode and **b)** the first harmonic.

the fundamental mode at selected pump powers (along with their fits) are presented in Fig. 6.11. The relevant coupling rates (g, $\kappa_{b,int}$, $\kappa_{b,ext}$ and κ_a) extracted from the fits are plotted in Fig. 6.12 as a function of the pump amplitude $\sqrt{P_p}$ in the cavity. The highest pump power we managed to deliver to the device before the NbTiN film entered the normal state in this experiment was -26 dBm, corresponding to a $g = 5.13$ MHz coupling strength between the modes. This g is greater than the total rate of loss for each mode $\kappa_b \approx 2$ MHz and $\kappa_a \approx 0.8$ MHz. Such a strong coupling is possible due to high pump power handling capability of the device. Moreover, as seen in Fig. 6.12 the coupling strength scales linearly with the pump amplitude as predicted by Eq. 6.11.

We can provide an estimate for the pump enhancement of g by calculating the single

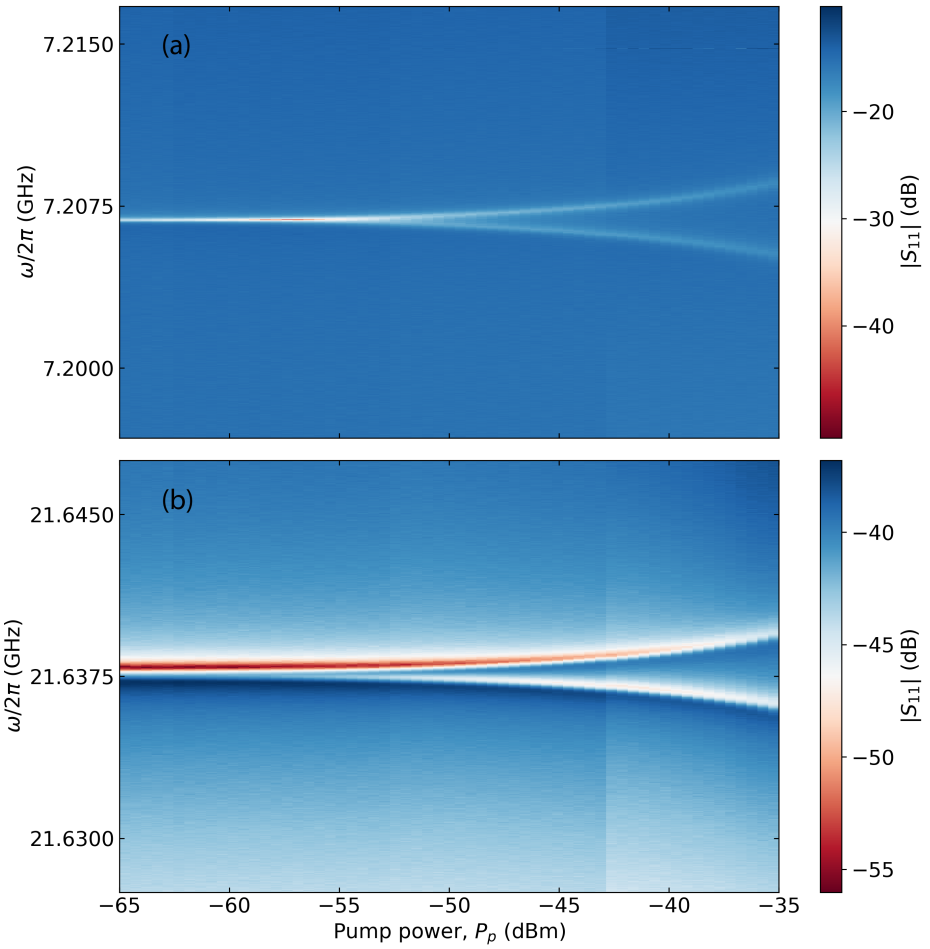

Figure 6.10: Coupling strength g between the modes as a function of the pump power. S_{11} measurements of the device centered on **a)** the fundamental mode and **b)** the first harmonic.

photon coupling strength g_0, obtained using Eq. 6.5. The zero-point fluctuations of the current in mode "b" (Eq. 2.15) is found to be $\delta I_b \approx 20$ nA. The current to frequency conversion factor is found from the biquadratic fit of the frequency tunability data in Fig. 6.8 for mode "a" (restricted to second order in I), performed about the DC bias I_{DC}, i.e. $|\delta\omega_a/\delta I|_{I_{DC}} \approx 2bI_{DC}$. We thus find $g_0 \approx |2bI_{DC}|\delta I_b = 850$ Hz, a value 3-4 orders of magnitude smaller than g. The parametric drive therefore allows us to tune the system from well within the weak coupling regime all the way to strong coupling.

The internal loss rate of the fundamental mode $\kappa_{b,int}$ displays a quadratic dependence on the pump amplitude in Fig. 6.12. This is predicted by theory, where the Purcell-enhanced relaxation rate of mode "b" caused by mode "a" is $\Gamma_b = 4g^2/\kappa_a$.

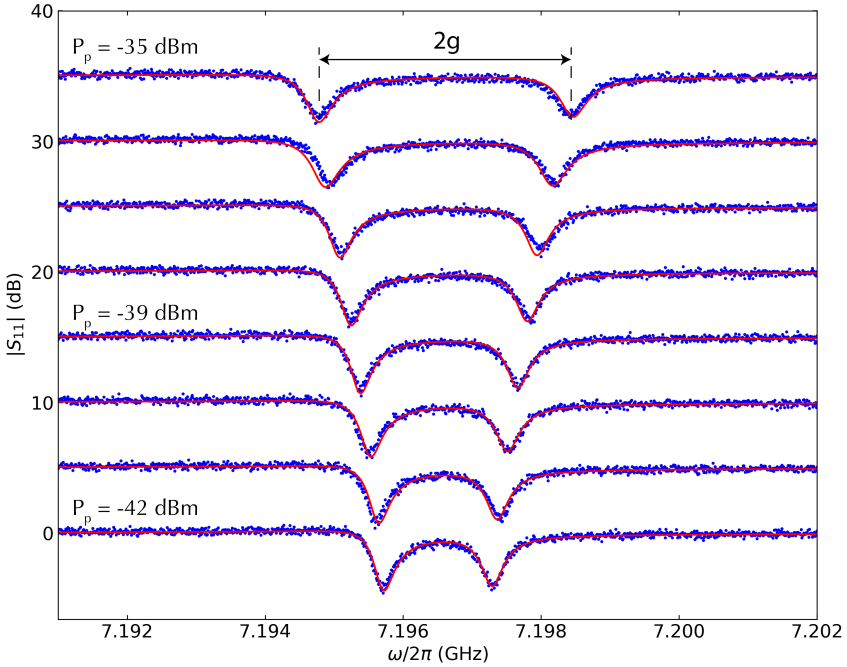

Figure 6.11: Individual S_{11} spectra about the fundamental mode with a fixed-frequency pump of varying power. Data sets are offset by 5 dB for clarity. The pump power increases by 1 dBm for each successive spectra. The red lines are fits to the normal-mode splittings using Eq. 6.20.

Physically, this is caused by photons being up-converted to and dissipated in mode "a" appearing to mode "b" as another channel of loss. Since g scales linearly with $\sqrt{P_p}$, then $\kappa_{b,int} = \kappa_{b,int}(0) + \Gamma_b$ should exhibit a quadratic dependence (where $\kappa_{b,int}(0)$ is the intrinsic loss rate for mode "b" with no pump).

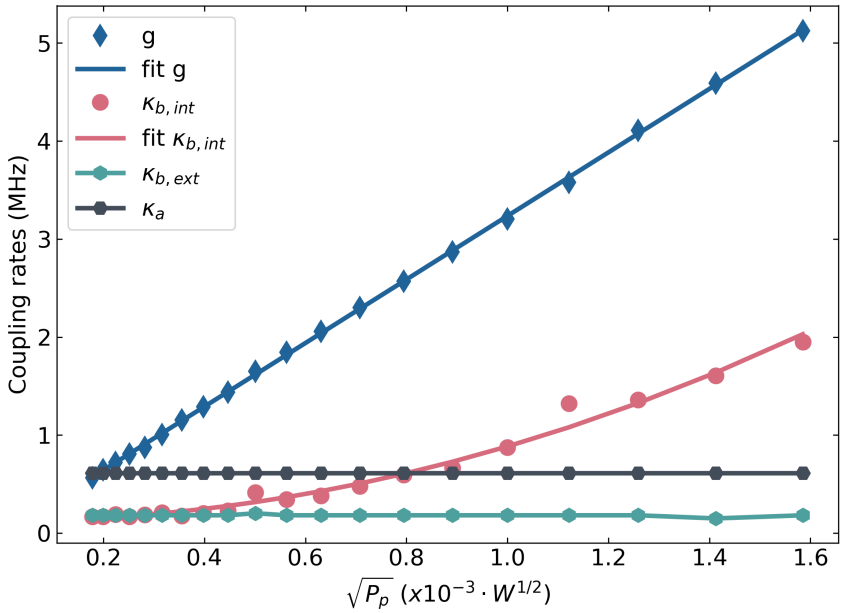

Figure 6.12: The parametric coupling rate g increases linearly with the pump amplitude $\sqrt{P_p}$. This coupling increases the internal loss rate $\kappa_{b,int}$ of the fundamental mode. $\kappa_{b,int}$ follows a quadratic dependence on the pump amplitude starting from its intrinsic value when the pump tone is absent. The external coupling rate $\kappa_{b,ext}$ of the fundamental mode and the linewidth of the first harmonic κ_a remain constant over the sweep.

6.4.3 Spins

The spin system investigated in this chapter is the same as in Ch. 5. Here we study the longitudinal relaxation processes described by the characteristic T_1 time to test if the system is in the Purcell regime, which is one of the requirements for implementing the cooling protocol. We focus on the ESR transition $|F, m_F\rangle = |4, -4\rangle \rightarrow |5, -5\rangle$ (see Sec. 2.5.1), which is found at 6.78 mT.

The Purcell energy relaxation rate of the spins is suppressed quadratically with the frequency detuning $\delta = \omega_0 - \omega_s$ between the cavity and the spin system according to $\Gamma_{phot} = \kappa g_{0s}^2/(\kappa^2/4 + \delta^2)$ (Eq. 2.95). This behavior was explored in the experiments presented in Ref. [48], where the enhanced spontaneous emission of an electron spin ensemble was experimentally demonstrated for the first time (see Fig. 6.13). In this work the electron spin T_1 was controlled over three orders of magnitude simply by detuning the spins from cavity by just a few megahertz.

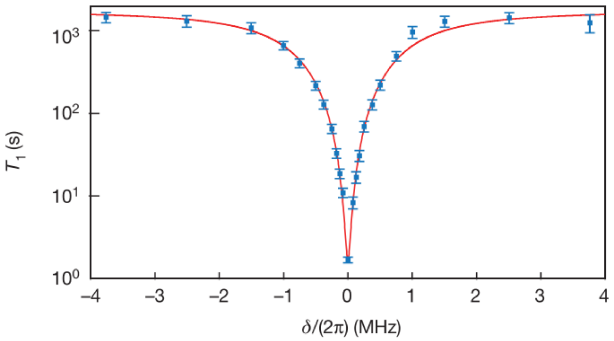

Figure 6.13: Measured T_1 relaxation time as a function of the spin-cavity detuning δ. The data is fit (solid line) to the expected Purcell relaxation rate (Eq. 2.95), confirming the device is in the Purcell regime. Plot taken from Ref. [48].

To test if our electron spin energy relaxation rate is Purcell limited we performed an inversion recovery experiment to measure T_1 (see Sec. 3.6.4) when spins are on-resonance with the cavity $\delta = 0$ and when they are detuned by $\delta/2\pi \approx 10$ MHz during the hold time T_{wait}. The spin-resonator detuning is realized by reducing the DC bias current in the resonator from $I_{DC} = 3.3$ mA to $I_{DC} = 2.8$ mA. The spin magnetization is measured after the wait period using a $N = 200$ CPMG pulse sequence (see Sec. 5.3) with an inter pulse duration of $\tau = 75$ μs. All pulses have a duration of $t_p = 10$ μs. The sequence was repeated 3 times with a repetition of $T_{rep} = 30$ s. The integrated echo quadrature I signals are presented in Fig. 6.14a as a function of T_{wait}. The echo decays are well fitted to an exponential function, allowing us to extract the longitudinal relaxation time $T_{1,on} \approx 600(60)$ ms when spins are resonant with the cavity and $T_{1,off} \approx 780(90)$ ms when cavity is detuned from the spins. Since $\delta/2\pi \gg \kappa$

in the detuned/off-resonance measurement, we would expect a much greater increase in the T_1 if the relaxation was Purcell-limited, indicating that some other mechanism must be dominant.

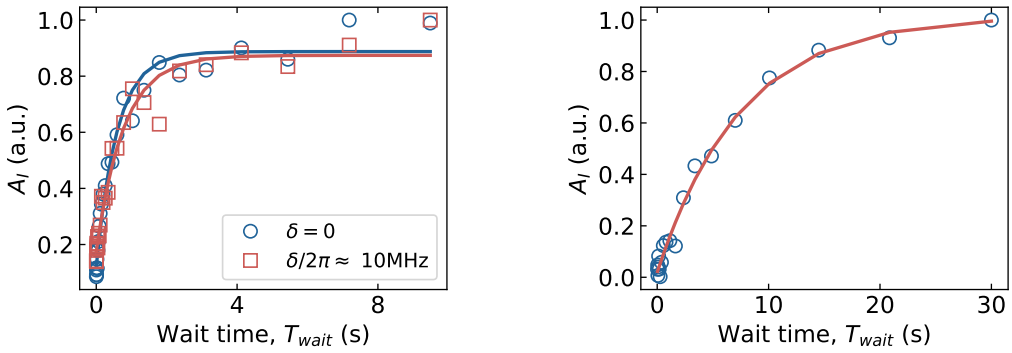

(a) (b)

Figure 6.14: Measurements of the longitudinal relaxation time T_1 for the electron spins. Integrated echo quadrature signal A_I is plotted as a function of the wait time T_{wait} after the spin magnetization is initially disturbed by the first pulse of a sequence. The signal is measured with a $N = 200$ pulse CPMG sequence. **a)** Inversion recovery experiment performed when spin-cavity detuning δ is zero and when $\delta/2\pi \approx 10$ MHz. Fits with exponential functions reveals $T_{1,on} = 600$ ms and $T_{1,off} = 780$ ms when $\delta = 0$ and $\delta \approx 10$ MHz, respectively. **b)** Saturation recovery experiment performed when $\delta = 0$. The exponential fit yields $T_1 = 7.5$ s.

To reveal the other relaxation mechanism we perform a saturation recovery experiment (see Sec. 3.6.4) when the spins are on-resonance with the cavity $\delta = 0$. The integrated echo quadrature response A_I and associated exponential fit is presented in Fig. 6.14b, indicating a $T_1 \approx 7.5$ s. The sequence commences with a 5 s long saturation pulse, followed by the wait period T_{wait} and spin magnetization measurement using a CPMG pulse sequence (see Sec. 5.3). The advantage of the saturation recovery sequence in comparison to an inversion recovery is that the saturation pulse strongly suppresses spin-diffusion relaxation mechanisms [99]. Comparing the values of T_1 obtained in the inversion recovery and saturation recovery measurements, it is clear that the dominant relaxation mechanism for our spin system is spin-diffusion. Spin-diffusion is caused by direct dipolar flip-flops between spins excited by a pulse and spins that are just outside its excitation bandwidth (see Sec. 2.4.1).

6.5 Future directions

To realize parametric cooling of the spins, the Purcell relaxation rate of the spins to the mode, that is actively cooled, should be larger than all other energy relaxation rates experienced by the spins. As presented above, this was unfortunately not the case for the current device, where the spin T_1 was limited by dipolar interactions (i.e. spin diffusion). We may take two approaches to reach the Purcell regime here, the first is to lower the spin diffusion rate and the second is to enhance the Purcell relaxation rate. The spin diffusion rate is strongly dependent on donor concentration, scaling inversely proportional to d^6, where d is the average donor-donor separation. Thus even a small reduction in the donor doping concentration can lead to a considerably longer T_1. We can increase the Purcell relaxation rate (Eq. 2.95) by improving the quality factor of the resonator or raising the spin-photon coupling strength g_s. Whilst there is some scope for small improvements in Q, we believe that more substantial gains will come from enhancing g_s. The Purcell rate scales quadratically with g_s, which itself depends on the distance of the spins from the resonator and the zero-point current fluctuations – factors that combine to determine the strength of the magnetic field fluctuations experienced by the spins. Since $\delta I_b = \omega_b \sqrt{\hbar/2Z_b}$, we must decrease the impedance of the resonator. Given $Z_b \approx 200\ \Omega$ this can readily be achieved by introducing an IDC into the design (Sec. 3.1.2), realistically lowering the impedance below 50 Ω. Adopting these changes should put the spins firmly in the Purcell regime.

Chapter 7

Conclusions

In this chapter we briefly summarize the results presented in this thesis and provide some insights on the future direction of this research.

7.1 Summary

In Ch. 3 we presented a design for a novel high-quality factor superconducting resonator. The resonator, based on CPW technology, is made from a thin film of superconducting NbTiN metal that provides a high fraction of kinetic inductance and behaves as a nonlinear medium for microwaves. Integration of a PBG structure between the resonator and external circuitry allows for a resonance to be confined without breaking the central line, permitting the passage of DC currents through the device. The DC current can be used to alter the kinetic inductance and thus the resonant frequency ω_r. We observed typical shifts of $\omega_r/2\pi$ of $\sim$ 100 MHz for DC currents a couple of milliamperes in strength.

We showed that combining the microwave signal $\omega_s \approx \omega_r$, DC current and a strong pump tone at $\omega_p \approx 2\omega_s$ in the nonlinear resonator produces near-perfect three wave mixing. In this process one pump photon with frequency ω_p splits into two photons; a signal (ω_s) and idler (ω_i) with the idler frequency selected so as to ensure energy conservation $\omega_p = \omega_s + \omega_i$. This mixing produces amplification, which was investigated experimentally in Ch. 4.

We showed that the device, named the KIPA, produces phase-insensitive (or phase preserving) parametric amplification when $\omega_p = 2\omega_s + \Delta\omega$ (where $\Delta\omega$ is within the resonator linewidth). We achieved signal power gains up to 40 dB in this non-degenerate mode of operation. When $\omega_p = 2\omega_s$, the device operates in so-called degenerate mode producing phase-sensitive parametric amplification. In this mode the maximum gain we measured was 50 dB, which is higher than in non-degenerate mode due to constructive interference between the signal and the idler. We found a 1 dB-compression point greater than ≈ -60 dBm for 20 dB of gain, which defines a measure of the maximum power of the input signal that can be effectively amplified. As far as we are aware, this is the highest 1 dB-compression point for any resonant microwave parametric amplifier.

When operated in degenerate mode we demonstrated that the KIPA can be used as an effective microwave squeezer. We measured the amplification and deamplification of a coherent signal which traces out an ellipse (or stretched circle) in the IQ-plane. The lack of any distortion to the ellipses suggests that the KIPA doesn't suffer from squeezing limitations observed in JPA-based phase sensitive amplifiers. Moreover, we performed noise measurements and found the device to operate at the quantum noise limit.

In Ch. 5 the KIPA was employed in spin resonance spectroscopy. Previous high-

sensitivity ESR spectrometers have combined high quality factor superconducting resonators separately with JPA-based quantum limited parametric amplifiers. In our experiments we used a single device, namely the KIPA, as both the cavity for inductive detection of spins and as a first-stage amplifier. This architecture offers a versatile and simple approach for quantum limited ESR where the spins are probed, detected and amplified on-chip with just a single nonlinear cavity. Specifically, we used the KIPA to measure spin echo signals from an electron spin ensemble of bismuth donors in silicon. We achieved an improvement in the SNR of inductively detected spin echo amplitudes by more than ≈ 10 dB comparing to when the parametric amplifier was off. Moreover, we demonstrated that our KIPA can withstand magnetic fields up to 250 mT, a value that allows for ESR of a $g = 2$ spin at the resonator frequency of 7 GHz and therefore of interest to conventional ESR.

In Ch. 6 we discussed the multi-mode nature of the KIPA and how a parametric drive can be used to couple modes together. We measured the coupling between the fundamental (ω_0) and the first harmonic (ω_1) modes as a function of pump power at the difference frequency $\omega_p = \omega_1 - \omega_0$ and were able to achieve interaction strengths of ~ 5 MHz, well into the strong coupling regime. This parametric mode coupling can be used for up-conversion of thermal photons from the fundamental mode to the first harmonic, effectively cooling the fundamental mode. We then presented a scheme to utilize the KIPA for cooling a spin ensemble. When spins are coupled to the fundamental mode and their longitudinal relaxation (T_1) is limited by spontaneous emission of photons into the cavity (Purcell relaxation), the spins will thermalize to this mode. This simple device architecture could therefore be used to cool the spin temperature below that of the cryostat, resulting in an enhanced spin polarization and improved sensitive in ESR. We studied spin relaxation in our device and found T_1 to be limited by spin diffusion and not Purcell relaxation, meaning cooling was not possible. We discussed simple device improvements necessary to successfully implement the proposed protocol.

This thesis has sown that the KIPA is a versatile device with potential use in low-noise microwave measurements. Its large critical magnetic field makes it particularly suited to applications in ESR spectroscopy where it can serve as a first-stage quantum-limited amplifier that is simultaneously able to hyperpolarize the spins. The high critical temperature ($T_c = 13$ K) should also allow operation at temperatures relevant for conventional ESR spectroscopy ($T > 2$ K) and we envisage one day integrating this

device into existing commercial spectrometer systems.

7.2 Future work

In this section we outline the future work based on the key results presented in this thesis.

The kinetic inductance parametric amplifier designed in this thesis has shown itself to be an excellent parametric amplifier that can be operated either in phase insensitive or phase sensitive modes. The latter was used to demonstrate parametric deamplification of a coherent signal. Based on this we believe that the KIPA can be used as an efficient vacuum squeezer and experiments to verify this are already in progress. Vacuum squeezed states can be used to perform measurements beyond the standard quantum limit [191]. This has already be used to enhance the sensitivity of ESR spectroscopy experiments [38]. However, in this work only a modest noise reduction of 1.2 dB was achieved using a JPA squeezer. This was limited by two factors, the first being the limited squeezing performance of a JPA, which experience distortions of the squeezed state typically beyond 10 dB of squeezing. The second factor arises from the microwave losses in the cables and microwave components connecting the squeezer and spins. We believe the first factor might be solved by using the KIPA as the squeezer, due to its higher dynamic range and the observed lack of distortions in our coherent state measurements of Sec. 4.5.

Another important milestone is to realize the implementation of our proposed cooling scheme. As was already noted in Ch. 6 for this to succeed our device must first reach the Purcell regime, which was unfortunately not the case for the device examined. We believe the Purcell regime can be readily accessed by reducing the donor concentration and/or lowering the impedance of the resonator to increase the spin-resonator coupling.

Whilst the discussion in this thesis has focused on spectroscopy applications of our device, another interesting use for the KIPA/spin hybrid system is as a long-lived microwave photon quantum memory [34], [192]. Superconducting quantum bits have emerged as excellent candidates for building a quantum computer, owing to their fast quantum logic gate operations and ease of fabrication [193]. However, superconducting qubits possess relatively short coherence times, of order ten microseconds, which restricts their use as long-term memory elements. Conversely, the electron spins of donors

in silicon have demonstrated coherence times up to 3 seconds [122]. One can exploit the strengths of each system in a hybrid quantum computing architecture, where the superconducting bits are used for processing and the spins for storage, interfaced by a superconducting resonator as a quantum bus [194]. The KIPA offers a high quality factor frequency-tunable resonator that is operable in magnetic fields, and thus is an ideal quantum bus in a spin-based microwave photon quantum memory. We have already demonstrated that the KIPA can be integrated with a highly-coherent bismuth donor spin ensemble in silicon, where $T_2 = 14$ ms was measured using a CPMG dynamical decoupling sequence. This therefore represents a very promising future direction and application of the work developed in this thesis.

Appendix A

Matlab script for photonic bandgap structure

```
clear all; close all;

% SI units everywhere
c=3e8;

Z1=30.9;
Ereff1=8.555;
L1=3400e-6;

Z2=120.3;
Ereff2=9.166;
% L2=L1;
L2=3455e-6;

Z_input=50;
Ereffin=7.294;
L_input=1000e-6;

N_cells=4; %(number of wavelengths)

Y1=1/Z1;
Y2=1/Z2;
Y_input=1/Z_input;

f_start=0;
```

```
26 f_finish=30e9;
27 N=10000;
28 f=linspace(f_start, f_finish, N);
29 omega=2*pi*f;
30 beta1=sqrt(Ereff1)*omega/c;
31 beta2=sqrt(Ereff2)*omega/c;
32 betain=sqrt(Ereffin)*omega/c;
33
34 A1=cos(beta1*L1);
35 B1=1i*Z1*sin(beta1*L1);
36 C1=1i*Y1*sin(beta1*L1);
37 D1=cos(beta1*L1);
38
39 A2=cos(beta2*L2);
40 B2=1i*Z2*sin(beta2*L2);
41 C2=1i*Y2*sin(beta2*L2);
42 D2=cos(beta2*L2);
43
44 S21dB=zeros(1,N);
45
46 %Add 50Ohms input & output
47 A_input=cos(betain*L_input);
48 B_input=1i*Z_input*sin(betain*L_input);
49 C_input=1i*Y_input*sin(betain*L_input);
50 D_input=cos(betain*L_input);
51
52 for n=1:N
53
54     ABCD_input=[A_input(n), B_input(n); C_input(n), D_input(n)];
55     ABCD_1=[A1(n),B1(n); C1(n),D1(n)];
56     ABCD_2=[A2(n),B2(n); C2(n),D2(n)];
57
58     unit_cell=ABCD_1*ABCD_2;
59     ABCD=ABCD_input*unit_cell^N_cells*ABCD_input;
60
61     A=ABCD(1,1);
62     B=ABCD(1,2);
63     C=ABCD(2,1);
64     D=ABCD(2,2);
```

```
65
66      S=abcd2s(ABCD);
67      S21_mag=abs(S(2,1));
68      S21dB(n)=20*log10(S21_mag);
69  end
70  figure;
71  plot(f/1e9,S21dB)
72  xlabel('Frequency (GHz)')
73  ylabel('S21 (dB)')
74
75  length=N_cells*(L1+L2)
```

Appendix B

Photonic bandgap resonator fabrication details

At the beginning of the PBG resonator fabrication process described below we have 330 μm thick silicon chip either implanted with donors in isotopically enriched ^{28}Si epilayer or natural FZ silicon without donors. On top of the silicon chip NbTiN thin film is sputtered. The deposition of this film was outsourced to "Star Cryo" and done by Dr Robin Cantor. Then the wafer was covered with protective layer of PMMA resist and diced into 11 mm by 4 mm pieces using dicing saw.

Cleaning the wafer before NbTiN deposition

1. Place silicon wafer in piranha solution $H_2SO_4 : H_2O_2$ (3:1) for 10 min at 115 °C
2. Rinse in DI water for 10 min
3. Dip the wafer in $HF : H_2O$ (1:10) for 15 s
4. Rinse in DI water for 5 min
5. Dry the wafer with N_2 gas

Step 1 - Cleaning the wafer after dicing

1. ultrasonicate (US) in acetone for $10 - 15$ min
2. US in IPA for 2 min
3. Dry the chip with N_2 gas

Step 2 - Resist spinning

1. Spin AR-P 6200 (CSAR 62) 9% resist at 4000 rpm for 60 s to get 200 nm thick layer
2. Bake at 150 °C for 3 min

Step 3 - E-beam exposure details

- ETH acceleration voltage: 20 kV
- Aperture: 60 μm
- Step size should be smaller than 100 nm
- Base dose should be about 85 $\mu C/cm^2$
- Writing current: $I \approx 1.3$ nA

Step 4 - Resist development

1. Handshake in n-amyl acetate for 60 s
2. Handshake in MIBK:IPA (1:3) for 60 s
3. Handshake in IPA for 30 s

Step 5 - Oxygen ash

O_2 plasma ash at 50 W for 3 min

Step 6 - Reactive ion etching

- Gases: CF_4/Ar with flows 20/10 sccm
- Gas pressure: 38 mTorr
- Power: 30 W
- V_{dc}: 137 V
- V_{pp}: 0.39 kV

- Time: 9 min or 17 min to etch through the 9.5 nm NbTiN or 50 nm NbTiN films respectively

Step 7 - Strip off the resist

1. US in remover AR 600-71 for 30 min
2. Rinse in DI water for 2 min
3. Dry the chip with N_2 gas
4. ultrasonicate (US) in acetone for 8 min
5. US in IPA for 2 min
6. Dry the chip with N_2 gas

References

[1] M. Planck, *Wege zur physikalischen Erkenntnis: Reden und Vortäge*. Hirzel, 1944, vol. 2.

[2] I. Newton, *Newton: philosophical writings*. Cambridge University Press, 2014.

[3] M. Planck. (1918). The nobel prize in physics 2012, [Online]. Available: https://www.nobelprize.org/prizes/physics/1918/summary/. (Accessed: 03.11.2021).

[4] H. Dehmelt, "Experiments with an isolated subatomic particle at rest," *Reviews of modern physics*, vol. 62, no. 3, p. 525, 1990.

[5] S. Haroche and D. Kleppner, "Cavity Quantum Electrodynamics," *Physics Today*, vol. 42, no. 1, p. 24, 1989.

[6] S. Haroche and J. M. Raimond, *Exploring the quantum: atoms, cavities, and photons*. Oxford University Press, 2006.

[7] E. Huss. (2012). The nobel prize in physics 2012, [Online]. Available: https://www.nobelprize.org/prizes/physics/2012/prize-announcement/. (Accessed: 16.12.2020).

[8] H. Walther, B. T. Varcoe, B.-G. Englert, and T. Becker, "Cavity quantum electrodynamics," *Reports on Progress in Physics*, vol. 69, no. 5, p. 1325, 2006.

[9] S. Haroche, M. Brune, and J. Raimond, "From cavity to circuit quantum electrodynamics," *Nature Physics*, pp. 1–4, 2020.

[10] A. Blais, R.-S. Huang, A. Wallraff, S. M. Girvin, and R. J. Schoelkopf, "Cavity quantum electrodynamics for superconducting electrical circuits: An architecture for quantum computation," *Physical Review A*, vol. 69, no. 6, p. 062 320, 2004.

[11] J. M. Martinis, M. H. Devoret, and J. Clarke, "Experimental tests for the quantum behavior of a macroscopic degree of freedom: The phase difference across a josephson junction," *Physical Review B*, vol. 35, no. 10, p. 4682, 1987.

[12] M. A. Nielsen and I. Chuang, *Quantum computation and quantum information*, 2002.

[13] Z. K. Minev, S. O. Mundhada, S. Shankar, P. Reinhold, R. Gutiérrez-Jáuregui, R. J. Schoelkopf, M. Mirrahimi, H. J. Carmichael, and M. H. Devoret, "To catch and reverse a quantum jump mid-flight," *Nature*, vol. 570, no. 7760, pp. 200–204, 2019.

[14] J. Dalibard, Y. Castin, and K. Mølmer, "Wave-function approach to dissipative processes in quantum optics," *Physical review letters*, vol. 68, no. 5, p. 580, 1992.

[15] C. W. Gardiner, A. S. Parkins, and P. Zoller, "Wave-function quantum stochastic differential equations and quantum-jump simulation methods," *Physical Review A*, vol. 46, no. 7, p. 4363, 1992.

[16] J. M. Martinis, M. H. Devoret, and J. Clarke, "Quantum josephson junction circuits and the dawn of artificial atoms," *Nature Physics*, vol. 16, no. 3, pp. 234–237, 2020.

[17] Y. Nakamura, Y. A. Pashkin, and J. S. Tsai, "Coherent control of macroscopic quantum states in a single-cooper-pair box," *Nature*, vol. 398, no. 6730, pp. 786–788, 1999.

[18] J. Mooij, T. Orlando, L. Levitov, L. Tian, C. H. Van der Wal, and S. Lloyd, "Josephson persistent-current qubit," *Science*, vol. 285, no. 5430, pp. 1036–1039, 1999.

[19] J. M. Martinis, S. Nam, J. Aumentado, and C. Urbina, "Rabi oscillations in a large josephson-junction qubit," *Physical Review Letters*, vol. 89, no. 11, p. 117 901, 2002.

[20] J. Koch, M. Y. Terri, J. Gambetta, A. A. Houck, D. Schuster, J. Majer, A. Blais, M. H. Devoret, S. M. Girvin, and R. J. Schoelkopf, "Charge-insensitive qubit design derived from the cooper pair box," *Physical Review A*, vol. 76, no. 4, p. 042 319, 2007.

[21] V. E. Manucharyan, J. Koch, L. I. Glazman, and M. H. Devoret, "Fluxonium: Single cooper-pair circuit free of charge offsets," *Science*, vol. 326, no. 5949, pp. 113–116, 2009.

[22] A. Wallraff, D. I. Schuster, A. Blais, L. Frunzio, R.-S. Huang, J. Majer, S. Kumar, S. M. Girvin, and R. J. Schoelkopf, "Strong coupling of a single photon to a superconducting qubit using circuit quantum electrodynamics," *Nature*, vol. 431, no. 7005, pp. 162–167, 2004.

[23] F. Arute, K. Arya, R. Babbush, D. Bacon, J. C. Bardin, R. Barends, R. Biswas, S. Boixo, F. G. Brandao, D. A. Buell, *et al.*, "Quantum supremacy using a programmable superconducting processor," *Nature*, vol. 574, no. 7779, pp. 505–510, 2019.

[24] A. Clerk, K. Lehnert, P. Bertet, J. Petta, and Y. Nakamura, "Hybrid quantum systems with circuit quantum electrodynamics," *Nature Physics*, pp. 1–11, 2020.

[25] M. V. Gustafsson, T. Aref, A. F. Kockum, M. K. Ekström, G. Johansson, and P. Delsing, "Propagating phonons coupled to an artificial atom," *Science*, vol. 346, no. 6206, pp. 207–211, 2014.

[26] A. D. O'Connell, M. Hofheinz, M. Ansmann, R. C. Bialczak, M. Lenander, E. Lucero, M. Neeley, D. Sank, H. Wang, M. Weides, *et al.*, "Quantum ground state and single-phonon control of a mechanical resonator," *Nature*, vol. 464, no. 7289, pp. 697–703, 2010.

[27] X. Mi, M. Benito, S. Putz, D. M. Zajac, J. M. Taylor, G. Burkard, and J. R. Petta, "A coherent spin-photon interface in silicon," *Nature*, vol. 555, no. 7698, pp. 599–603, 2018.

[28] Y. Kubo, F. Ong, P. Bertet, D. Vion, V. Jacques, D. Zheng, A. Dréau, J.-F. Roch, A. Auffèves, F. Jelezko, *et al.*, "Strong coupling of a spin ensemble to a superconducting resonator," *Physical Review Letters*, vol. 105, no. 14, p. 140 502, 2010.

[29] Y. Tabuchi, S. Ishino, T. Ishikawa, R. Yamazaki, K. Usami, and Y. Nakamura, "Hybridizing ferromagnetic magnons and microwave photons in the quantum limit," *Physical Review Letters*, vol. 113, no. 8, p. 083 603, 2014.

[30] N. J. Lambert, A. Rueda, F. Sedlmeir, and H. G. Schwefel, "Coherent conversion between microwave and optical photons — an overview of physical implementations," *Advanced Quantum Technologies*, vol. 3, no. 1, p. 1 900 077, 2020.

[31] A. Bienfait, J. Pla, Y. Kubo, M. Stern, X. Zhou, C. Lo, C. Weis, T. Schenkel, M. Thewalt, D. Vion, *et al.*, "Reaching the quantum limit of sensitivity in electron spin resonance," *Nature Nanotechnology*, vol. 11, no. 3, p. 253, 2016.

[32] C. W. Zollitsch, J. O'Sullivan, O. Kennedy, G. Dold, and J. J. Morton, "Tuning high-q superconducting resonators by magnetic field reorientation," *AIP Advances*, vol. 9, no. 12, p. 125 225, 2019.

[33] J. T. Muhonen, J. P. Dehollain, A. Laucht, F. E. Hudson, R. Kalra, T. Sekiguchi, K. M. Itoh, D. N. Jamieson, J. C. McCallum, A. S. Dzurak, *et al.*, "Storing quantum information for 30 seconds in a nanoelectronic device," *Nature Nanotechnology*, vol. 9, no. 12, pp. 986–991, 2014.

[34] Y. Kubo, C. Grezes, A. Dewes, T. Umeda, J. Isoya, H. Sumiya, N. Morishita, H. Abe, S. Onoda, T. Ohshima, *et al.*, "Hybrid quantum circuit with a superconducting qubit coupled to a spin ensemble," *Physical Review Letters*, vol. 107, no. 22, p. 220 501, 2011.

[35] V. I. Chizhik, Y. S. Chernyshev, A. V. Donets, V. V. Frolov, A. V. Komolkin, and M. G. Shelyapina, *Magnetic resonance and its applications*. Springer, 2014.

[36] S. Probst, A. Bienfait, P. Campagne-Ibarcq, J. Pla, B. Albanese, J. Da Silva Barbosa, T. Schenkel, D. Vion, D. Esteve, K. Mølmer, *et al.*, "Inductive-detection electron-spin resonance spectroscopy with 65 spins/$\sqrt{\text{Hz}}$ sensitivity," *Applied Physics Letters*, vol. 111, no. 20, p. 202 604, 2017.

[37] V. Ranjan, S. Probst, B. Albanese, T. Schenkel, D. Vion, D. Esteve, J. Morton, and P. Bertet, "Electron spin resonance spectroscopy with femtoliter detection volume," *Applied Physics Letters*, vol. 116, no. 18, p. 184 002, 2020.

[38] A. Bienfait, P. Campagne-Ibarcq, A. Kiilerich, X. Zhou, S. Probst, J. Pla, T. Schenkel, D. Vion, D. Esteve, J. Morton, *et al.*, "Magnetic resonance with squeezed microwaves," *Physical Review X*, vol. 7, no. 4, p. 041 011, 2017.

[39] B. Albanese, S. Probst, V. Ranjan, C. W. Zollitsch, M. Pechal, A. Wallraff, J. J. Morton, D. Vion, D. Esteve, E. Flurin, *et al.*, "Radiative cooling of a spin ensemble," *Nature Physics*, pp. 1–5, 2020.

[40] D. M. Pozar, *Microwave engineering*. John Wiley & Sons, 2011.

[41] U. Vool and M. Devoret, "Introduction to quantum electromagnetic circuits," *International Journal of Circuit Theory and Applications*, vol. 45, no. 7, pp. 897–934, 2017.

[42] A. A. Clerk, M. H. Devoret, S. M. Girvin, F. Marquardt, and R. J. Schoelkopf, "Introduction to Quantum Noise, Measurement, and Amplification: Online Appendices," Tech. Rep., 2009.

[43] D. F. Walls and G. J. Milburn, *Quantum optics*. Springer Science & Business Media, 2007.

[44] B. Yurke and J. S. Denker, "Quantum network theory," *Physical Review A*, vol. 29, no. 3, p. 1419, 1984.

[45] H. B. Chan, V. A. Aksyuk, R. N. Kleiman, D. J. Bishop, and F. Capasso, "Quantum mechanical actuation of microelectromechanical systems by the Casimir force," *Science*, vol. 291, no. 5510, pp. 1941–1944, 2001.

[46] W. E. Lamb Jr and R. C. Retherford, "Fine structure of the hydrogen atom by a microwave method," *Physical Review*, vol. 72, no. 3, p. 241, 1947.

[47] M. Silveri, S. Masuda, V. Sevriuk, K. Y. Tan, M. Jenei, E. Hyyppä, F. Hassler, M. Partanen, J. Goetz, R. E. Lake, *et al.*, "Broadband Lamb shift in an engineered quantum system," *Nature Physics*, vol. 15, no. 6, pp. 533–537, 2019.

[48] A. Bienfait, J. Pla, Y. Kubo, X. Zhou, M. Stern, C. Lo, C. Weis, T. Schenkel, D. Vion, D. Esteve, *et al.*, "Controlling spin relaxation with a cavity," *Nature*, vol. 531, no. 7592, pp. 74–77, 2016.

[49] P. Krantz, M. Kjaergaard, F. Yan, T. P. Orlando, S. Gustavsson, and W. D. Oliver, "A quantum engineer's guide to superconducting qubits," *Applied Physics Reviews*, vol. 6, no. 2, p. 021 318, 2019.

[50] W. Heisenberg, "Schwankungserscheinungen und quantenmechanik," *Zeitschrift für Physik*, vol. 40, no. 7, pp. 501–506, 1927.

[51] M. Planck, "Ueber das Gesetz der Energieverteilung im Normalspectrum," *Annalen der Physik*, vol. 309, no. 3, pp. 553–563, 1901.

[52] A. Einstein, "Über einen die Erzeugung und Verwandlung des Lichtes betreffenden heuristischen Gesichtspunkt," *Annalen der Physik*, vol. 322, no. 6, pp. 132–148, 1905.

[53] C. W. Gardiner and M. J. Collett, "Input and output in damped quantum systems: Quantum stochastic differential equations and the master equation," *Physical Review A*, vol. 31, no. 6, p. 3761, 1985.

[54] A. A. Clerk, M. H. Devoret, S. M. Girvin, F. Marquardt, and R. J. Schoelkopf, "Introduction to Quantum Noise, Measurement, and Amplification," *Reviews of Modern Physics*, vol. 82, no. 2, p. 1155, 2010.

[55] J. Goetz, F. Deppe, M. Haeberlein, F. Wulschner, C. W. Zollitsch, S. Meier, M. Fischer, P. Eder, E. Xie, K. G. Fedorov, E. P. Menzel, A. Marx, and R. Gross, "Loss mechanisms in superconducting thin film microwave resonators," *Journal of Applied Physics*, vol. 119, p. 15 304, 2016.

[56] R. Barends, J. Wenner, M. Lenander, Y. Chen, R. C. Bialczak, J. Kelly, E. Lucero, P. O'Malley, M. Mariantoni, D. Sank, *et al.*, "Minimizing quasiparticle generation from stray infrared light in superconducting quantum circuits," *Applied Physics Letters*, vol. 99, no. 11, p. 113 507, 2011.

[57] E. Belohoubek and E. Denlinger, "Loss Considerations for Microstrip Resonators," *IEEE Transactions on Microwave Theory and Techniques*, vol. 23, no. 6, pp. 522–526, 1975.

[58] J. M. Sage, V. Bolkhovsky, W. D. Oliver, B. Turek, and P. B. Welander, "Study of loss in superconducting coplanar waveguide resonators," *Journal of Applied Physics*, vol. 109, no. 6, p. 063 915, 2011.

[59] A. Houck, J. Schreier, B. Johnson, J. Chow, J. Koch, J. Gambetta, D. Schuster, L. Frunzio, M. Devoret, S. Girvin, *et al.*, "Controlling the spontaneous emission of a superconducting transmon qubit," *Physical Review Letters*, vol. 101, no. 8, p. 080 502, 2008.

[60] J. M. Martinis, K. B. Cooper, R. McDermott, M. Steffen, M. Ansmann, K. Osborn, K. Cicak, S. Oh, D. P. Pappas, R. W. Simmonds, *et al.*, "Decoherence in Josephson qubits from dielectric loss," *Physical Review Letters*, vol. 95, no. 21, p. 210 503, 2005.

[61] J. Gao, M. Daal, A. Vayonakis, S. Kumar, J. Zmuidzinas, B. Sadoulet, B. A. Mazin, P. K. Day, and H. G. Leduc, "Experimental evidence for a surface distribution of two-level systems in superconducting lithographed microwave resonators," *Applied Physics Letters*, vol. 92, no. 15, 2008.

[62] A. D. O'Connell, M. Ansmann, R. C. Bialczak, M. Hofheinz, N. Katz, E. Lucero, C. McKenney, M. Neeley, H. Wang, E. M. Weig, A. N. Cleland, and J. M. Martinis, "Microwave dielectric loss at single photon energies and millikelvin temperatures," *Applied Physics Letters*, vol. 92, no. 11, p. 112 903, 2008.

[63] S. Kwon, A. Fadavi Roudsari, O. W. Benningshof, Y.-C. Tang, H. R. Mohebbi, I. A. Taminiau, D. Langenberg, S. Lee, G. Nichols, D. G. Cory, *et al.*, "Mag-

netic field dependent microwave losses in superconducting niobium microstrip resonators," *Journal of Applied Physics*, vol. 124, no. 3, p. 033 903, 2018.

[64] A. A. Abrikosov, "The magnetic properties of superconducting alloys," *Journal of Physics and Chemistry of Solids*, vol. 2, no. 3, pp. 199–208, 1957.

[65] S. A. Maas, *Nonlinear microwave and RF circuits*. Artech house, 2003.

[66] P. Franken, A. E. Hill, C. e. Peters, and G. Weinreich, "Generation of optical harmonics," *Physical Review Letters*, vol. 7, no. 4, p. 118, 1961.

[67] M. Bass, P. Franken, A. Hill, C. Peters, and G. Weinreich, "Optical mixing," *Physical Review Letters*, vol. 8, no. 1, p. 18, 1962.

[68] S. Akhmanov, A. Kovrigin, A. Piskarskas, V. Fadeev, and R. Khokhlov, "Observation of parametric amplification in the optical range," *Jetp Lett*, vol. 2, no. 7, p. 191, 1965.

[69] R. G. Gould *et al.*, "The LASER, light amplification by stimulated emission of radiation," in *The Ann Arbor conference on optical pumping, the University of Michigan*, vol. 15, 1959, p. 92.

[70] J. Kerr, "On reflection of polarized light from the equatorial surface of a magnet," *The London, Edinburgh, and Dublin Philosophical Magazine and Journal of Science*, vol. 5, no. 30, pp. 161–177, 1878.

[71] E. Jeffrey, D. Sank, J. Mutus, T. White, J. Kelly, R. Barends, Y. Chen, Z. Chen, B. Chiaro, A. Dunsworth, *et al.*, "Fast accurate state measurement with superconducting qubits," *Physical Review Letters*, vol. 112, no. 19, p. 190 504, 2014.

[72] B. Abdo, F. Schackert, M. Hatridge, C. Rigetti, and M. Devoret, "Josephson amplifier for qubit readout," *Applied Physics Letters*, vol. 99, no. 16, p. 162 506, 2011.

[73] F. Mallet, M. Castellanos-Beltran, H. Ku, S. Glancy, E. Knill, K. Irwin, G. Hilton, L. Vale, and K. Lehnert, "Quantum state tomography of an itinerant squeezed microwave field," *Physical Review Letters*, vol. 106, no. 22, p. 220 502, 2011.

[74] X. Zhou, V. Schmitt, P. Bertet, D. Vion, W. Wustmann, V. Shumeiko, and D. Esteve, "High-gain weakly nonlinear flux-modulated Josephson parametric amplifier using a SQUID array," *Physical Review B*, vol. 89, no. 21, p. 214 517, 2014.

[75] I. C. Rodrigues, D. Bothner, and G. A. Steele, "Coupling microwave photons to a mechanical resonator using quantum interference," *Nature Communications*, vol. 10, no. 1, pp. 1–7, 2019.

[76] R. C. Jaklevic, J. Lambe, A. H. Silver, and J. E. Mercereau, "Quantum interference effects in Josephson tunneling," *Physical Review Letters*, vol. 12, no. 7, pp. 159–160, 1964.

[77] B. D. Josephson, "Possible new effects in superconductive tunneling," *Physics Letters*, vol. 1, no. 7, pp. 251–253, 1962.

[78] B. D. Josephson, "Coupled superconductors," *Reviews of Modern Physics*, vol. 36, no. 1, pp. 216–220, 1964.

[79] B. D. Josephson, "Supercurrents through barriers," *Advances in Physics*, vol. 14, no. 56, pp. 419–451, 1965.

[80] Y. P. Reshitnyk, "Nonlinearity and parametric driving in a SQUID-tunable microchip resonator," PhD thesis, 2014.

[81] L. Planat, R. Dassonneville, J. P. Martínez, F. Foroughi, O. Buisson, W. Hasch-Guichard, C. Naud, R. Vijay, K. Murch, and N. Roch, "Understanding the Saturation Power of Josephson Parametric Amplifiers Made from SQUID Arrays," *Physical Review Applied*, vol. 11, no. 3, p. 034 014, 2019.

[82] A. Bienfait, "Magnetic resonance with quantum microwaves," PhD thesis, 2016.

[83] A. Pippard, "The surface impedance of superconductors and normal metals at high frequencies. The anomalous skin effect in normal metals," *Proceedings of the Royal Society of London. Series A. Mathematical and Physical Sciences*, vol. 191, no. 1026, pp. 385–399, 1947.

[84] C. Bockstiegel, Y. Wang, M. R. Vissers, L. F. Wei, S. Chaudhuri, J. Hubmayr, and J. Gao, "A tunable coupler for superconducting microwave resonators using a nonlinear kinetic inductance transmission line," *Applied Physics Letters*, vol. 108, no. 22, p. 222 604, 2016.

[85] J. Gao, M. R. Vissers, M. O. Sandberg, F. C. Da Silva, S. W. Nam, D. P. Pappas, D. S. Wisbey, E. C. Langman, S. R. Meeker, B. A. Mazin, H. G. Leduc, J. Zmuidzinas, and K. D. Irwin, "A titanium-nitride near-infrared kinetic inductance photon-counting detector and its anomalous electrodynamics," *Applied Physics Letters*, vol. 101, no. 14, p. 142 602, 2012.

[86] P. K. Day, H. G. LeDuc, B. A. Mazin, A. Vayonakis, and J. Zmuidzinas, "A broadband superconducting detector suitable for use in large arrays," *Nature*, vol. 425, no. 6960, pp. 817–821, 2003.

[87] H. G. LeDuc, B. Bumble, P. K. Day, B. H. Eom, J. Gao, S. Golwala, B. A. Mazin, S. McHugh, A. Merrill, D. C. Moore, O. Noroozian, A. D. Turner, and J. Zmuidzinas, "Titanium nitride films for ultrasensitive microresonator detectors," *Applied Physics Letters*, vol. 97, no. 10, p. 102 509, 2010.

[88] J. Zmuidzinas, "Superconducting Microresonators: Physics and Applications," *Annual Review of Condensed Matter Physics*, vol. 3, no. 1, pp. 169–214, 2012.

[89] J. Bardeen, L. N. Cooper, and J. R. Schrieffer, "Theory of superconductivity," *Physical Review*, vol. 108, no. 5, pp. 1175–1204, 1957.

[90] J. Bardeen, L. N. Cooper, and J. R. Schrieffer, "Microscopic theory of superconductivity," *Physical Review*, vol. 106, no. 1, pp. 162–164, 1957.

[91] D. C. Mattis and J. Bardeen, "Theory of the anomalous skin effect in normal and superconducting metals," *Physical Review*, vol. 111, no. 2, pp. 412–417, 1958.

[92] A. J. Annunziata, D. F. Santavicca, L. Frunzio, G. Catelani, M. J. Rooks, A. Frydman, and D. E. Prober, "Tunable superconducting nanoinductors," *Nanotechnology*, vol. 21, no. 44, 2010.

[93] A. Anthore, H. Pothier, and D. Esteve, "Density of states in a superconductor carrying a supercurrent," *Physical Review Letters*, vol. 90, no. 12, p. 127 001, 2003.

[94] J. B. Johnson, "Thermal agitation of electricity in conductors," *Physical Review*, vol. 32, no. 1, p. 97, 1928.

[95] H. Nyquist, "Thermal agitation of electric charge in conductors," *Physical Review*, vol. 32, no. 1, p. 110, 1928.

[96] D. H. Slichter, "Quantum jumps and measurement backaction in a superconducting qubit," PhD thesis, 2011.

[97] H. A. Haus and J. Mullen, "Quantum noise in linear amplifiers," *Physical Review*, vol. 128, no. 5, p. 2407, 1962.

[98] C. M. Caves, "Quantum limits on noise in linear amplifiers," *Physical Review D*, vol. 26, no. 8, p. 1817, 1982.

[99] A. Schweiger and G. Jeschke, *Principles of pulse electron paramagnetic resonance*. Oxford University Press on Demand, 2001.

[100] A. Abragam, *The principles of nuclear magnetism*. Oxford University Press, 1961.

[101] G. Feher, "Electron spin resonance experiments on donors in silicon. Electronic structure of donors by the electron nuclear double resonance technique," *Physical Review*, vol. 114, no. 5, p. 1219, 1959.

[102] J. Klauder and P. Anderson, "Spectral diffusion decay in spin resonance experiments," *Physical Review*, vol. 125, no. 3, p. 912, 1962.

[103] A. M. Tyryshkin, S. Tojo, J. J. Morton, H. Riemann, N. V. Abrosimov, P. Becker, H. J. Pohl, T. Schenkel, M. L. Thewalt, K. M. Itoh, and S. A. Lyon, "Electron spin coherence exceeding seconds in high-purity silicon," *Nature Materials*, vol. 11, no. 2, pp. 143–147, 2012.

[104] E. L. Hahn, "Spin echoes," *Physical Review*, vol. 80, no. 4, p. 580, 1950.

[105] E. T. Jaynes and F. W. Cummings, "Comparison of quantum and semiclassical radiation theories with application to the beam maser," *Proceedings of the IEEE*, vol. 51, no. 1, pp. 89–109, 1963.

[106] T. Niemczyk, F. Deppe, H. Huebl, E. Menzel, F. Hocke, M. Schwarz, J. Garcia-Ripoll, D. Zueco, T. Hümmer, E. Solano, *et al.*, "Circuit quantum electrodynamics in the ultrastrong-coupling regime," *Nature Physics*, vol. 6, no. 10, pp. 772–776, 2010.

[107] F. Yoshihara, T. Fuse, S. Ashhab, K. Kakuyanagi, S. Saito, and K. Semba, "Superconducting qubit-oscillator circuit beyond the ultrastrong-coupling regime," *Nature Physics*, vol. 13, no. 1, pp. 44–47, 2017.

[108] M. Afzelius and C. Simon, "Impedance-matched cavity quantum memory," *Physical Review A*, vol. 82, no. 2, p. 022 310, 2010.

[109] M. Afzelius, N. Sangouard, G. Johansson, M. Staudt, and C. Wilson, "Proposal for a coherent quantum memory for propagating microwave photons," *New Journal of Physics*, vol. 15, no. 6, p. 065 008, 2013.

[110] E. M. Purcell, "Spontaneous emission probabilities at radio frequencies," *Physical Review*, vol. 69, p. 681, 1946.

[111] E. M. Purcell, "Spontaneous emission probabilities at radio frequencies," in *Confined Electrons and Photons*, Springer, 1995, pp. 839–839.

[112] M. D. Reed, B. R. Johnson, A. A. Houck, L. DiCarlo, J. M. Chow, D. I. Schuster, L. Frunzio, and R. J. Schoelkopf, "Fast reset and suppressing spontaneous emission of a superconducting qubit," *Applied Physics Letters*, vol. 96, no. 20, p. 203 110, 2010.

[113] S. B. Tenberg, S. Asaad, M. T. Mądzik, M. A. Johnson, B. Joecker, A. Laucht, F. E. Hudson, K. M. Itoh, A. M. Jakob, B. C. Johnson, *et al.*, "Electron spin relaxation of single phosphorus donors in metal-oxide-semiconductor nanoscale devices," *Physical Review B*, vol. 99, no. 20, p. 205 306, 2019.

[114] K. M. Itoh and H. Watanabe, "Isotope engineering of silicon and diamond for quantum computing and sensing applications," *MRS communications*, vol. 4, no. 4, pp. 143–157, 2014.

[115] J. P. Gordon and K. D. Bowers, "Microwave spin echoes from donor electrons in silicon," *Physical Review Letters*, vol. 1, no. 10, pp. 368–370, 1958.

[116] K. Saeedi, S. Simmons, J. Z. Salvail, P. Dluhy, H. Riemann, N. V. Abrosimov, P. Becker, H. J. Pohl, J. J. Morton, and M. L. Thewalt, "Room-temperature quantum bit storage exceeding 39 minutes using ionized donors in silicon-28," *Science*, vol. 342, no. 6160, pp. 830–833, 2013.

[117] B. E. Kane, "A silicon-based nuclear spin quantum computer," *Nature*, vol. 393, no. 6681, pp. 133–137, 1998.

[118] S. Asaad, V. Mourik, B. Joecker, M. A. Johnson, A. D. Baczewski, H. R. Firgau, M. T. Mądzik, V. Schmitt, J. J. Pla, F. E. Hudson, *et al.*, "Coherent electrical control of a single high-spin nucleus in silicon," *Nature*, vol. 579, no. 7798, pp. 205–209, 2020.

[119] R. E. George, W. Witzel, H. Riemann, N. V. Abrosimov, N. Nötzel, M. L. Thewalt, and J. J. Morton, "Electron spin coherence and electron nuclear double resonance of Bi donors in natural Si," *Physical Review Letters*, vol. 105, no. 6, p. 067 601, 2010.

[120] N. Butler, P. Fisher, and A. Ramdas, "Excitation spectrum of bismuth donors in silicon," *Physical Review B*, vol. 12, no. 8, p. 3200, 1975.

[121] M. H. Mohammady, G. W. Morley, and T. S. Monteiro, "Bismuth qubits in silicon: The role of EPR cancellation resonances," *Physical Review Letters*, vol. 105, no. 6, p. 067 602, 2010.

[122] G. Wolfowicz, A. M. Tyryshkin, R. E. George, H. Riemann, N. V. Abrosimov, P. Becker, H. J. Pohl, M. L. Thewalt, S. A. Lyon, and J. J. Morton, "Atomic clock transitions in silicon-based spin qubits," *Nature Nanotechnology*, vol. 8, no. 8, pp. 561–564, 2013.

[123] M. Mohammady, G. Morley, A. Nazir, and T. Monteiro, "Analysis of quantum coherence in bismuth-doped silicon: A system of strongly coupled spin qubits," *Physical Review B*, vol. 85, no. 9, p. 094 404, 2012.

[124] A. T. Asfaw, A. J. Sigillito, A. M. Tyryshkin, T. Schenkel, and S. A. Lyon, "Multi-frequency spin manipulation using rapidly tunable superconducting coplanar waveguide microresonators," *Applied Physics Letters*, vol. 111, no. 3, p. 032 601, 2017.

[125] R. N. Simons, *Coplanar waveguide circuits, components, and systems*. John Wiley & Sons, 2004, vol. 165.

[126] M. Göppl, A. Fragner, M. Baur, R. Bianchetti, S. Filipp, J. M. Fink, P. J. Leek, G. Puebla, L. Steffen, and A. Wallraff, "Coplanar waveguide resonators for circuit quantum electrodynamics," *Journal of Applied Physics*, vol. 104, no. 11, p. 113 904, 2008.

[127] M. J. Hartmann, "Quantum simulation with interacting photons," *Journal of Optics*, vol. 18, no. 10, p. 104 005, 2016.

[128] A. J. Sigillito, "Electrical manipulation of donor spin qubits in silicon and germanium," PhD thesis, 2017.

[129] H. Riemann, N. Abrosimov, and N. Noetzel, "Doping of Silicon Crystals with Bi and other Volatile Elements by the Pedestal Growth Technique," *ECS Transactions*, vol. 3, no. 4, pp. 53–59, 2019.

[130] T. Nishinaga, *Handbook of Crystal Growth: Fundamentals*. Elsevier, 2014.

[131] W. G. Pfann, *Zone melting*. John Wiley & Sons, 1966.

[132] J. F. Ziegler, M. D. Ziegler, and J. P. Biersack, "SRIM-The stopping and range of ions in matter," *Nuclear Instruments and Methods in Physics Research Section B: Beam Interactions with Materials and Atoms*, vol. 268, no. 11-12, pp. 1818–1823, 2010.

[133] E. Abramof, A. Ferreira Da Silva, B. E. Sernelius, J. P. De Souza, and H. Boudinov, "Metal-nonmetal transition and resistivity of silicon implanted with bismuth," *Journal of Materials Research*, vol. 12, no. 3, pp. 641–645, 1997.

[134] G. Hobler, "Critical angles and low-energy limits to ion channeling in silicon," *Radiation effects and defects in solids*, vol. 139, no. 1, pp. 21–85, 1996.

[135] C. Weis, C. Lo, V. Lang, A. Tyryshkin, R. George, K. Yu, J. Bokor, S. A. Lyon, J. Morton, and T. Schenkel, "Electrical activation and electron spin resonance measurements of implanted bismuth in isotopically enriched silicon-28," *Applied Physics Letters*, vol. 100, no. 17, p. 172 104, 2012.

[136] D. Holmes, W. Lawrie, B. Johnson, A. Asadpoordarvish, J. McCallum, D. McCamey, and D. Jamieson, "Activation and electron spin resonance of near-surface implanted bismuth donors in silicon," *Physical Review Materials*, vol. 3, no. 8, p. 083 403, 2019.

[137] D. M. O. Ltd. (2020). Micro writer ml3 pro, [Online]. Available: https://www.durhammagnetooptics.com/?product=microwriter. (accessed: 18.12.2020).

[138] D. I. Schuster, "Circuit quantum electrodynamics," PhD thesis, 2007.

[139] A. Webb, "Cavity- and waveguide-resonators in electron paramagnetic resonance, nuclear magnetic resonance, and magnetic resonance imaging," *Progress in Nuclear Magnetic Resonance Spectroscopy*, vol. 83, pp. 1–20, 2014.

[140] J. R. Ball, Y. Yamashiro, H. Sumiya, S. Onoda, T. Ohshima, J. Isoya, D. Konstantinov, and Y. Kubo, "Loop-gap microwave resonator for hybrid quantum systems," *Applied Physics Letters*, vol. 112, no. 20, p. 204 102, 2018.

[141] I. Rosu, "Microstrip, stripline, and cpw design," *YO3DAC/VA3IUL*, 2012.

[142] J. R. Clem and K. K. Berggren, "Geometry-dependent critical currents in superconducting nanocircuits," *Physical Review B*, vol. 84, no. 17, p. 174 510, 2011.

[143] H. L. Hortensius, E. F. C. Driessen, T. M. Klapwijk, K. K. Berggren, and J. R. Clem, "Critical-current reduction in thin superconducting wires due to current crowding," *Applied Physics Letters*, vol. 100, no. 18, pp. 1–5, 2012.

[144] F. Pobell, *Matter and Methods at Low Temperatures*. Springer, 2007.

[145] M. Biercuk, A. Doherty, and H. Uys, "Dynamical decoupling sequence construction as a filter-design problem," *Journal of Physics B: Atomic, Molecular and Optical Physics*, vol. 44, no. 15, p. 154 002, 2011.

[146] R. Weber and E. ELEXSYS, "580 Pulse EPR Spectrometer Users Manual," *EPR Division Bruker BioSpin Corporation USA*, 2001.

[147] G. Khutsishvili, "Spin diffusion," *Soviet Physics Uspekhi*, vol. 8, no. 5, p. 743, 1966.

[148] H. Y. Carr and E. M. Purcell, "Effects of diffusion on free precession in nuclear magnetic resonance experiments," *Physical Review*, vol. 94, no. 3, p. 630, 1954.

[149] S. Meiboom and D. Gill, "Modified spin-echo method for measuring nuclear relaxation times," *Review of Scientific Instruments*, vol. 29, no. 8, pp. 688–691, 1958.

[150] F. Mentink-Vigier, A. Collauto, A. Feintuch, I. Kaminker, V. Tarle, and D. Goldfarb, "Increasing sensitivity of pulse EPR experiments using echo train detection schemes," *Journal of Magnetic Resonance*, vol. 236, pp. 117–125, 2013.

[151] J. Heinsoo, C. K. Andersen, A. Remm, S. Krinner, T. Walter, Y. Salathé, S. Gasparinetti, J.-C. Besse, A. Potočnik, A. Wallraff, *et al.*, "Rapid high-fidelity multiplexed readout of superconducting qubits," *Physical Review Applied*, vol. 10, no. 3, p. 034 040, 2018.

[152] S. Lamoreaux, K. Van Bibber, K. Lehnert, and G. Carosi, "Analysis of single-photon and linear amplifier detectors for microwave cavity dark matter axion searches," *Physical Review D*, vol. 88, no. 3, p. 035 020, 2013.

[153] M. Castellanos-Beltran, K. Irwin, G. Hilton, L. Vale, and K. Lehnert, "Amplification and squeezing of quantum noise with a tunable josephson metamaterial," *Nature Physics*, vol. 4, no. 12, pp. 929–931, 2008.

[154] C. Eichler, Y. Salathe, J. Mlynek, S. Schmidt, and A. Wallraff, "Quantum-limited amplification and entanglement in coupled nonlinear resonators," *Physical Review Letters*, vol. 113, no. 11, p. 110 502, 2014.

[155] M. Malnou, D. Palken, L. R. Vale, G. C. Hilton, and K. Lehnert, "Optimal operation of a josephson parametric amplifier for vacuum squeezing," *Physical Review Applied*, vol. 9, no. 4, p. 044 023, 2018.

[156] S. Boutin, D. M. Toyli, A. V. Venkatramani, A. W. Eddins, I. Siddiqi, and A. Blais, "Effect of higher-order nonlinearities on amplification and squeezing in josephson parametric amplifiers," *Physical Review Applied*, vol. 8, no. 5, p. 054 030, 2017.

[157] C. Macklin, K. O'Brien, D. Hover, M. Schwartz, V. Bolkhovsky, X. Zhang, W. Oliver, and I. Siddiqi, "A near–quantum-limited josephson traveling-wave parametric amplifier," *Science*, vol. 350, no. 6258, pp. 307–310, 2015.

[158] C. Eichler and A. Wallraff, "Controlling the dynamic range of a josephson parametric amplifier," *EPJ Quantum Technology*, vol. 1, no. 1, p. 2, 2014.

[159] M. R. Vissers, R. P. Erickson, H.-S. Ku, L. Vale, X. Wu, G. Hilton, and D. P. Pappas, "Low-noise kinetic inductance traveling-wave amplifier using three-wave mixing," *Applied Physics Letters*, vol. 108, no. 1, p. 012 601, 2016.

[160] M. Malnou, M. Vissers, J. Wheeler, J. Aumentado, J. Hubmayr, J. Ullom, and J. Gao, "A three-wave mixing kinetic inductance traveling-wave amplifier with near-quantum-limited noise performance," *arXiv preprint arXiv:2007.00638*, 2020.

[161] R. P. Erickson and D. P. Pappas, "Theory of multiwave mixing within the superconducting kinetic-inductance traveling-wave amplifier," *Physical Review B*, vol. 95, no. 10, p. 104 506, 2017.

[162] G. Milburn and D. Walls, "Production of squeezed states in a degenerate parametric amplifier," *Optics Communications*, vol. 39, no. 6, pp. 401–404, 1981.

[163] D. Parker, "Parametric amplification and squeezing with a superconducting resonator," Master's thesis, 2021.

[164] A. Bengtsson, P. Krantz, M. Simoen, I.-M. Svensson, B. Schneider, V. Shumeiko, P. Delsing, and J. Bylander, "Nondegenerate parametric oscillations in a tunable superconducting resonator," *Physical Review B*, vol. 97, no. 14, p. 144 502, 2018.

[165] B. H. Eom, P. K. Day, H. G. LeDuc, and J. Zmuidzinas, "A wideband, low-noise superconducting amplifier with high dynamic range," *Nature Physics*, vol. 8, no. 8, pp. 623–627, 2012.

[166] J. Aasi, J. Abadie, B. Abbott, R. Abbott, T. Abbott, M. Abernathy, C. Adams, T. Adams, P. Addesso, R. Adhikari, *et al.*, "Enhanced sensitivity of the ligo gravitational wave detector by using squeezed states of light," *Nature Photonics*, vol. 7, no. 8, pp. 613–619, 2013.

[167] M. H. Devoret and R. J. Schoelkopf, "Superconducting circuits for quantum information: An outlook," *Science*, vol. 339, no. 6124, pp. 1169–1174, 2013.

[168] C. Eichler, A. Sigillito, S. A. Lyon, and J. R. Petta, "Electron spin resonance at the level of 10^4 spins using low impedance superconducting resonators," *Physical Review Letters*, vol. 118, no. 3, p. 037 701, 2017.

[169] S. Probst, F. B. Song, P. A. Bushev, A. V. Ustinov, and M. Weides, "Efficient and robust analysis of complex scattering data under noise in microwave resonators," *Review of Scientific Instruments*, vol. 86, no. 2, p. 24 706, 2015.

[170] M. S. Khalil, M. J. A. Stoutimore, F. C. Wellstood, and K. D. Osborn, "An analysis method for asymmetric resonator transmission applied to superconducting devices," *Journal of Applied Physics*, vol. 111, no. 5, p. 054 510, 2012.

[171] N. Kirsh, E. Svetitsky, A. L. Burin, M. Schechter, and N. Katz, "Revealing the nonlinear response of a tunneling two-level system ensemble using coupled modes," *Physical Review Materials*, vol. 1, no. 1, p. 012 601, 2017.

[172] C. C. Chin, D. E. Oates, G. Dresselhaus, and M. S. Dresselhaus, "Nonlinear electrodynamics of superconducting NbN and Nb thin films at microwave frequencies," *Physical Review B*, vol. 45, no. 9, pp. 4788–4798, 1992.

[173] B. Abdo, E. Arbel-Segev, O. Shtempluck, and E. Buks, "Observation of bifurcations and hysteresis in nonlinear NbN superconducting microwave resonators," *IEEE Transactions on Applied Superconductivity*, vol. 16, no. 4, pp. 1976–1986, 2006.

[174] J. Pla, A. Bienfait, G. Pica, J. Mansir, F. Mohiyaddin, Z. Zeng, Y.-M. Niquet, A. Morello, T. Schenkel, J. Morton, *et al.*, "Strain-induced spin-resonance shifts in silicon devices," *Physical Review Applied*, vol. 9, no. 4, p. 044 014, 2018.

[175] V. Ranjan, S. Probst, B. Albanese, A. Doll, O. Jacquot, E. Flurin, R. Heeres, D. Vion, D. Esteve, J. Morton, *et al.*, "Pulsed electron spin resonance spectroscopy in the purcell regime," *Journal of Magnetic Resonance*, vol. 310, p. 106 662, 2020.

[176] J. O'Sullivan, O. W. Kennedy, C. W. Zollitsch, M. Šimėnas, C. N. Thomas, L. V. Abdurakhimov, S. Withington, and J. J. Morton, "Spin-resonance linewidths of bismuth donors in silicon coupled to planar microresonators," *Physical Review Applied*, vol. 14, no. 6, p. 064 050, 2020.

[177] T. V. Duzer and C. W. Turner, *Principles of superconductive devices and circuits*, 2nd ed. Prentice Hall PTR, 1999.

[178] B. Julsgaard, C. Grezes, P. Bertet, and K. Mølmer, "Quantum memory for microwave photons in an inhomogeneously broadened spin ensemble," *Physical review letters*, vol. 110, no. 25, p. 250 503, 2013.

[179] V. Ranjan, B. Albanese, E. Albertinale, E. Billaud, D. Flanigan, J. Pla, T. Schenkel, D. Vion, D. Esteve, E. Flurin, *et al.*, "Spatially-resolved decoherence of donor spins in silicon strained by a metallic electrode," *arXiv preprint arXiv:2101.04391*, 2021.

[180] S. Probst, V. Ranjan, Q. Ansel, R. Heeres, B. Albanese, E. Albertinale, D. Vion, D. Esteve, S. J. Glaser, D. Sugny, *et al.*, "Shaped pulses for transient compensation in quantum-limited electron spin resonance spectroscopy," *Journal of Magnetic Resonance*, vol. 303, pp. 42–47, 2019.

[181] C. Eichler and J. R. Petta, "Realizing a circuit analog of an optomechanical system with longitudinally coupled superconducting resonators," *Physical Review Letters*, vol. 120, no. 22, p. 227 702, 2018.

[182] M. Aspelmeyer, T. J. Kippenberg, and F. Marquardt, "Cavity optomechanics," *Reviews of Modern Physics*, vol. 86, no. 4, p. 1391, 2014.

[183] C. Law, "Interaction between a moving mirror and radiation pressure: A Hamiltonian formulation," *Physical Review A*, vol. 51, no. 3, p. 2537, 1995.

[184] J. Johansson, G. Johansson, and F. Nori, "Optomechanical-like coupling between superconducting resonators," *Physical Review A*, vol. 90, no. 5, p. 053 833, 2014.

[185] F. Marquardt, J. P. Chen, A. A. Clerk, and S. Girvin, "Quantum theory of cavity-assisted sideband cooling of mechanical motion," *Physical Review Letters*, vol. 99, no. 9, p. 093 902, 2007.

[186] F. Marquardt, A. Clerk, and S. Girvin, "Quantum theory of optomechanical cooling," *Journal of Modern Optics*, vol. 55, no. 19-20, pp. 3329–3338, 2008.

[187] I. Wilson-Rae, N. Nooshi, W. Zwerger, and T. J. Kippenberg, "Theory of ground state cooling of a mechanical oscillator using dynamical backaction," *Physical Review Letters*, vol. 99, no. 9, p. 093 901, 2007.

[188] J. D. Teufel, T. Donner, D. Li, J. W. Harlow, M. S. Allman, K. Cicak, A. J. Sirois, J. D. Whittaker, K. W. Lehnert, and R. W. Simmonds, "Sideband cooling of micromechanical motion to the quantum ground state," *Nature*, vol. 475, no. 7356, pp. 359–363, 2011.

[189] J. M. Dobrindt, I. Wilson-Rae, and T. J. Kippenberg, "Parametric normal-mode splitting in cavity optomechanics," *Physical Review Letters*, vol. 101, no. 26, p. 263 602, 2008.

[190] N. Manson, J. Harrison, and M. Sellars, "Nitrogen-vacancy center in diamond: Model of the electronic structure and associated dynamics," *Physical Review B*, vol. 74, no. 10, p. 104 303, 2006.

[191] R. Movshovich, B. Yurke, P. Kaminsky, A. Smith, A. Silver, R. Simon, and M. Schneider, "Observation of zero-point noise squeezing via a josephson-parametric amplifier," *Physical Review Letters*, vol. 65, no. 12, p. 1419, 1990.

[192] C. Grezes, B. Julsgaard, Y. Kubo, W. Ma, M. Stern, A. Bienfait, K. Nakamura, J. Isoya, S. Onoda, T. Ohshima, *et al.*, "Storage and retrieval of microwave fields at the single-photon level in a spin ensemble," *Physical Review A*, vol. 92, no. 2, p. 020 301, 2015.

[193] R. Schoelkopf and S. Girvin, "Wiring up quantum systems," *Nature*, vol. 451, no. 7179, pp. 664–669, 2008.

[194] J. H. Wesenberg, A. Ardavan, G. A. D. Briggs, J. J. Morton, R. J. Schoelkopf, D. I. Schuster, and K. Mølmer, "Quantum computing with an electron spin ensemble," *Physical Review Letters*, vol. 103, no. 7, p. 070 502, 2009.